www.impactmin.eu

IMPACT MONITORING
OF MINERAL RESOURCES
EXPLOITATION

CONTRACT Nº
2 4 4 1 6 6

Funded by:
European Commission
Framework Programme 7

Cooperation

Thematic Area
Environment 6.4
Earth Observation and assessment tools for sustainable development

WP7 – DEMO-SITE IMPLEMENTATION

DELIVERABLE D.7.4
REPORT ON CHELYABINSK-ORENBURG CASE STUDY INVESTIGATIONS

Compiled by
Pavel Aminov - IMIN, Institute of Mineralogy, Russian Academy of Sciences, Russia
Ben Williamson - UNEXE, University of Exeter - Camborne School of Mines, UK
Marc Goossens - Geosense B.V., the Netherlands
Valery Udachin - IMIN, Institute of Mineralogy, Russian Academy of Sciences, Russia
William Purvis - UNEXE, University of Exeter - Camborne School of Mines, UK
Carolien Tote - VITO, Flemish Institute for Technological Research, Belgium
Ils Reusen - VITO, Flemish Institute for Technological Research, Belgium
Stephanie Delalieux - VITO, Flemish Institute for Technological Research, Belgium
Oleg Telenkov - IMIN, Institute of Mineralogy, Russian Academy of Sciences, Russia
Calin Baciu - UBB, Universitatea Babes Bolyai, Romania

Submitted by:
GEONARDO Environmental Technologies Ltd.
(Project Coordinator)

Project Coordinator name:
Mr. Peter Gyuris

Project Coordinator organization name:
GEONARDO, Hungary

SEVENTH FRAMEWORK PROGRAMME

EXECUTIVE SUMMARY

This report contains details of the Earth observation studies for the Chelyabinsk-Orenburg regions of the southern Urals of Russia. Two 'demo' sites were selected for study which show a representative range of mining-related contamination in the South Urals, and from different climatic/vegetative zones: Karabash in the Chelyabinsk district, in the South Taiga vegetative zone (moderate continental climate), and Mednogorsk in the Orenburg district, in the Steppe zone (strong continental climate). Sources of contaminants in Karabash include a Cu smelter, metallurgical and mine waste dumps, tailings, abandoned underground mine workings and contaminated soils and sediments.

The Mednogorsk site contains an active Cu smelter, 2 abandoned open pit mines (now pit lakes), metallurgical and mine waste dumps and tailings, a water treatment plant, and an abandoned underground mine and beneficiation mill. Studies undertaken in 2001-2002 at the Karabash site, as part of the FP5 MinUrals contract (ICA2-CT-2000-10011) and a Royal Society Joint Collaborative grant showed that atmospheric SO_2 and metal-rich particulate emissions from the Karabash smelter were of most immediate environmental concern, likely to be impacting on human health and ecosystems for more than 30km from the smelter. Low cost, discreet and sensitive methodologies were developed to assess the temporal and special fallout of particulates from the smelter, including the sampling of snow, pine needles, garden vegetables, lake sediments, lichen transplants and soils. Surface water and stream and lake sediment sampling was carried out to assess the extent of contamination from acid rock/mine drainage from wastes, tailings and abandoned mine workings and effluents from the smelters and processing plants.

The most successful of these methodologies were repeated for Karabash under the ImpactMin project, to both 'ground truth' data obtained from remote sensing studies and to determine if the installation of new 'cleaner' smelter technologies in 2006 have been effective. At Mednogorsk, because of the very different climatic and vegetative conditions, tree and epiphytic lichen studies could not be undertaken; studies were therefore based on soil sampling and geochemical and spectral analysis, and remote sensing.

The main results from the study are that: the main zone of impact extends around 8 to 15 km from the smelter, depending on wind direction; soil Pb concentrations are ca. 15 times greater than background levels (~20 ppm) at a distance of 5 km, and 150 times background levels within 2 km of the smelter. Similar enrichment factors were observed for Cd, Mo, Cu, Zn and As; Pb concentrations in native lichens (preliminary data) were higher in 2011 than in 2001, despite the installation of the Ausmelt system; SO_2 and airborne particulate from different processes in the smelter are decoupled during atmospheric transport, with large Cu-Fe-rich (30 to >100 μm) particulate from the blast furnace deposited in lichens closest to the smelter (<12 km), finer (<2 μm) particulate from the converter carried up to and probably beyond 30 km, and SO_2 (and related secondary particulate) impacting the forest either locally, in discrete areas (as identified from airborne imagery) due to temperature inversions and topographic effects, or carried along with the converter particulate to greater distances; there is an excellent correlation, showing a zonal pattern of impacts around the smelter, between the data from the spectral analysis of birch leaves, the results from time series analysis of hypertemporal satellite imagery and the geochemical data for lichens, snows and soils. The implications of these findings are discussed.

TABLE OF CONTENTS

LIST OF FIGURES

LIST OF TABLES

1 INTRODUCTION

The objective of the ImpactMin project was to develop new methods and a corresponding toolset for the environmental impact monitoring of mining operations using Earth observation (EO). Four demo-site regions were considered: Kristineberg (Sweden), the Vihovici mine in Mostar (Bosnia and Herzegovina), Rosia Montana (Romania), and two mining sites in the Orenburg region (Russia) (Fig. 1.1).

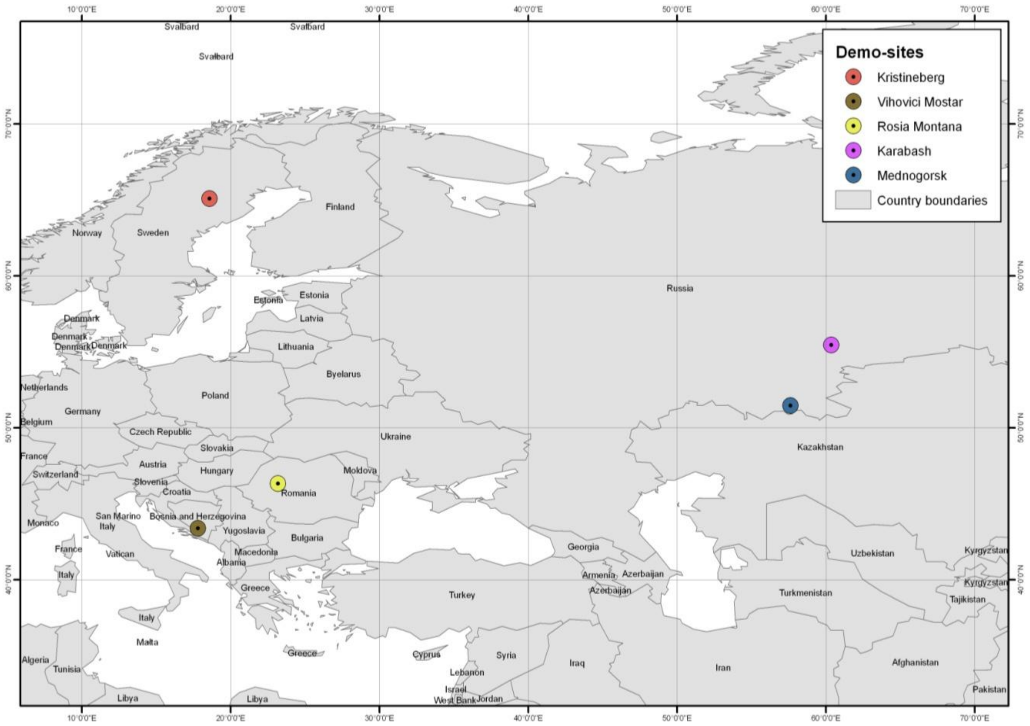

Fig. 1.1 Location of the ImpactMin demo-sites

The objectives of WP7.4 were the calibration, testing and verification ('ground-truthing') of remote sensing concepts and tools (WP6) for environmental and socio-economic impact monitoring of mineral resource exploitation in the Chelyabinsk-Orenburg regions of the South Urals of Russia. Environmental assessment in the southern Urals needs to be: 1) relatively low cost, to meet the requirements of local monitoring agencies and to yield results within the budget-limited framework of the ImpactMin project; 2) discreet, to avoid monitoring devices being tampered with or removed, and to prevent any misunderstandings amongst the local population that the environmental assessments being carried out will result in the closure of operations. This is a politically and socially sensitive issue as the mining-related industries in the southern Urals are major employers and therefore closure would have devastating consequences for the local population. The closure of the Karabash smelter in October 1989 (on environmental and public health grounds) brought severe economic hardship which resulted in its re-opening in 1997.

From Deliverable 4.3 – 'Satellite mission planning for the demo-sites', it was recommended that WP7.4 should focus on two demo-sites, one from each of the main climatic-vegetative zones in the South Urals, Karabash in the Chelyabinsk district, in the South Taiga vegetative zone, and Mednogorsk, Orenburg district, in the Steppe zone. The results of the studies, together with published data (mainly from the FP5 MinUrals contract (ICA2-CT-2000-10011)) and geological and geo-topographic maps (including pattern of industry) at 1:200,000 scale and available remote sensing datasets (from WP4 and WP6), were incorporated into a database for statistical analysis. The aim of the studies was to determine the impacts of smelter emissions, acid rock/mine waters and effluents on soils, vegetative zones and water resources.

The results will be considered in the light of socio-economic data collected in Karabash and Mednogorsk (WP3, Fig. 1.2) and fed into WP8 (Dissemination, mainly through the publication of the results in the scientific and popular science literature, and via ImpactMin web pages) and WP9 (Training).

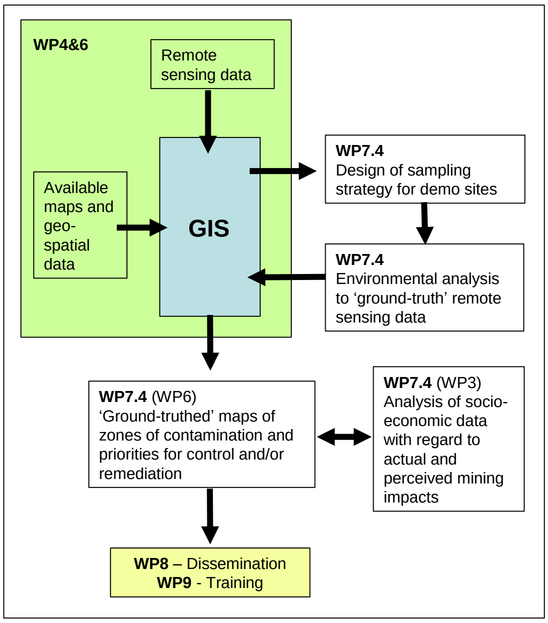

Fig. 1.2 Workflow diagram showing sequence of activities under WP7.4 and linkages to other work packages.

The structure of this report is as follows: Chapter 2 describes the background to the Karabash and Mednogorsk demo sites and previous studies, Chapter 3 the data available for WP6 and WP7.4, Chapter 4 the tools and methods used in WP7.4, Chapter 5 the results of the ground-based studies, Chapter 6 the results of the remote sensing studies, Chapter 7 interpretations of mining-related impacts and developed tools for environmental assessment, Chapter 8 conclusions and recommendations for future studies.

The main contributors to this report were IMIN, UNEXE, GEOS, VITO.

1.1 Aims and objectives

The specific objective of WP7.4 was to demonstrate the use, and to 'ground-truth' by collecting relevant environmental data, of remote sensing for the assessment and monitoring of environmental impacts of mining-related industries in the Chelyabinsk and Orenburg regions of the South Ural Mountains of Russia. This objective is linked to that of WP6, to develop, validate and deploy methods for the assessment and monitoring of environmental impacts from mining operations, based on the knowledge pool generated in WP4 and WP5.

The three principal stages in metals production – mining, minerals processing and metallurgical extraction (often based on smelting) – can all pose a threat to the environment (Lottermoser, 2007). The different demo-sites show varying environmental impacts. In work package WP4.1, environmental variables that are associated with mining activities and detectable with satellite earth observation methods were identified. The findings of WP4.1 were included in deliverable D4.1. Variables (or impacts) are effects on natural resources and on the components, structures and functioning of affected ecosystems. The variables are separated into direct and indirect variables. Direct variables are related to direct and predictable effects of mineral mining operations itself, occurring at the same time and place. Indirect variables are caused by mineral mining operations, but occur later in time and/or farther removed in distance. Indirect variables may include cumulative effects related to induced changes in the pattern of land use and related effects on soil, air and water and other natural systems.

For the Karabash and Mednogorsk studies, the following direct variables were considered: acid mine drainage (AMD), contaminated soils and atmospheric pollution. The indirect variables that were considered were mainly: vegetation stress, contamination of surface waters and soils, and sediment load and metal contamination.

Pollution of the atmosphere in mining areas can be complex, as it is often not just a phenomenon restricted to mining itself, but also extends to activities around the mine, such as refining, smelting, other related industries, and human settlement. Significant levels of dust, above 3 kg/t of ore mined, and ranging from 0.003 to 27 kg/t, may be generated by extraction activities, crushing, ore beneficiation, transport and traffic, and wind-borne losses (World Bank Group, 1998). Significant releases of dust containing metals, including mercury, may result from the drying of the ore concentrate. The main impact of smelting operations, whereby metals are extracted from ore by heating and melting, is the release of gaseous and particulate pollutants, including oxides of sulphur, nitrogen and carbon, and metal-rich and sometimes radioactive particles. Sulphur dioxide (SO_2) emissions can be responsible for acid deposition on vegetation and other surfaces and the occurrence of winter smog episodes (Khokhar et al., 2004). The spatial scale of airborne pollution related to mining, and particularly smelting activities, is typically quite large. Depending on substances and particle sizes, the area affected can range from a few hundred square meters to thousands of square kilometres. Large scale atmospheric pollution has been monitored using MODIS imagery, which has a high spectral but low spatial resolution, and using ASTER or even Landsat imagery (e.g. for monitoring urban air quality). A number of studies have used satellite remote sensing to analyze the secondary effects of atmospheric pollution related to mining activities, especially vegetation stress. Mikkola (1996) and Rees and Williams (1997) monitored the changes in land cover induced by atmospheric pollution (SO_2) in the Kola Peninsula, Russia, using Landsat images. In the same area, Hagner and Rigina (1998) compared Landsat reflectance data with a mathematical model of SO_2 concentration in ambient air around a metallurgical complex, and concluded that the strong statistical correspondence as well as the nature of the spectral change indicate that the airborne pollutants were the major factor causing forest vegetation decline. Hyperion imagery may be used to study mineralogy of particulates in windblown dust. Nevertheless, the applicability of satellite remote sensing for monitoring atmospheric pollution depends on the severity and the spatial scale of the event.

The importance of mapping *land use* and monitoring their changes has been widely recognized in the scientific community and the mining of natural resources is invariably associated with land use and land cover changes (Prakash and Gupta, 1998). Therefore, mining is an important factor of anthropogenic influence on the environment, causing alteration of the landscape (Rigina, 2002), including land use and land cover change, urbanisation and industrialisation, land degradation and erosion. For successful monitoring of land use and land cover change related to mineral mining and their dynamics, observations with frequent temporal coverage over a longer period of time are required. The scale and characteristics of land use and land cover change will determine at which spatial resolution the processes can be monitored. Landsat imagery is widely used for monitoring conversions from natural vegetation to surface mines, and afterwards to secondary vegetation after reclamation. However, the extent of land use and land cover change is often larger than the mine itself. Vegetation indices or other transformations are frequently used. Also time series of low resolution imagery (e.g. NOAA-AVHRR) have been used to monitor large scale land use and land cover change induced by mineral mining (Latifovic et al., 2005).

Mining induced *vegetation stress* is mainly an indirect consequence of altering environmental variables. Many mine wastes are structureless, prone to crusting, and low in organic matter and essential plant nutrients (P, N, K). They mostly have low water-holding capacity, and contain contaminants such as salts, metals, metalloids, acid, and radionuclides. Furthermore, conservative, non-reactive ions such as sulfate, nitrate, manganese, magnesium, and calcium may migrate into the local aquifer and surface waters. Vegetation indices are used to monitor mining induced vegetation stress. Depending on the scale of the impact, high spatial resolution QuickBird or IKONOS, medium resolution Landsat or ASTER, or low resolution MODIS or NOAA-AVHRR is applied. Hyperspectral imagery from Hyperion facilitates a more detailed study of pigment concentration changes.

1.2 Approach

The work (person months) carried out by each partner in WP7.4 (Chelyabinsk-Orenburg Demo Site Implementation) is shown in Table 1.1. The main partners are IMIN and UNEXE, with IMIN responsible for deliverable D7.4, in collaboration with UNEXE, GEOS, UBB and ULRMC (Report on the Chelyabinsk-Orenburg case study investigations herein).

Table 1.1 Number of person months (PM) per partner contributing to WP7, and specifically to WP7.4 - Chelyabinsk-Orenburg case study investigation.

Participant name	GEO	GEOS	UNEXE	LTU	Photon	GFMO	IMIN	UBB	ULRMC	DMT	VITO
PM/Partner WP7	3	8	12	12	9	7	12	10	8	-	-
PM/Partner WP7.4	-	2	10	-	-	-	12	1	1	-	-

1.2.1 Tasks carried out by IMIN

Task a – i) Collection of pertinent feedstock, production, emissions, discharge and associated data from current mining-related operations (where possible) and the field estimation of area covered, volume and characteristics of wastes and tailings in the Karabash and Mednogorsk demo sites; ii) Provision of detailed maps of the Karabash and Mednogorsk demo-sites showing the pattern of past and current mining-related activities, waste dumps and tailings, surface water channels, ponds and lakes, domestic housing and public roads, buildings, services and amenities. No data for feedstock, production, emissions, discharge and associated data could be obtained from the smelter companies at Karabash and Mednogorsk due to political problems.

Task b - Collection and analysis of environmental samples for the assessment of atmospheric and surface water contamination to 'ground-truth' data from the remote sensing studies (WP4, WP6) carried out at the Karabash and Mednogorsk demo sites, in collaboration with UNEXE. Analyses undertaken at IMIN included pH, conductivity and Eh of waters, X-ray diffraction (XRD), and Inductively Coupled Plasma Optical Emission Spectrometry (ICP-OES).

Task c – Provide field and sample analytical data for input into the GIS being developed under WP6 by GEOS/GEO, for the purposes of 'ground-truthing' the remote sensing data.

Task d - Spatial and temporal geostatistical analysis/interpretation in the GIS environment of the integrated data (from d) to determine the impacts of smelter emissions, acid rock/mine waters and effluents on different soils, vegetative zones and water resources (in collaboration with GEOS and ULRMC).

1.2.2 Tasks carried out by UNEXE

Task a - Planning and implementation of the lichen study at the Karabash site, including collection of suitable lichen transplant materials from a reference site, outside the main zone of impact from the smelter, transplantation to monitoring sites in a spoke pattern around Karabash, and collection of the transplants following a 3 month exposure period. These works were carried out in collaboration with IMIN. The lichen samples were analysed by ICP-MS in the laboratories of UNEXE and IMIN. Carryout complementary geochemical studies of tree and twig bark.

Task c – Assess socio-economic data for the Karabash and Mednogorsk demo sites (collected under WP3) in the light of the outcomes of the integrated analysis of climatic, geo-topographic, mapped land use, remote sensing and field and laboratory-based 'ground-truthing' studies.

Task d – To provide a major role in the drafting of the report for deliverable D7.4 - Report on the Chelyabinsk-Orenburg case study investigations, in collaboration with IMIN, GEOS, UBB and GEO.

1.2.3 Tasks carried out by GEOS

Task a - Purchase of imagery, mainly high spatial resolution/8 spectral band WorldView (WV)-2 images, to be requested for collection during a favourable weather window in June or July 2011 (linked with WP6).

Task b – Field-based infrared spectroscopy, using a portable infrared spectrometer, sensitive in the VNIR-SWIR range (400-2500 nm), at the Karabash and Mednogorsk demo sites, to be carried out in July 2011 (14 days in the field). The aim of this is to ground truth the satellite imagery so that the results can be correlated with those from in-situ sampling (above).

Of particular interest will be to:

i) Ground truth the ground-footprint of the plume of airborne contamination for Karabash;
ii) Ground truth the ground-footprint of the plume of airborne contamination around the Mednogorsk smelter (clearly visible on the Landsat images);
iii) To characterise and map the extent of deforestation and vegetation stress in proximity to the sources of contamination (potentially by measuring leaf spectra at the same sites as the lichen stations).

Task c – Assistance in the integration of field and laboratory data into the GIS being developed under WP6, and image/data processing for the development of models and maps of the impacts of mining-related activities on sensitive zones in the South Urals (linked to WP6). This will mainly focus on the analysis and integration of WV-2 and ASTER time series images. Of particular interest will be to determine the effects on vegetation resulting from the closure of the smelter in October 1991, and reopening in March 1997.

1.2.4 Tasks carried out by UBB

Management of WP7, making sure that the data from all demo site investigations in WP7 is compatible, i.e. uses the same protocols, data formats and specifications. Additionally, UBB will be involved in disseminating the results of WP7.4 for educational and training purposes, under WP8 and WP9 (Fig. 1.2).

1.2.5 Tasks carried out by VITO

Although VITO does not have any PM budgeted in WP7, the time foreseen in WP6 permitted VITO to assist in the time series analysis of low resolution imagery. The study focuses on the use of hypertemporal vegetation indicators derived from SPOT-Vegetation in order to gain an understanding of the spatial and temporal effects of environmental impacts in Karabash and Mednogorsk.

2 BACKGROUND TO THE KARABASH AND MEDNOGORSK DEMO SITES

The South Ural Mountains of Russia has been a centre for precious and base metal production for well over 3000 years. During the Soviet era, in the early- to mid-20th century, production activities were heavily intensified with little long-term planning or consideration for the environment. Today, many of the mineral deposits are exhausted or are uneconomic in current world markets. The extraction technologies used in most operations are inefficient and environmentally unsound. In certain areas, pollution from past and current mining-related activities is known to be heavily impacting on human and environmental health (Polluted Places, 2005). From a political and sociological perspective, large-scale closure of operations is currently impossible as mining industries are major employers which underpin the economy of the region.

A detailed literature review of previous studies on Karabash and Mednogorsk was carried out in the report for Deliverable 4.3 – ‘Satellite mission planning for the demo-sites’. Below is a brief summary:

2.1 Karabash

The smelter town of Karabash is situated within the Chelyabinsk District in the northern part of the South Ural Mountains. It lies at an altitude of ca. 320 m within a SW-NE trending flat-bottomed valley, surrounded by hills with an altitude up to 610 m (Fig. 2.1). It is situated within the South Taiga vegetative zone, close to the contact with the Forest-Steppe zone, with a moderate continental climate. The area is extensively forested apart from small agricultural plots and other areas affected by anthropogenic activities. The geology is dominated by relatively mafic metamorphic rocks of low buffering capacity. Soil cover is generally thin and sporadic and mainly consists of Luvisoils (Udachin et al., 2003).

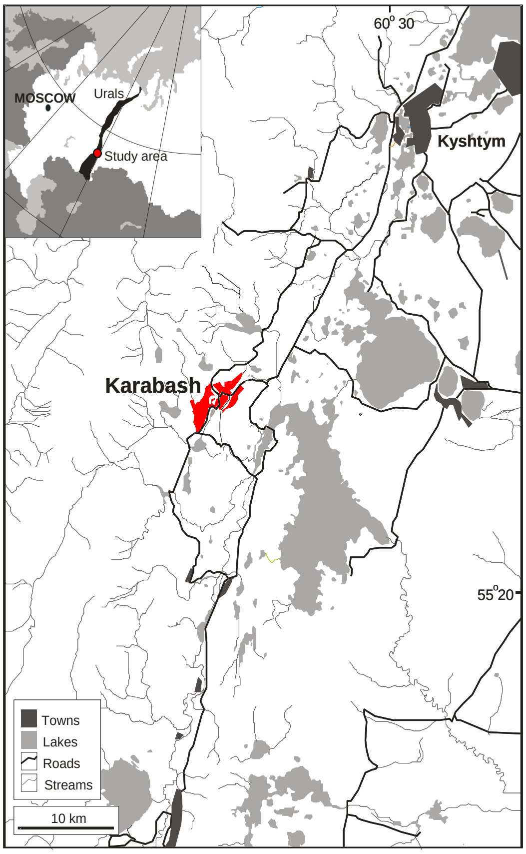

Fig. 2.1 Map showing the location of Karabash town in the northern part of the South Urals of Russia.

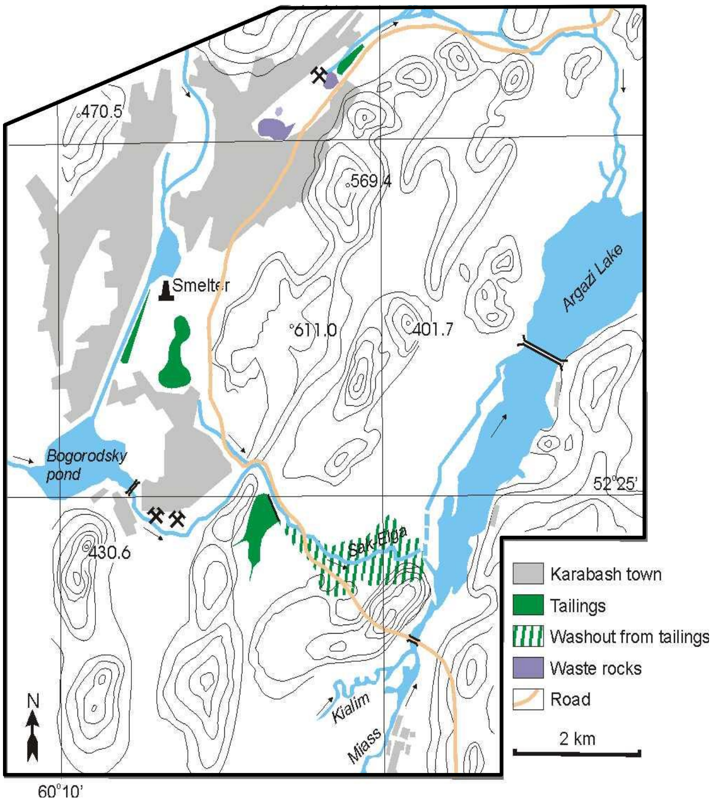

Fig. 2.2 Map of Karabash town and the local area, showing the location of the smelter, wastes dumps, tailings, and abandoned underground workings.

Karabash has a current population of around 12,500, which is much less than the 50,000 in the 1960s when mining, ore beneficiation and smelting operations were at their peak. Mining of iron ore began in the area in 1776 but it was not until 1822, following the discovery of alluvial gold, that the town of Karabash was established. Mining activity increased following the discovery of a secondary Cu deposit in 1834. Small-scale Cu smelting operations were carried out between 1837 and 1842, which produced 22 tonnes of blister Cu. A second Cu smelter was built in 1907 but this was rapidly superseded in 1910 by the building of a much larger operation on the site of the current smelter. In 1934, a beneficiation mill was constructed to produce Cu concentrate by froth flotation, which from 1954 also produced zinc and pyrite concentrate. The beneficiation mill, smelter and the last mine were closed in 1991. The smelter resumed activities in 1997, processing concentrates from Cu mines in the Central and South Urals. In 2003, around 1500 workers were employed in the smelter (no current figures (2012) are available).

Karabash was described in 1992 by the United Nations Environment Programme (UNEP) as one of the most polluted towns in the world. Nesterenko (2006) characterised the area as an ‘ecological disaster zone’, based on the chemical analysis of soil samples in the area. Karabash and the surrounding areas have been affected by gaseous and particulate emissions from the smelter, acid drainage from abandoned mine workings, leachates and dusts from waste dumps, and contaminated stream sediments (Udachin et al., 2003). Metallurgical slags from the smelter (containing 614-830 ppm As, 2581-3659 ppm Cu and 417-628 ppm Pb, Williamson et al., 2008) are used to grit roads in and around the Karabash area. The spatial extent and nature of contamination from this activity is not known. The Sak-Elga river valley contains deep deposits (often > 0.5 m) of pyrite-rich tailings over a length of more than 10 km between Karabash and a freshwater reservoir (Argazi Lake, Fig. 2.2). Untreated domestic wastewater is discharged into the same river. The reservoir is the main freshwater source for the city of Chelyabinsk (1.2 million inhabitants). Several ponds are filled with acid waters from underground mine shafts. Highly acid and toxic mine waters are continuously released into the environment.

Recently, in 2006, the Russian Copper Company modernised the smelter in Karabash (Yokogawa, 2008). The new smelting system processes approximately 460,000 tonnes per year of concentrates. Ausmelt Ltd claims the smelter is now one of the most modern plants of its type in Russia and the complex is among the most up-to-date and environmentally safe Cu smelters globally (AZoM News, 2007).

Fig. 2.3 Photographs showing a smelter-facing hillside to the east of Karabash town in a) 1910, the year the Cu smelter was commissioned, and b) in 2004 with the hillside largely deforested.

A number of studies have looked into the effects of atmospheric pollution in Karabash (Udachin et al., 1998, 2002, 2003; Purvis et al., 2004; Spiro et al., 2004; Williamson et al., 2004a,b; Brooks et al., 2005; Purvis et al., 2006; Williamson et al., 2008). The smelter was not large by international standards, but until 2006 had no controls on gaseous or particulate emissions (Voskresensky, 2002). There are no recent or reliable data in the public domain concerning the levels of emissions from the smelter (Williamson et al., 2004b). However, before the political changes in 1991, official SO_2 emissions estimates were in the order of 90,000 to 150,000 tonnes per year (Udachin et al., 1998). From studies of airborne total suspended particulate (TSP) collected in Karabash town in 2001, using air pump apparatus (Williamson et al., 2004b), particulate downwind from the smelter were mainly anglesite ($PbSO_4$), zincite (ZnO), gunningite ($(Zn,Mn)SO_4.H_2O$), a phase with the composition Zn_2SnO_4, and poorly ordered Zn sulphates, with lesser amounts of pyrite, sphalerite, chalcopyrite and galena. This material had a maximum particle size (equivalent spherical diameter) of around 2 μm (average of 0.5 μm, s.d. = 0.2). From their composition and size, these particles were thought to mostly originate from the smelter converter (Williamson et al., 2004b). More Fe–Cu-rich particles on lichen surfaces, not present in the air filters, which had a mean equivalent spherical diameter of 2.2 μm (s.d. = 2.4), are thought to have been mainly derived from the blast furnace (Williamson et al., 2004b).

The close proximity of townspeople to these sources of pollution is of most immediate environmental concern (Brooks et al., 2005). The people living in the town show high rates of congenital defects, central nervous system disorders, cancer and other diseases (La Franiere, 1999). Two-thirds of the children suffer from Pb, As or Cd poisoning (La Franiere, 1999) and many suffer from asthma and respiratory diseases (Ferriera-Marques, 2003). Vegetation is almost absent from the hills immediately downwind of the smelter (Fig. 2.3) and the Sak-Elga river floodplain, to the south of the town (Fig. 2.1), contains 9.2 million tonnes of heavy metal-rich tailings (Brooks et al., 2005).

Particularly sensitive in determining the spatial extend of impacts from the smelter was the use of lichen transplants. Tree bark samples of the lichen *Hypogymnia physodes* were collected in July 2001 from a ‘control’ site (30 km SW of Karabash) and transplanted to 10 stations along a ~60 km NE-SW transect centred on Karabash. The transplants were collected after 2 and 3 month exposure periods. Particulates on the lichen surfaces were analysed by scanning electron microscopy with energy-dispersive X-ray analysis (SEM-EDX). The elemental compositions of the lichen transplants, as well as smelter stack dusts, tailings, road dusts, metallurgical slags and top soils, were determined by quadrupole inductively coupled plasma mass spectrometry (ICP-MS).

SEM-EDX studies were carried out to compare the size, shape and elemental compositions of individual particles on lichen transplant surfaces from Karabash (715 analyses) and the ‘control’ site (598 analyses). Particulates in the Karabash samples showed high levels of S, Pb, Cu, Sn and Zn, mainly in the form of 5 to 200 μm sized, commonly spherical sulphide and silicate metallurgical slag particles, similar in composition to dust particles from the blast furnace stack. These particles were also found in small numbers on lichens from the ‘control’ site, indicating >30 km dispersion from the smelter. Particles <5 μm in diameter, and especially those < 2.5 μm, were poorly represented in lichens from both Karabash and the ‘control’ site, either because they were not efficiently captured or they were preferentially washed off or solubilised.

Lichen transplants showed a decrease in metal concentrations (e.g. Pb in Fig. 2.4) away from the smelter following 2 and 3 month exposure periods. Multi-element least-squares modelling was carried out to determine the relative contribution of particles from different potential sources (smelter, tailings etc.) to the compositions of the lichen transplants in the transect. The blast furnace, which emits dusts containing particularly high levels of Fe, Cu and S, was found to be the main source of particulate in transplants close to the smelter (<10 km). Particulate from the Peirce-Smith converter, with relatively high Zn, As and Pb, was found to be more widely dispersed. From SEM-EDX analysis of converter stack dusts and air-pump filter samples from Karabash town, converter-derived particulate was found to be relatively fine grained (generally <1.5 μm in diameter), and therefore likely to show longer atmospheric residence times and wider dispersion (depending on meteorological conditions). Leaching tests on the converter stack dust showed that a high proportion of Zn (32%) and As (8.5%) was in a water-soluble form, which could at least partly explain the paucity of converter stack particulates on the lichen surfaces.

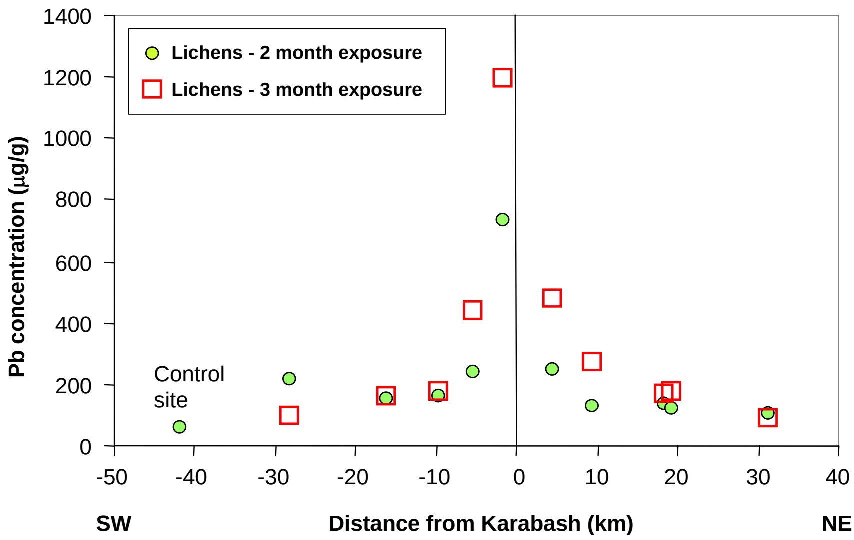

Fig. 2.4 Pb concentrations in lichens transplanted from the control site in July 2001 and exposed for 2 and 3 month periods at stations in a SW-NE transect centred on Karabash (after Spiro et al., 2004).

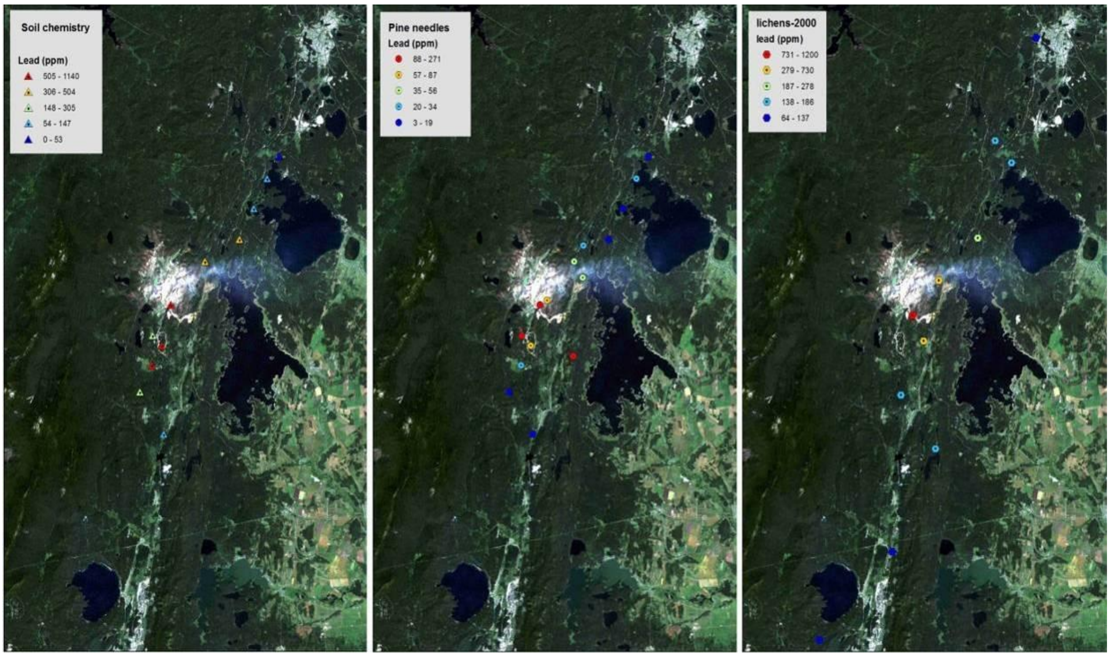

Fig. 2.5 Pb concentrations in soils (left), pine-needles (centre) and native and transplanted lichens (right). Data from the MinUrals project (2001-2). These plots clearly show a similar pattern of metal zonation around the Karabash smelter.

2.2 Mednogorsk

The Mednogorsk demo-site is located on the western slope of the South Ural Mountains, in the Steppe vegetative zone and with a strong continental climate. The main sources of contamination in the Mednogorsk demo-site area are the Blyava and Yaman-Kasy open pit mines (now pit lakes), abandoned beneficiation mill and the active Cu smelter (Fig. 2.6 and Fig. 2.7). The Blyava VMS deposit was exploited via open pit and underground workings from the 1930s onwards, with the main period of activity being between 1936 and 1972. The Yaman-Kasy VMS Cu-Zn deposit was operated via open pit between 1987 and 2002. The currently active Mednogorsk Cu plant has been operational since 1937, having been run as a Cu-S plant between 1954 and 1998. Initially, the plant produced low purity S, but after the second World War, began to produce Cu concentrate (12-17%) which was transported for refining to the Karabash smelter and the Kirovgrad smelter (Sverdlovsk district). Between 1959 and 1962, following the construction of converters, the plant began to produce non-refined copper. In 1960, the plant started processing ores from the Gay deposit and from 1961 produced sulfuric acid (H_2SO_4). It is thought, from undisclosed sources, that the smelter currently emits around 68,000 t/year of gases and dust.

There has been little work on the nature and extent of contamination from Mednogorsk. It would seem likely that the main impacts will be from atmospheric gaseous and dust emissions from the Cu smelter. Of additional concern is contamination of surface and ground waters by acid mine/rock waters from the many waste dumps, open pits and tailings dams in the area. Acid waters flowing in the Zhiriclya river have been treated since 2006, however there is little data on how effective this treatment is.

Fig. 2.6 Photograph of the Mednogorsk Cu smelter.

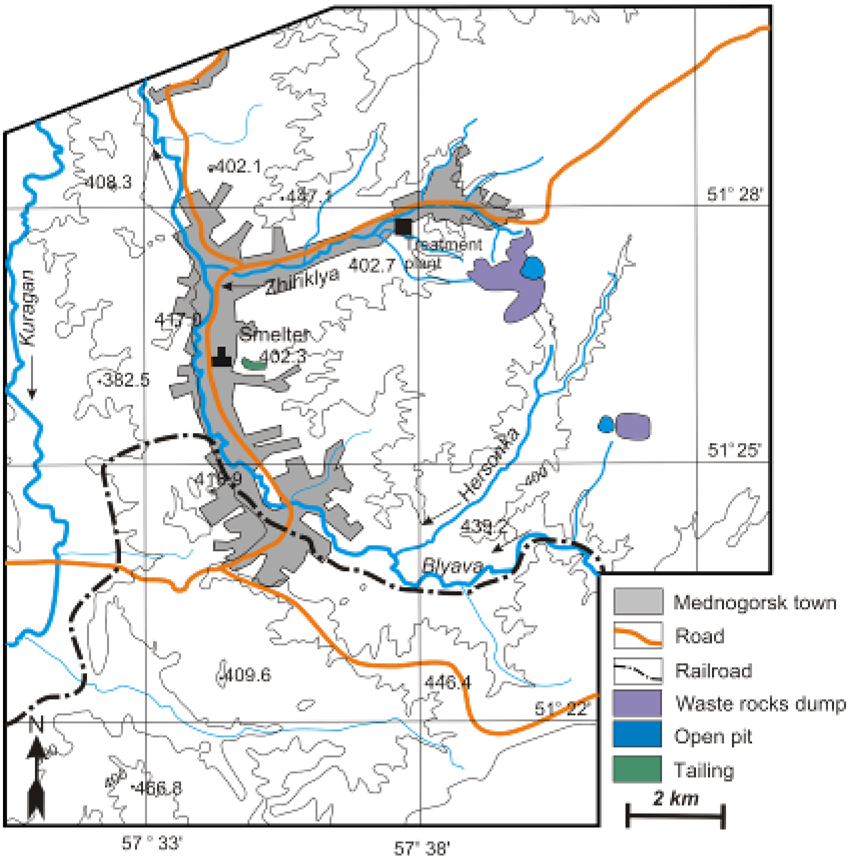

Fig. 2.7 Map of the Cu smelter town of Mednogorsk.

3 DATA AVAILABLE FOR WP7.4

3.1 *In-situ data*

Datasets for environmental samples available at the start of WP7.4 are shown in Table 3.1. These include data collected during the TACIS project (Udachin et al., 1998), EU-FP5 MinUrals project, Royal Society Joint Collaborative grant, and subsequently by IMIN.

Table 3.1 Environmental datasets (including data from the TACIS and MinUrals projects, Royal Society Joint Collaborative grant and IMIN datasets, see text) available for use under WP7.4, and for incorporation into the GIS under WP6.

Karabash demo site	
Dataset	**Date collected**
Surface waters (122 samples)	2002-2010
Suspended sediments in surface waters (24 samples)	2008-2010
“Ochres” (8 samples)	2008-2010
Surface sediments (12 samples)	2010
Snow samples (46 samples of snow melt and 35 samples of snow dust)	2002-2009
Lake sediments (265 samples)	2002-2010
‘Anthropogenic’ horizon in soils (102 samples)	2007-2010
Tailings materials (76 samples)	2003-2005
Waste rocks from dumps (15 samples)	2007

Mednogorsk demo site	
Dataset	**Date collected**
Surface waters (27 samples)	2009-2010
Water from water column in pit lakes (14 samples)	2007
Suspended sediments in surface waters(20 samples)	2004-2010
“Ochres” (10 samples)	2008-2010
“Fe-mud in two settling ponds” (35 samples)	2004
Snow samples (22 samples of snow melt+15 snow dusts)	2009-2010
‘Anthropogenic’ horizon in soils (83 samples)	2004-2009
Dust from stacks (3 samples)	2010
Road dusts (5 samples)	2010

3.2 *Ancillary geospatial data*

IMIN provided geospatial data at a scale of 1:200,000 for Karabash (Fig. 3.1) and Mednogorsk (Fig. 3.2), including topography (‘Relief’ shapefile), Roads (‘Dorogi’ shapefile) and Routes (‘Trackname’ shapefile), administrative boundaries (‘Granica’ shapefile), river

('River' shapefile) and protected waters ('Water' shapefile), towns ('Town_big' shapefile) and settlements ('Town' shapefile), nature monuments ('Monuments' shapefile), and archaeological monuments ('Posel_arch' shapefile).

Metadata for these geospatial data layers are also available for Karabash and Mednogorsk.

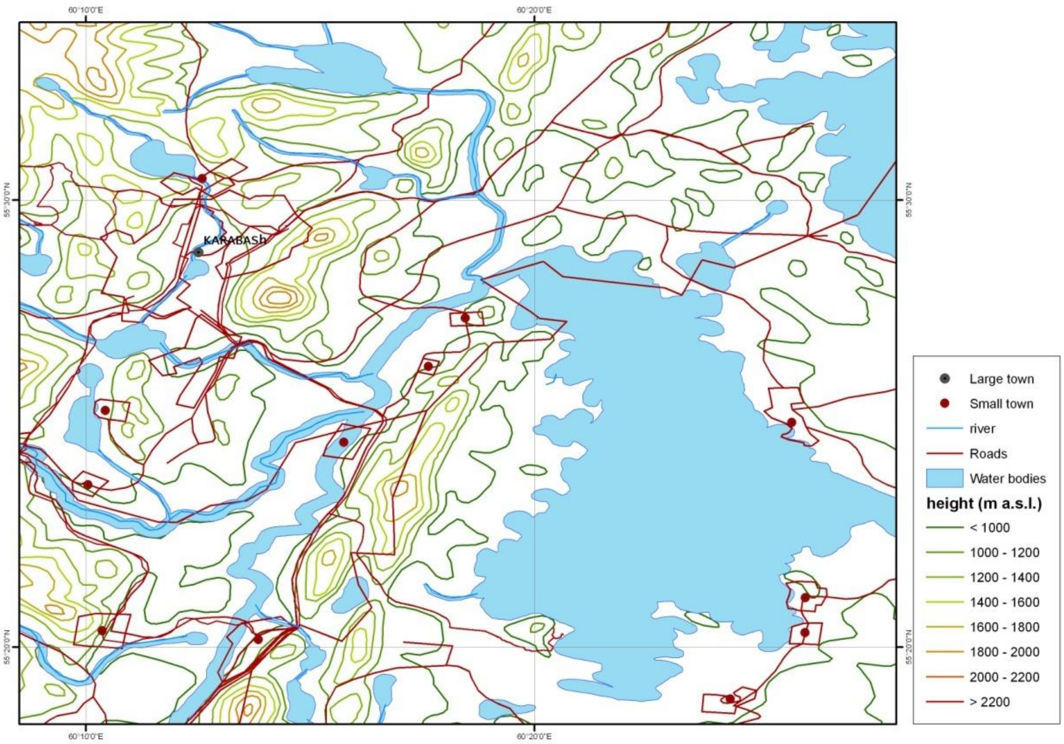

Fig. 3.1 Base map of the Karabash mining area and surroundings

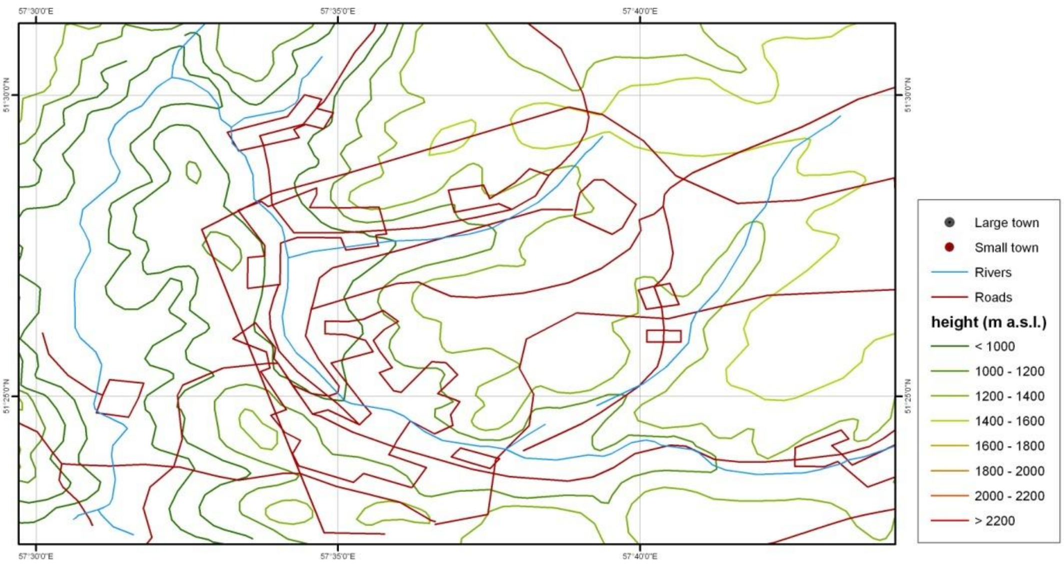

Fig. 3.2 Base map of the Mednogorsk mining area and surroundings

Topographic maps at a scale of 1:100,000 may become available, depending on permission being granted. However, a digital elevation model (DEM) is available for Mednogorsk at 30m resolution (ASTER GDEM - D4.3).

GlobCover was available for Karabash and Mednogorsk. As a reference dataset, the GlobCover land cover map (Arino et al., 2007) was used (Fig. 3.3). This land cover map, derived from ENVISAT-MERIS at a spatial resolution of 1/360°, was resampled to the SPOT-Vegetation pixel resolution, whereby the predominant class of each larger pixel was retained.

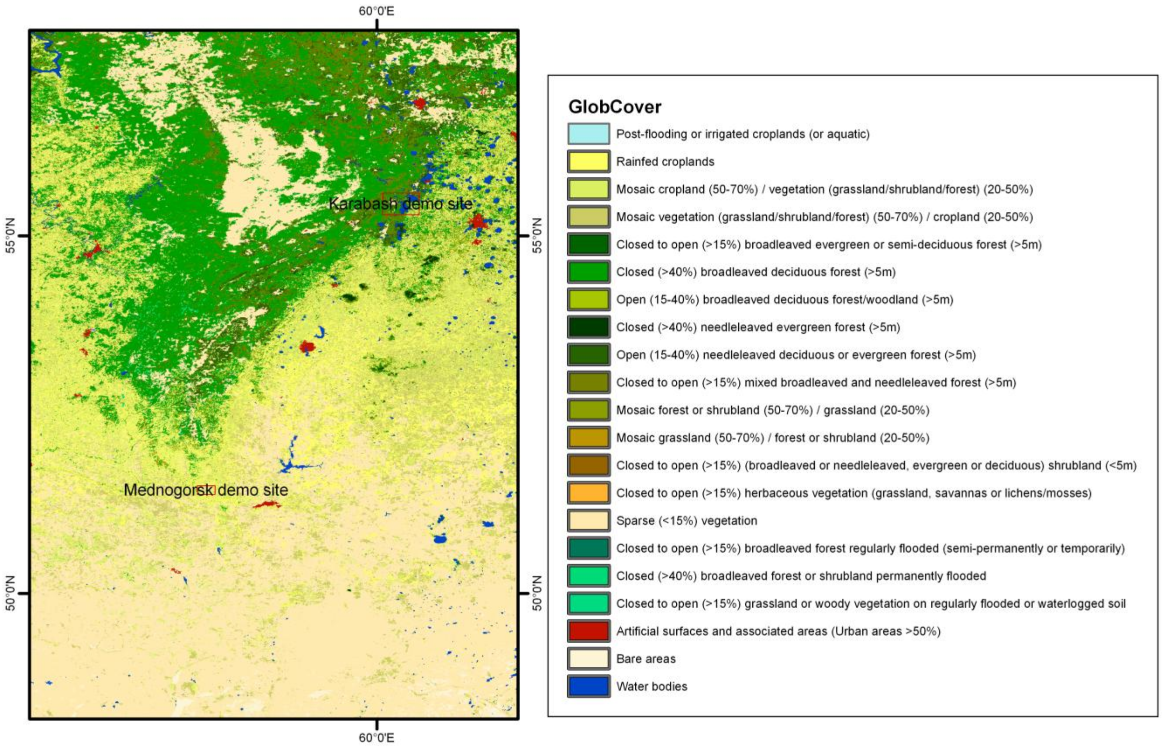

Fig. 3.3 GlobCover map of the wider surroundings of the Karabash and Mednogorsk demo sites.

Some specific analyses were performed on only a few land cover classes. In order to focus on a range of different vegetation densities, the analysis concentrated on 6 GlobCover classes. The classes were re-coloured, in order to make a clear distinction, and a shorter description was used (Table 3.2).

Fig. 3.4 gives a more detailed view of the GlobCover land cover classification maps of the surroundings of both the Karabash and Mednogorsk demo-sites. Although the direct surroundings of Karabash show a sparse vegetation cover, the area around Karabash is extensively forested apart from small agricultural plots and the conspicuously de-vegetated (smelter-facing) western slopes of the nearby Karabash 'Mountain' (Spiro et al., 2004). In contrast, the Mednogorsk demo-site, and its surroundings, show a very general sparse vegetation cover, with patches of a mosaic of shrubland/cropland.

Table 3.2 Color table of focus GlobCover classes

GlobCover class number	Class name	GlobCover color	Short description	Color
20	Mosaic cropland (50-70%) / vegetation (grassland/shrubland/forest) (20-50%)	yellow	Mosaic crops/veg	Yellow
30	Mosaic vegetation (grassland/shrubland/forest) (50-70%) / cropland (20-50%)	Beige	Mosaic veg/crops	Purple
50	Closed (>40%) broadleaved deciduous forest (>5m)	Green	Closed forest	Green
90	Open (15-40%) needleleaved deciduous or evergreen forest (>5m)	Dark green	Open forest	Blue
100	Closed to open (>15%) mixed broadleaved and needleleaved forest (>5m)	Green-brown	Mixed forest	Brown

150	Sparse (<15%) vegetation	Sand	Sparse vegetation	Red

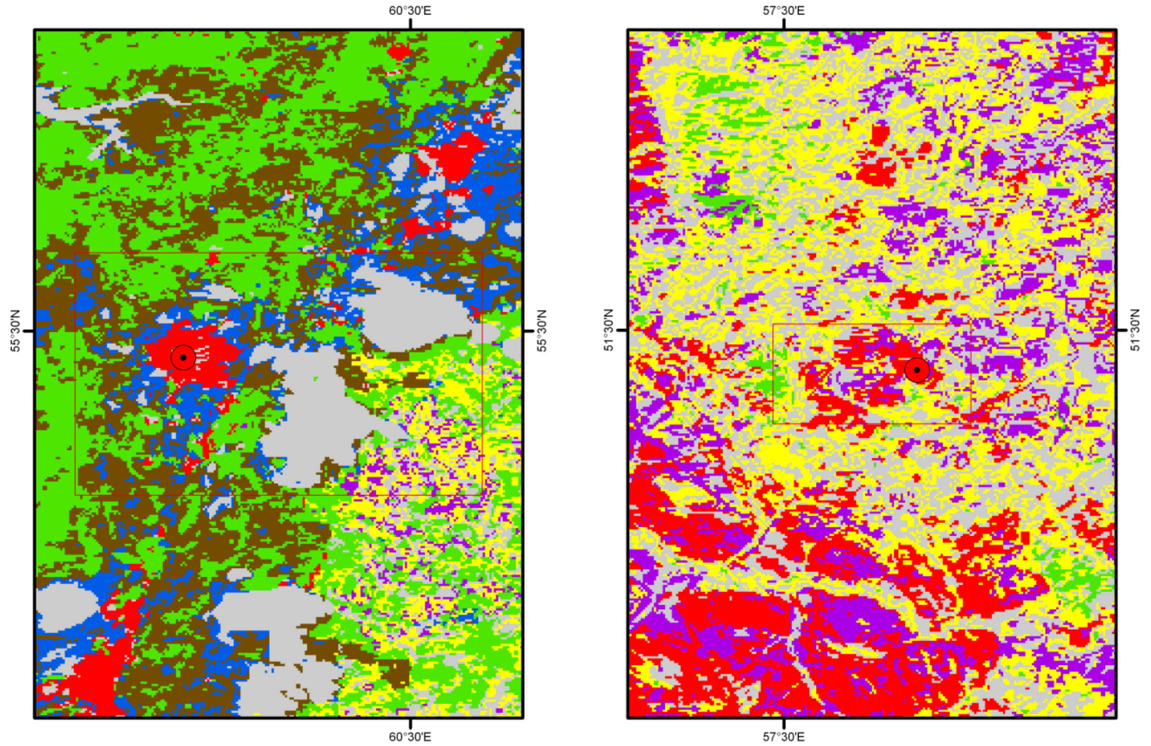

Fig. 3.4 GlobCover map of the Karabash (left) and Mednogorsk (right) demosites, recolored according to Table 3.2. Grey areas are not considered in the following analyses.

3.3 Remote sensing data

No satellite data were available before the start of the ImpactMin project. A satellite ‘quicklook’ of Karabash was available from Google Earth (Fig. 3.5).

Fig. 3.5 Google Earth image of the town of Karabash

Landsat, ASTER and SPOT-Vegetation images for the Karabash and Mednogorsk demo sites were obtained under WP4, Deliverable 4.3 - Satellite mission planning for the demo-sites‘ (details in Table 3.3 and Table 3.4). The SPOT-Vegetation dataset consisted of a time series of 10-daily NDVI and fAPAR (Weiss et al., 2010) images (S10) from January 1999 to December 2011 at 1/112° resolution (http://www.vgt.vito.be/ and http://www.marsop.info/, n=468).

Table 3.3 Remote sensing data acquired for Karabash

Karabash (Chelyabinsk)

SENSOR	Date	Format	Level of preprocessing	Remarks	Cost	Download (y/n)	Acquired by...	source
SPOT-VGT	10/98-now	ENVI	L3 (S10 NDVI/DMP/...)		null	-	VITO	
NOAA-AVHRR	07/1981 - 12/2006	ENVI	L3 (S30 NDVI)	GIMMS dataset	null	y	VITO	
Landsat 4	1983/07/04	GeoTIFF	Ortho-UTM40N-WGS84				Geosense	USGS-GLOVIS
Landsat 5	1987/05/20	GeoTIFF	Ortho-UTM40N-WGS84				Geosense	USGS-GLOVIS
Landsat 4	1989/06/18	GeoTIFF	Ortho-UTM40N-WGS84				Geosense	USGS-GLOVIS
Landsat 5	1989/07/28	GeoTIFF	Ortho-UTM40N-WGS84				Geosense	USGS-GLOVIS
Landsat 4	1990/08/08	GeoTIFF	Ortho-UTM40N-WGS84				Geosense	USGS-GLOVIS
Landsat 5	1991/07/02	GeoTIFF	Ortho-UTM40N-WGS84				Geosense	USGS-GLOVIS
Landsat 7	2000/07/18	GeoTIFF	Ortho-UTM40N-WGS84				Geosense	USGS-GLOVIS
Landsat 7	2001/07/19	GeoTIFF	Ortho-UTM40N-WGS84				Geosense	USGS-GLOVIS
Landsat	2000/05/31	GeoTIFF	Ortho			y	ULRMC	
Landsat	2000/07/18	GeoTIFF	Ortho			y	ULRMC	
Landsat	2001/05/11	GeoTIFF	Ortho			y	ULRMC	
Landsat	2001/06/19	GeoTIFF	Ortho			y	ULRMC	
Landsat	2001/07/12	GeoTIFF	Ortho			y	ULRMC	
Landsat	2004/05/26	GeoTIFF	Ortho			y	ULRMC	
Landsat	2004/07/06	GeoTIFF	Ortho			y	ULRMC	
Landsat	2006/07/19	GeoTIFF	Ortho			y	ULRMC	
landsat 7	2003/08/12	GeoTIFF	Ortho-UTM40N-WGS84	SLC-OFF			Geosense	USGS-GLOVIS
landsat 7	2006/07/19	GeoTIFF	Ortho-UTM40N-WGS84	SLC-OFF			Geosense	USGS-GLOVIS
landsat 7	2008/07/24	GeoTIFF	Ortho-UTM40N-WGS84	SLC-OFF			Geosense	USGS-GLOVIS
Landsat 5	2009/07/19	GeoTIFF	Ortho-UTM40N-WGS84				Geosense	USGS-GLOVIS
Landsat 7	2010/08/30	GeoTIFF	Ortho-UTM40N-WGS84	SLC-OFF			Geosense	USGS-GLOVIS

Table 3.4 Remote sensing data acquired for Mednogorsk

Mednogorsk (Orenburg)

SENSOR	Date (yyyy-mm-dd)	Format	Level of preprocessing	Identifier	Remarks	Cost	Acquired by...	source
SPOT-VGT	10/98-now	ENVI	L3 (S10 NDVI/DMP/...)			null	VITO	
NOAA-AVHRR	07/1981 - 12/2006	ENVI	L3 (S30 NDVI)		GIMMS dataset	null	VITO	
Landsat 5	1984/07/30	GEOTIFF	Ortho-UTM40N-WGS84	1984-07-30-L5-p164r024			geosense	USGS-GLOVIS
Landsat 5	1986/06/02	GEOTIFF	Ortho-UTM40N-WGS84	1986-07-2-L5-p164r024			geosense	USGS-GLOVIS
landsat 4	1988/07/01	GEOTIFF	Ortho-UTM40N-WGS84	1988-07-1-L4-p164r024			geosense	USGS-GLOVIS
landsat 5	1989/07/28	GEOTIFF	Ortho-UTM40N-WGS84	1989-07-1-L5-p164r024			geosense	USGS-GLOVIS
landsat 7	1999/08/17	GEOTIFF	Ortho-UTM40N-WGS84	1999-08-17-L7-p164r024			geosense	USGS-GLOVIS
Landsat	1999/07/09	GeoTIFF	Ortho	1999-07-09-L7-p163r024			ULRMC	
Landsat	2000/07/27	GeoTIFF	Ortho	2000-07-27--L7-p163r024			ULRMC	
Landsat	2001/09/23	GeoTIFF	Ortho	2001-09-23-L7-p164r024			ULRMC	
landsat 7	2002-0708	GEOTIFF	Ortho-UTM40N-WGS84	2002-07-8-L7-p164r024			Geosense	USGS-GLOVIS
Landsat	2005/08/17	GeoTIFF	Ortho	2005-08-17-L7-p164r024			ULRMC	
landsat 7	2006/06/01	GEOTIFF	Ortho-UTM40N-WGS84	2006-07-1-L7-p164r024	slc-off		Geosense	USGS-GLOVIS
landsat 5	2007/08/15	GEOTIFF	Ortho-UTM40N-WGS84	2007-08-15-L5-p164r024			Geosense	USGS-GLOVIS
landsat 5	2009/06/17	GEOTIFF	Ortho-UTM40N-WGS84	2009-06-17-L5-p164r024			Geosense	USGS-GLOVIS
landsat 5	2009/07/03	GEOTIFF	Ortho-UTM40N-WGS84	2009-07-3-L5-p164r024			Geosense	USGS-GLOVIS
landsat 5	2009/07/19	GEOTIFF	Ortho-UTM40N-WGS84	2009-07-19-L5-p164r024			Geosense	USGS-GLOVIS
landsat 5	2009/09/21	GEOTIFF	Ortho-UTM40N-WGS84	2009-09-21-L5-p164r024			Geosense	USGS-GLOVIS
Aster	2005/08/10	HDF-L1A	L1A	10aug2005-p163r72v2-L1A	Raw	88 €	Geosense	Ersdac
			Ortho-UTM40N-WGS84	10aug2005-p163r72v2-vnir	VNIR			
			Ortho-UTM40N-WGS84	10aug2005-p163r72v2-swir	SWIR			
			Ortho-UTM40N-WGS84	10aug2005-p163r72v2-tir	TIR			
Aster	2007/08/14	HDF-L1A	L1A	14aug2007-p164r71v7-L1A	Raw	88 €	Geosense	Ersdac
			Ortho-UTM40N-WGS84	14aug2007-p164r71v7-vnir	VNIR			
			Ortho-UTM40N-WGS84	14aug2007-p164r71v7-swir	SWIR			
			Ortho-UTM40N-WGS84	14aug2007-p164r71v7-tir	TIR			
Aster	2008-0818	HDF-L1A	L1A	18aug2008-p163r72v2-L1A	Raw	88 €	Geosense	Ersdac
			Ortho-UTM40N-WGS84	18aug2008-p163r72v2-vnir	VNIR			
			Ortho-UTM40N-WGS84	18aug2008-p163r72v2-tir	TIR			
Aster	2001/08/22	HDF-L1A	L1A	22aug2001-p164r71v4-L1A	Raw	88 €	Geosense	Ersdac
			Ortho-UTM40N-WGS84	22aug2001-p164r71v4-vnir	VNIR			
			Ortho-UTM40N-WGS84	22aug2001-p164r71v4-swir	SWIR			
			Ortho-UTM40N-WGS84	22aug2001-p164r71v4-tir	TIR			
Aster	2010/08/06	HDF-L1A	L1A	6aug2010-p165r71v7-L1A	Raw	88 €	Geosense	Ersdac
			Ortho-UTM40N-WGS84	6aug2010-p165r71v7-vnir	VNIR			
			Ortho-UTM40N-WGS84	6aug2010-p165r71v7-tir	TIR			
Aster	2002/08/09	HDF-L1A	L1A	9aug2002-p164r71v4-L1A	Raw	88 €	Geosense	Ersdac
			Ortho-UTM40N-WGS84	9aug2002-p164r71v4-vnir	VNIR			
			Ortho-UTM40N-WGS84	9aug2002-p164r71v4-swir	SWIR			
			Ortho-UTM40N-WGS84	9aug2002-p164r71v4-tir	TIR			

4 TOOLS AND METHODS USED

From the results of the MinUrals project (2000-2), it was clear that there is a distinct zonal pattern of contamination around Karabash. However, due to the pilot nature of these studies, a lack of detailed maps and poor access away from the main road in the area, sampling was only undertaken in a NE-SW transect. The full 2D spatial distribution of contamination from the smelter was not established. Sampling under the ImpactMin project was therefore designed in such a way that we would obtain a better idea of the spatial variation in different directions. Navigation difficulties were overcome with the help of high-resolution imagery (WV-2 and Geo-eye) loaded on an ipad, allowing sampling in most planned locations.

4.1 In-situ data acquisition at the demo sites

The aims of the in-situ data acquisition were twofold: a) to determine the impacts of mining-related activities in Karabash and Mednogorsk, and to assess whether there had been any improvement to the environment around Karabash following the installation of a new cleaner Ausmelt smelter in 2006; b) to ground-truth data acquired using remote sensing methodologies. In order to characterise airborne pollutants from the smelter, air filter samples were collected. To determine the spatial pattern of fallout of acid aerosols and metal-rich particulate from the smelter at Karabash, native and transplanted lichens, birch leaves, pine needles, soils, birch trunk and twig bark were collected and analysed. In addition, a visual assessment was made of vegetation density and type, and lichen species diversity, and birch and soil reflectance spectra were collected. A list of sample media, when collected, by which organization, and type of analysis is shown in Table 4.1.

Table 4.1 Data collected at the Karabash and Mednogorsk demo sites under WP7.4

Karabash - Media	**Data collection**	**Collection period**	**Type of analyses**
General vegetation	IMIN, UNEXE, GEOS	July and September 2011, July 2012	Visual assessment Infrared Spectroscopy
Lichens, tree and twig bark	UNEXE, IMIN, GEOS	June to September 2011	Lichens and twigs analysed by ICP-MS (UNEXE), pine bark and needles by AAC (IMIN), birch bark and birch leaves by ICP OES (IMIN). pH measured for twigs and bark (IMIN).
Smelter stack dusts	IMIN	July 2010	AAC, ICP-MS
Air filters, snow dusts, snow melt waters	UNEXE, IMIN	February – July 2011	Air filters analysed by ICP-MS and SEM-EDX (UNEXE), snow dusts and waters by ICP-MS & ICP-OES (IMIN)
Soils	IMIN	July 2011, 2012 only Karabash	ICP-OES of soils (IMIN).
Soils	GEOS	July 2011 and 2012	Infra-red Spectroscopy
Surface waters and sediments	IMIN	Waters - end April and July	ICP-MS, AAC

		2011, 2012	

Mednogorsk - Media	**Data collection**	**Collection period**	**Type of analyses**
General vegetation	IMIN, GEOS	July 2011	Visual assessment, Infrared Spectroscopy
Smelter stack dusts	IMIN	July 2010	AAC, ICP MS
Air filter, snow dusts, snow melt waters	UNEXE, IMIN	February – July 2011	Air filters analysed by ICP-MS and SEM-EDX (UNEXE)' snow dusts and waters by ICP-MS & ICP-OES (IMIN)
Wastes	IMIN, GEOS	July 2011	ICP-OES of wastes (IMIN).
Surface waters and sediments	IMIN	Waters - end April and July 2011, 2012	ICP MS, AAC (IMIN)

4.1.1 General vegetation

Floristic observations (tree and understory diversity and extent of leaf litter) were made at lichen monitoring stations, and also at each site where leaf spectra were taken. Photographs (geotagged) of transplants, lichens, trees, soil cover and their habitats were taken and times synchronised with cameras and GPS.

4.1.2 Lichen monitoring

Twenty two sites were monitored in two transects centred on the Karabash smelter, and a reference site (U0) 6 km N of Zlatoust, 30-40 km from Karabash.

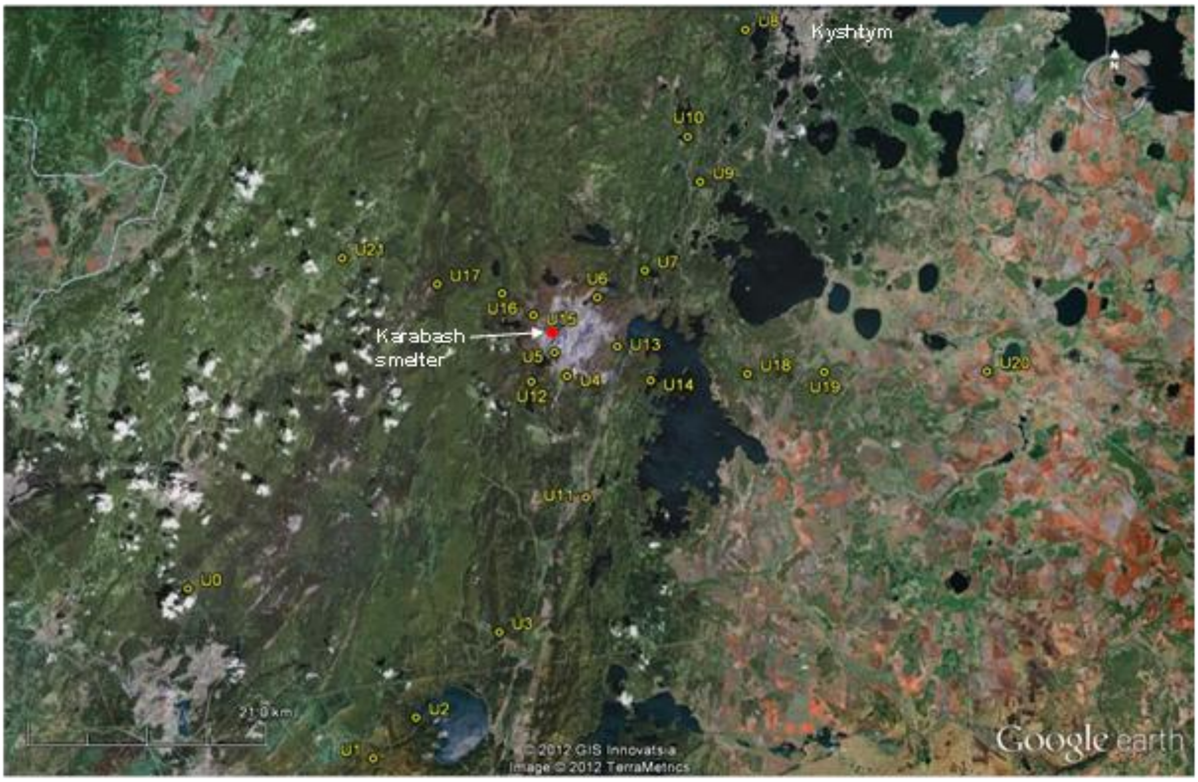

Fig. 4.1 Google image showing the locations of monitoring stations around Karabash

Lichen sampling, with multi-element geochemical analysis, is widely used to investigate spatial and temporal patterns of metal contamination. Like mosses, lichens can accumulate trace elements such as Pb, Cu and other elements of environmental concern. One of the most commonly used lichens is *Hypogymnia physodes* (L.) Nyl., which grows naturally in most parts of Europe. *Hypogymnia* transplants are often used where insufficient native samples are available (Mikhailova, 2002).

Over 150 twigs colonised by the lichen *Hypogymnia physodes* were collected in June 2011 at Nazminsky ridge ('reference site U0'). Samples were transplanted to stations along a NE-SW transect from Kyshtym (*ca* 33 km northeast of Karabash) to Severnye Peche, 6 km NE of Turgoyak Lake (*ca* 25 km south of Karabash, Purvis et al., 2004). Encouragingly, all sites (apart from U10 and U12) were within *ca* 500 m of sites established in July 2001. In some cases, the original monitoring trees were located. To better characterise the 2D nature of contamination from the Karabash smelter, a new W-E transect was established based on seven sites, 3 lying W (<20.44 km) and 4 E of Karabash (<38 km), extending to the Forest-Steppe Zone. All stations were located in medium-aged birch stands at between 280 and 695 m elevation, apart from site U0 at Nazminsky Ridge (800 m), and more than 150 m from roads, apart from site 11 (Novoandreevka). At each transplant site, in June 2011, two *Hypogymnia*-covered twigs, obtained from the reference site (U0), were attached to the base of 6 trees. These twigs were collected in September 2011, after a 3 month exposure period. In the laboratory, *Hypogymnia* was removed from the twigs using powder-free latex gloves and stainless steel knives, and stored dry in zip-lock plastic bags. Samples were either bulked for chemical analysis or else treated as replicates and analysed by ICP-MS at UNEXE and IMIN. At each transplant site, where present (generally >16.5 km from the Karabash smelter), samples were also taken of naturally growing *Hypogymnia*.

Fig. 4.2 Site 'U0' at 800 m elevation. in *Betula* - mixed coniferous forest (A-G). Many lichens colonise *Betula* trunks and twigs, 2 June 2011 (A); General view with boxes of transplants in the foreground, 3 June 2011 (B); Pavel Aminov assessing twig biodiversity, 5 September 2011 (C-E); Close-up of *Betula* twigs bearing different crustose, foliose and fruticose species. Scale in mm.

4.1.3 Lichen Frequency

In 2011, the frequency of *Hypogymnia physodes* was assessed at the base of birch trunks and at 1.5 m above ground level on each of the 6 birch trees randomly selected for monitoring at each site. This was achieved by fixing a sampling grid to each tree (method of Mikhailova and Vorobeichik, 1995). In addition, accessible branches were cut from an elevation of 2-4 m above ground level and twig lichen frequency assessed for crustose, foliose and fruticose growth forms at each site (Fig. 4.2).

4.1.4 Twig, pine needle, birch leaf and bark sampling and pH measurement

Since the 1970s, bark samples have been analysed for S and heavy metals in regional and nationwide surveys (Bargagli, 1998). Around Karabash, twig, tree bark, pine needles, birch leaves and bark samples were taken from the same localities as the lichen samples (Fig. 4.1). Smooth and approximately flat bark samples (ca. 4 x 10 cm patches, 2-3 mm thick) were collected at each site between 1.5 - 2.5 m above ground level. Between 1 and 6 per site were selected for pH measurement. Twigs were also sampled (ca 10 mm long x 0.5 - 0.7

mm thick) and 3 to 18 selected per site for pH determination. The pH of 132 twig and 85 trunk samples were measured at IMIN in triplicate in the laboratory using the following methods. Twigs were cut into 7 cm lengths, the cut ends sealed with paraffin wax and soaked in tubes filled with 6 cm^3 25 mM KCl. Samples were shaken for 1 hour at room temperature using an automatic shaker, the twigs removed and the pH of the solution measured with a Jenway Model 370 pH/mV/temp meter using an epoxy combination pH electrode (924 001) and ATC probe (027 500). Small, ca. 2.5 cm^2 pieces of *Betula* trunk (lower surfaces not waxed) were placed in small beakers, immersed for 5 minutes in 2 cm^3 25 mM KCl and surface bark pH measured using a BDH Gelplas Flat Tip combination membrane electrode (cat ref: 309-1070-03). Mean pH values were calculated from H^+ concentrations and average values calculated for twig and bark samples at each site.

4.1.5 Chemical analysis of lichens, bark and twig samples

Elemental analysis of lichen samples was carried out at UNEXE and IMIN. Lichens were sorted under magnification to remove extraneous material including bark, twigs, leaves, and lichens of species other than *hypogymnia physodes*. At UNEXE, up to 4 g of air dried lichen was ground with an agate mortar and pestle with liquid nitrogen, mixed, and dried in a dessicator for at least 24 hours, noting the average weight loss. Bark was removed from 7 cm length twigs (0.1 – 0.2 g) with a scalpel and also dessicator dried. Aliqouts of about 0.2 g were digested with 5 ml high purity concentrated nitric acid and 0.5 ml high purity hydrofluoric acid with a closed vessel microwave digestion system and diluted as appropriate with doubly deionised water. At IMIN, lichen samples were sorted under a binocular microscope to remove extraneous material including bark, twigs, leaves, and lichens of species other than *hypogymnia physodes*. The sorting was carried out in a ‘clean cabinet’ using gloves and ceramic forceps. Bark samples (7 x 4 cm strips) were taken from the trunks of trees with diameters of about 20-35 cm. Twigs were collected up to 1 cm in diameter and 10 cm long. Aliqouts (for lichen and bark samples) of about 0.6 g were digested with 14 ml high purity concentrated nitric acid over night. The solutions were then heated at 120^{o}C for 3 hours. On cooling, 6 ml of pure H_2O_2 was added and then the solutions heated at 50^{o}C for 30 minutes. The temperature was then slowly increased to 120 °C until no brown fumes were visible. The solution was poured into a 50 ml flask, and then washed with deionized water. Multielement analysis at UNEXE and IMIN was performed by inductively coupled plasma mass spectrometry (ICP-MS) calibrated against commercially available standard solutions. Quality control was provided through identical analysis of the reference materials BCR 482 Lichen and SRM 1547 Peach Leaves, accepting elements within ±10% of the published reference or information values. Sulphur analysis was performed under contract on the same samples by University of Sheffield by ICP atomic emission spectrometry.

Samples of pine needles and bark were collected from trees (Pinus Sylvestris L.) 70 to 150 years in age (ages estimated from either annual tree rings in cores drilled with a Pressler borer or from the visual diameter of the trunk). All trees were representative of the site of observation. Samples were taken only from healthy living branches, containing no observed necrotic tissue, mechanical damage or signs of illness. Needles were collected separately for the current year of growth, and then each year previously, for 3 years. Bark samples were taken from a height of 1.5 m above ground level. Samples consisted of the outer layer of the cortex to a thickness of no more than 1-1.5 cm. Samples were dried in the laboratory and stored in paper bags. The pine needle and bark samples were mixed with acid (HCl + HNO_3; 3:1 ratio) and then ashed in a muffle furnace at 450^{o}C. To the samples of dry matter, ranging in mass from 1 to 5 g, was added 1N. HNO_3 to a total volume of 14 ml. The resulting solution was analysed in an AAC Perkin-Elmer 3110 atomic absorption spectrophotometer with either air-acetylene flame atomisation or Analyst 300 with HGA 850 electrothermal mode atomization.

Birch leaves were picked from young trees with no signs of disease and pests. Trees were visually divided into categories – large (> 4 m), average (4-2 m) and small (<2 m in height). At each sampling point, 100 birch leaves were selected from 5-10 trees. The samples were dried in the laboratory and stored in paper bags. The samples were then ground and 3 g of powder placed into a glass beaker (150 ml) with 40 ml HNO_3 overnight. The solution was then heated to 120 ^{o}C for 3 hours, 15 ml of H_2O_2 added, and then heated to 50^{o}C for 30 minutes. The temperature was then increased to 120 °C and held until no brown fumes could be observed emanating from the beaker. 20 ml of HNO_3 and 10 ml of H_2O_2 were then added and the solution again heated to 120 °C until no brown fumes were observerable. The solution was then washed into a 50 ml flask using deionised water. Metal contents were determined by ICP OES (Varian 720 ES)

4.1.6 Air filters, snow dusts and melt waters

The aim of this sampling was to determine the nature of airborne particulate being emitted from the smelters, to aid in atmospheric dispersion modelling and to understand patterns of dispersion of different particle types from the smelter. It was not within the remit of the project to provide an assessment or maps of air quality.

Stack dust samples were collected in 2010 from the stack at Karabash by the copper smelter company and in Mednogorsk by the Office of Environment. Air filter samples were collected in both Karabash and Mednogorsk using a Tuff 4 Plus Personal Air Sampler operated at a flow rate of 1.5 l/m (5% accuracy). The pump was calibrated each evening using a 0.3 to 3 l/m flowmeter. Total suspended particulate was collected onto 25 mm diameter, 0.4 μm pore size, polycarbonate filters, as these provide a smooth flat substrate for imaging and elemental analysis in the scanning electron microscope. Prior to sample collection, the filters were preconditioned in a desiccator for 2 days, each in an individual plastic box, and then weighed three times. All filter handling was carried out using ceramic forceps in a 'clean cabinet'. The filters were then placed in the sampling head of the air filter system which was fixed at a standard height of 1 m above ground level. Sampling was carried out between 3 and 11 hours at each site. The following were recorded: location (GPS – WGS84 UTM), time/date, wind direction and strength, temperature, sampling duration and air volume sampled. Following sampling, the filters were removed from the sampling head and placed back in their plastic boxes. In the laboratory, the filters were conditioned in exactly the same way as before and then weighed three times. The sample weight was calculated from the difference between the average of the post sampling and pre sampling filter weights. Each filter was then cut into quarters, one quarter weighed in order to calculate the proportion of the total filter analysed (necessary for the calculation of element concentrations on the filter per m^3 of air sampled), in preparation for wet chemical analysis. The filters were digested in 5 ml conc. nitric and 1 ml HF using a Mars microwave digestion system. The resulting solution was diluted to 50 ml for analysis.

Fig. 4.3 Air sampling apparatus set up downwind from the Karabash smelter

For imaging and elemental analysis in the SEM, small piece (~4 x 4 mm) of each of the airborne particulate filters was mounted onto a 12 mm diameter SEM stub using Araldite. The stubs were loaded into a Jeol JSM-7001F field emission SEM with solid state X-Max 80 energy dispersive X-ray element detector with Oxford Instruments INCA analysis system at Plymouth University, UK. The SEM was operated at 15 kV in high vacuum mode. The filter surface was imaged at a magnification of x5000 and every particle analysed in a number of randomly selected fields (depending on the number of particles in each field).

Snow dusts and melt waters – Snow sampling was carried out at the end of the winter season, a few days before the first signs of thaw in Karabash and Mednogorsk, so that the samples represented the longest time period possible, estimated to be around 65 days. At each snow sampling point, the location and depth of snow cover was recorded. Snow was sampled using a polyvinyl cylinder with a diameter of 104 mm and a height of 1600 mm. Between 4 and 6 snow 'cores' were placed in sterile plastic bags.

Samples were thawed out in the laboratory at room temperature in a plastic container. The volume of snow melt water was between 3 and 4 litres, sufficient to filter enough dust for geochemical analysis. pH, Eh and other physical and chemical parameters were measured in the melt waters, using the same methods as in the analysis of river waters. The melt waters were then passed through 0.45 μm pore size cellulose acetate membrane filters. The filters were then dried to determine the mass of snow dust in each sample. The melt waters and dusts were then analysed by ICP-MS (Perkin Elmer ELAN 9000) to determine their metals contents.

The mass of dust for a given area per day (P) was calculated using the formula:

$P = P_o/(St)$

where P is in kg/day/km^2 or mg/day/m^2;

P_o = mass of dust in the snow sample (mg);

S = cross-sectional area of the 'core' (m^2);

t = time from the beginning the first snow to the sampling day (days).

Knowing the chemical composition of snow dust, we can estimate the total load (in the snow cover) of its constituent chemical elements and their compounds:

Pi = (CiPp)/100

where Pi = the total load (supply) of a chemical element "i" in the snow cover (kg/day/km^2 or mg/day/m^2);

Ci = concentration of element "i" in the snow cover (ppm);

P = dust load (kg/day/km^2 or mg/day/km^2).

4.1.7 Wastes

Samples of wastes were collected by IMIN from the Karabash and Mednogorsk demo sites. Large waste dumps were sampled by collecting around 2 kg of material at approximately 1 to 2 m intervals from around the base of the dumps. When between 5 and 10 samples had been collected, depending on the size of the dump, the material was homogenized on a polythene sheet using a trowel. The material was then 'cone and quartered' twice and one quarter of the final batch bagged for transportation to the laboratory. The samples were then dried at 60 °C in an oven and then pulverized in a jaw crusher. The resulting material was then 'cone and quartered', and one quarter passed through a series of sieves. Around 250 g of the 2.2-0.63 mm size fraction was then ground in a tungsten carbide mill (Retsch RM 100).

For the tailings dumps, a trench was dug to a depth of between 1 and 2 m. The trench wall was then cleaned and material sampled by depth, according to colour and mineralogical variations within the tailings. Where time was not permitting, surface samples only were collected (Mednogorsk). Samples were air dried in the laboratory, sieved to < 0.6 mm, and then ground to a fine powder in a tungsten carbide mill (Retsch RM 100).

Powders of both the wastes and tailings were acid digested in HF+HNO_3+HCl in Teflon vessels and analysed using ICP-OES (Varian 720 ES).

4.1.8 Surface waters and sediments

Surface water samples were collected by IMIN during the wet season in May 2011, following snow melting, and the dry season in July 2011. Samples were taken at key points within the drainage system: representative of background surface waters (Sak-Elga river before the

Bogorodsky pond and the Miass river before the Sak-Elga river), waters impacted by mining-related activities (Serebryanka river and "Red Stream"), and from approx. 100m below the confluence of natural and contaminated watercourses (confluence of the Sak-Elga river and "Red Stream" and Miass river and Sak-Elga river) (Fig. 4.4).

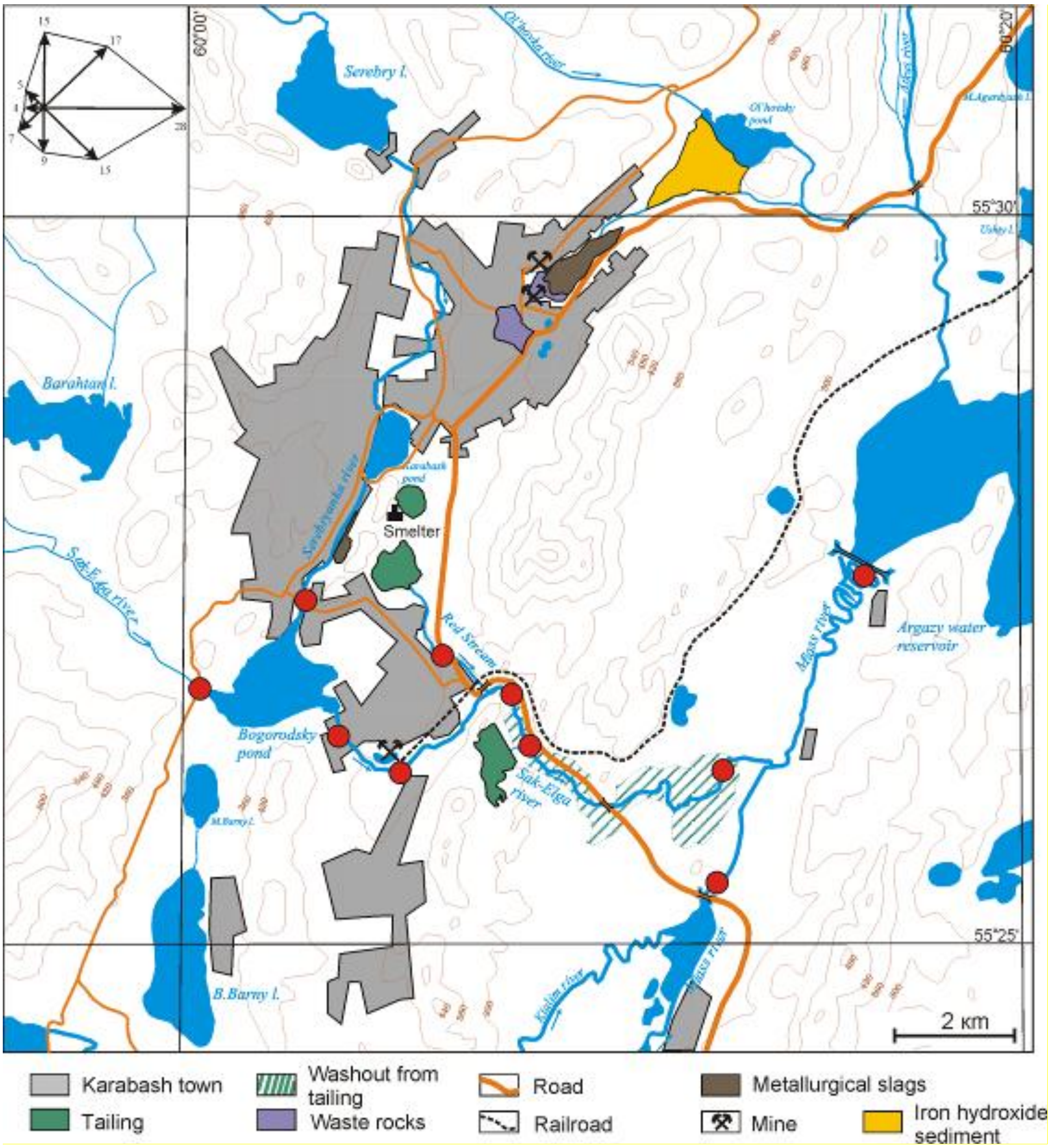

Fig. 4.4 Water and sediment sampling localities around Karabash.

Water samples were collected into clean 1.5 liter plastic bottles, until full, and clearly labeled. The samples were taken to the laboratory for analysis on the same day as collection. pH and redox potential were determined using a Yokogava 8221-E meter (Japan). The instrument had a measuring range for pH of 0-14, and Eh of 0 - ± 1999 mV. The absolute error of the instrument was ± 0.01 units for pH and 1 mV for Eh. pH was calibrated using standard buffer solutions (pH 3.56 and 6.86). Conductivity was measured using a HI – 933000 (Germany) conductivity meter with automatic temperature compensation. The measurement range of the instrument is 0-199.9 mS /cm, and it has an accuracy of 1%.

Water samples were filtered using 47 mm diameter 0.45 μm pore size Whatman cellulose nitrate filters, using a Sartorius 1651 hand pump. For cation determinations, 30 ml of filtered samples were collected in Nalgene bottles and acidified with 0.5 ml high purity conc. HNO_3. Element concentrations were determined by ICP-MS (ELAN 6000, ELAN 9000), using standard techniques (with reference to synthetic solution standards). For anion determinations, 300 ml of filtered water were collected in Nalgene bottles and analyses carried out by colourimetry, titrimetry and turbidimetry.

Sediment samples were collected during July 2011. Samples were placed in polythene bags, air dried in the laboratory, sieved to <0.6 mm, ground to a fine powder in a tungsten carbide mill (Retsch RM 100), acid digested in $HF+HNO_3+HCl$ in Teflon vessels and analysed using AAC (Perkin Elmer 3110). A certified reference material (JSD-1, stream sediment) was regularly digested and analysed, which gave Pb and Cd values within 10% and 6% of the certification, respectively.

4.1.9 Spectral analysis of leaves and soils

The leaf and soil spectral analysis programme was designed to identify parameters that correlate with observational and chemical datasets collected by IMIN, UNEXE and GEOS. The aim was to develop ground-based methods for Earth observation related to the environmental impacts of mining-related activities and to ground truth interpretations from the satellite imagery.

The approach was to collect spectra from leaves and soils in both Karabash and Mednogorsk using a portable spectrometer. In addition, we intended to fly a number of airborne surveys with a Smartplanes unmanned aircraft (UAV). Unfortunately, it was not possible to fully carry out our planned work as we encountered a number of severe logistical problems. During the inspection of the ATA-carnet for our equipment, issued by the Dutch Chamber of commerce, the Yekaterinburg Airport customs officials discovered a small mistake in the document, and for this reason they confiscate all equipment. It took a full week and very significant effort by IMIN to recover the portable infrared spectrometer. The UAV was not allowed entry into Russia and had to be returned to Holland. We lost a full week waiting for the Terraspec to be released and one day at the end of the period because the spectrometer had to be returned to customs. As a result we only had one week to visit both Karabash and Mednogorsk. As Mednogorsk is a full day drive from Miass, it meant that we only had 5 effective field days instead of the planned 13 days.

After collecting the spectrometer at customs, we found that the fibre optic cable of the Terraspec instrument was badly damaged, and as a result we could not use the instrument for soil analysis. Leaf measurements could still be performed, but the spectra were extremely noisy and therefore only semi-qualitative at best. Since we could not measure the soils and rocks in situ, we planned to take the samples to the Netherlands for analysis. Unfortunately, Russian regulations did not allow the export of the soil and rock samples, and therefore a portion of the samples (mostly from Mednogorsk) had to stay behind without being measured.

In spite of these issues, the results of our 2011 fieldwork were encouraging and therefore we decided to organise a second field visit in 2012, even though it was not foreseen in the original project plan. Based on the 2011 field results, in combination with the outcome of the processing of the satellite images, it was decided that in 2012 we should focus on Karabash. The aims of this fieldwork were to repeat the 2011 measurements, to extend our sampling program further away from the smelter, and to obtain a denser measurement grid for the area already sampled. Because some of the problems with the spectrometer were not easily solved, and in order to be able to conduct solar reflectance measurements, GEOS decided to replace its old spectrometer with a new state-of-the-art Spectral Evolution portable infrared spectroradiometer.

Birch leaves were measured in more than 140 locations using the Spectral Evolution spectrometer with bifurcated vegetation probe. The preferred size of trees for sampling was between 2m and 5m but in some cases only smaller trees were available. Leaf sampling was done at a height of approximately 1.5 m. In most locations we sampled three separate trees, and for each tree we measured three leaves. A number of parameters were then calculated as vegetation indices (see Results).

For the Karabash demo-site, where *in situ* vegetation spectra were available, in total 11 vegetation indices were derived from the *in situ* reflectance data (Table 4.2). Vegetation indices correlate closely with vegetative biochemical constituents, since its computation is based on spectral characteristics which maximize sensitivity to the parameter of interest whilst minimizing sensitivity to other terms (Asner et al., 2003).

Table 4.2 Spectral vegetation indices derived from in situ vegetation spectra

Name	Abbrev.	Formula[a]	References
Normalized green red difference index	*NGRDI*	$(R_g - R_r)/(R_g + R_r)$	Tucker (1979)
Triangular greenness index	*TGI*	$-0.5 \cdot [(\lambda_r - \lambda_b) \cdot (R_r - R_g) - (\lambda_r - \lambda_g) \cdot (R_r - R_b)]$	Hunt et al. (2011)
Modified chlorophyll absorption reflectance index	*MCARI*	$[(R_{700} - R_r) - 0.2 \cdot (R_{700} - R_g)] \cdot (R_{700}/ R_r)$	Daughtry et al. (2000)
Transformed chlorophyll absorption reflectance index	*TCARI*	$3 \cdot [(R_{700} - R_r) - 0.2 \cdot (R_{700} - R_g) \cdot (R_{700}/ R_r)]$	Haboudane et al. (2002)
Triangular chlorophyll index	*TCI*	$1.2 \cdot (R_{700} - R_g) - 1.5 \cdot (R_r - R_{550}) \cdot \sqrt{(R_{700}/ R_r)}$	Haboudane et al. (2008)
Soil adjusted vegetation index	*SAVI*	$(1 + 0.5) \cdot (R_n - R_r)/(R_n + R_r + 0.5)$	Huete (1988)
Optimized soil adjusted vegetation index	*OSAVI*	$(1 + 0.16) \cdot (R_n - R_r)/(R_n + R_r + 0.16)$	Rondeaux et al. (1996)
Modified soil adjusted vegetation index	*MSAVI*	$0.5 \cdot \{2 \cdot R_n + 1 - \sqrt{[(2 \cdot R_n + 1)^2 - 8 \cdot (R_n - R_r)]}\}$	Qi et al. (1994)
Normalized difference vegetation index	*NDVI*	$(R_n - R_r)/(R_n + R_r)$	Tucker (1979)
Triangular vegetation index	*TVI*	$0.5 \cdot [120 \cdot (R_n - R_g) - 200 \cdot (R_r - R_g)]$	Broge and Leblanc (2000)
Ratio vegetation index R_{760}/R_{900}	$RVI_{760\text{-}900}$	R_{760}/R_{900}	-

[a] R_λ is the reflectance at wavelength λ; R_b, R_g, R_r, R_n are the reflectances at 480, 550, 670, 800 nm, respectively (e.g. Zarco-Tejada et al., 2004).

The vegetation indices used in this study include intrinsic, soil-adjusted and angular indices. Intrinsic indices, including normalized difference vegetation and ratio indices, involve the extraction of spectral information from two spectral bands (e.g. *NDVI*, *NGRDI*, $RVI_{760\text{-}900}$). However, an inherent drawback of these indices is the loss of uniqueness in information by the fact that different plants can have different spectral responses, but have band ratio values that are equal. Soil-adjusted vegetation indices attempt to improve the extraction of spectral information of vegetation considering soil influences. Soil reflectance is generally lower in near-infrared (NIR) wavelengths and higher in red wavelengths compared to vegetation reflectance. The basic assumption on which the soil-adjusted vegetation indices are based is that all soils establish an equal linear relationship between NIR and red reflectances. Intrinsic soil-adjusted vegetation indices are intrinsic indices which include a soil-adjustment factor, based on the coefficients of the soil line, in their calculations (e.g. *SAVI*, *MSAVI*, and *OSAVI*).

Broge and Leblanc (2000) developed the Triangular Vegetation Index, *TVI*, based on the area of a triangle with vertices at green, red and NIR wavelengths, which is sensitive to chlorophyll content. Other angular indices include *TCI* and *TGI*. Commonly used chlorophyll-related indices containing information from the green band, such as *TCARI*, and *MCARI*, were also included in this study.

5 RESULTS OF IN-SITU SAMPLING AND ANALYSIS

5.1 Karabash demo site

5.1.1 General vegetation

Karabash lies on the border between Taiga and Forest-Steppe zones, on the eastern slopes of the South Ural Mountains. The vegetation of the eastern slopes of the mountains (mainly pine and birch) differs considerably from that of the western slopes, dominated by broad-leaved forests, intermixed with conifers. In the southern part there is forest-steppe vegetation. At higher elevations, and on wetter slopes, conifers normally predominate and pioneer species, particularly birch are locally frequent due to forest management and other anthropogenic activities. However, individual forest parcels, varying from almost 100% pine to almost 100% birch, do occur at least partly reflecting anthropogenic activities. Vegetation type and density is also affected by geology. The area is transected by a major fault zone which marks the suture between the Siberian and East European cratons. Many different rocks occur in the area as narrow fault slices, including granitoids, miaskites, ultrabasic rocks (dunites, harzburgites) which will influence both soils and plants. Humic soils are generally thick and well developed.

An appraisal of vegetation type was carried out at each lichen transplant site (Table 5.1) and each point for leaf spectral analysis (Fig. 5.4). In general, at a distance of >10 km from the smelter, the forest exhibits considerable diversity in terms of tree species and understory, often at a local (<100 m) scale. Whilst a species-rich herbaceous layer is often present, considerable variations do occur over short distances reflecting various factors (soils, management, shading etc).

Table 5.1 Notes on vegetation types and abundances at lichen monitoring sites.

Site	Date	Latitude	Longitude	Vegetation notes
U0	03/06/2011	55.26490	59.69443	Mixed coniferous (*Abies*, *Picea*, *Pinus*) / deciduous (*Betula*, *Sorbus* and *Populus* etc) woodland in herb-rich grassland.
U1	09/06/2011	55.12957	59.95104	*Betula* woodland with scattered *Larix* in herb-rich grassland.
U2	09/06/2011	55.16255	60.00993	*Betula* woodland with scattered *Pinus* and *Sorbus* saplings in herb-rich grassland.
U3	09/06/2011	55.23111	60.12449	*Betula* woodland with scattered *Pinus* and *Sorbus* saplings in herb-rich grassland.
U4	05/06/2011	55.43630	60.21800	*Betula* woodland with scattered Pinus. <75% ground cover dominated by bryophytes and-lichen with scattered forbs characteristic of serpentiniferous soils.
U5	04/06/2011	55.45522	60.20063	*Betula* woodland with deep litter layer and impoverished herbaceous ground cover (< 1%).
U6	04/06/2011	55.49907	60.25987	*Betula* woodland with scattered young *Pinus* and *Populus*. Ground flora generally impoverished with deep litter layer; however tolerant species locally dominant.
U7	08/06/2011	55.52071	60.32602	*Pinus* / *Betula* woodland influenced by logging activities. Moderately herb-rich grassland.
U8	07/06/2011	55.71354	60.46695	*Betula* / *Pinus* forest with young *Sorbus* and *Malus*. Well developed species-rich herbaceous layer.
U9	08/06/2011	55.59170	60.40317	*Betula* woodland with *Sorbus* and scattered *Pinus*. Species-rich herbaceous layer.
U10	07/06/2011	55.62779	60.38590	*Betula* / *Pinus* woodland with abundant *Sorbus* saplings in moderately species-rich grassland.
U11	06/06/2011	55.33907	60.24405	*Betula* woodland with *Populus tremula* saplings and diverse, species-rich herbaceous layer.
U12	04/06/2011	55.43190	60.16841	*Betula* woodland with scattered *Pinus*, *Picea*, *Larix*, *Abies* and *Sorbus*. Species poor herbaceous layer.
U13	12/09/2011	55.45991	60.28773	*Betula* woodland with extensive (>90%) leaf litter; herbaceous layer absent; terricolous bryophytes and lichens occasional.
U14	12/09/2011	55.43260	60.33366	*Betula* woodland with scattered *Pinus*. Species-impoverished grassland. Leaf litter ca 50%.

U15	15/09/2011	55.48501	60.17124	*Betula* woodland with deep litter layer; ground cover absent.
U16	15/09/2011	55.50231	60.12805	Mixed *Pinus, Betula* woodland in grassland dominated by ericaceous species.
U17	15/09/2011	55.50972	60.03794	Coniferous woodland dominated by *Abies* and *Pinus*; *Betula* rare. Tall herbaceous layer well developed.
U18	16/09/2011	55.43771	60.46793	*Betula* woodland with scattered *Pinus* saplings and diverse flora.
U19	16/09/2011	55.43891	60.57418	*Betula* woodland with *Populus tremula* and *Pinus* saplings in grassland with a few locally dominant species.
U20	16/09/2011	55.43861	60.80022	*Betula* woodland with *Populus tremula* saplings in grazed herb-rich grassland, grazed by cattle.
U21	17/09/2011	55.53030	59.90569	*Betula* woodland with *Pinus*, *Larix*, *Abies*, *Sorbus* and *Populus tremula* saplings in herb-rich grassland with diverse and abundant mosses and lichens.

At distances between ~10 and 4 km from the smelter, the forest noticeably starts to thin. Pine trees become reduced in abundance and size and have a discoloured (brown) appearance (Fig. 5.2), and the herbaceous layer can disappear entirely or else is restricted to a few tolerant species (including pollution tolerant ground-dwelling lichens and bryophytes). In sheltered areas extensive undecomposed leaf litter is often present and soil quality markedly deteriorates. In many places there is only a very thin layer of poorly decomposed organic matter covering exposed rock (see Fig. 5.2).

At distances less than ~4-5 km, the conditions rapidly deteriorate (Fig. 5.3). Pine trees are absent, there is little or no undergrowth and very little top-soil. The ground surface consists of weathered rock with varying iron oxide enrichment. Slopes in this area are often heavily eroded, such as the west face of Karabash ‘mountain’ with serpentiniferous soils generally unfavourable for plant growth.

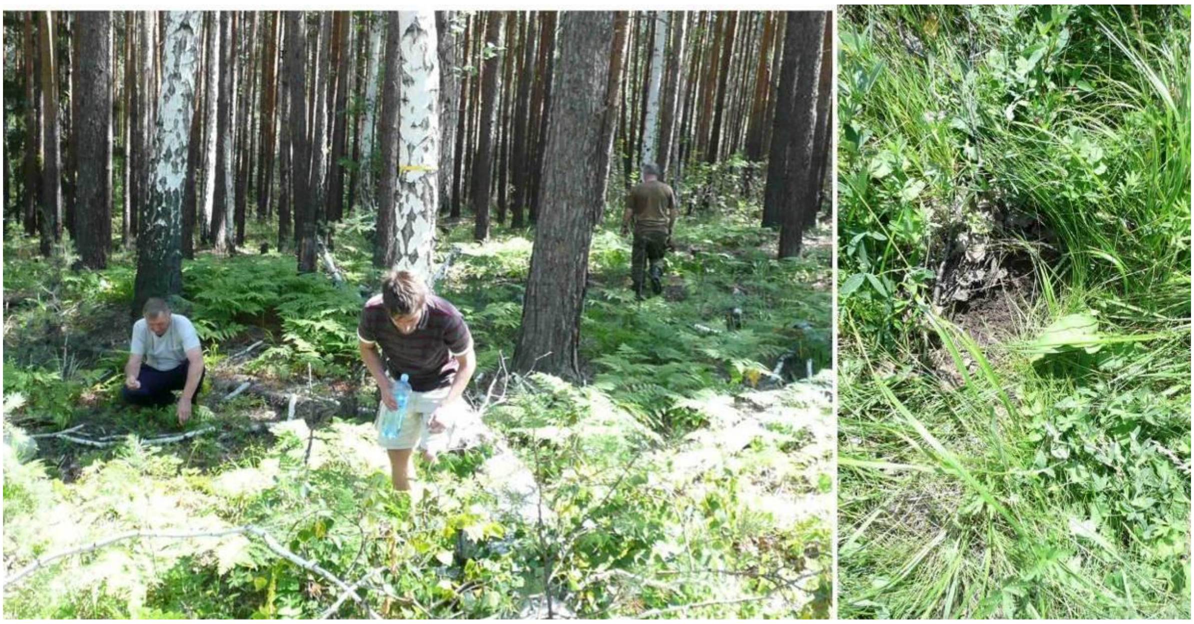

Fig. 5.1 *Pinus / betula* mixed forest vegetation. Diverse undergrowth and well-developed soils occur at distances greater than 10-15 km from the Karabash smelter.

Fig. 5.2 Vegetation and soils at less than 10 km from the smelter.

Fig. 5.3 Less than 4 km from the smelter; vegetation is typically denuded and soils eroded. Right-hand picture shows the smoke moving eastwards from the smelter stack towards Karabash 'Mountain'.

At each site where leaf spectra were taken, an estimate was made as to the relative abundance of pine trees and the condition of the herbaceous understory. Four groups were identified, with pine trees and understory defined as absent, scarce, moderate or abundant. Although this information was not collected in a systematic and statistically sound manner, and hence should be regarded as indicative only, these parameters clearly show a zoned pattern around the smelter (Fig. 5.4). The abundance of pine trees may not be as reliable an environmental indicator as the herbaceous layer as the presence of pine trees depends strongly on other factors such as forestry management.

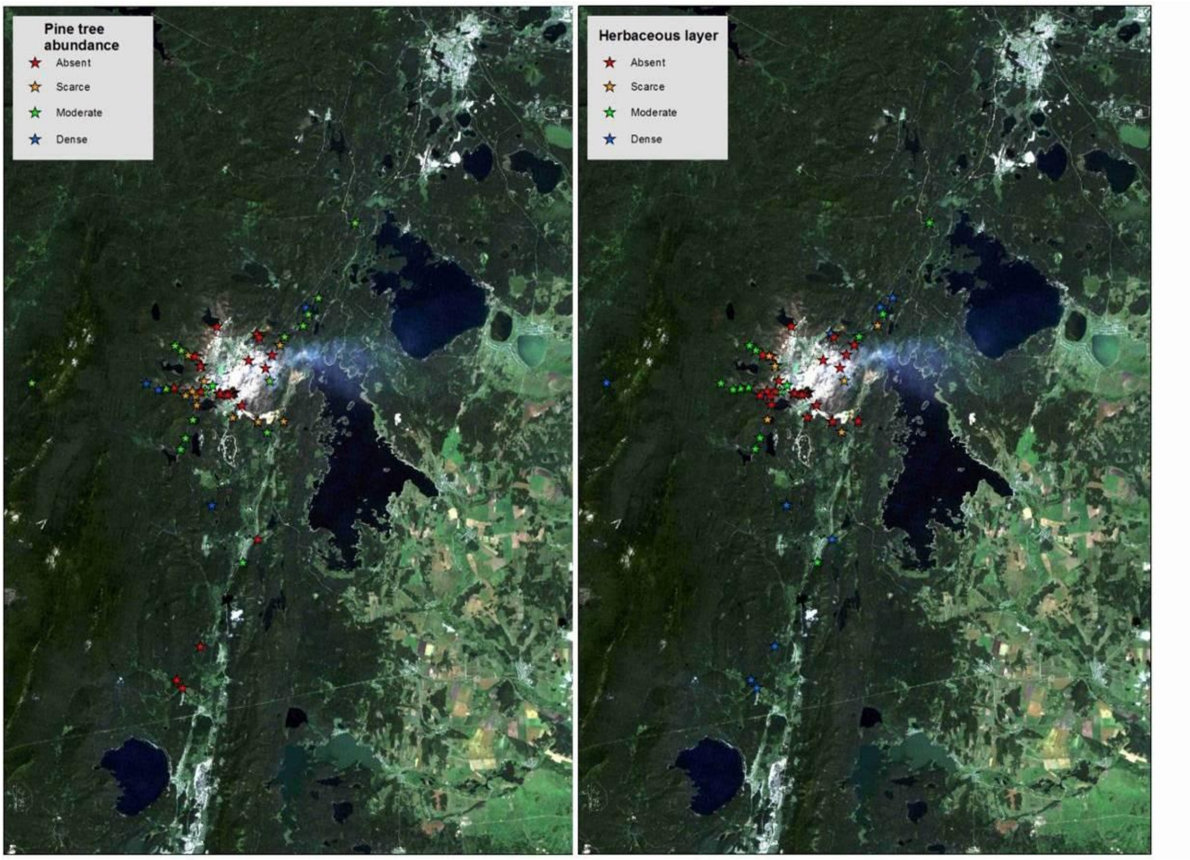

Fig. 5.4 Distribution of pine trees (left) and density of the herbaceous understory (right) at each point where leaf spectra were acquired.

5.1.2 Lichens and tree bark

Hypogymnia lichen frequency was measured at monitoring stations U0, U3-16 & 18-21 (Fig. 4.1), results in Table 5.2. Different lichens were recorded on twigs, either crustose, foliose and fruticose growth forms (Table 5.3).

Table 5.2 *Hypogymnia* frequency (at tree base and 1.5m above ground level), together with birch twig and bark pH at lichen monitoring sites.

Site	Date	Latitude	Longitude	% *Hypogymnia* frequency (base)	% *Hypogymnia* frequency (at 1.5m)	**Twig lichen frequency**	Twig pH	Trunk pH
U0	03/06/2011	55.26490	59.69443	70	100	23	4.1	4.8
U1	09/06/2011	55.12957	59.95104					
U2	09/06/2011	55.16255	60.00993					
U3	09/06/2011	55.23111	60.12449	100	55	3	4.5	4.3
U4	05/06/2011	55.43630	60.21800	0	0	0	4.5	4.6
U5	04/06/2011	55.45522	60.20063	0	0	0	4.6	5.0
U6	04/06/2011	55.49907	60.25987	0	0	0	4.0	4.3
U7	08/06/2011	55.52071	60.32602	10	0	0	4.5	4.7
U8	07/06/2011	55.71354	60.46695	88	25	0	4.0	4.7
U9	08/06/2011	55.59170	60.40317	93	35	0	4.6	4.9
U10	07/06/2011	55.62779	60.38590	0	0	0	4.4	4.5
U11	06/06/2011	55.33907	60.24405	78	7	0	4.4	4.6
U12	04/06/2011	55.43190	60.16841	0	0	0	4.9	4.9
U13	12/09/2011	55.45991	60.28773	0	0	0	4.6	5.5
U14	12/09/2011	55.43260	60.33366	0	0	0	4.5	5.0
U15	15/09/2011	55.48501	60.17124	0	0	0	3.7	4.7
U16	15/09/2011	55.50231	60.12805	8	0	0	3.6	4.7
U17	15/09/2011	55.50972	60.03794	N/A	N/A	0		4.3
U18	16/09/2011	55.43771	60.46793	35	0	0	3.9	4.5
U19	16/09/2011	55.43891	60.57418	48	0	0	3.8	4.4
U20	16/09/2011	55.43861	60.80022	80	8	0	4.1	4.7
U21	17/09/2011	55.53030	59.90569	45	53	0	3.7	5.4

Hypogymnia frequency ranged from 0 to 100% on trunk bases and at 1.5 m above ground level. The frequency of *Hypogymnia* with distance from the smelter showed an inverse bell-shaped curve away from the smelter in both the NE-SW and W-E transects (Fig. 5.5). Similar trends were observed at 1.5 m above ground level.

Five groupings in lichen frequency data were resolved by multivariate analysis:

(A) Reference Site 'U0'. Characterised by the high frequency of lichens occurring on *Betula* twigs (9 crustose, 6 foliose and 3 fruticose) and the highest recorded frequency of *Hypogymnia* on *Betula* trunks at 1.5 m above ground level.

(B) Site 'U3'. Southernmost site of the SW transect characterised by a few lichens recorded on twigs (1 crustose and 4 fruticose) recorded on *Betula* twigs and the highest recorded frequency of *Hypogymnia* at the base of *Betula*.

(C) Sites 'U21', 'U8', 'U9', 'U11', and 'U20'. Outer sites characterised by the absence of lichens recorded on twigs, moderate *Hypogymnia physodes* frequency at 1.5 m above ground level and high frequency at ground level.

(D) Sites 'U18', 'U19', 'U7', 'U16'. Inner sites characterised by the low *Hypogymnia* frequency at ground level, absence of *Hypogymnia* at 1.5 m above ground level and absence of lichens on twigs.

(E) Sites 'U12', 'U4', U5', 'U6', 'U10', 'U15', 'U13', and 'U14'. Central sites and 'U10' lying to the NE. A virtual *Hypogymnia* lichen desert with no lichens recorded on twigs.

Table 5.3 Numbers of different lichens recorded on twigs at lichen monitoring sites U0 (lichen reference site) and U3 according to growth form. No lichens were found growing on twigs at other monitoring sites.

Site	Crustose	Foliose	Fruticose
UO	9	6	3
U3		4	1

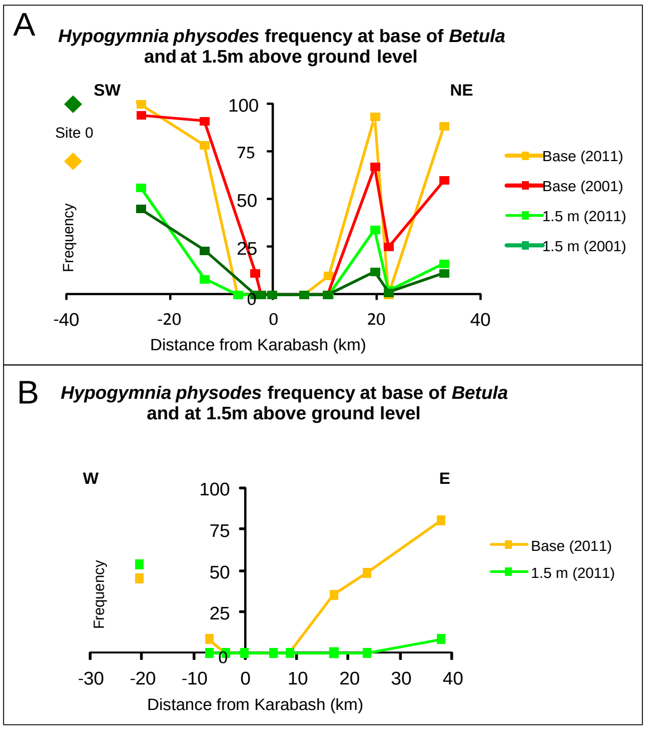

Fig. 5.5 *Hypogymnia* frequency at the base, and 1.5m above ground level, of birch trees with distance from the smelter in NE-SW (A) and W-E (B) transects.

5.1.3 Birch trunk bark and twig pH

Both birch bark and twig pH was acidic throughout the study area, average site values ranging from 3.57 (site U16) to 4.88 (site U12) for twigs and from 4.29 (site U17) to 5.51 (site U13) for trunk bark (Fig. 5.6). There was a decrease in pH in both tree bark and twigs towards the east of Karabash (< 24 km) and towards the W (<15 km) and SW (<30 km). Both bark and twigs showed increasing pH towards the NE (<24 km).

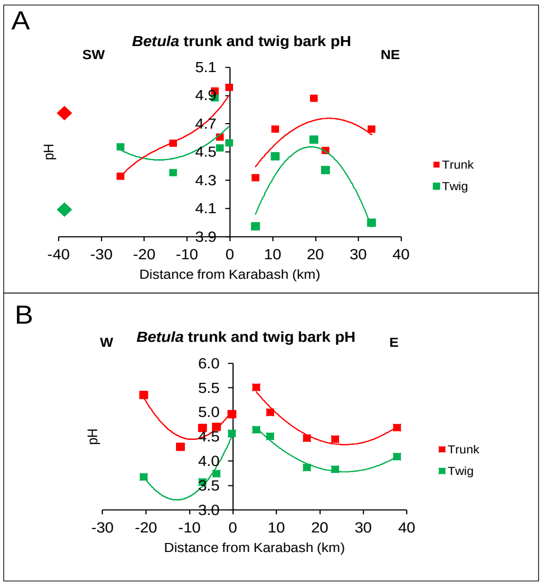

Fig. 5.6 Birch trunk bark and twig pH with distance from the smelter in NE-SW (A) and W-E (B) transects.

5.1.4 Lichen and twig elemental compositions

Lichens are widely used in biomonitoring studies as they can provide cost effective and discrete tools for mapping spatial and temporal patterns of pollutants deposited from the atmosphere. Lichens accumulate metals either from uptake of soluble chemical species from wet or dry deposition or as particles from dry deposition (Williamson et al., 2004a). The presence of metal-rich particles on thallus surfaces and within their interiors has been directly demonstrated using scanning electron microscopy (Williamson et al., 2004a).

Plots of selected element concentrations in lichens (transplant and naturally occurring) with respect to distance from the Karabash smelter are shown in Fig. 5.7 and 5.8. In *Hypogymnia* transplants, Pb concentrations show a characteristic sharp increase within ca. 10 km from the Karabash smelter, both to the NE and SW (Fig. 5.8). In the lichen transplants closest to the smelter (Site 5), of all elements analysed, Zn reached the highest concentration (1894 µg/g), followed by Cu, Pb, As, Sn, Ni, Sb, Cd, Bi, Co and Tl (in order of decreasing concentrations).

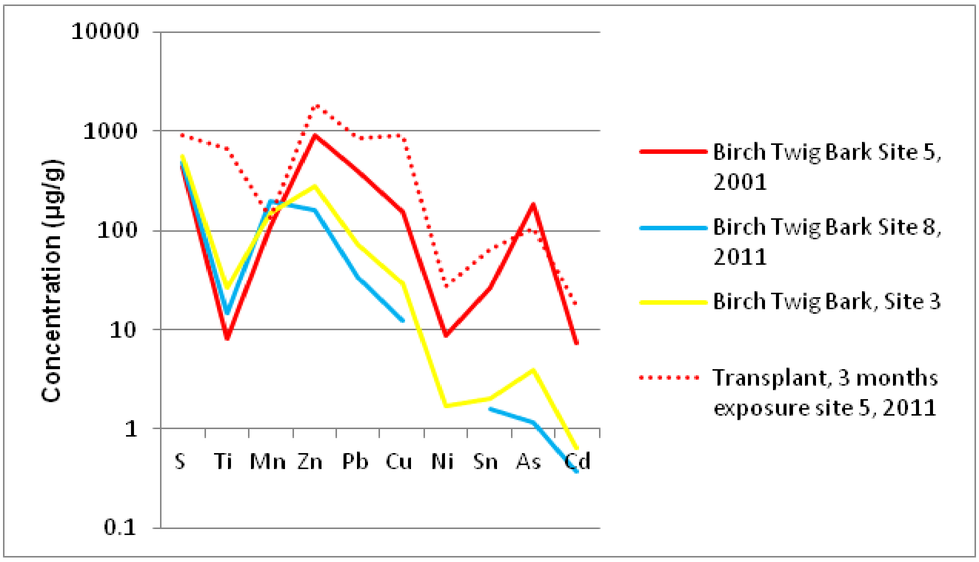

Fig. 5.7 Selected element concentrations recorded in birch twig bark from sites U3, U5 and U8 and transplanted lichen material exposed for 3 months closest to the smelter at site U5 in 2011.

However, Pb levels in the lichen transplants have not yet reached those recorded in native *Hypogymnia* present at the same sites. The bell-shaped curve shown by the 2011 lichen transplants in Fig. 5.8 is consistent with Pb contamination from a point source. Conspicuous in Fig. 5.8 and 5.9 is the high Pb and Cu levels in the native lichens to the east of the smelter, far higher than for native lichens to the NE or SW.

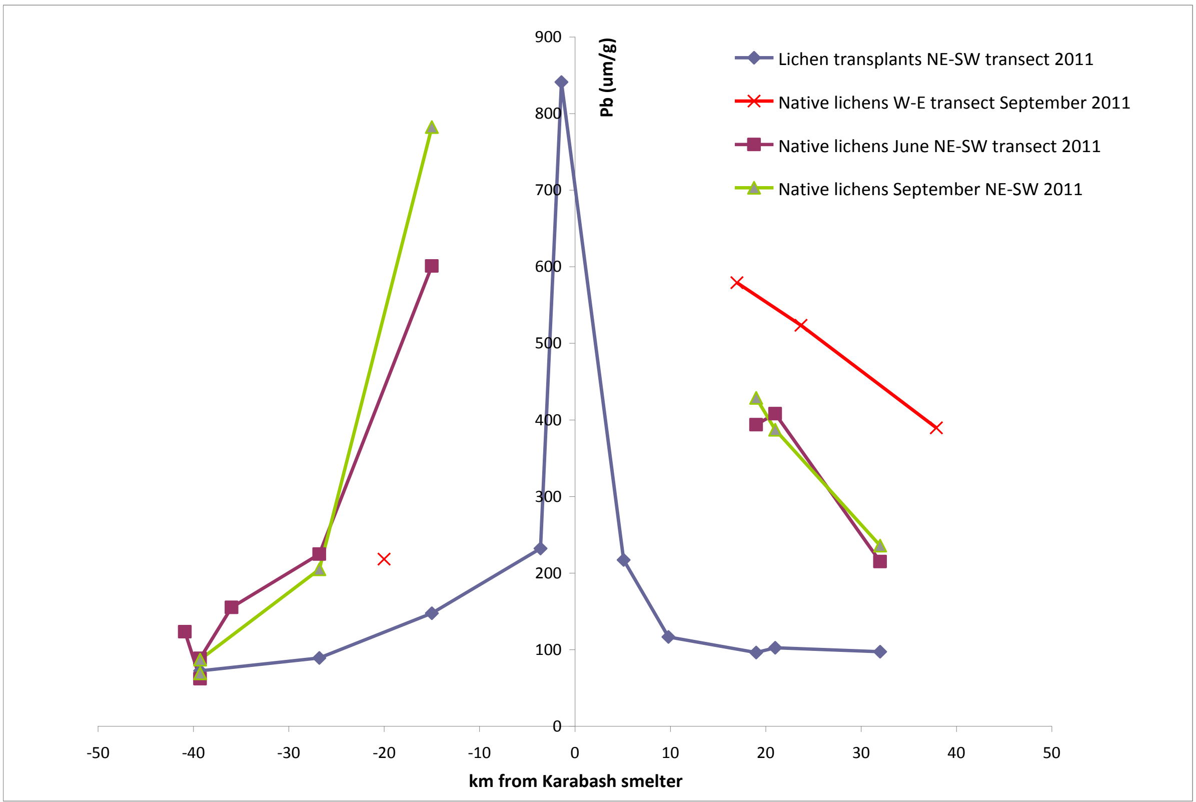

Fig. 5.8 Pb concentrations in native and transplanted lichens around Karabash.

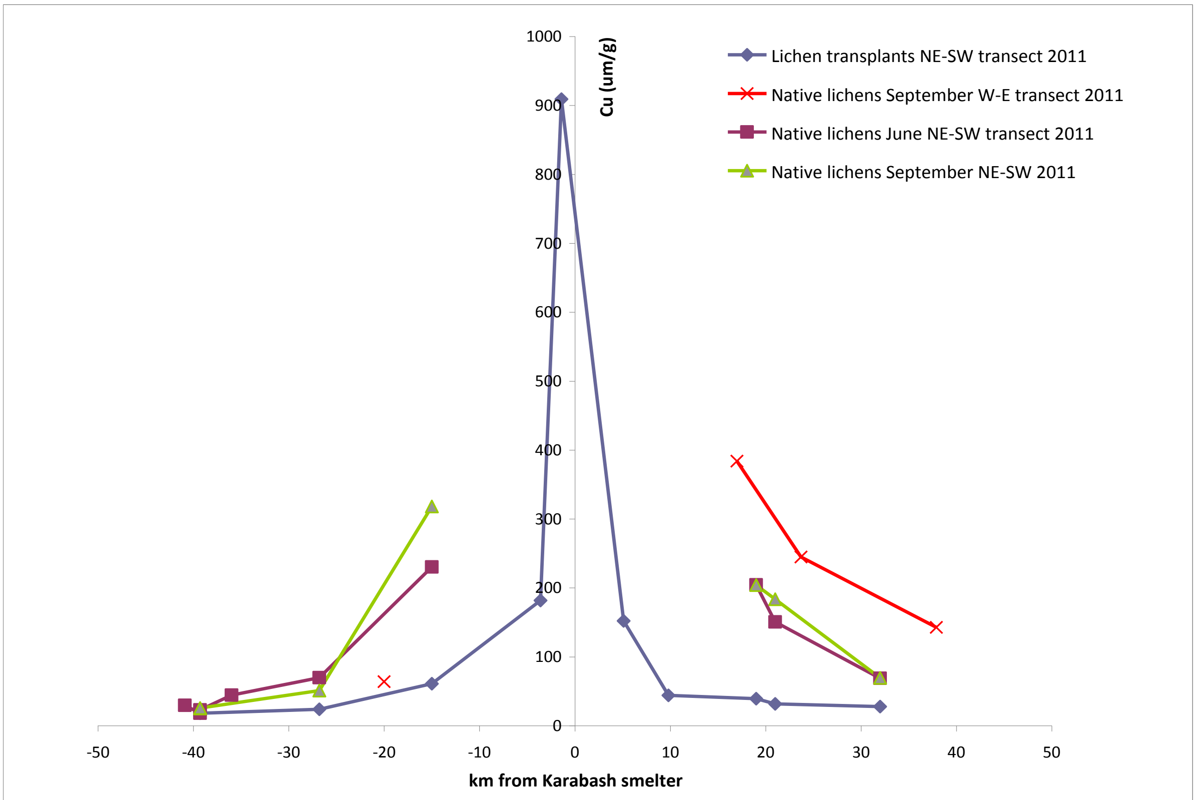

Fig. 5.9 Cu concentrations in native and transplanted lichens around Karabash.

Similar spatial patterns of element concentrations were recorded in birch twig bark along the NE-SW and W-E transects (Fig. 5.10 and 5.11). Unlike the lichen transplants, the twig bark samples from the W-E transect show very similar, or in the W slightly lower Pb and Cu concentrations to those at the same distance from the smelter in the NE-SW transect.

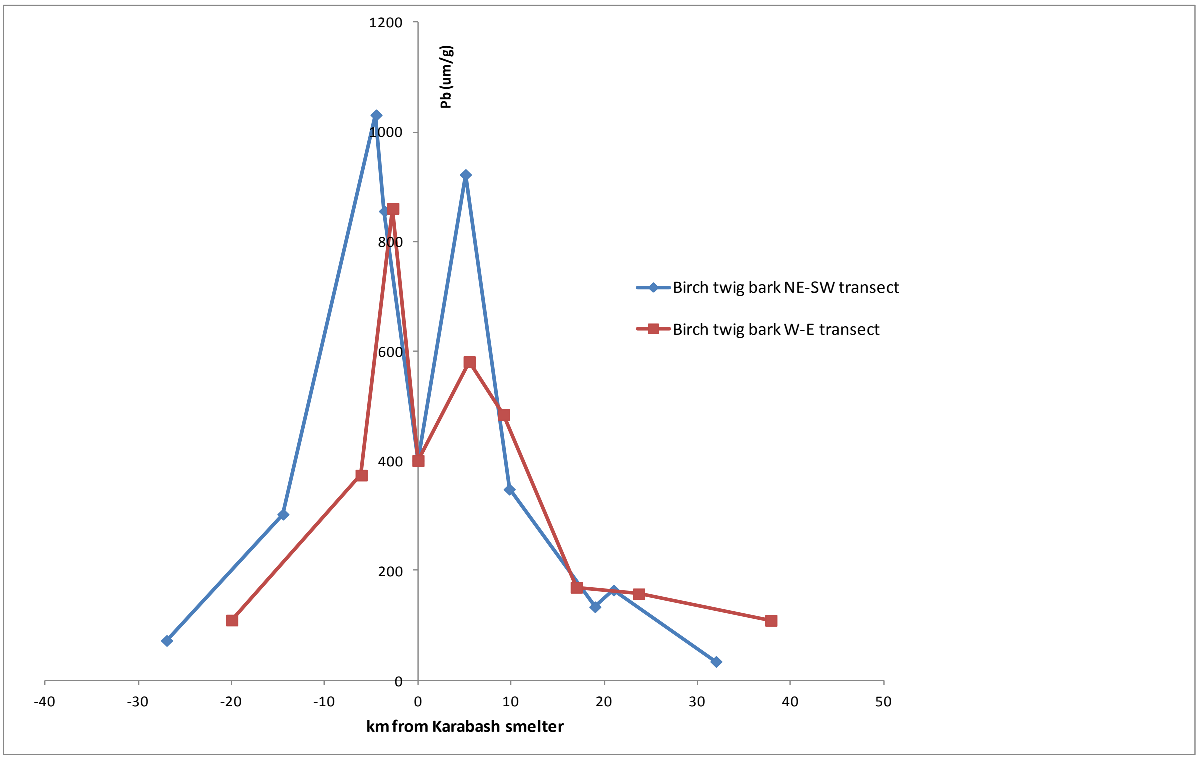

Fig. 5.10 Pb concentrations in birch twig bark around Karabash.

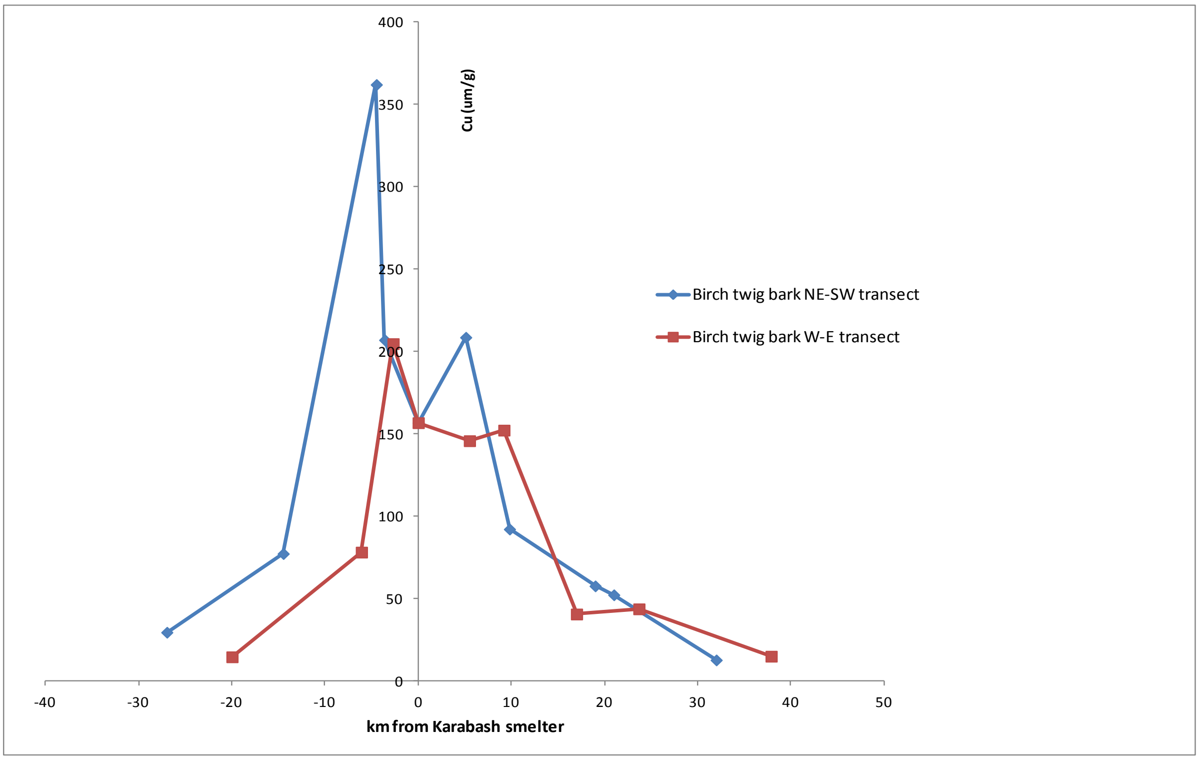

Fig. 5.11 Cu concentrations in birch twig bark around Karabash.

For S, from the graph in Fig. 5.12, the native lichens from 2011 almost always show lower levels than those collected from the same sites in 2001.

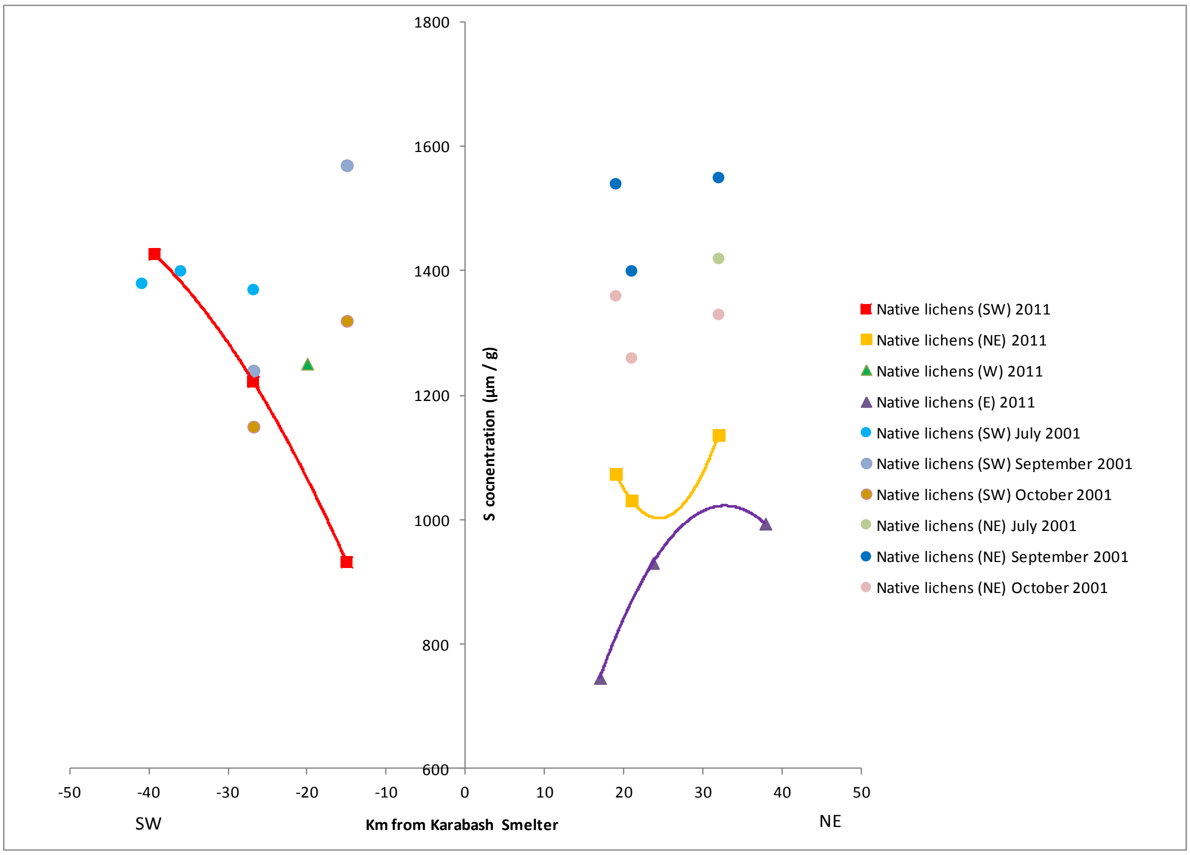

Fig. 5.12 S concentrations in naturally occurring lichens sampled across the NE-SW transect (●) in 2001 and 2011, and an additional W-E transect (▲) in 2011.

5.1.5 Air filter samples

Five air filter samples were collected, 4 from Karabash town, and one from Mednogorsk (Table 5.4). The highest levels of most metals, except Cd and Sb, were in Filter #1, sampled within the plume of the smelter, 2 km SE of the Karabash smelter. In all filters, the dominant metals are Pb and Zn, followed by As. The Mednogorsk air filter has a very similar element profile to the Karabash filters, with the exception of having relatively high Sb.

Table 5.4 Metals concentrations in air filters from Karabash (KA) and Mednogorsk (MD).

Filter	Sample	E	N	Date collected	As ng/m^3	Bi ng/m^3	Cd ng/m^3	Pb ng/m^3	Sb ng/m^3	Zn ng/m^3
1	KA(AR)950	60°13” 24.3’	55°27”20.5’	16/07/2011	2.5	0.1	0.073	13.4	0.34	12.8
2	KA(AR)956	60°08” 04.7’	55°13”07.7’	17/07/2011	0.6	0.011	0.029	1.2	0.12	0.8
3	KA(AR)957	60°09”29.2’	55°00”57.9’	18/07/2011	0.3	0.009	0.005	0.5	0.03	1.0
5	KA(AR)977	60°10”42.8’	55°27”27.7’	20/07/2011	1.5	0.044	0.111	9.3	0.62	9.0
6	MD(AR)350	57°34”23.4’	51°25” 39.4’	23/07/2011	0.4	0.013	0.031	2.1	0.65	3.5

Individual particles, imaged in field emission SEM, were found to be less than 2 µm in diameter, made up of aggregates of nano-sized (<100 nm) particles (Fig. 5.13). These <2 µm particles are respirable, i.e. able to penetrate into the deepest, alveolar, regions of the lungs where they can do most harm. Qualitative elemental data for individual particles, determined using X-ray elemental analysis in the field emission SEM, are shown in Fig. 5.14. Like in the whole-filter analyses, the composition of the particles is dominated by Pb, Zn and As.

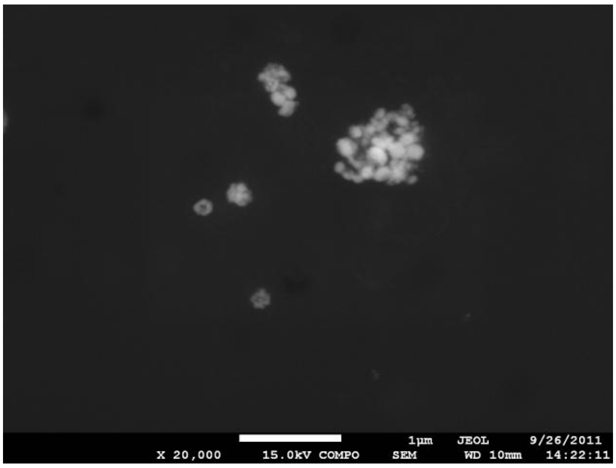

Fig. 5.13 Scanning electron photomicrograph of airborne particulate downwind from the Karabash smelter (Filter 1). The particles appear to represent aggregates of nano-size (< 100 nm) particles.

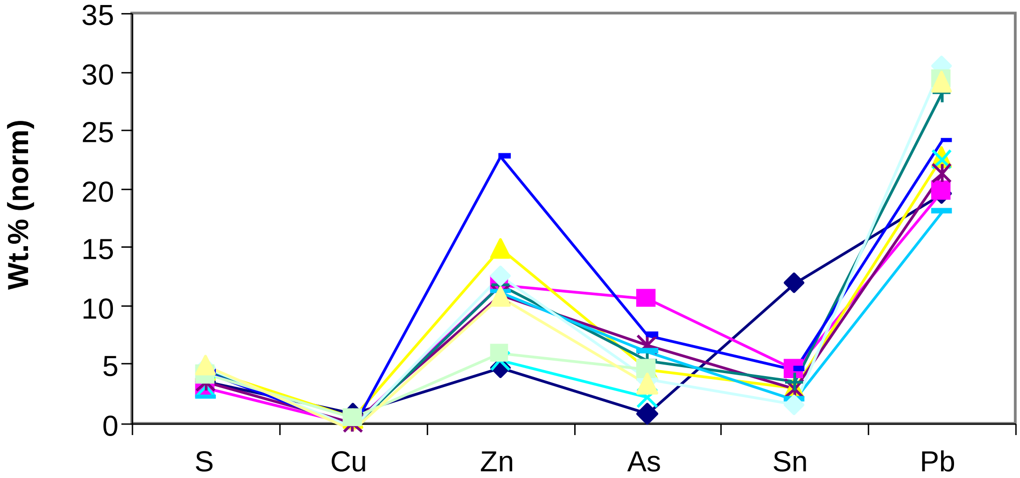

Fig. 5.14 Qualitative data for metals in individual airborne particulate (each coloured line) collected downwind of the Karabash smelter (Filter 1).

5.1.6 Soils

Chemical analysis of soil samples taken in 2011 were performed by IMIN, see results for Pb and As in Fig. 5.15, and Cr and Ba in Fig. 5.16. Three groups of elements can be identified in the soils. The first group includes Cu, Pb, Zn, As, Sb and Cd that display enhanced values in the surroundings of the smelter (Fig. 5.15) and decrease with distance to the smelter. The second group includes Ni, Cr, V, Co (Fig.5.16), which are likely to be influenced by local mafic bedrock geology. The third group includes Ti, Mn, Ba, for which the association is not clear (Fig. 5.16).

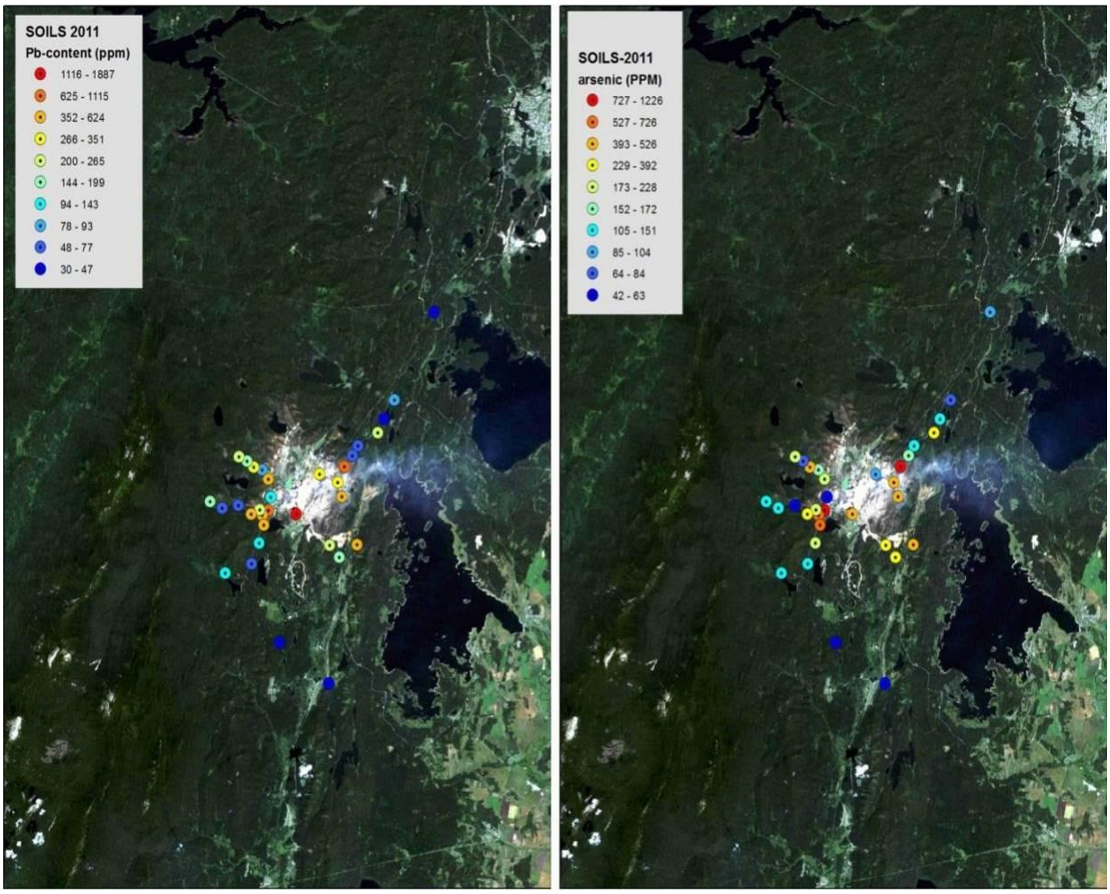

Fig. 5.15 Plots for Pb and As concentrations in soil samples.

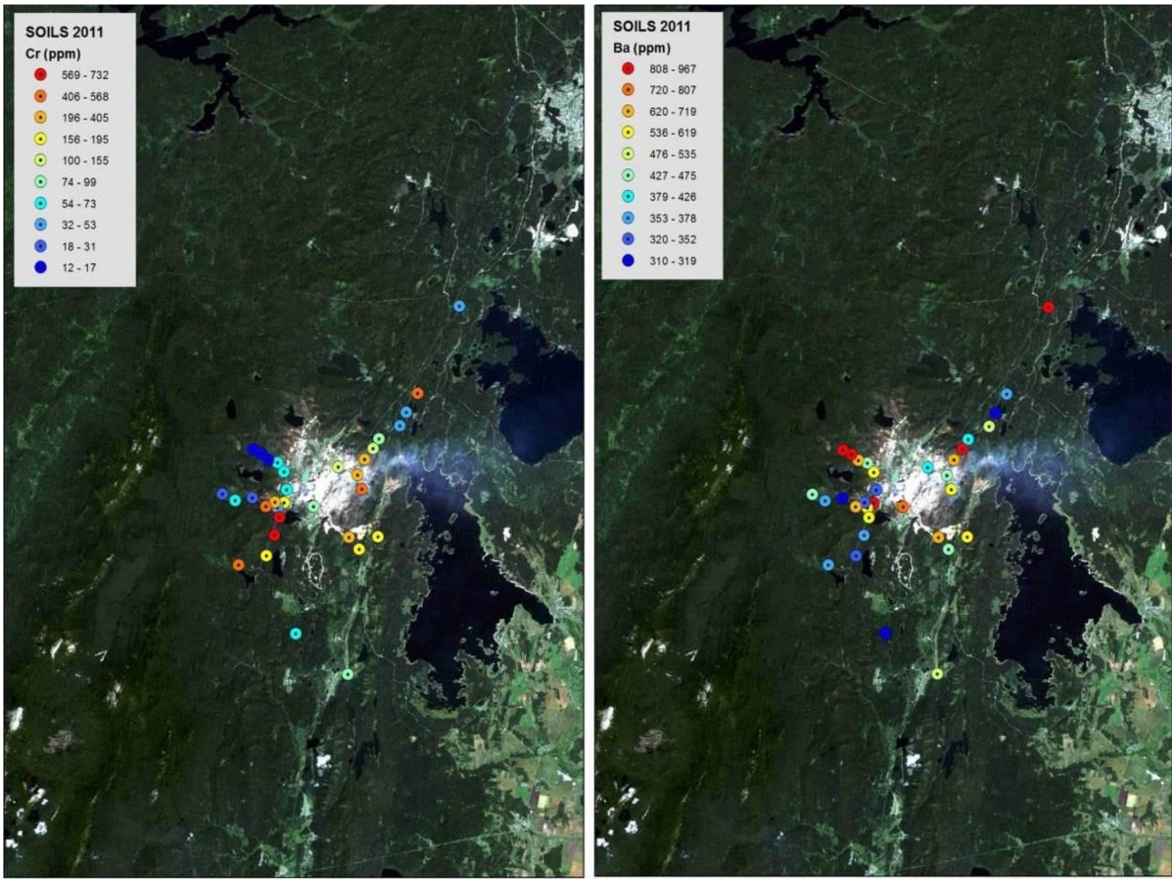

Fig. 5.16 Cr in soil samples (left image), which appears to correlate with bedrock geology; Ba content of soil samples (right image), showing no clear spatial correlation.

During the 2012 field-campaign, from July 20 to July 31, many additional soil samples were collected. We extended the profiles sampled in 2011 to include a number of additional profiles in a radial pattern around the smelter in order to improve our ability to map variations in all directions. Enhanced values for heavy metals can be seen in all directions up to more than 10 km from the smelter (Fig. 5.15). Soil Pb values are 15 times greater than background (assumed to be 20 ppm Pb) at a distance of 5 km, and 150 times the background value within 2 km from the smelter. Similar enrichment factors are observed for Cd, Mo, Cu, Zn and As.

5.1.7 Wastes

The location, volume, tonnage and composition of waste dumps in Karabash has been determined as these are potential sources of acid rock waters, invariably containing elevated levels of toxic elements such as As, and producing wind blown dusts. A list of waste dumps, with their main characteristics, is given in Table 5.5.

Name of waste dump	**Mineralogical composition**	Million tonnes	Composition, in μg/g
Tailing 1 'Starogodneye' 1958 to 1991	Pyrite, chalcopyrite, sphalerite, tennantite and galena with quartz, feldspar, sericite, chlorite and barite. Alteration phases (to 20 cm depth) copiapite, melanterite, epsomite and alunogen. Around 65% < 0.074 mm.	5.9	As 84-945 (772) Cu 1235-2884 (2155) Mn 1389-2273 (1781) Pb 471-2477 (1053) Zn 1033-3482 (2477) N=7
Tailing 2 'Novoye'	Pyrite, chalcopyrite, sphalerite, tennantite, galena with quartz, feldspar, sericite, chlorite,	3.2	As 580-1228 (690) Cu 923-1360 (1187)

1974 to 1989	barite, behind a 35m high dam. 3 zones: oxidation (depth 1.5 m) with sulfides and silicates + alteration phases; transition zone with iron hydroxides and gypsum; zone with primary and secondary sulfides		Mn 1645-1990 (1805) Pb 498-1641 (833) Zn 1404-3783 (1948) N=5
Tailing 3 'Sak-Elga' 1933 to 1958	Tailings in river valley. Mineralogical composition similar to Tailing 2, oxidation zone. 20% >0.63 mm, 12% 0.63-0.315, 20% 0.315-0.16, 37% 0.16-0.074, 10% 0.074-0.04, 1% <0.04 mm.	9.2	As 309-1173 (488) Cu 1037-2966 (1468) Mn 983-2154 (1550) Pb 368-1800 (697) Zn 1178-3650 (2497) N=6
Metallurgical slag dump 1	Metallurgical slag from smelter, mainly glass	15.6	As 614-830 (735) Cu 2581-3659 (3073) Mn 4389-5266 (4806) Pb 417-628 (467) Zn 14855-21576 (18254) N=11
Metallurgical slag dump 2	Metallurgical slag from smelter, mainly glass	2.5	As 792-1047 (835) Cu 3045-3712 (3436) Mn 3331-4012 (3770) Pb 1733-1970 (1840) Zn 15749-18888 (16994) N=8

Table 5.5 List of waste dumps in the Karabash area.

5.1.8 Surface waters and sediments

Surface water and stream and lake sediment sampling was carried out to verify the extent of contamination from acid rock/mine drainage from wastes, tailings and abandoned mine workings and effluents from the smelters and processing plants. The sampling locations for rivers and streams in Karabash is shown in Fig. 5.17(labeled 897 to 904).

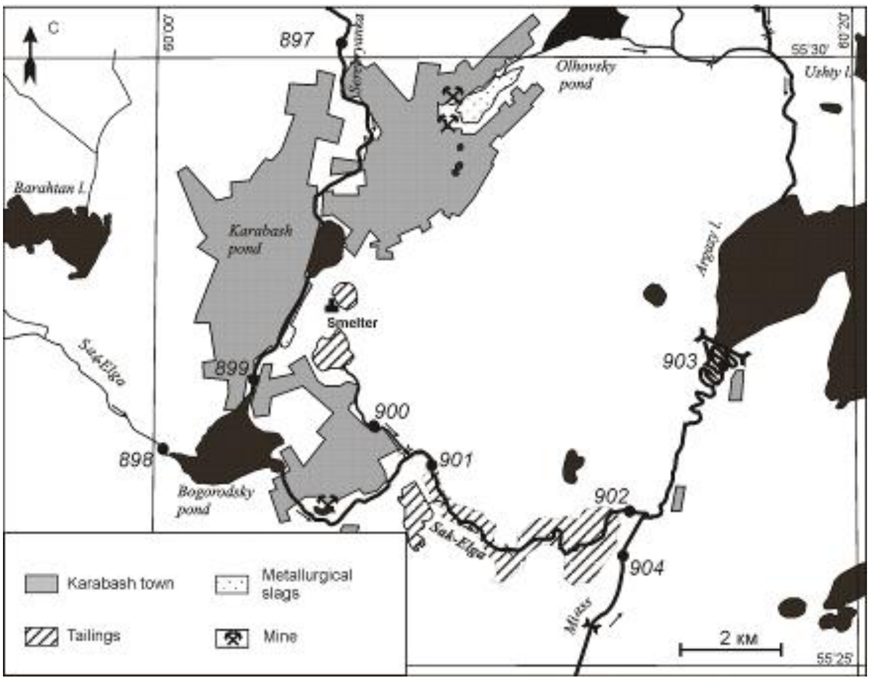

Fig. 5.17 Sampling localities for rivers and streams around Karabash.

Geochemical data for waters from Karabash are presented in Table 5.6. All mine waters analysed have low pH and high levels of heavy metals, particularly iron and aluminum (Fig.

5.18). The high content of Fe is caused by acid decomposition of iron disulfide - pyrite, and aluminium by hydrolysis of aluminosilicate phases in wastes and tailings.

	KA(W)897	KA(W)898	KA(W)899	KA(W)900	KA(W)901	KA(W)902	KA(W)903	KA(W)904
Physico-chemical parameters, mg/l								
pH	6.4	5.85	4.28	3.2	3.45	4.28	6.76	7.1
Eh	290	340	380	450	450	380	285	280
Электр.	199.7	68.5	819	3660	754	559	201	221
HCO_3^-	32.9	12.2	1.9	<1.0	<1.0	2.3	64.6	93.9
Cl^-	11.2	13.3	22.0	78.1	27.6	18.4	18.8	18.8
SO_4^{2-}	67.5	31.1	566	3000	505	370	46	36.2
NH_4^+	<0.01	0.07	1.35	1.75	0.35	0.01	0.01	0.06
NO_2^-	0.016	<0.003	0.102	<0.003	0.048	0.01	0.01	0.02
NO_3^-	2.84	1.92	<0.02	<0.02	<0.02	2.00	3.10	4.92
Ca	24.4	7.2	79.0	395.2	69.7	53.5	18.1	19.8
Mg	8.2	6.2	57.8	324.2	54.9	28.9	10.5	14.7
K	2.9	1.8	7.3	8.7	4.2	3.9	1.7	1.9
Na	3.1	2.9	23.9	35.3	18.2	15.4	7.8	9.1
Trace elements, μg/l								
Li	3.26	0.89	8.52	75.67	7.14	4.38	1.84	1.62
Al	1.7	36.8	108	17314	834	312	12.5	6.4
Sc	0.01	0.08	0.07	4.20	0.26	0.06	0.01	0.01
Cr	0.05	0.37	0.61	18.66	1.38	1.84	0.22	0.38
Mn	452	37	2883	30640	3502	2361	35	1.0
Fe	12.4	24.5	6583	129726	2375	86	9.7	8.8
Co	2.4	0.2	40	430	38	25	0.2	0.1
Ni	6.1	5.9	180	1364	165	138	11.5	4.2
Cu	29.8	17.5	248	24296	1381	532	17.1	2.8
Zn	1057	111.4	32173	52796	11669	9052	388	9.3
As	1.8	2.5	322	17.1	5.1	3.0	1.8	2.1
Se	0.65	0.22	3.32	3.80	0.19	0.76	0.28	0.18
Sr	116	40.7	193	1177	190	138	97	113
Mo	0.46	0.10	4.37	2.64	2.45	1.68	0.41	0.64
Cd	3.99	0.41	26.1	204	23.4	14.2	0.48	0.02
Sn	<0.05	<0.05	28.6	24.4	22.6	21.1	<0.05	<0.05
Sb	3.62	1.10	0.46	0.57	0.19	0.21	0.59	0.36
Ba	72.0	38.4	63	14	92	37	37.1	25.9
Tl	0.131	0.077	0.94	2.60	0.48	0.52	0.020	<0.001
Pb	1.04	1.46	20.7	369	71	74	0.25	0.22
Bi	0.002	0.004	0.014	0.011	0.002	0.001	0.002	0.001
Th	0.001	0.039	0.067	0.53	0.012	<0.001	0.005	0.007
U	0.030	0.077	0.899	4.8	0.49	0.31	0.48	0.94

Table 5.6 Chemical composition of surface waters around Karabash.

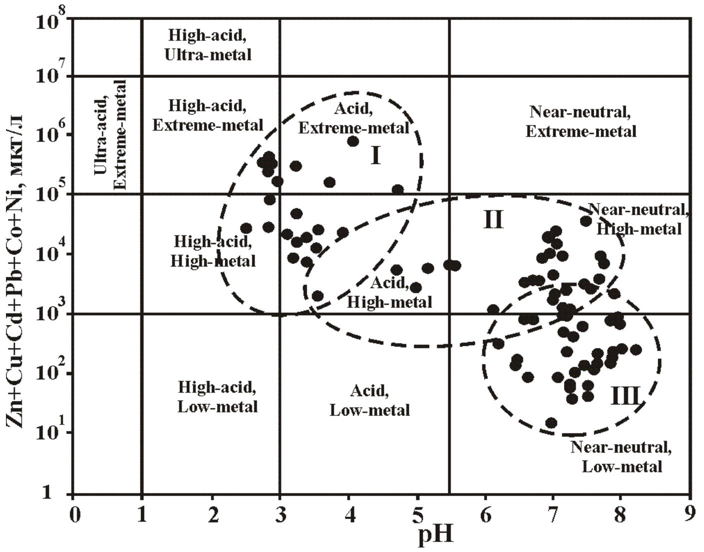

Fig. 5.18 Classification diagram (pH vs Zn+Cu+Cd+Pb+Co+Ni mg/l) concentrations for industrially impacted waters in the Southern Urals and background areas (I - Ultrakislye podotvalnye water (acid), II - mixed waters, III - Neutral background waters).

The form of metals in background waters and AMD, and mixed waters, is shown in Fig. 5.19. Cu and Zn are generally transported in solution in AMD and background waters. In the zones of mixing, Cu is mainly transported in coarse colloidal particles and 'slick', whilst Zn continues to be transported in solution. Fe and Al in the mixing zones is almost all transported in the form of coarse colloids. The formation of colloids, containing jarosite, schwertmannite and basaluminite, occurs due to hydrolysis as a result of mixing with background waters. The particles provide large surface area substrates for sorption of Zn, Cu, Pb, Cd, As, Se, Tl, Sb and Bi.

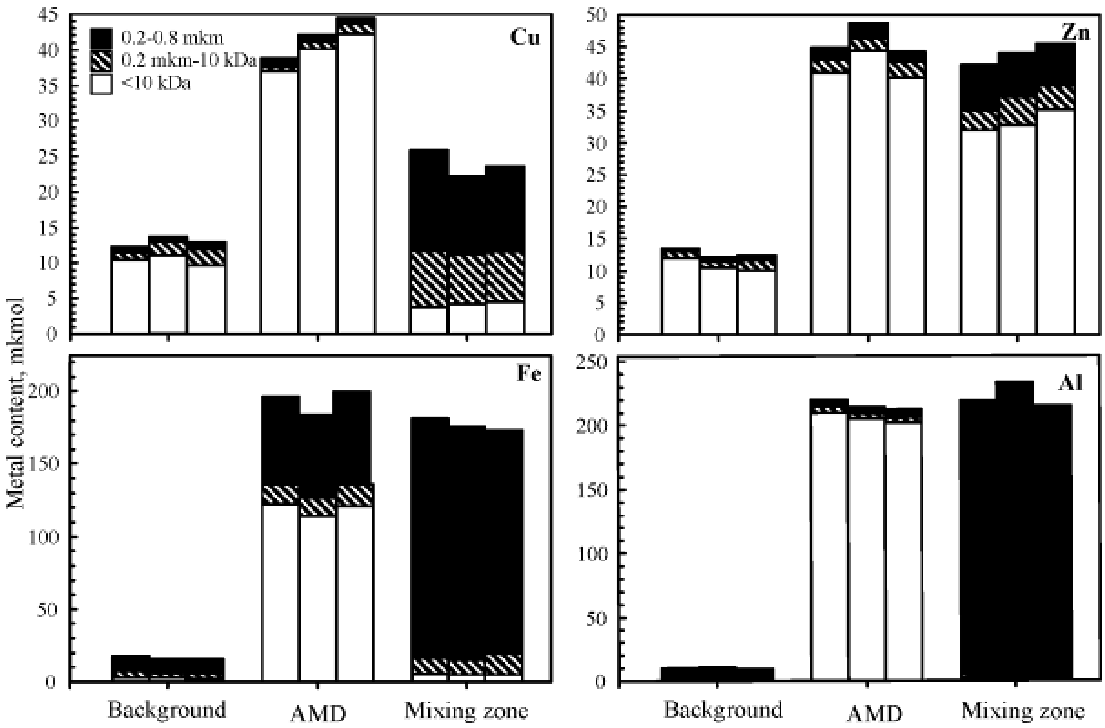

Fig. 5.19 Forms of metals in different types of water around Karabash.

From electron microscopy, suspended particles in the mixed waters contain all of the main sulphide minerals present in the wastes and tailings: pyrite, chalcopyrite, sphalerite, galena and barite. All of these phases, except galena, are also present as suspended solids in flood waters in the northern Argazy water reservoir (Fig. 5.17), one of the sources of drinking water for the major Russian city of Chelyabinsk. The distance of transport of sulfide particles, 2 to 50 μm in size, from their source to the northern part of the Argazi reservoir is about 10 km (Fig. 5.17). The colloidal fraction is dominated by Fe hydrosulphate and gypsum (Fig. 5.20, 5.21).

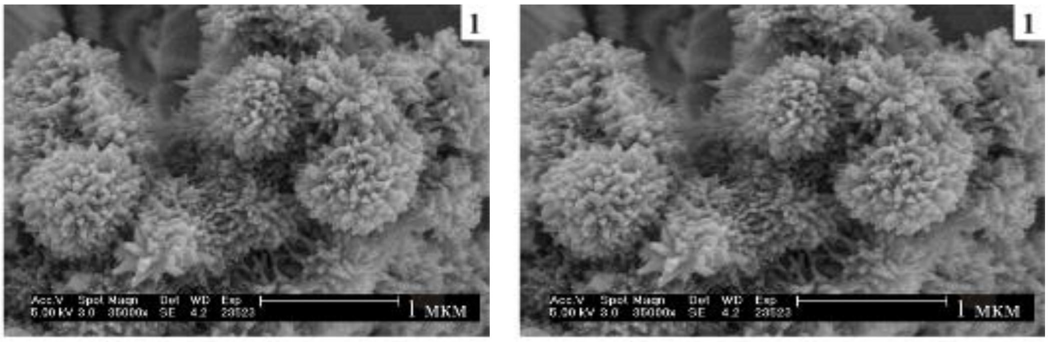

Fig. 5.20 Scanning electron micrograph of newly-formed minerals in sediments from water mixing zones (1. Fe hydrosulphate, 2. Fe hydrosulphate with iron bacteria *Gallionella*).

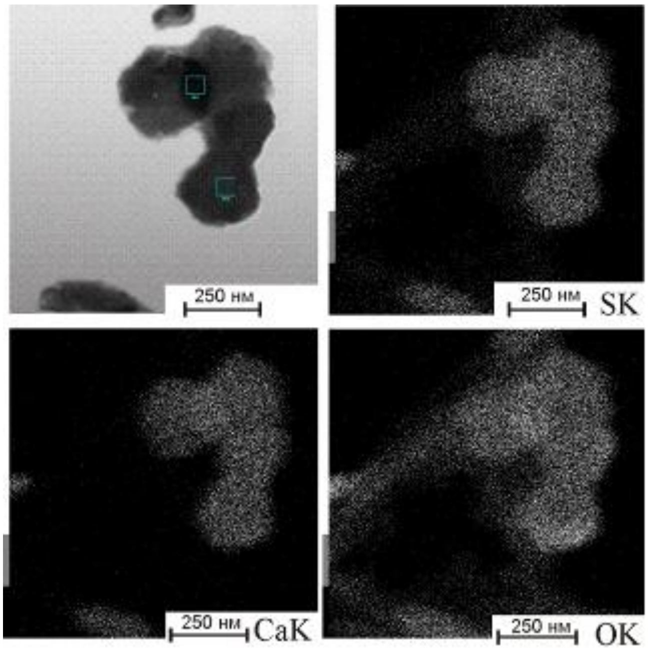

Fig. 5.21 Transmission electron micrograph of colloidal particles of gypsum from the water mixing zone.

The overwhelming majority of the Cu, As, Se, Bi, Sb, and, to a lesser extent Zn, Cd, is bound to Fe and Al colloids which reduces the potential toxicity of these substances. The main types of hydrolysis reaction are:

$$\text{Acid}\ Fe^{3+} + 3OH^- \leftrightarrow FeOH^{2+} + 2OH^- \leftrightarrow Fe(OH)^+_2 + OH^- \leftrightarrow Fe(OH)_3\ \text{Neutral}$$

$$\text{Acid}\ Al^{3+} + 3OH^- \leftrightarrow AlOH^{2+} + 2OH^- \leftrightarrow Al(OH)^+_2 + OH^- \leftrightarrow Al(OH)_3\ \text{Neutral}$$

Thus, the alkaline natural barrier formed in the mixing zones of AMD and background waters can be used to build embedded artificial geochemical barriers in the rehabilitation of man-made landscapes.

5.1.9 Reflectance spectra of leaves and soils

Summer 2011

As reported in Section 4, the leaf spectra collected during the 2011 field-campaign were of poor quality because of a broken fibre-optic cable, which gave spectra which were noisy and of variable intensity. This meant that the absolute reflectance data collected during this campaign could not be used. However, we could still use the shape of the spectra as this remained largely unaffected in the VNIR region (350-1000 nm).

There are many vegetation indices that use band-ratios or derivatives thereof, but since we have no control over the quality of absolute reflectance of the leaf spectra, we cannot use these indices. There is one vegetation index however that uses a specific wavelength feature instead of the reflectance values. This is the so called red-edge position, defined as the wavelength position of the inflection point of the slope between the red and NIR. The red-edge position is a valuable parameter to assess plant chlorophyll concentration and is often used as a vegetation stress index (Horler et al., 1983). A decrease in red-edge position is usually related to increasing plant stress. As the position of this inflection point is probably not affected by changes in reflectance, we were able to use our spectra to calculate the red-edge position for the birch-leaves with reasonable confidence (see Fig. 5.22).

a)

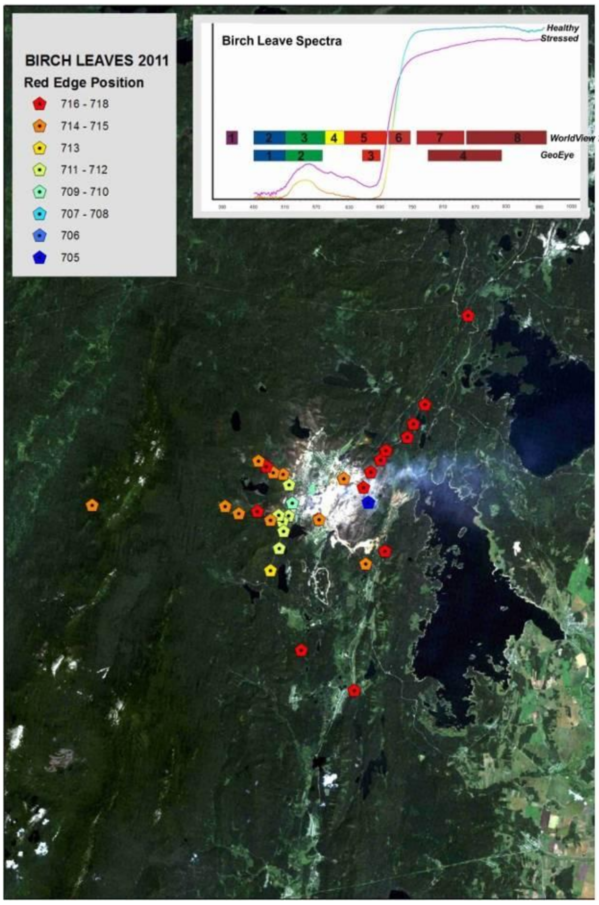

b)

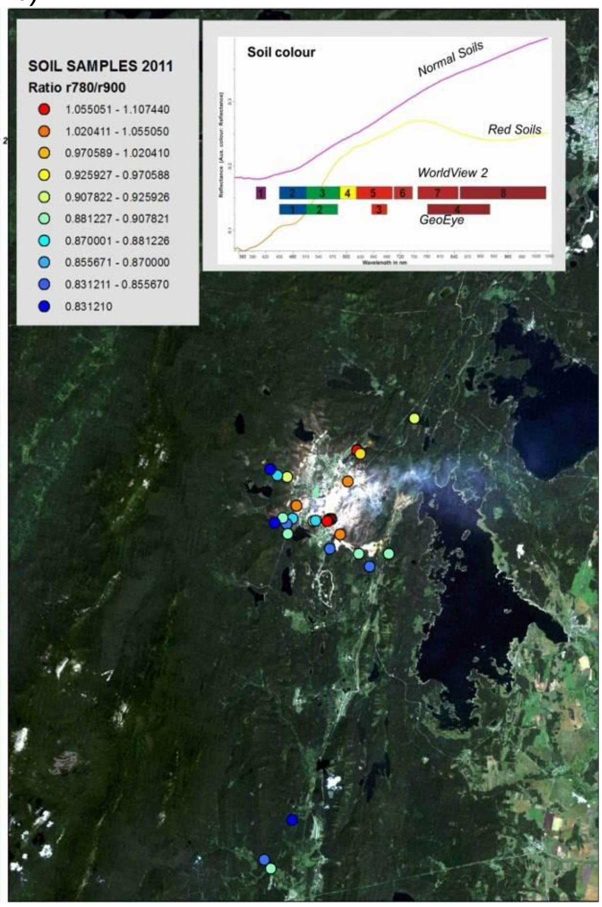

Fig. 5.22 Plot of red-edge position of birch leaf spectra (left image). The inset shows an example of a healthy leaf spectrum (blue spectrum) and a stressed leaf spectrum (pink), and the relative band positions of WV-2 and Geo-eye imagery; Plot of r780/r900 for soil samples (right image). Higher ratios indicate higher Fe-oxide content. The inset shows a spectrum for normal soil, without Fe-oxides, and a spectrum for Fe-oxide rich soil.

As reported in section 4, the soil samples collected in 2011 could not be taken out of Russia, and were therefore left at IMIN in Miass. When we returned to Miass in 2012, we could retrieve part of these samples, and perform the spectral analysis with our new spectrometer. Apart from clear mineralogical variations that could be correlated with underlying geology, the Fe-oxide enrichment trend towards the smelter was clearly visible in the spectra (Fig. 5.22b).

In the previous sections we have described how soils change as a function of distance to the smelter. We observed a dramatic decrease in the abundance of understory towards the smelter, and an increasing intensity of weathering and development of oxidation minerals such as goethite and sulphates. The extent of acid attack on exposed rocks, particularly on minerals such as pyroxene and olivine is shown in Fig. 5.23. Clear chemical changes demonstrate the pattern of fallout of acid and metal-rich particles from the smelter (Fig. 5.24).

Fig. 5.23 Photo taken about 5 km southwest of the Karabash smelter. Clearly visible are the holes where mafic minerals such as olivine and pyroxenes have been leached out. The composition of the black varnish has not been analysed.

In order to determine how these changes can be identified using remote sensing data, we extracted relevant mineralogical information from the soil spectra, and combined this information with soil geochemical data. From a visual inspection, the spectra show the presence of montmorillonite, kaolinite, chlorite, serpentine and goethite (see Fig. 5.25). Other minerals such as illite, gypsum and jarosite are found sporadically, and hence not plotted here.

However, visual interpretation is subjective, and subtle differences are easily missed. For that reason, it is more suitable to work with mineral indices such as ratios of reflectances at specific band positions. The great advantage of this method is that this allows us to quantify gradual changes in certain mineral proportions, which can be correlated with other data, such as chemical composition.

In Fig. 5.26 we have plotted the band ratio of reflectances (r) 2190nm/2325nm “serpentine index”. This ratio describes the depth of the 2325-absorption feature that is characteristic for serpentine minerals (but also for other minerals such as chlorite, see Fig. 5.26).

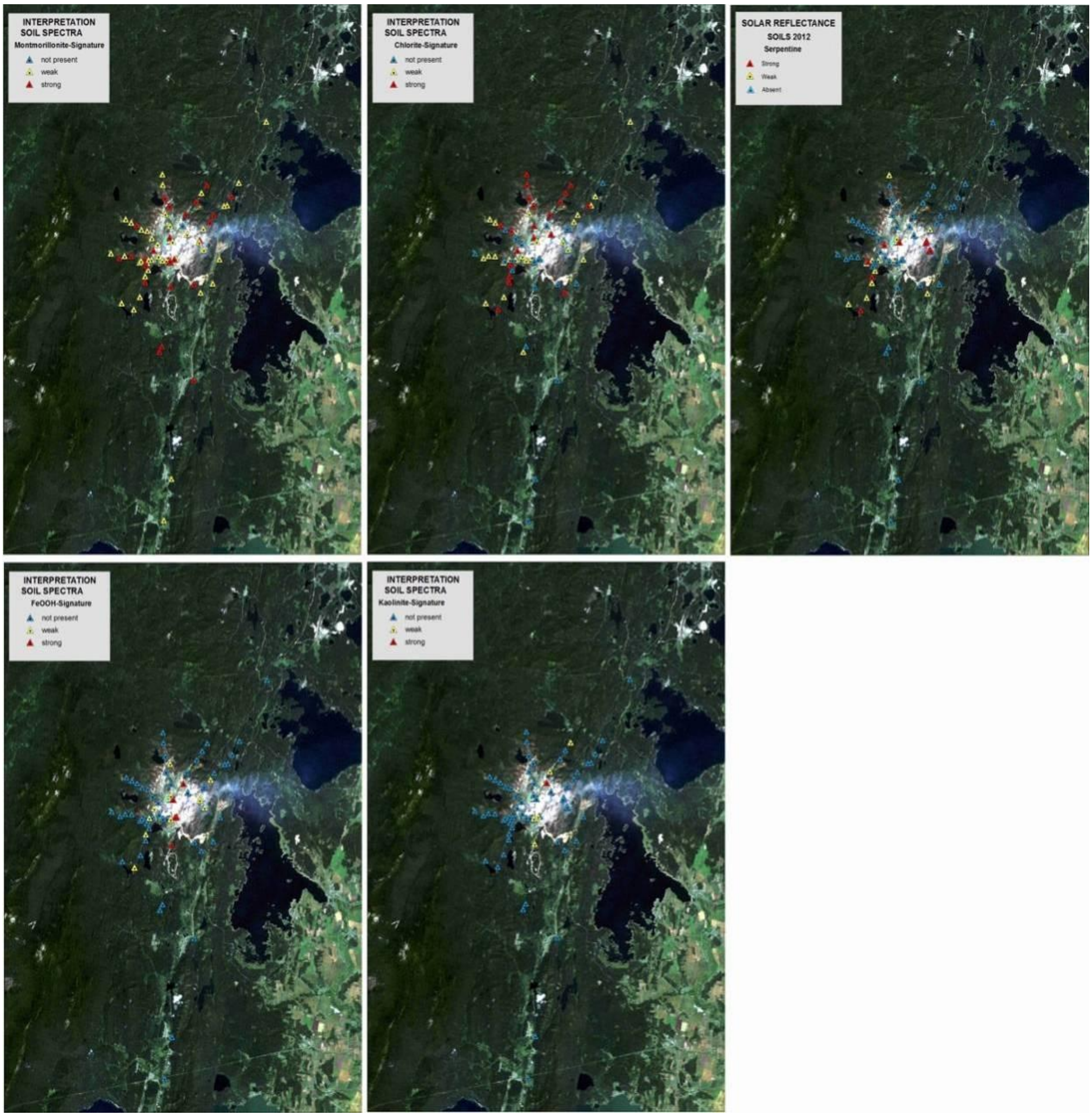

Fig. 5.24 Results of qualitative visual interpretation of soil spectra for A: montmorillonite (top left), B: chlorite (top centre), C: serpentine (top right), D: goethite (bottom left) and E: kaolinite (bottom right). Blue symbols indicate that the mineral could not be identified, yellow indicates that the diagnostic signature is present but weak, and red indicates that the diagnostic signature is strong.

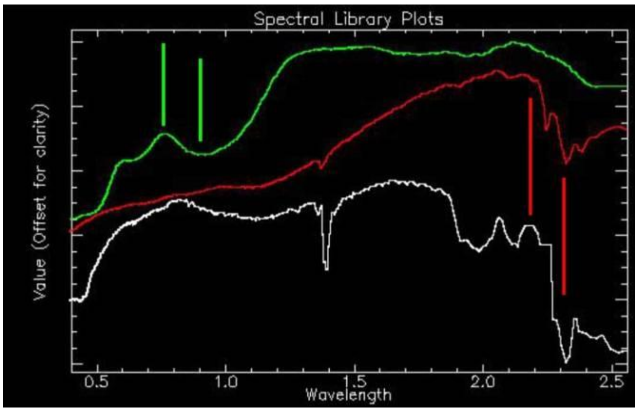

Fig. 5.25 Spectral library plots for goethite (green) chlorite (red) and lizardite (white). Spectra from USGS spectral library. The vertical red lines indicate the band positions used for

calculation of the "serpentine-index" and the green lines the positions for calculation of the "goethite-index"

When we compare this with the distribution of high Ni values (Fig. 5.26b) we observe a similarity in the patterns. The plot of Ni versus the value of the band ratio seems to confirm that there is a trend, even though the correlation coefficient is only 0.32; most high Ni values are found in soils with a high band-ratio value. The fact that the correlation is relatively low could have to do with several factors, such as heterogeneity of soils, and the presence of minerals such as chlorite that also exhibit the 2325-absorption feature but are likely to contain much less Ni.

a) b)

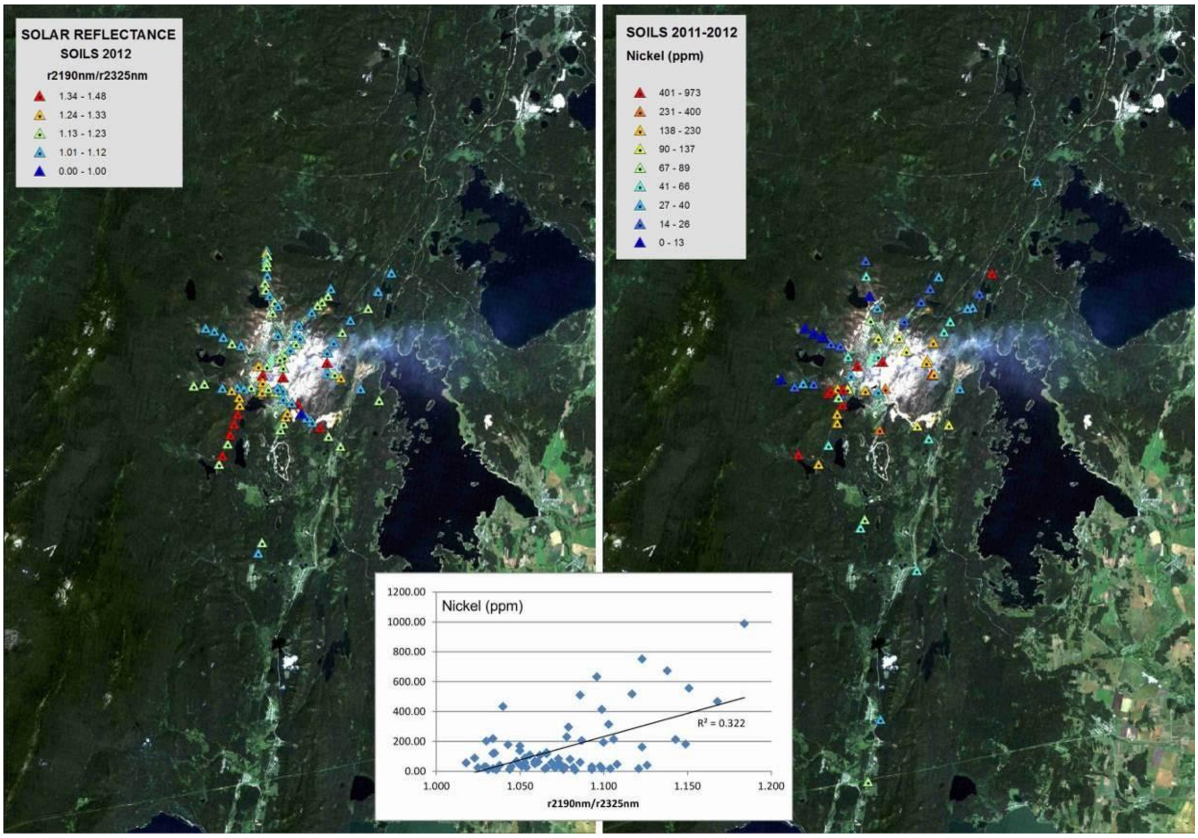

Fig. 5.26 a) Band ratios taken from solar reflectance spectra; b) Ni content of soil samples. The inserted graph shows the relation between the Ni content in soils and the spectral "serpentine-index".

In Fig. 5.27 we plotted band ratio r759nm/r937 nm. This band ratio can be used to identify subtle changes in the ferric-iron absorption region (around 900nm, see Fig. 5.28), and is a good indicator for the presence of Fe-oxides like goethite. For convenience sake we call this ratio the "Goethite-index". If we compare this plot with the map of the visual interpretation for Fe-oxides (Fig. 5.27), we may conclude that the area where Fe-oxides have been developed in soils is much larger than that found on the basis of visual interpretation, and that there is a much more gradual change in the Fe-oxides-signature as a function of the distance to the smelter.

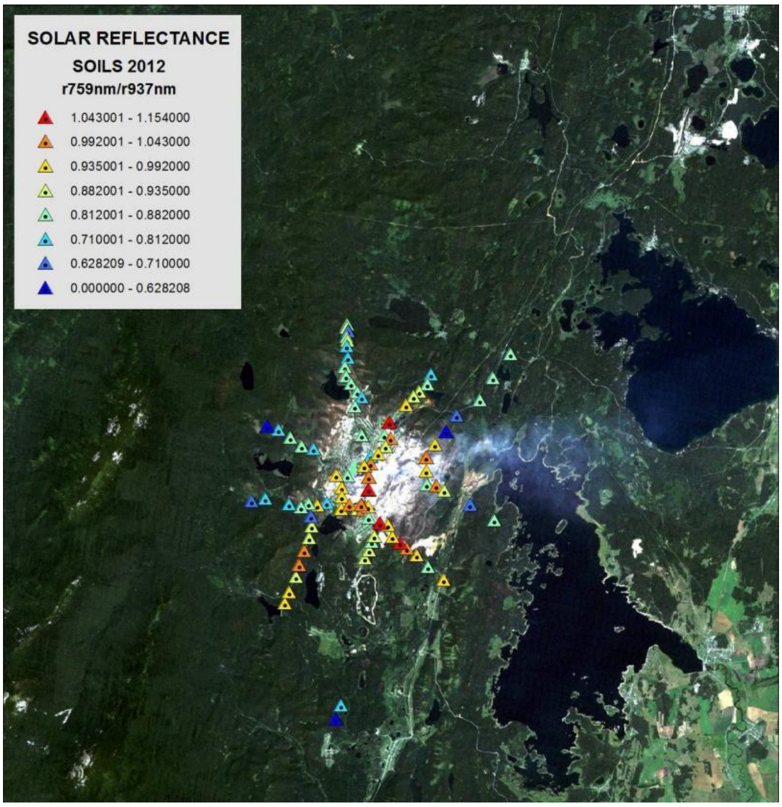

Fig. 5.27 Goethite-index calculated from solar reflectance measurements of soils.

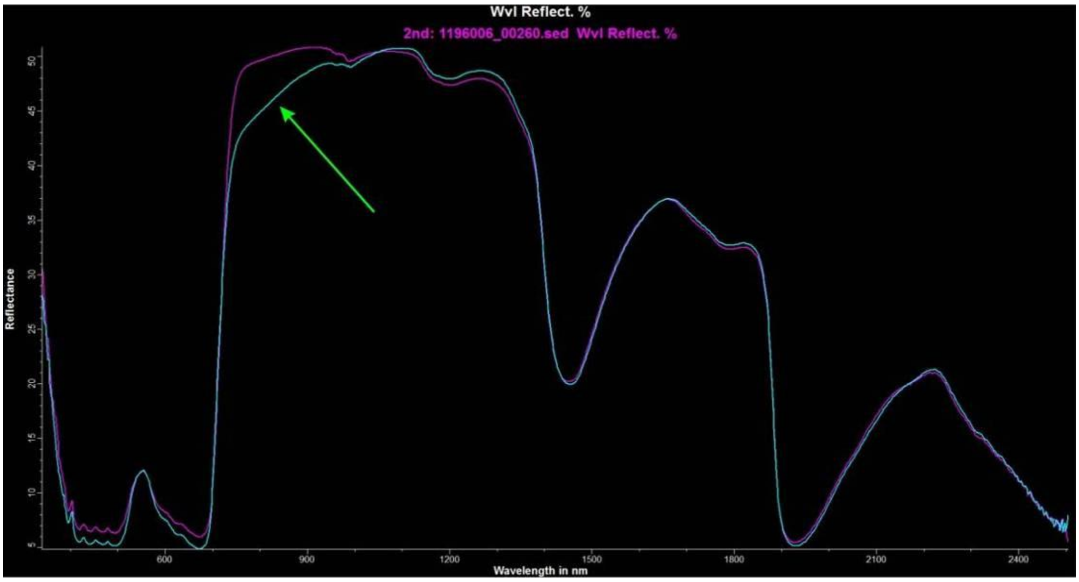

Fig. 5.28 Spectra for birch leaves in a little contaminated area (pink spectrum) and a strongly contaminated area (magenta spectrum). The green arrow indicates the wavelength region where we observe significant changes.

Summer 2012

The results of the 2011 field work indicated the existence of well-defined vegetation zoning around the smelter, both in terms of species diversity and the spectral properties of birch leafs. The spectral analysis of birch leaves were at best indicative as the measurements were performed with a broken fibre-optic cable. For the 2012 field program, the 2011 measurements were repeated, and the sampling extended to a greater distance from the smelter and in more directions.

Birch leaves were measured in more than 140 locations using the Spectral Evolution spectrometer with bifurcated vegetation probe. The preferred size of trees for sampling was between 2 and 5 m but in some cases only smaller trees were available. Leaf sampling was done at a height of approximately 1.5 m. In most locations we sampled three separate trees, and for each tree we measured three leaves. A number of parameters were then calculated as vegetation indices (see Fig. 5.29a-e, f).

Fig. 5.29 gives an overview of the 140 *in situ* reflectance spectra of birch leaves in the surroundings of the Karabash smelter. The main differences between the spectra of leaves in very close proximity and located at larger distances are especially noticed in the near-infrared (NIR) and visible (VIS) region of the spectrum, revealing differences in leaf biochemistry and anatomy.

Absorption in the VIS (400-750 nm) is primarily driven by pigments, such as chlorophylls, generally regarded as a good indicator of plant physiological health (Peñuelas and Filella, 1998), and carotenoids. The increase in the VIS and blue shift in the red edge inflection point (Ayala-Silva and Beyl, 2005; Li et al., 2006) of the stressed vegetation spectra (see yellow spectrum Fig. 5.29 is the result from a decreased chlorophyll content, related to vegetation stress. Visually, chlorotic changes are perceived as yellowing of leaves (Adams et al., 1999). Reflectance patterns in the NIR (750-1000 nm) are influenced by leaf surface features, internal architecture and biochemical composition. In stressed leaves epidermal cell walls may collapse, leading to less vacuolation and therefore less multiple scattering, i.e., less reflection above 750 nm as can be seen in Fig. 5.29. Above 1000 nm, the degree of hydration of a leaf influences its spectral properties whereby reflectance of a dry leaf is higher than that of fresh leaves across the visible range. Absorption of water determines the shape of the middle infrared reflectance curve with strong absorption bands around wavelengths at 1400 nm and 1900 nm. In this portion of the spectrum, no significant differences between healthy and stressed leaves can be seen in Fig. 5.29.

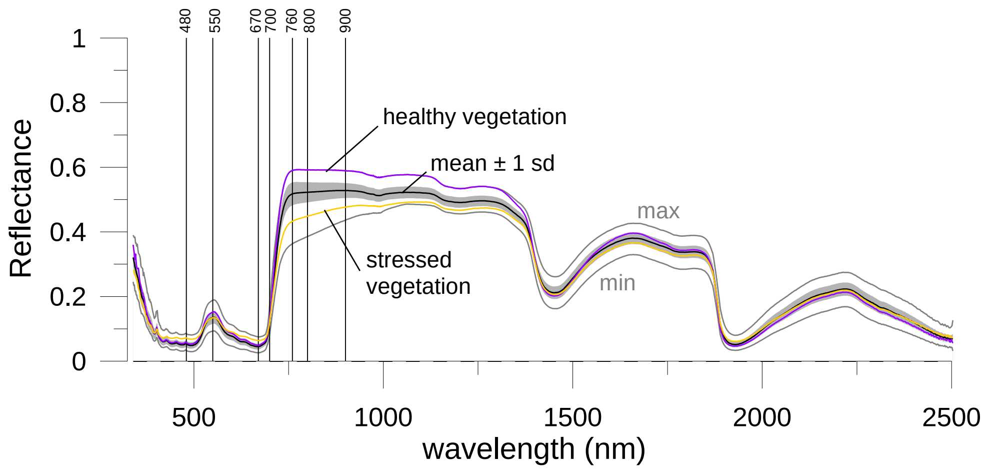

Fig. 5.29 Overview of 140 in situ reflectance spectra of birch leaves in the direct surroundings of the Karabash smelter: mean (black line), minimum and maximum (grey lines) and one standard deviation in each direction (grey shading). Positions of the most important wavelengths used for vegetation index calculation are shown. Example spectra of a relatively healthy birch far from the smelter (in purple) and one in very close proximity to the smelter (in yellow) are highlighted.

The most remarkable change we observed in our spectra was in the slope between 750nm and 900nm, often referred to as the VNIR-plateau. Fig. 5.29 shows examples of spectra for birch leaves taken in a relatively uncontaminated area, approximately 15 km away from the smelter (pink line), and for a birch leaf taken in a highly contaminated location less than 1 km from the smelter (yellow). The difference in slope between the two spectra was calculated from the ratio of the reflectances at 750nm and 900nm.

When plotted on the map (Fig. 30a) this ratio shows a very clear consistent zoning around the smelter (also observed in the qualitative data from 2011). Unfortunately we were not able to find any references in the literature to this phenomenon, and further research is needed in order to be able to find an appropriate explanation.

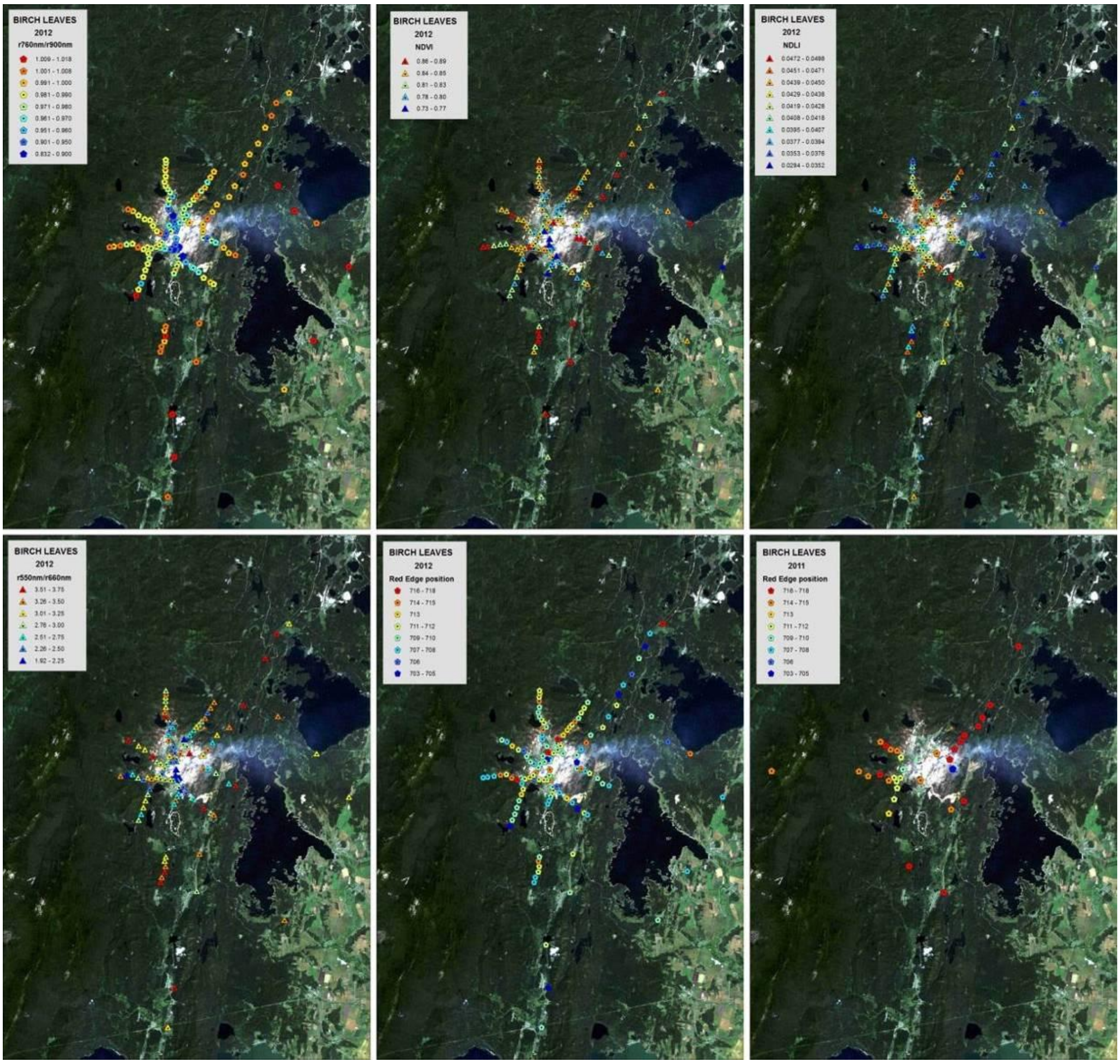

Fig. 5.30 Plots of various indices calculated from the birch leaf spectra. a: r760/r900; b: Normalised Difference Vegetation Index; c: Normalised difference Lignin Index; d: Greenness (green/red); e: Red Edge Position 2012 samples; f: Red Edge Position 2011 samples.

The plot of the NDVI (Fig. 30b) shows a similar but less consistent pattern. The general pattern nevertheless appears to be that the NDVI, and hence the amount of active biomass, increases with distance from the smelter. The Normalised Difference Lignin Index (NDLI Fig. 30c) was calculated as [log (1/R1754)_log (1/R1680)]/[log (1/R1754) + log (1/R1680)] (Serrano et al., 2002). This index is used to estimate the foliar lignin concentration in leaves. An increase in lignin content is considered to be a common plant response to various stress factors, including heavy metals (Jbir et al., 2001; Diaz et al. 2001; Dixon et al., 2002; Janas et al., 2002; Mandre, 2002; Winkel-Shirley, 2002; Jouili and Ferjani, 2003; Lin et al., 2005; Yang et al., 2007; Kovacik and Klejdus, 2008).

NDLI (Fig. 30c) exhibits significantly enhanced values in the area considered to be impacted by the smelter. As this pattern is in line with the findings of the above referred authors, it is possible that we are observing the effects of plant stress as a result of heavy metal and SO_2

contamination. The green/red ratio (r550nm/r665nm) was shown to be effective for estimating leaf senescence (Adamsen et al., 1999). Gallagher et al. (2008) and Gamon and Surfus (1999) used the red/green ratio index for estimating chlorophyll concentration in birch leaves. Gallagher et al. (2008) demonstrated a strong correlation between this ratio and Zn in birch leaves. The plot of this ratio (Fig. 5.30d) confirms the patterns described above.

With respect to the red edge position, we observe significant differences between the measurements from 2011 and 2012. Nearly all samples from 2012 show a significant decrease in red edge position compared to 2011. Furthermore, when examining the distribution patterns of the two years, we seem to observe some kind of inversion. In the 2011 data we observe a decrease in the red edge position towards the smelter, whereas in 2012 the pattern is not very clear, but it seems that there is a decrease away from the smelter. These observed differences could be related to the fact that summer 2012 was, in contrast to summer 2011, very hot and dry, and although the birch trees in the Karabash area looked normal, it could be that the drop in the red-edge positions for 2012 reflects some kind of drought stress.

Since trace element analysis was performed on soils for a significant number of locations where leaf measurements were taken, we were able to investigate the correlation (see Fig. 5.31) of the indices reported above with elements of the different chemical groups that we distinguished earlier in this report. Elevated contents of elements such as Pb, Zn, Cu, Cd, Sb and As in soils are highly likely to be caused by smelter emissions, whereas Ni and Sr contents in soils probably reflect underlying lithology, and no clear association was found for elements such as Li, Ba, Ti and Mn.

Fig. 5.31a-c show the relation between the slope of the NIR-plateau and representative examples of the first group of elements. The red arrows indicate the direction of increased plant stress, and except for some extremely polluted soil samples, the correlation with the slope of the NIR-plateau seems to be a reasonable, taking into account that the observed plant stress probably results from a combination of more factors than just the chemistry of the soils.

For the other two groups, represented by Ni and Sr (Fig. 5.31d-e) and Ba (Fig. 5.31f), no correlation is observed.

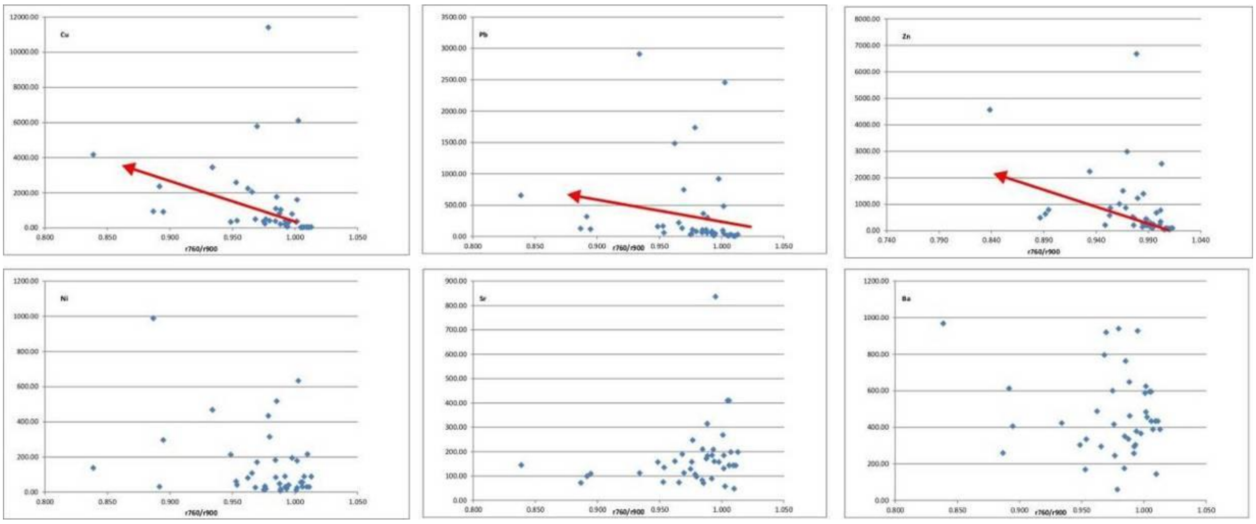

Fig. 5.31 Correlation of the slope of the NIR-plateau with a: Cu; b: Pb; c: Zn; d: Ni; e: Sr and f: Ba. Red arrows indicate the direction of increased plant stress.

The relation of the NDLI with representative examples of the first group of elements is shown in Fig. 5.32a-c. These plots suggest that there is a general tendency of increasing NDLI with enhanced metal content in soils. Unlike the previous parameter, it seems that the NDLI also correlates to some extent with the Ni content in soils. However, no correlation is observed for

Sr and Ba. The relationship between the NDVI and Cu, Pb and Zn (Figs. 5.32), and between the green/red ratio and Cu, Pb and Zn (Figs. 5.33), although much weaker than observed for the previous indices, seem to show similar trends.

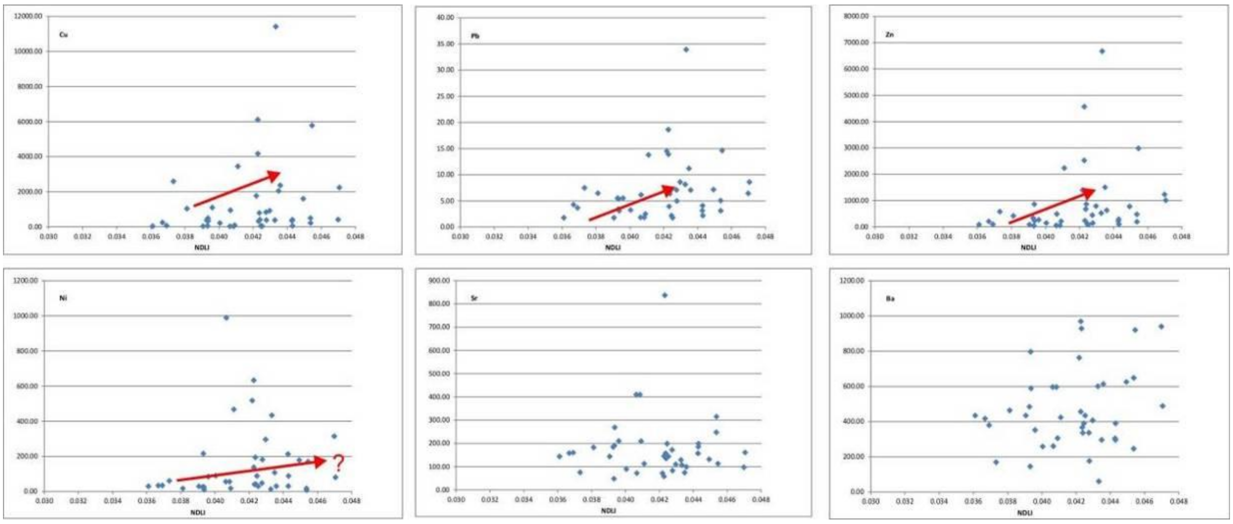

Fig. 5.32 Correlation of the NDLI with a: Cu; b: Pb; c: Zn; d: Ni; e: Sr and f: Ba. Red arrows indicate the direction of increased plant stress.

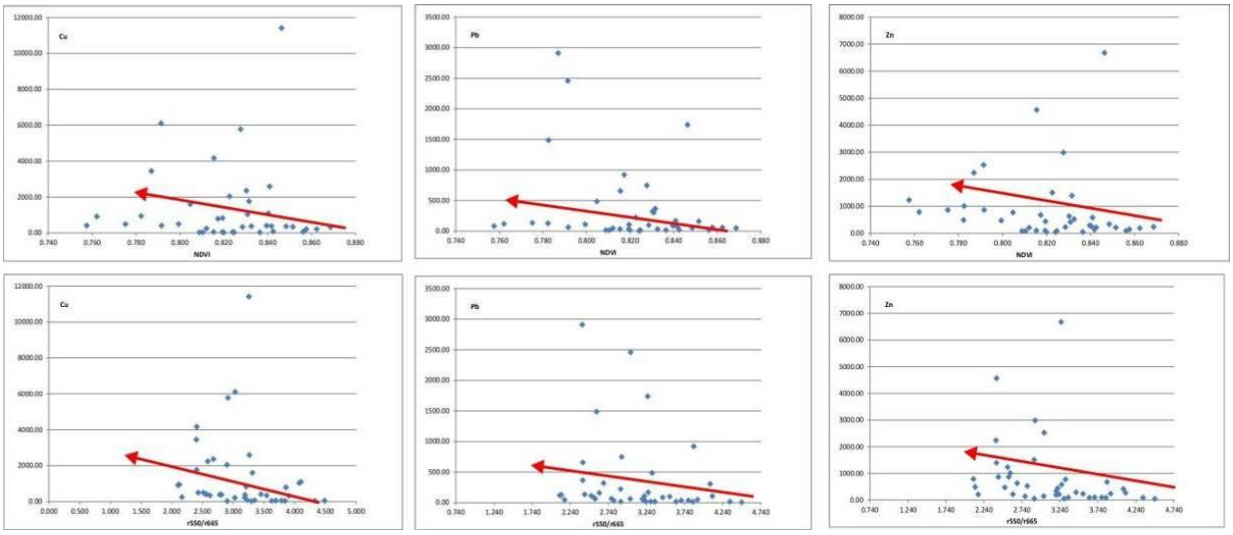

Fig. 5.33 Correlation of the NDVI with a: Cu; b: Pb; c: Zn; and of the green/red ratio with d: Cu; e: Pb; f: Zn. Red arrows indicate the direction of increased plant stress.

Fig. 5.34 shows the relation between several spectral vegetation indices and the distance to the Karabash smelter, whereby higher vegetation index values are related to healthier vegetation. In general, the indices are related to the distance to the smelter, for *in situ* samples within a range of 10 km. At larger distances, there is no relation between the indices and the *in situ* vegetation indices. One of the most significant vegetation indices is $RVI_{760\text{-}900}$. This index is related to the slope of the NIR plateau in the vegetation reflectance spectrum: when the curve is flat, the index will obtain a value close to 1, typical of healthy vegetation. The stressed vegetation in the proximity of Karabash shows a relatively low reflectance around 760 nm, leading to lower values of $RVI_{760\text{-}900}$.

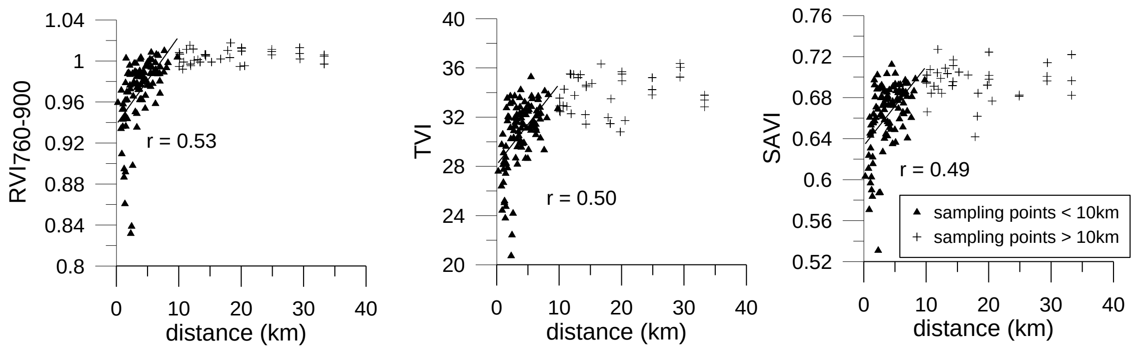

Fig. 5.34 Relationship between an intrinsic (RVI760-900), angular (TVI) and soil-adjusted (SAVI) index derived from in situ vegetation spectra and the distance to the Karabash smelter. Sampling points within a distance of 10 km (triangles) with correlation and Pearson correlation coefficients, and beyond 10 km (crosses).

5.2 Mednogorsk demo site

Three days were spent in the Mednogorsk area during July 2011. The landscape consists of upland ridges with elongated or rounded hills with hollows between them. The slopes of the ridges and hills are steep or flat, unvegetated or covered with grass and scrub. The soils of the area are common and southern chernozems. The main river in the district is the Blyava (Fig. 2.7), which runs into the Kuragan, which originates on the western slope of the main divide of the Southern Urals.

The climate of the region is sharply continental. Most rain (up to 60%) falls in the summer and autumn months. The period of snow cover is generally from November to December. The average temperature of the warmest month is +22.1 ° C, and the coldest month -10.4 ° C.

The main source of contaminants in the area is the copper-sulfur plant (Table 5.7).

Table 5.7 Emissions of air pollutants in the Mednogorsk town (2000)

(Internet resource bank.ooipkro.ru)

Population of Mednogorsk	Area (km^2)	Emissions to air (tonnes per year)	
		Per person	Per km^2
39100	73.38	1.74	0.929

5.2.1 General vegetation

The Mednogorsk area is a very dry region, characterized by grass-steppe with scarce trees, mostly birch and black poplar (Fig. 5.35a), and fairly clay-rich grey weathering soils. Within a distance of about 10 km from the smelter we observe very clear gradual changes: vegetation becomes thinner and shrubbier, soils deteriorate and become red (Fig. 5.35b), and grass almost disappears at distances less than 3 km from the smelter (Fig. 5.35c). As can be seen in the photos, birch trees become scarcer, smaller and shrubbier.

Fig. 5.35 a.(left): Typical regional grass-steppe vegetation; b.(center): Vegetation cover near the open pits (5-6 km east of the smelter); c.(right): Typical landscape at distances less than 3 km from the smelter. Note the differences in the appearance of the birch trees in the three pictures.

In vicinity of the smelter, soils become increasingly reddened, probably caused by the presence of hematite, and the surface is more deeply eroded (Fig. 5.36a,b). Outcropping rocks in many places have a black surface colouration (Fig. 5.36c)

Fig. 5.36 a.(left): View of the smelter from the east (note the shrubby vegetation and hematite-rich soils). B. (centre): View on the smelter, looking east. The trees in the background occupy the river valley. C(right): Typical black staining of outcropping rocks.

5.2.2 Soil geochemistry and spectral signatures

Soil samples were collected in July 2011 for chemical and spectral analysis. These show significantly elevated levels of Pb, Zn, Cu, As, Cd and Sb in the vicinity of the smelter, in particular 1 to 2 km towards the east (Fig. 5.37a). Values up to 30 times the background are recorded for Pb, up to 30 times the background for Cd, and up to 20 times the background for As. One soil sample collected in the town of Mednogorsk itself contained low levels of toxic metals, only slightly above the background value.

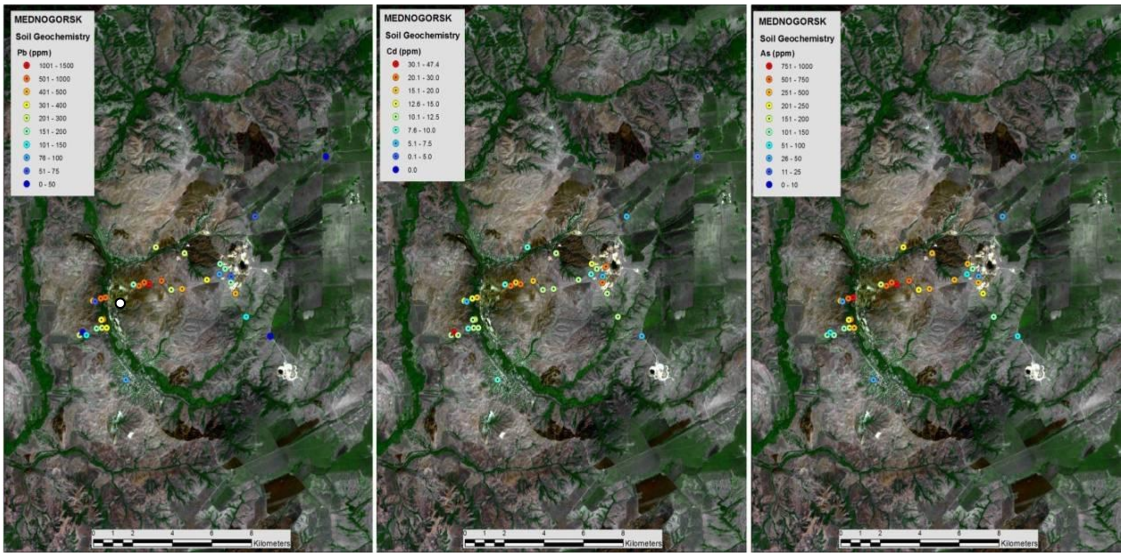

Fig. 5.37 Plots for (a) Pb, (b) Cd and (c) As in soils. The location of the smelter is indicated by the white dot in the left hand figure.

The distribution of Li, Sr, Ba, Ti and Mn (Fig. 5.38) appear to be related to lithology while Ni, Cr and Co do not show any particular pattern.

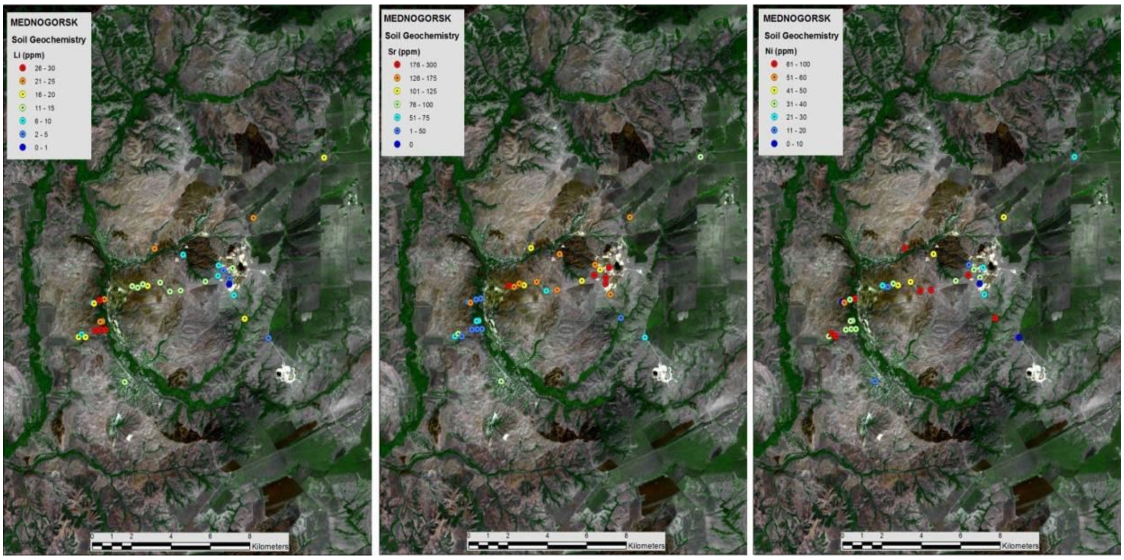

Fig. 5.38 Plots for (a) Li, (b) Sr and (c) Ni.

From the soil spectra we find that the soil mineralogy in the area is dominated by montmorillonite (Fig. 5.39). Locally we find illite and at the mine dumps we find goethite.

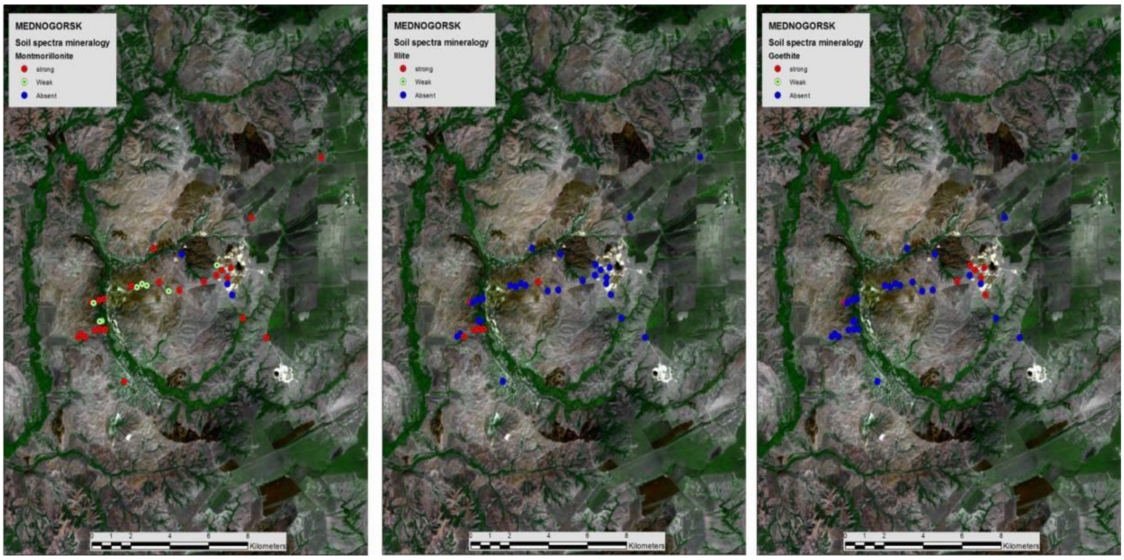

Fig. 5.39 Plots for soil minerals determined from Infrared spectra.

The increasing red colour (goethite, hematite) in soils as a function of proximity to the smelter is probably the most noticeable. As described in the section for Karabash, there are specific absorption features in the spectral reflectance curves that can be used for mapping iron oxides, and by calculating the size of these features, using for example ratios of specific bands, we are able to identify much more subtle changes in mineralogy than is possible by visual interpretation of the spectra. The ratio of the reflectances at 650nm/465nm (Fig. 5.40a) is most likely to indicate the presence of goethite, while the ratio of 757nm/937nm probably reflects a more general presence of ferric iron minerals, such as hematite (Fig. 5.40b). Both plots seem to correspond well with our field observations concerning the red colour of the soils.

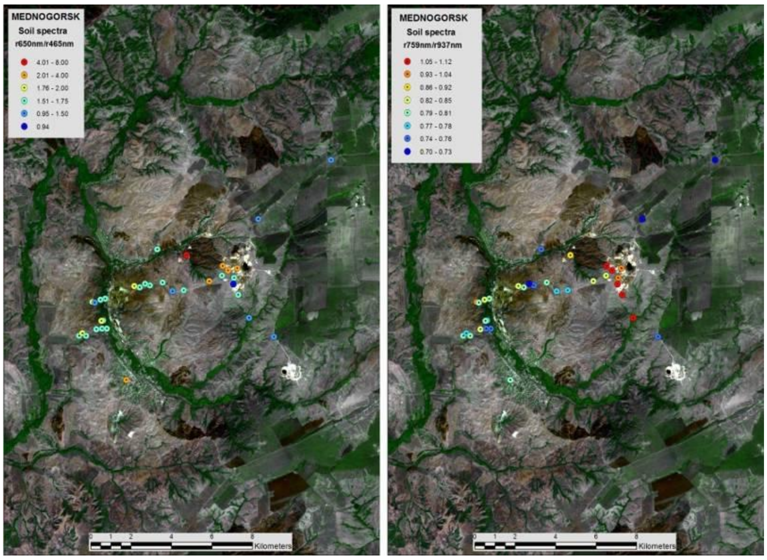

Fig. 5.40 a(left) Ratio of reflectances at 650/465nm; b(right) Ratio of reflectances at 759/937nm.

5.2.3 Air filter sample

Only one air filter sample was collected in Mednogorsk, mainly because of the short time spent in the town during the 2011 field season. Chemical data for this air filter sample is shown in Table 5.4. The airborne particulate has an elemental signature very similar to that of air filters collected from Karabash, i.e. dominated by Pb, Zn and As, with the exception of having relatively high Sb.

5.2.4 Surface waters and sediments

Surface water samples were taken downstream from the waste dumps and from background steams (Fig. 5.41).

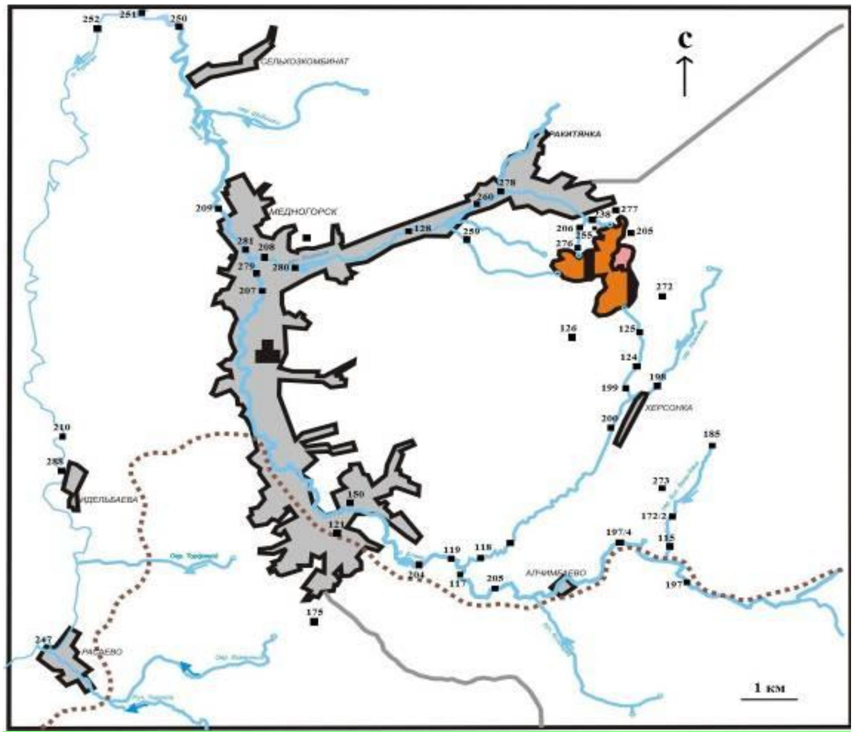

Fig. 5.41 Map of Mednogorsk showing locations of surface water sampling points.

The compositions of mine and background (Kuragan river - Md (w) 251) waters are shown in Table 5.6. The histograms in Fig. 5.42 and 5.43 compare the metal concentrations in waters from different sampling points, compared with the 'maximum allowable concentration' (MAC) for potable water. Compared with the MAC value, Mednogorsk samples Md (w) 124, 197/1, 199, 200, 206, 208, 238 contain 10-100 times the Cu, 2-1000 times Zn, 3 times Pb, 2-110 times Mn, 8-80 times Fe, 2 to 80 times Cd, compared with the MAC value. The concentration of metals in the other samples is below the MAC for potable water use, namely, Md (w) 198, 202, 203, 210, 200, 204, 205, 207.197/4, 117, 118, 123, 250, 288 . Sample Md (w) 251 is the 'background' sample for the water from the river Kuragan.

No. sample	pH	Eh, mv	γ, μS	HCO_3^-	Ca	Mg	Na	Fe	Mn	Cu	Zn	Ni	Co	Ba	Pb	Cd
					ppm			ppb								
Md(W)251	7.26	251	174	15.3	47.2	284.4	16.9	3.2	11.7	15.8	11.6	3.4	11.6	1.1	0.5	0.08
Md(W)197	7.63	233	365	54	87.6	262.3	17.7	3.9	27.1	10.8	29	9	14	1.4	0.7	0.18
Md(W)197/1	4.33	407	2009	124.1	1851	26	55.6	4.8	95	29855	15880	9554	4815	80.6	362	226
Md(W)197/4	6.88	250	894	106	283.1	216	28.2	4.2	68	926	831	732	720	12.3	29	7.2
Md(W)117	7.27	247	565	23.1	62.2	247.7	17.1	4.3	43.3	352	80	62	103	9.2	6.1	1.7
Md(W)118	7.23	276	1442	68.3	588.4	186.7	53	2.9	49	850	93	1290	306	33.6	104	9.3
Md(W)119	7.26	243	1319	46	302.9	231.8	32	7.7	58	0.28	20	33	120	12	25	7.5
Md(W)123	7.11	246	1267	39	438.7	157.6	33	3.6	57.9	817	515	1231	418	32	11	4.1
Md(W)124	3.14	525	12500	83.3	13341	—	495	12.1	130	427865	28564	101800	141805	1462	13682	920
Md(W)238	3.2	503	11500	65.5	10328	—	486	15.2	155	383942	52500	142967	150362	1934	15004	530
Md(W)208	5.78	372	1730	33.6	995.8	42.7	81.7	4.9	79.8	2855	2412	5184	1552	65	324	163
Md(W)250	7.06	274	800	32	277.5	118.4	36.7	5.5	42	196	390	2423	176	58	90	182
Md(W)288	7.49	252	356	17.2	85.7	195.2	25.8	2.6	23	31	49	522	32	8.6	2.1	0.36
Md(W)198	8.25	280	1078	238	167	32	98	20	3	10	10	10	20	410	170	0.04
Md(W)199	4.78	395	4230	9.15	371	430	89	80	1300	9800	33000	230	350	360	820	75
Md(W)200	7.5	330	1786	189.1	240	123	99	40	2080	340	26000	50	70	400	190	10.7
Md(W)202	7.9	230	1501	176.9	217	90	76	40	9	100	40	20	30	550	10	0.66
Md(W)203	8	260	1221	210.4	202	41	95	100	3	100	60	20	30	590	230	0.36
Md(W)204	7.9	270	1283	204.3	193	52	97	40	3	100	50	20	20	550	190	0.48
Md(W)205	7.74	260	2260	137.2	398	102	128	50	540	130	27000	40	50	540	200	3.28
Md(W)206	4.1	350	9750	6.1	310	1560	147	4220	1340	134000	94000	23000	4430	130	1710	578
Md(W)207	7.75	237	1202	192.1	193	50	69	40	2500	60	680	50	40	620	290	8.5
Md(W)209	7.8	242	1275	140.3	226	54	66	30	1170	20	420	30	20	1930	160	6.49
Md(W)210	7.95	237	820	192.1	134	35	46	150	32	10	2100	10	20	1710	130	1.82

Table 5.8 Geochemical data for surface waters in the Mednogorsk area.

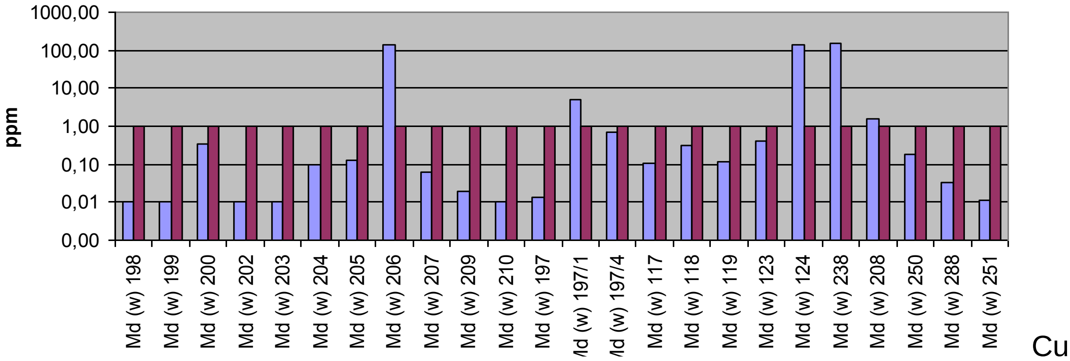

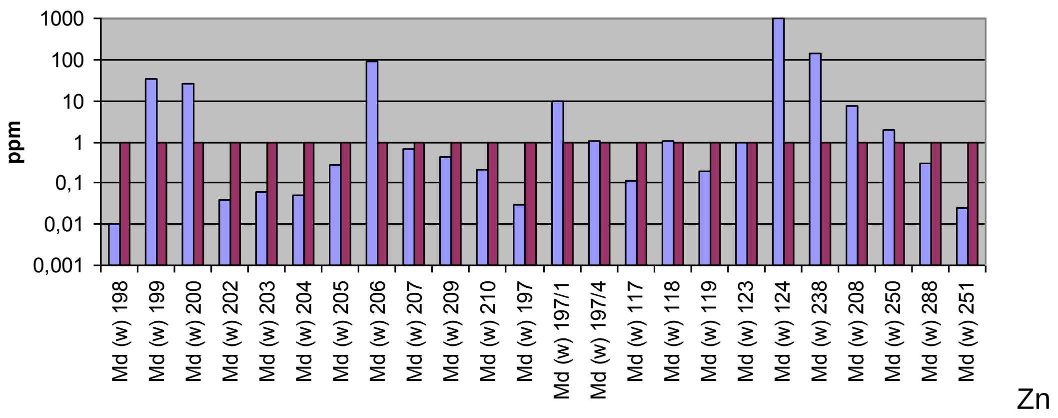

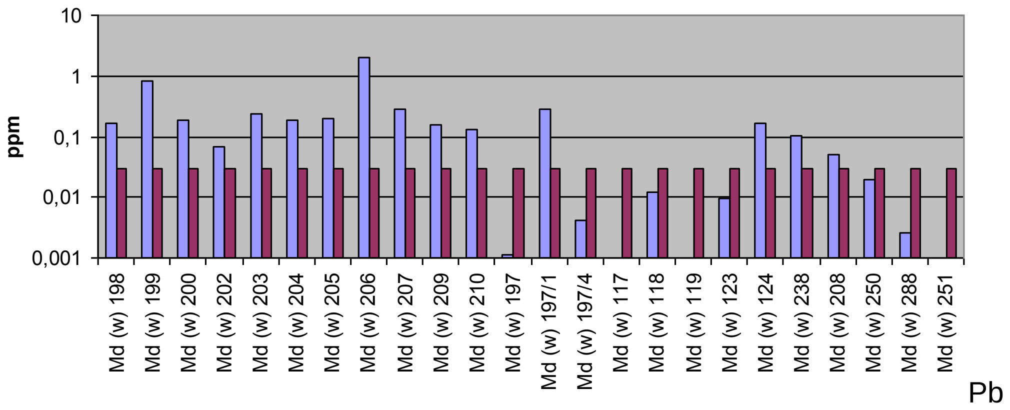

Fig. 5.42 Concentration of elements in waters (in solution) from Mednogorsk compared with the maximum allowable concentration (MAC) for potable water applications.

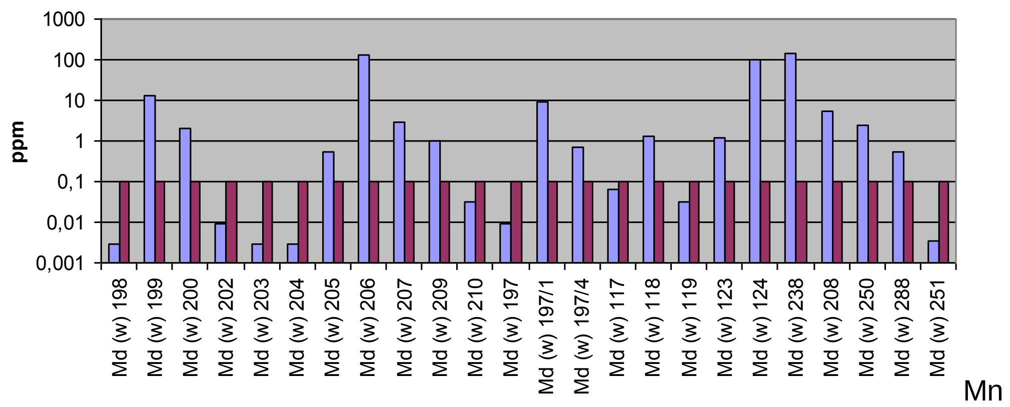

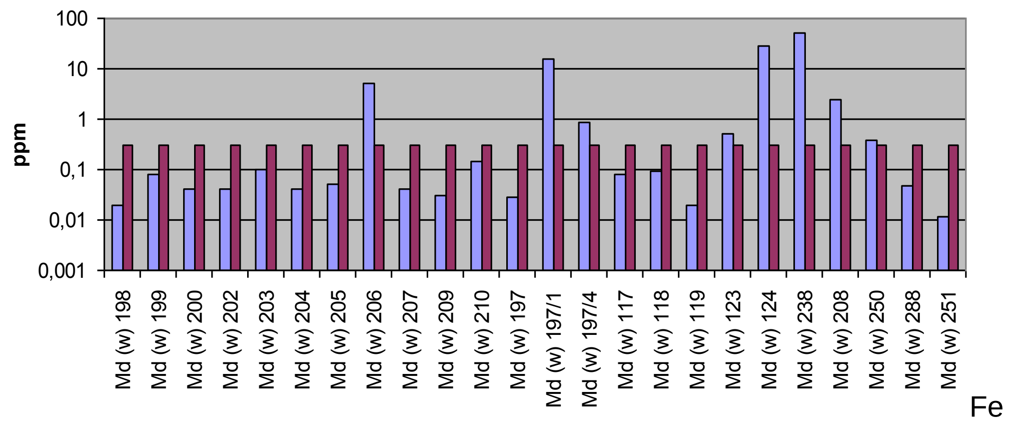

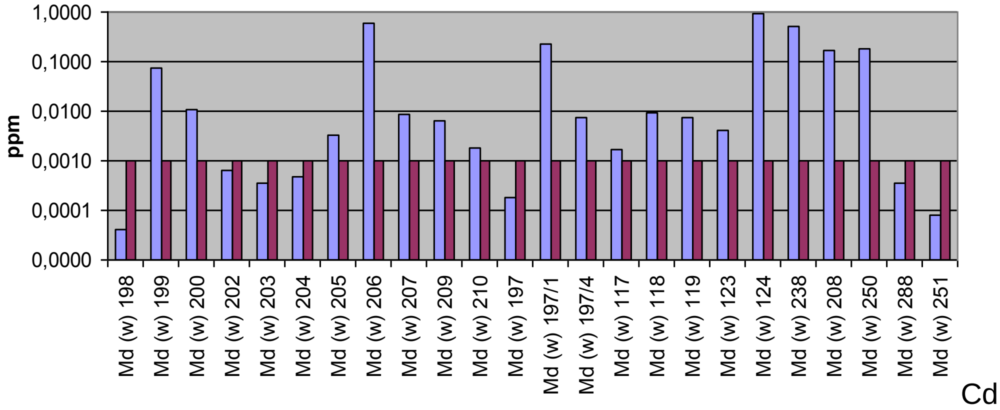

Fig. 5.43 Concentration of elements in waters (in solution) from Mednogorsk compared with the maximum allowable concentration (MAC) for potable water.

The sediment samples (Table 5.9) from Mednogorsk all have chalcophile and siderophile element concentrations (except Cr) 2 to 7 times higher than the average for bottom sediments worldwide (Martin and Whitfield, 1983), see Fig. 5.44. The low values for Pb from many of the sampling points are difficult to explain, given the presence of this element in ores/mineralisation from the Blyava and Yaman-Kasy deposits and some pyrite deposits of the Southern Urals.

Table 5.9 Concentration of metals in sediments from Mednogorsk (ppm).

№	№ of sample	Fe	Mn	Cu	Zn	Ni	Co	Pb	Cd	Ba	Sr	Cr	Al	Li
1	Md(Sd)128/1	232484	697	47930	10419	60	109	120	43,57	61	20	22	72456	5,4
2	Md(Sd)185	260806	910	1727	3393	60	54	392	21,79	454	107	27	83622	21,8
3	Md(Sd)197	89237	980	1362	2413	44	54	98	32,68	300	55	44	96694	27,2
4	Md(Sd)197/1	145882	387	2042	1117	54	49	109	16,34	149	22	5	97347	16,3
5	Md(Sd)199	14728	16558	32407	16302	338	610	87	141,61	242	42	33	81117	10,9
6	Md(Sd)205	138802	1236	1182	2249	131	87	93	21,79	449	82	142	70169	21,8
7	Md(Sd)207	259717	1765	37582	24472	163	54	398	212,42	192	62	11	41955	10,9
8	Md(Sd)208	283682	3938	6373	4428	191	191	349	38,13	686	199	289	148001	49,0
9	Md(Sd)209	145338	2184	26144	13578	120	153	534	70,81	263	57	0	82914	21,8
10	Md(Sd)210	41852	3954	3655	7042	153	93	163	70,81	581	145	142	36127	27,2
11	Md(Sd)276/2	148061	828	1672	1024	65	22	370	16,34	445	90	185	71639	16,3
12	Md(Sd)277	129542	975	1313	2032	98	22	191	16,34	404	69	163	75779	16,3
13	Md(Sd)278/1	118649	1280	2505	2249	125	38	343	27,23	400	73	71	56389	27,2
14	Md(Sd)252	37495	4036	735	1868	163	38	136	27,23	238	83	185	57914	32,7

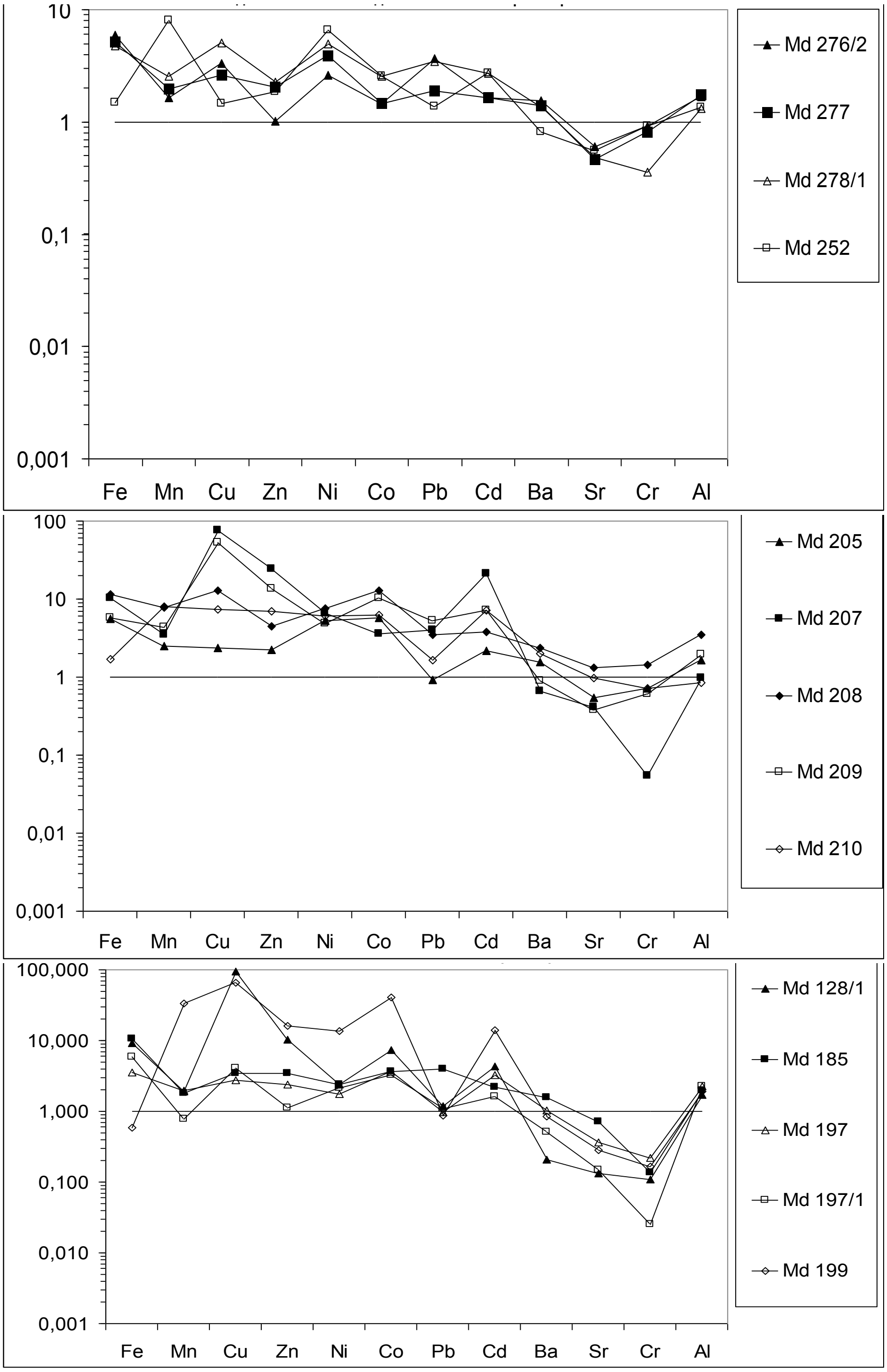

Fig. 5.44 The distribution of elements in the sediments of rivers and streams with acidic waters from Mednogorsk, normalized to the average composition of bottom sediments of rivers in the world (Martin and Whitfield, 1983).

6 RESULTS OF REMOTE SENSING STUDIES FOR KARABASH AND MEDNOGORSK

6.1 *Landsat and WorldView-2*

6.1.1 Data processing

Fig. 6.1 shows spectral parameters from soil samples and birch leaves overlain on a processed Landsat image from 2011. The spectral ratio r780/r900 for surface 'soils' in the Landsat Band3/Band1 ratio is plotted in Fig. 6.1a. This ratio can be used to calculate the size of the ferric iron absorption feature in the 900 nm region, and hence is a good indicator of the proportion of Fe-oxides in top 'soils'. Unfortunately, the spectral range of 760nm-900nm is covered by one single Landsat band (band 4), and because of this it is not possible to directly reproduce the r780/r900 ratio using Landsat. However, there are several alternative ways to estimate the iron-oxide contents of top 'soils' using Landsat as band ratios (e.g. 1/3, 2/3, 3/4, Harris et al 1998) the Crosta-technique (Loughlin, 1991).

The Crosta technique is probably the most sensitive method, but the disadvantage is (in particular when comparing multi-temporal imagery) that it is a principal component-based method, and hence relies on image statistics. This problem does not exist when using band-ratios, and hence it is easier to compare multi-temporal results from band ratios (provided that the images are properly calibrated). For this reason we choose to use the ratio of band1/band3 to map iron oxides.

In Fig. 6.1b we have plotted the red-edge position of birch leaf spectra on a Landsat NDVI-image. The red-edge can be mathematically defined as the position of the inflection point of the slope connecting the local minimum reflectance in the red (650nm) and the maximum reflectance in the NIR (750 nm) spectral regions (Dawson and Curran, 1998; Mutanga and Skidmore, 2007; Pu et al., 2003). In physiological terms this steep increase of reflectance marks the transition between the photo-synthetically affected region of the spectrum (maximum absorption of chlorophyll a and b at 662 nm and 642 nm, respectively), and the region with high reflectance values of the NIR plateau affected by plant cell structure or leaf layers. This feature enables a clear representation of chlorophyll absorption dynamics, illustrating a shoulder shift towards longer wavelengths when the chlorophyll absorption increases (higher chlorophyll content) and a shift towards the shorter wavelengths with decreasing chlorophyll absorption (Moran et al., 2004). Thus, the position of the red-edge, at canopy scale, provides an indication of plant condition that might be related to a variety of factors such as Leaf Area Index (LAI), nutrients, water and chlorophyll contents, seasonal patterns, and canopy biomass (Blackburn and Steele, 1999; Tarpley et al., 2000).

Since it is not possible to calculate the red-edge position (REP) from the Landsat data, we have used the NDVI instead. The Normalized Difference Vegetation Index (NDVI) is a measure of the amount and vigor of vegetation on the land surface. NDVI spatial composite images are developed to more easily distinguish green vegetation from bare soils.

In general, NDVI values range from -1.0 to 1.0, with negative values indicating clouds and water, positive values near zero indicating bare soil, and higher positive values of NDVI ranging from sparse vegetation (0.1 - 0.5) to dense green vegetation (0.6 and above).

NDVI is also directly related to the:

- "leaf area index" (LAI), which is often used in crop growth models,
- herbaceous or total green biomass (tons/ha) for given vegetation types,
- photosynthetic activity of the vegetation,
- percent ground cover.

Kriegler et al. (1969) were the first to propose NDVI and it is calculated by subtracting the red channel from the near-infrared (NIR) channel and dividing their difference by the sum of the two channels, or:

NDVI= (NIR - RED) / (NIR + RED)

where RED = the red portion of the electromagnetic spectrum (0.6-0.7 μm) and NIR = the near infrared portion of the electromagnetic spectrum (0.75-1.5 μm).

The NDVI is generally accepted as a good proxy for the amount of chlorophyll in plants. It has been correlated to many variables that can cause plant stress (e.g. Verhulst and Govaerts, 2010, Glenn et al., 2008), and may be used to estimate stress-induced variation (Eitel et al., 2010). The NDVI and the REP may be strongly correlated (Kanke et al., 2012), but this is not necessarily always the case.

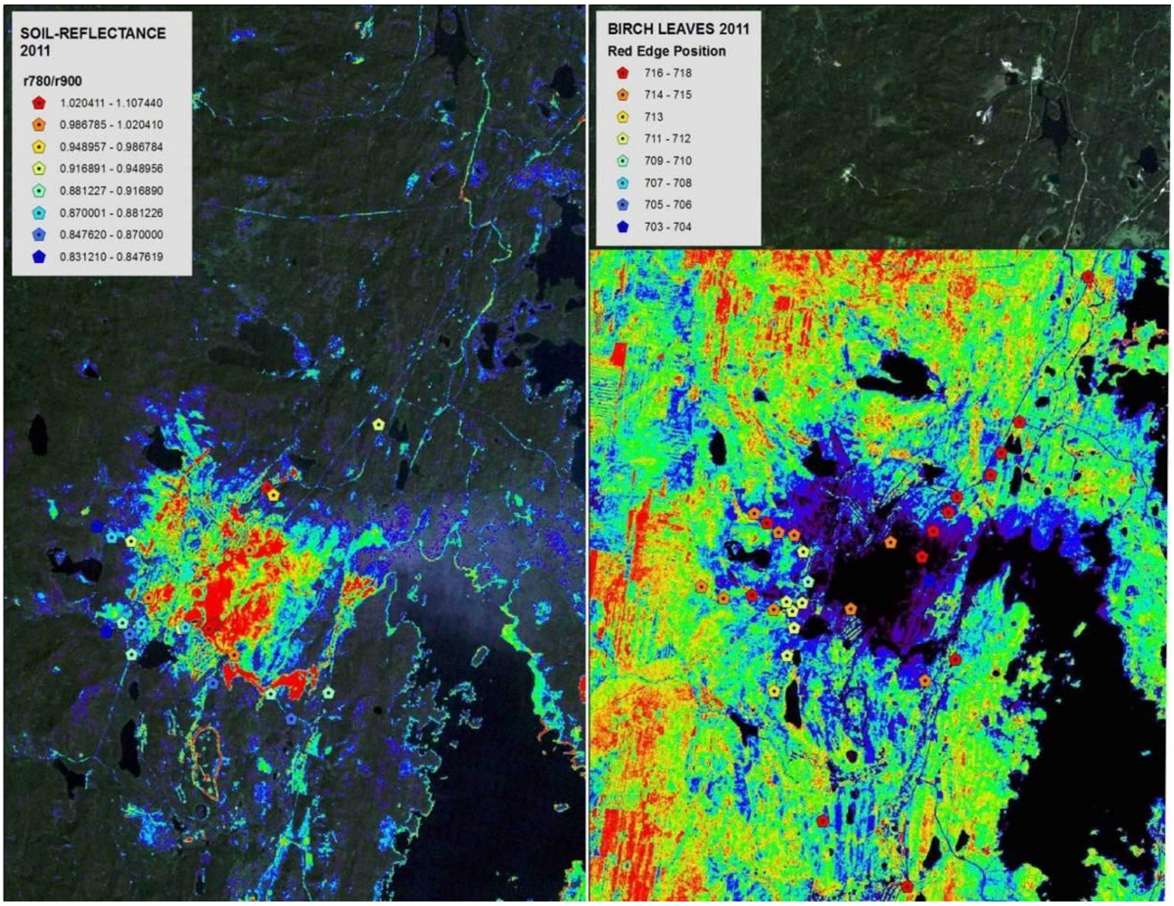

Fig. 6.1 a: ratio of r780/900 for soil samples plotted on the Landsat B3/b1 ratio; b: Red edge position of birch trees plotted on Landsat NDVI.

The plot in Fig. 6.1a suggests a generally good correlation between the size of the measured ferric iron absorption feature and the mapped Fe-Oxide content using Landsat. However, the number of samples – especially in the transitional zone - may be too limited to fully confirm the patterns we obtain from Landsat, and it would be very useful to have a denser grid of soil samples, that continues to greater distances from the smelter.

The plot in Fig. 6.1b indicates that there is at best a modest correlation between Landsat NDVI and the red-edge position of the birch leaf spectra. While both datasets support the zoned pattern on a regional scale, on a detailed scale the correlation is not great. We suspect that one of the reasons for this relatively low correlation is the low spatial resolution of the Landsat imagery, which implies that we may actually be observing changes in soil/vegetation proportions rather than spectral changes in individual trees.

We concluded that, in order to be able to obtain a better understanding of these differences, and of the response of the birch trees to the airborne pollution from the smelter stack, we would need denser sampling, with transects in more directions, and better located.

In the previous section, we have demonstrated that smelter emissions have a profound impact on soils and vegetation up to a distance of at least 10 km away from the smelter. This impact is readily visible by a dramatic decrease in vegetation species diversity, soil biotic activity and changes in soil mineralogy. We identified well defined chemical and spectral trends for soil and vegetation, showing a more or less concentric zoning around the smelter. Heavy metal content of soils could be directly correlated with spectral stress indicators in birch leaves. This allows us to map the extent of the environmental impact using field spectroscopy. Whilst this field spectroscopy is a fast, non-destructive and very cost-effective method, it would be very advantageous if we could use satellite imagery to map these variations, as this allows us to cover very large and continuous areas, while we are not limited by restrictions such as access. Also, the use of satellite imagery may enable us to monitor these changes over time.

In this study we have investigated the possibilities to map the observed trends in soils and vegetation using Very High Resolution WV-2 imagery and GeoEye, medium resolution Landsat, and Low-resolution Spot-vegetation. Aster unfortunately was not an option, as the available imagery was very poor quality due to cloud-cover. In addition, we submitted a request for Hyperion images to be acquired, but this was not awarded.

We started our investigation with the analysis of WV-2 imagery, because its high spatial resolution allows us to examine individual trees and accurately locate the soil samples, while its increased number of spectral bands in the VNIR should allow us to replicate some of the spectral trends found in the field. A new acquisition of WV2-imagery was therefore requested for summer 2011. The first image was acquired on September 1st, but unfortunately this image could not be used for spectral analysis because of the abundance of clouds and haze (Fig. 6.2a). A second image was acquired on September 15th. This image (Fig. 6.2b) has some clouds in the northern part, but it has much less haze, and the quality was sufficient for spectral analysis.

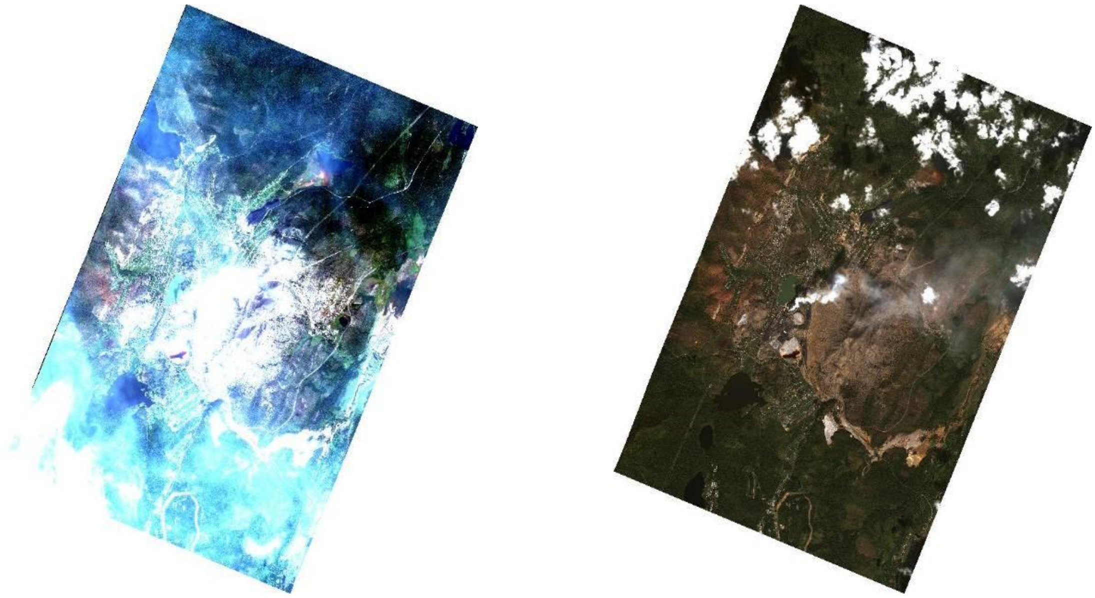

Fig. 6.2 a: WV-2 image of September 1st (left), b: WV-2 image of September 15th (right)

The WV-2 image was calibrated for radiance using the automatic Envi (4.8) routine for WV-2. Subsequent atmospheric correction to reflectance was done using the solar spectra of various targets collected in the field in 2012. Although the reference spectra were collected a year after acquisition of the image, we felt that this procedure could be used since the reference spectra were taken in locations that are spectrally stable (e.g. a black slag dump, a quarry, paved road). After calibration, all field-spectrometer soil spectra were converted to WV2-band positions using the Envi 4.8 Spectral Library Resampling module, and compared with the WV2-image in order to confirm the quality of the reflectance calibration (Fig. 6.3).

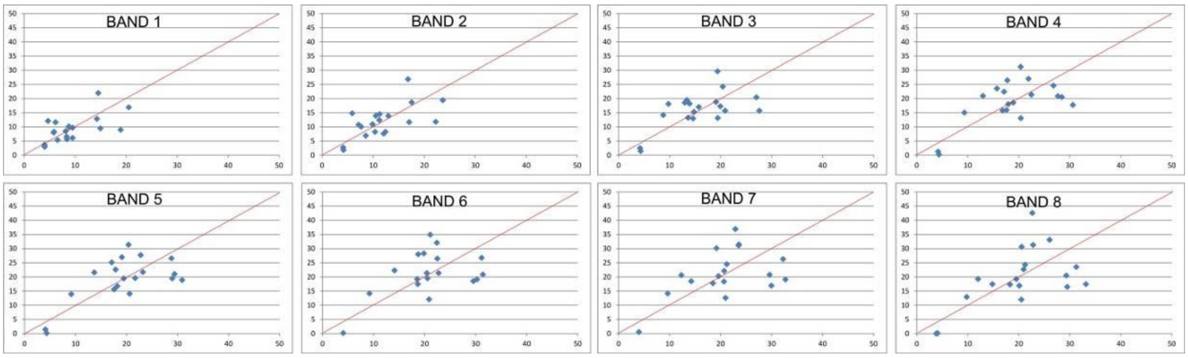

Fig. 6.3 Comparison of WV2-spectra and field spectra for representative soil samples. Along the vertical axis is the WV2-reflectance (in %). Along the horizontal axis is the field reflectance (in %), resampled to WV2-band positions.

6.1.2 Soils

As described above, one of the characteristic, and spectrally measurable, changes in the soil properties as a function of vicinity to the smelter is the increase in iron oxides. There are a variety of different methods to detect spectral features in imagery, such as band-ratio techniques and supervised spectral classification methods. Band ratio techniques work particularly well to identify subtle changes within one particular spectral group. However the method has several major disadvantages.

The main disadvantage is that it is extremely dependent on the calibration. Incorrect calibration can lead to errors that, in particular in dark spectra, can lead to inversion of band ratios (see Fig. 6.4).

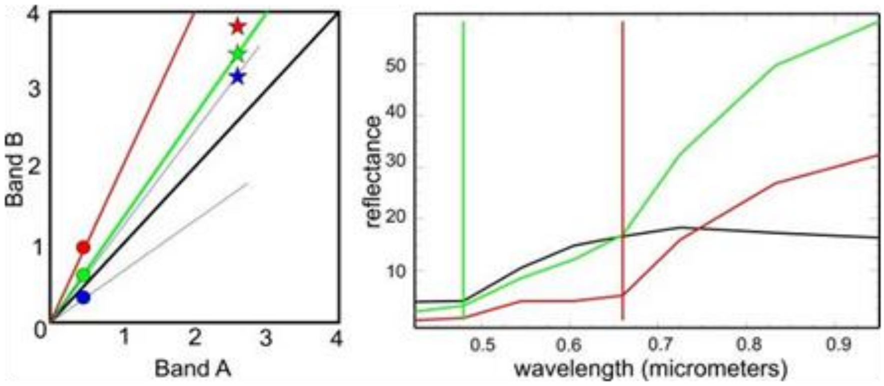

Fig. 6.4 (a) Left: illustration of ratio inversion. Black line indicates the points with a band ratio of 1. (b) Right: spectrum of a goethite-rich soil (black), and soils covered with abundant organic litter (red and green).

Fig. 6.4a demonstrates how a small shift in data values as a result of a minor error in the atmospheric correction can lead to very significant changes for darker pixels. Assuming that the correct situation for two different pixels is indicated by the blue symbols, the blue circle has a band ratio <1, and blue star a band ratio >1. A relatively small error in Band B will result in the same band ratios for the two samples (green symbols), and a slight further increase of the error will result in the circle having a much higher band ratio than the star (red symbols). This means that when we apply a band ratio technique, the chances are very significant that all kinds of misclassifications will appear in the darker parts of the image. This situation is very clearly illustrated in Fig. 6.5, where we compare the band ratio results for the raw WV2-image (Fig. 6.5b), and for the atmospherically corrected image (Fig. 6.5c).

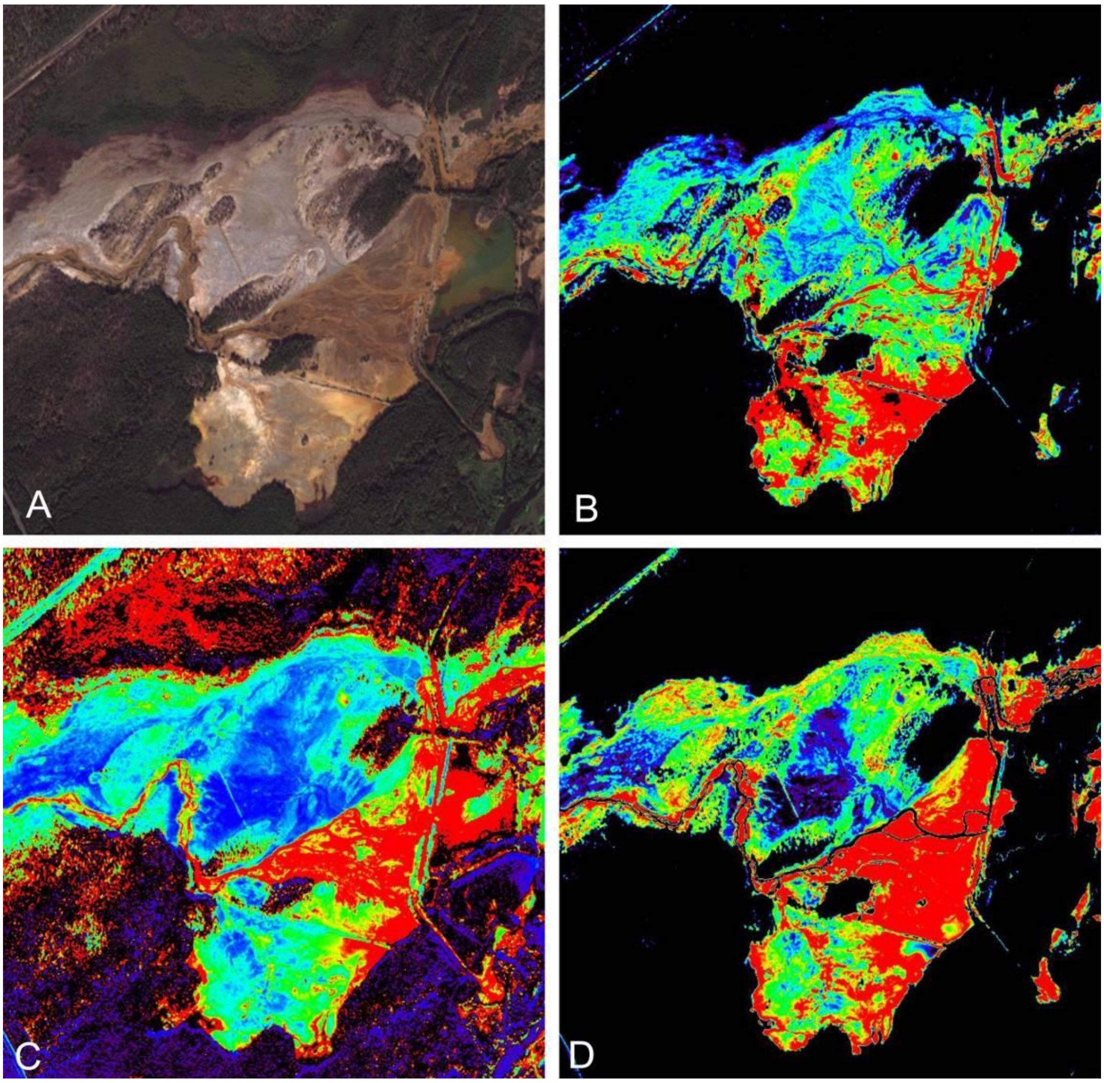

Fig. 6.5 a: WV2 Natural colour composite of area clearly showing rusty colours of iron oxides. b: Ratio of bands 5/2 for raw WV2-image. c: Ratio of band 5/2 for atmospherically corrected WV2-image. d: results of spectral angle classification.

The second problem associated with band ratios is that we can have different materials with completely different spectra, but with identical band ratios, as illustrated in Fig. 6.5. In this case the soils with the organic litter both have a band ratio of b5/b2 that is identical to the ratio for goethite-rich soils. Hence, this ratio technique is not sufficiently discriminative.

Therefore it is important that, when using the ratio technique, everything which is not soil should be masked out. As this is often impossible, it might be more appropriate to use other techniques such as the spectral angle classification, which is a classification technique that uses an n-dimensional (n is the number of bands) angle between the reference spectrum and each image pixel. The disadvantage of this technique is that it is not able to pick out subtle changes such as changing slopes between two bands. This may for example become an issue when there is a need to compare multi-temporal imagery. In that case, it can be helpful to use a combination of classification and band-ratios, where the Spectral Angle method is used to make a broad classification of pure soils, and subsequent band ratioing is used to identify changes within this soil class.

Once we have isolated only the pure soils, the band ratio technique shows a good correlation with the field data, as is shown in Fig. 6.6.

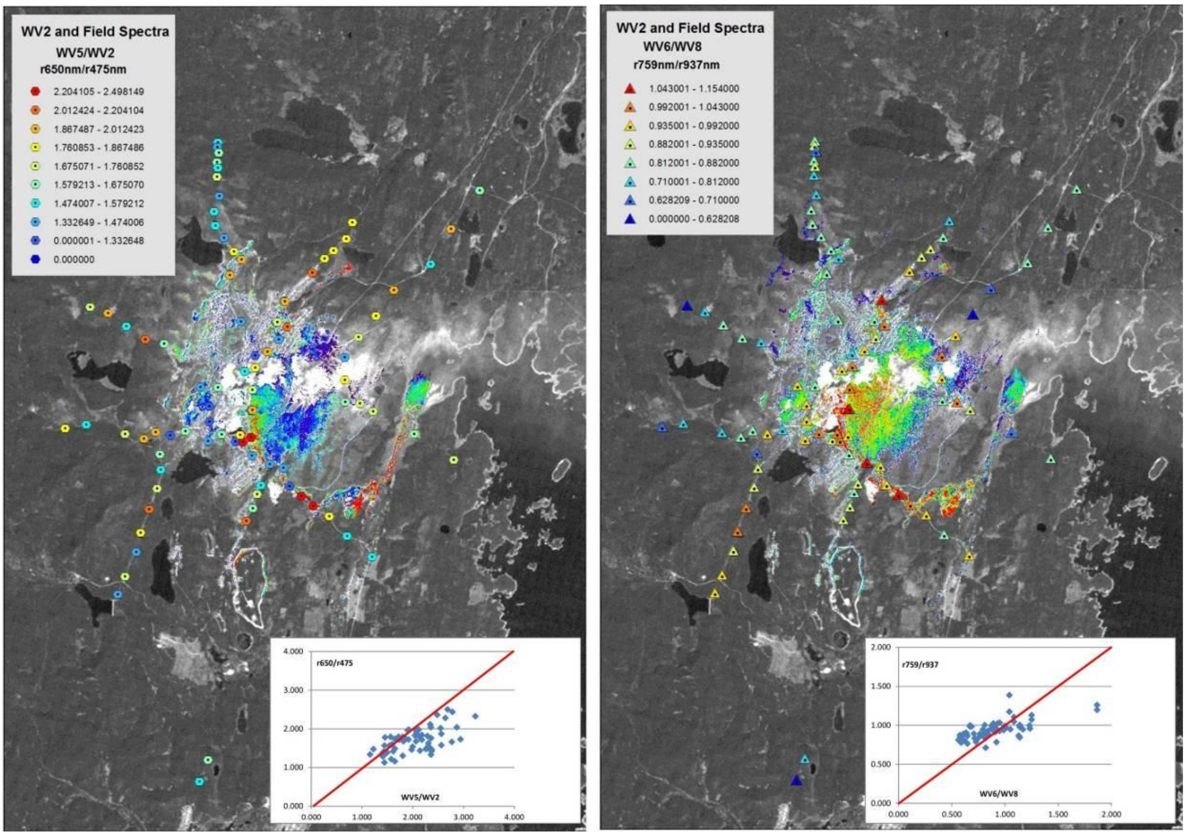

Fig. 6.6 Comparison of band ratios derived from WV-2 and from field spectra. The symbols for the samples have the same colour scaling as the images. The two images show different patterns. We suspect that this is due to the fact that the WV5/WV2-image maps mostly goethite, whereas the WV6/WV8 is more generally related to minerals that show a ferric iron absorption feature in the 900nm-wavelength range.

6.1.3 Vegetation

In a previous section we have identified 5 spectral parameters (R760nm/r900nm, NDVI, NDLI, r550nm/r660nm and the red edge) that allow us to map the impact of the smelter-emissions using field spectra. The NDLI and red edge position cannot be computed from the WV-2 imagery because it does not have the spectral bands that we would need to do so. Vegetation pixels are relatively dark compared to other materials in the image, and since the changes in the vegetation spectra are relatively subtle, and tree crowns are rather inhomogeneous due to shadows, it is essential that we carefully mask out everything that is not vegetation.

We used a procedure that involves a sequence of steps in order to successively mask remove all undesired pixels, such as clouds, water, dark pixels, mixed vegetation/soil pixels, shadows etc. The remaining vegetation image was used to generate band ratio images (see Fig. 6.7).

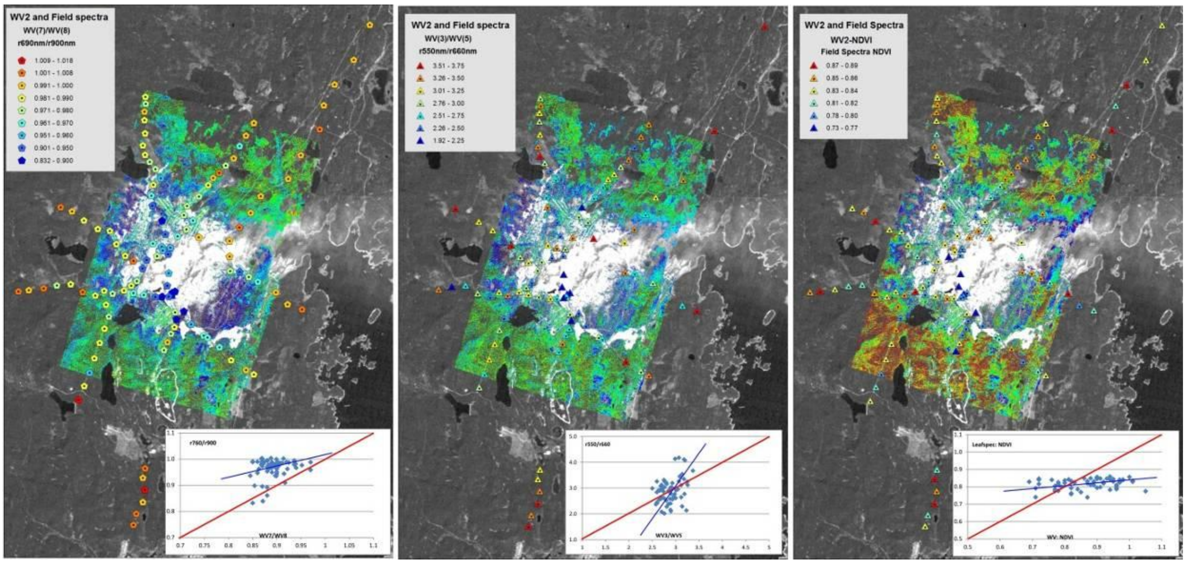

Fig. 6.7 Comparison of band ratios derived from WV-2 and from Field Spectra. The symbols for the samples have the same colour scaling as the images. Red lines indicate a slope of 1. Blue lines indicate the slope for the trends.

Since the WV2-data do not have the same spectral resolution as the field spectra, we obviously had to use the bands that corresponded best to the band positions of the field spectra. For the ratio r760nm/r900nm we used WV7/WV8 and for the ratio r550/r660 we used WV3/WV5. For calculation of the NDVI from the field spectra we resampled the field spectra to WV2-spectra using Envi's spectral resampling module. All three ratio images very clearly reproduce the zoning that was observed in all other data. For the WV7/WV8 ratio part of the data seem to follow the expected trend, but there is a cloud of data that is slightly offset and seems to follow a different trend (blue line). For the WV5/WV3 ratio, there seems to be a reasonable correlation, although the trend might be steeper than should be the case (see blue line). For the NDVI the trend is much flatter than expected, implying that the NDVI in the imagery changes much more strongly than the NDVI calculated from the field spectra.

Although we do not completely understand those observed differences, we can think of various reasons why this is the case:

1) The WV2 calibration is not perfect. This will lead to slopes deviating from unity;
2) We sampled only a few leaves per tree fairly close to the ground; It could be that the tree-crowns are spectrally different;
3) Tree crowns spectra in the imagery for individual trees are very diverse as a result of variations in shadow, local changes in leaf area, changes in illumination angle;
4) The WV2 image mostly covers the area that is affected. Most unaffected samples fall outside of the WV2-image, which means that we have an incomplete picture of the variation;
5) With a spatial resolution of 2 meters mixed pixels cannot be avoided. Factors such as mixed forest, or variations in soil/undergrowth will therefore impact the response received by the satellite;
6) We have demonstrated significant zoning in the herbaceous canopy, especially in the affected areas, where the leaf area of single trees is much smaller than in healthy areas. The changes of the surface underneath the trees will have a significant impact.

Despite these deviations from the ideal correlation between field spectra and image spectra, we have shown that it is possible to map the environmental impact on soils and vegetation quite effectively using WV2-imagery. However, WV2 imagery is expensive, and a single scene covers a strip of no more than 16 km when the sensor is pointing down vertically. In the situation of Karabash this is not enough to cover the full extent of the impacted area.

Acquisition of WV2-imagery is difficult because the programming of the satellite depends on the availability and priority given to a particular request. Combined with the fact that the weather conditions in Karabash are often not suitable for image acquisition, the chances of getting cloud-free images at the desired time are small. In that respect, other satellites such as Landsat provide a good alternative, because this satellite passes on a regular basis (for Landsat every 16 days), and has a much larger swath width (180 km for Landsat), and is cheap or even free of charge. Therefore, the next step in our analysis was to investigate the possibilities of using Landsat as an alternative to WV2 imagery for mapping the effects of environmental impacts.

The Landsat image used for the initial comparison was acquired on August 10th, 2011, which should be close enough in time to the WV2-image (September 15th, 2011) to allow a comparison. The raw Landsat image was calibrated to radiance using the ENVI Landsat calibration module, and subsequently an empirical Line atmospheric correction was applied using ground control points. The results of the correction was not fully in agreement with the WV2 data and since we know that the spectral calibration of the WV2-image was the best we could obtain, a subsequent gain-offset correction was necessary to fully correlate the Landsat image with the WV2 image (see Fig. 6.8). The resulting Landsat image shows a good overall correlation with the WV2-images. The tail in the scattergrams in the vertical direction is caused by clouds in the WV2-image.

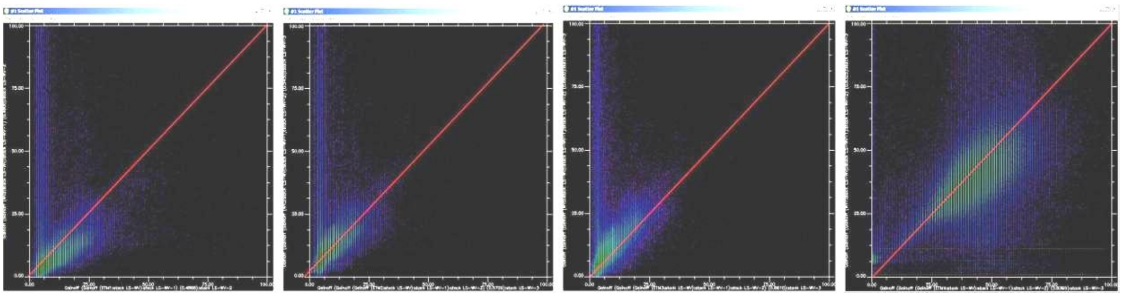

Fig. 6.8 Plots showing the relation between Landsat bands 1,2,3 and 4 (horizontal) and WV2 bands 2,3,5 and 7. The red line has a slope of 1.

Computation of the band ratio reveals some interesting features. First we computed the Landsat Band ratio 3/1, which corresponds with the ratio of WV5/WV2, which was used to map goethite (see Fig. 6.5) in soils. The results reveal that the band ratio produces a very noisy image (Fig. 6.5a). The noise dominates in the darker parts of the image, indicating a very poor signal/noise ratio for the 2011 Landsat image. After masking out the dark and noisy parts of the image, the results are very much improved (Fig. 6.5c), and correspond to a large extent with the results obtained earlier from the WV-2 image (Fig. 6.5d).

For mapping the zoning in vegetation Landsat has less possibilities than WV2, as we cannot compute the equivalent for the WV7/WV8 ratio, which was particularly effective for this study area. However, the available Landsat bands allow us to compute the green/red ratio and the NDVI, which were demonstrated to be effective in the WV2-imagery. The results for the NDVI (Fig. 6.9) show a very strong correlation between the Landsat image and the WV2-image, which implies that the Landsat NDVI will be a good alternative for the WV2 NDVI.

The Landsat NDVI was masked (Fig. 6.9) according to the WV2-coverage in order to allow better comparison between the two images. For the WV2-image (Fig. 6.9c) we applied a mask to remove clouds from the image.

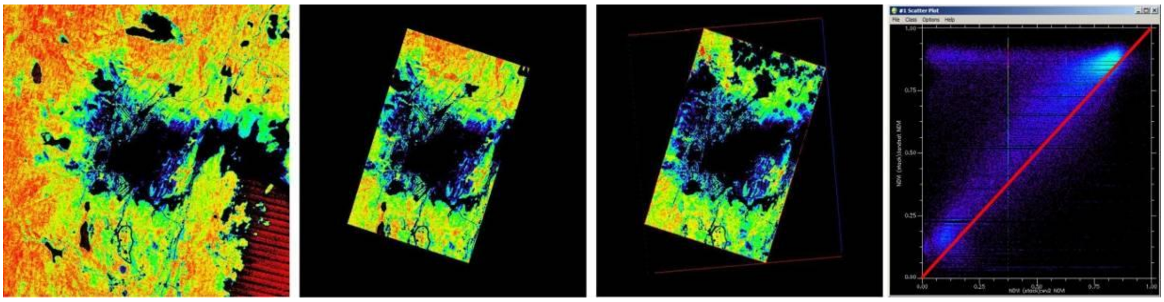

Fig. 6.9 NDVI for Landsat (a and b) and WV2 (c). The scattergram (d) shows the correlation between the NDVI for Landsat and WV2. The red line has a slope of 1.

The comparison of green/red ratio, which also was demonstrated to be quite effective for WV2, is presented below (Fig. 6.10). The full Landsat image (Fig. 6.10a) shows that for this ratio we have a serious noise problem. However, if we compare the Landsat ratio image with the ratio for WV2 (Fig. 6.10b and c respectively), we can still quite clearly see the similarity between the two datasets. For both images we have applied a mask in order to remove shadows, bare soil, clouds, lakes etc, which means that a lot of the noise related to differences in albedo within in the Landsat image could be removed.

The scatter plot between the two ratios as a whole shows an excellent correlation between the two datasets, but it also very clearly illustrates the noise problem. The fact that in certain positions the data are concentrated in vertical lines implies that some data in the Landsat image do not exist, and basically get accumulated in specific positions. Since it is not the purpose of this study to explain instrument noise, we will restrict ourselves to reporting that the problem exists.

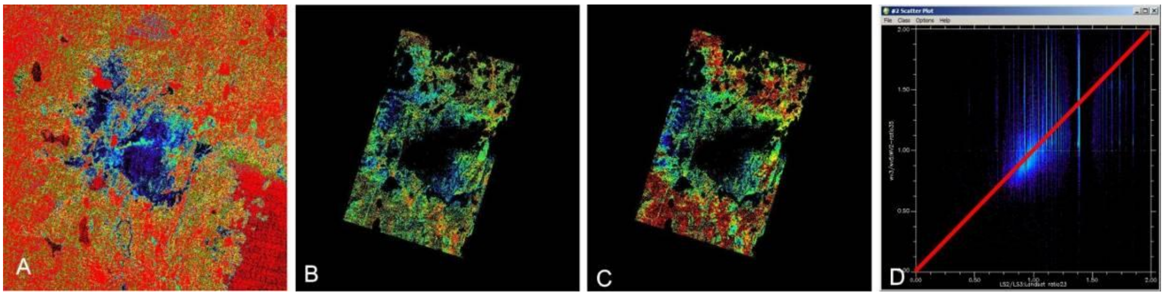

Fig. 6.10 Green/red ratios for Landsat (a and b) and for WV2 (c). The scattergram (d) shows the correlation between the green/red ratios for Landsat and WV2. The red line has a slope of 1.

6.2 SPOT-Vegetation time series

6.2.1 Data processing

Time series analysis of satellite-derived data with coarse geometric but high temporal resolution is a powerful tool for vegetation monitoring, in particular as it may differentiate between gradual and abrupt changes and inter-annual variations of phenology caused by external factors, such as changing climatic conditions, land-cover changes or land degradation (Udelhoven, 2011).

The Normalized Difference Vegetation Index (NDVI), is an index of vegetation activity that can be derived from broad band measurements in the visible and infrared channels onboard of satellite instruments and which is directly related to the photosynthetic capacity of plants (Sellers, 1985):

$$NDVI = (\mathrm{NIR} - \mathrm{Red})/(\mathrm{NIR} + \mathrm{Red})$$

where NIR and Red are the surface reflectances in the near-infrared band (0.73-1.1 µm) and in the red band (0.58-0.68 µm), respectively (Justice et al., 1985). The NDVI is closely related to the amount of absorbed photosynthetically active radiation, which means trends in NDVI reflect trends in photosynthetic activity of land-surface vegetation (Slayback et al., 2003).

The NDVI has also been used to quantify crop variables such as wet biomass, or leaf area per unit ground area, grain yield and chlorophyll content (e.g. Curran et al. 1990, Baret and Guyot 1991, Elvidge and Chen 1995, Blackburn 1998), but has also been widely used to monitor the effects of mining on vegetation.

In order to account for missing values and undetected clouds affecting the observations, the 10-daily NDVI and fAPAR time series were smoothed to S10s (Klisch et al., 2006). Monthly maximum S30 NDVI and fAPAR composite images were generated, retaining the highest value in order to minimize cloud and view angle effects (Holben, 1986): $NDVI_{imy}$ and $fAPAR_{imy}$, the monthly maximum NDVI resp. fAPAR value for pixel *i*, in month *m* and year *y*. Fig. 6.11 shows an example of a monthly maximum value NDVI composite derived from SPOT-Vegetation for August 2010.

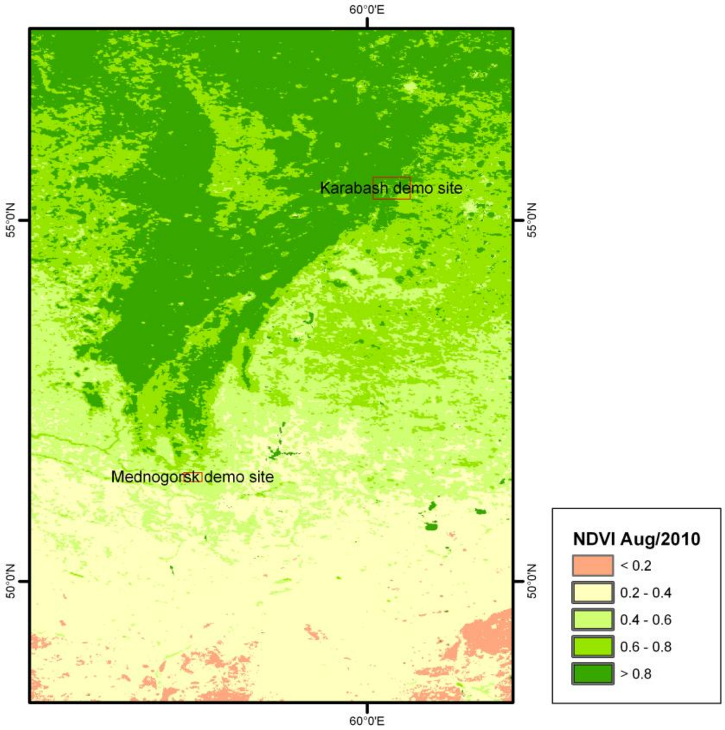

Fig. 6.11 Example of a monthly composite of NDVI images derived from SPOT-Vegetation (August 2010) of the wider surroundings of the Karabash and Mednogorsk demo sites.

Mean NDVI and fAPAR values ($\mu[NDVI_{i..}]$ and $\mu[fAPAR_{i..}]$) and coefficients of variation ($CV[NDVI_{i..}]$ and $CV[fAPAR_{i..}]$) were calculated from the monthly dataset (n=156) in order to have a quantitative index of the overall variation.

To remove seasonal vegetation changes and thus facilitate the interpretation through the historical record, a Standardized Difference Vegetation Index (SDVI) was calculated for each pixel and for each record of both the NDVI and fAPAR S30 series. The resulting Z_{NDVI} and Z_{fAPAR} are monthly z-scores representing the deviation from the mean in units of the standard deviation (Peters et al., 2002):

$$Z_X = Z_{X_{imy}} = (X_{imy} - \mu\lfloor X_{im.}\rfloor)/\sigma\lfloor X_{im.}\rfloor$$

where X_{imy} is the monthly maximum NDVI or fAPAR value for pixel *i* during month *m* for year *y*, $\mu[X_{im.}]$ is the mean NDVI or fAPAR value for pixel *i* during month *m* over the time series, and $\sigma[X_{im}]$ is the standard deviation of NDVI or fAPAR for pixel *i* during month *m* over the time series.

The monthly NDVI and fAPAR datasets were further synthesised to yearly datasets (S360) by averaging the monthly data over each calendar year (January - December): $NDVI_{iy}$ and $fAPAR_{iy}$, the yearly average NDVI resp. fAPAR value for pixel *i*, in year *y*. Coefficients of variation ($CV[NDVI_{i.}]$ and $CV[fAPAR_{i.}]$) were calculated from the yearly NDVI and fAPAR dataset (n=13) in order to have a quantitative index of the between-years variation.

In order to evaluate trends over time, a linear least squares trend analysis was applied on the entire monthly SDVI time series (Z_{NDVI} and Z_{fAPAR}, each with n=156), resulting in maps with Pearson correlation coefficients (*r*): $r[Z_{NDVI}]$, $r[Z_{fAPAR}]$. Finally, and in order to evaluate if the trend over time could be related to changes in the phenological status of vegetation cover, for the Karabash study area a linear least squares trend analysis was performed on the per month time series ($Z_{NDVI,m}$ and $Z_{fAPAR,m}$, where *m* is replaced by Jan, Feb, etc.). This trend analysis was performed on groups of pixels, defined by the distance to the Karabash smelter (< 10 km or 10 – 30 km) and by its land cover, as defined by the GlobCover land cover map (Arino et al., 2007). This resulted in an $r[Z_{NDVI,m}]$ and $r[Z_{fAPAR,m}]$, for each month *m*.

Table 6.1 gives an overview of the in total 32 indices derived from the time series analysis of SPOT-Vegetation derived NDVI and fAPAR. All operations were performed at pixel level.

Table 6.1 Indices derived from time series analysis of SPOT-Vegetation derived NDVI and fAPAR.

Abbreviation	Description
$\mu[NDVI_{i..}]$, $CV[NDVI_{i..}]$	Mean NDVI value and coefficient of variation from monthly dataset (n=156)
$CV[NDVI_{i.}]$	Coefficient of variation from yearly NDVI dataset (n=13)
$r[Z_{NDVI}]$	Pearson correlation coefficient of the linear trend of monthly Z_{NDVI} (n=156)
$r[Z_{NDVI,Jan}]$	Pearson correlation coefficient of the linear trend of Z_{NDVI} in January[a] (n=13 x number of pixels in mask)
$\mu[fAPAR_{i..}]$, $CV[fAPAR_{i.}]$	Mean fAPAR value and coefficient of variation from monthly dataset (n=156)
$CV[fAPAR_{i.}]$	Coefficient of variation from yearly fAPAR dataset (n=13)
$r[Z_{fAPAR}]$	Pearson correlation coefficient of the linear trend of monthly Z_{fAPAR} (n=156)
$r[Z_{fAPAR,Jan}]$	Pearson correlation coefficient of the linear trend of Z_{fAPAR} in January[a] (n=13 x number of pixels in mask)

[a] Idem for Feb, Mar, Apr, May, Jun, Jul, Aug, Sep, Oct, Nov, Dec

6.2.2 Correlation analysis

For the Karabash demo-site, the pixel-values of the 32 time series derived indices were extracted at the position of the 140 in situ vegetation spectra. Pearson's correlation coefficients (r) were calculated between all spectral vegetation indices, the distance to the smelter, the latitude and longitude, the altitude above sea level and the extracted NDVI and fAPAR time series indices, in order to determine associations between leaf reflectance derived indices and the results of time series analysis. This correlation analysis was performed on groups of indices, defined by the distance to the smelter (< 10 km or > 10 km). For the Mednogorsk demo-site, correlation analysis was performed on the distance to the smelter, and the NDVI and fAPAR time series indices for all pixels in the surroundings of the mine.

6.2.3 Time series profiles

Fig. 6.12 and Fig. 6.13 show the NDVI profiles derived from SPOT-Vegetation for individual pixels in the Karabash and Mednogorsk area, respectively. All profiles show a very clear seasonality, related to the vegetative season. The very low values in winter months are probably related to undetected snow cover, resulting in NDVI values less than zero. After the smoothing operation, these values are equal or close to 0.

Apparently, there are no large differences between the different years. However, clear differences can be seen between different land cover types, especially in the Karabash case. The 'sparse vegetation' class (red) shows in general a lower NDVI profile, with lower maxima and lower minima. Also the start of the season is later, and the end is earlier, than the 'open' or 'closed forest' classes. In Mednogorsk, both the NDVI maxima and minima are in general lower than in Karabash. The vegetative season is more pronounced, with a minimum vegetative cover during December till February.

Karabash

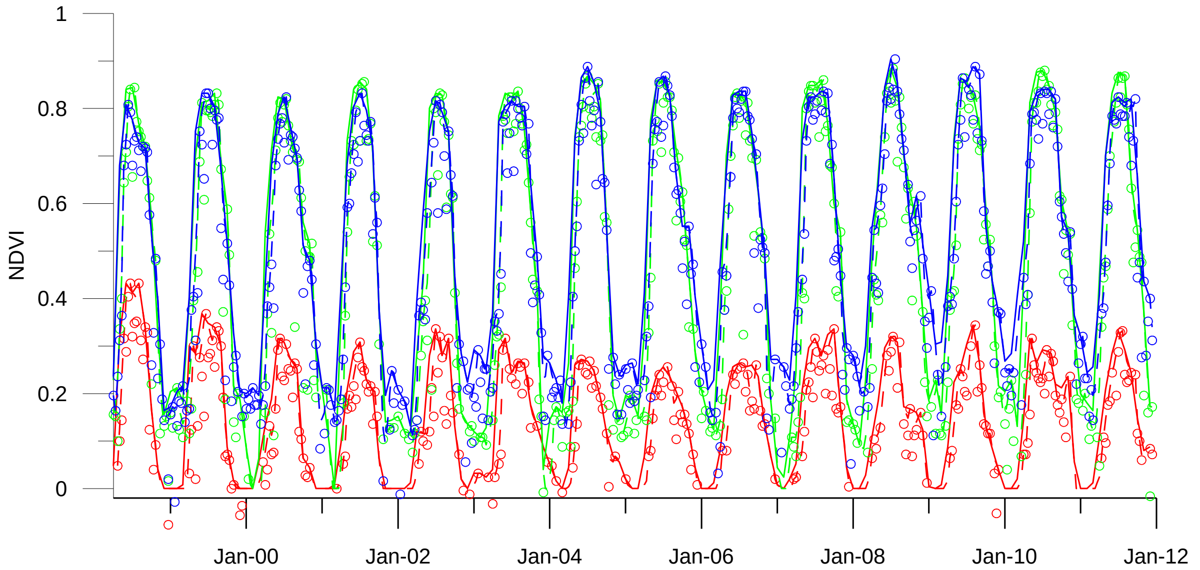

Fig. 6.12 NDVI profiles derived from SPOT-Vegetation for individual pixels in the Karabash area. Land cover type derived from the GlobCover dataset (Arino et al., 2007). Red: sparse (< 15%) vegetation; blue: open (15-40%) needleleaved deciduous or evergreen forest; green: closed (> 40%) broadleaved deciduous forest (> 5m). Circles: 10-daily observations. Dashed line: smoothed S10 profile. Solid line: monthly composites.

Mednogorsk

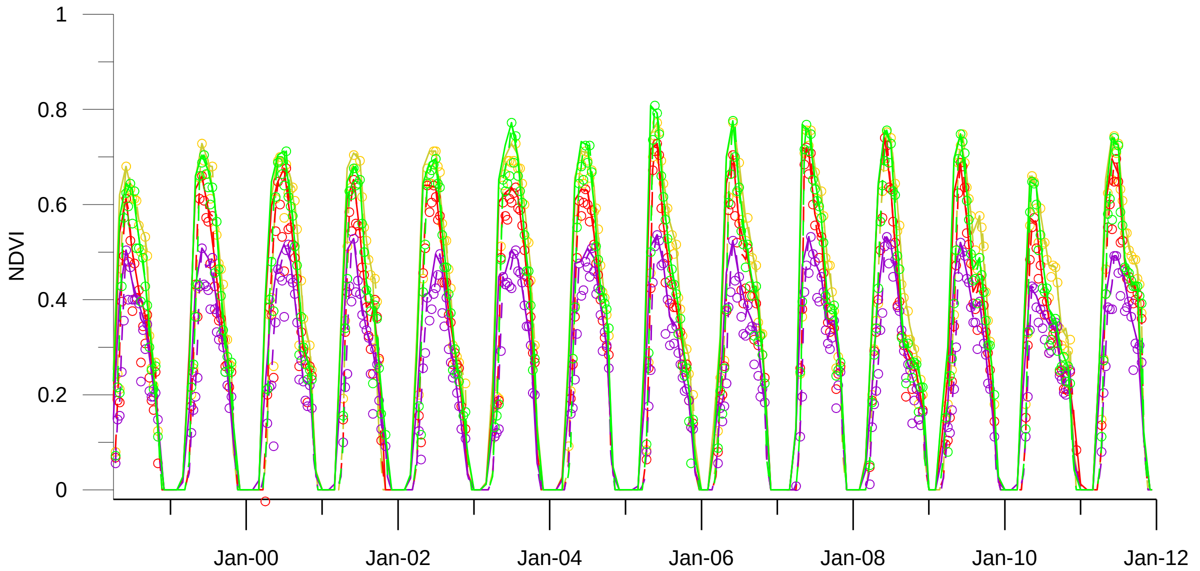

Fig. 6.13 NDVI profiles derived from SPOT-Vegetation for individual pixels in the Mednogorsk area. Land cover type derived from the GlobCover dataset (Arino et al., 2007). Red: sparse (< 15%) vegetation; purple: mosaic vegetation (50-70%)/cropland (20-50%); yellow: Mosaic cropland (50-70%)/vegetation (20-50%); green: closed (> 40%) broadleaved deciduous forest (> 5m). Circles: 10-daily observations. Dashed line: smoothed S10 profile. Solid line: monthly composites.

6.2.4 Long term averages

Fig. 6.14 and Fig. 6.15 show the long term average NDVI profiles derived from SPOT-Vegetation for individual pixels in the Karabash and Mednogorsk area, respectively, and some phenological indicators, such as the timing of largest increases, and the maximum and timing of largest decreases. The vegetation in Karabash shows a more smooth profile, with a much broader phenological cycle, compared to Mednogorsk.

Karabash

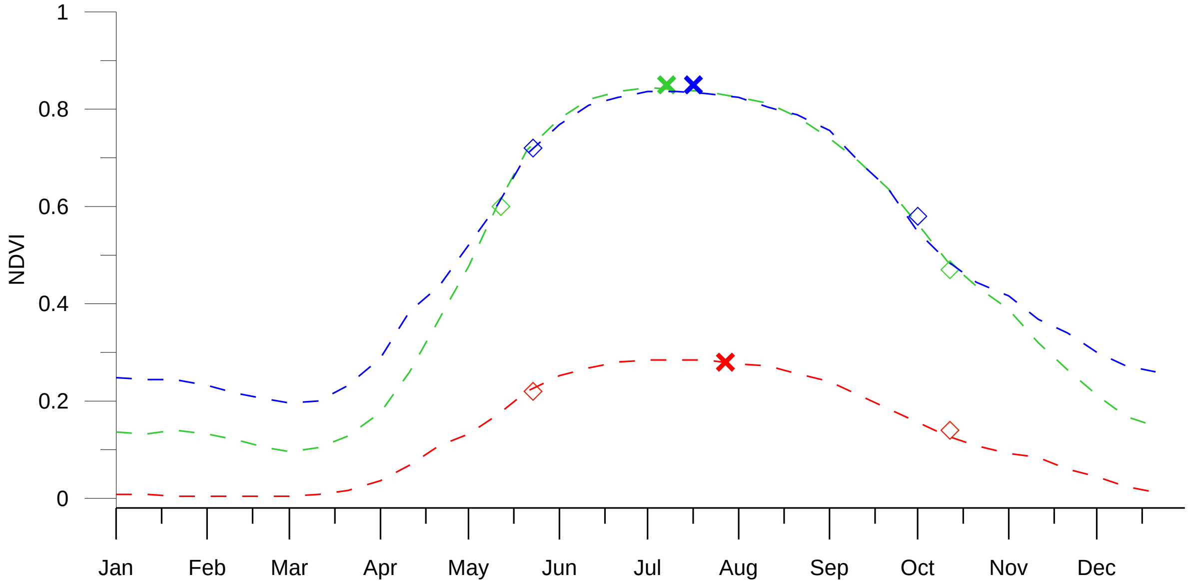

Fig. 6.14 Long term average NDVI profiles derived from SPOT-Vegetation for individual pixels in the Karabash area. Land cover type derived from the GlobCover dataset (Arino et al., 2007). Red: sparse (< 15%) vegetation; blue: open (15-40%) needle leaved deciduous or evergreen forest; green: closed (> 40%) broadleaved deciduous forest (> 5m). Dashed line: smoothed S10 profile. Symbols mark the timing of largest increase, maximum and largest decrease.

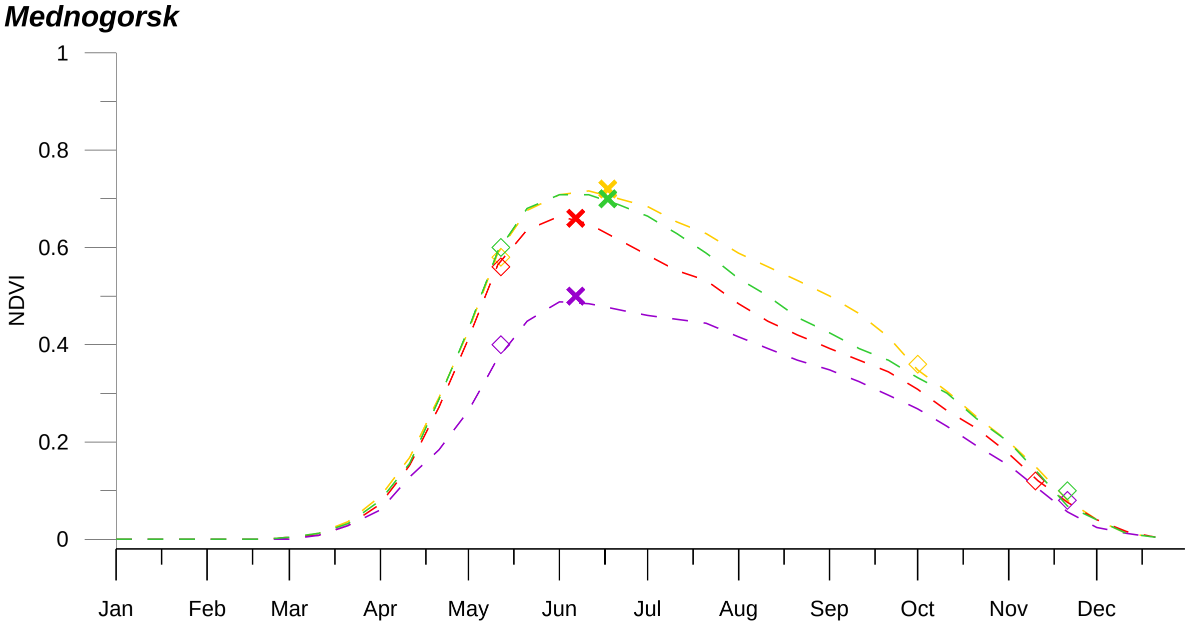

Fig. 6.15 Long term average NDVI profiles derived from SPOT-Vegetation for individual pixels in the Mednogorsk area. Land cover type derived from the GlobCover dataset (Arino et al., 2007). Red: sparse (< 15%) vegetation; purple: mosaic vegetation (50-70%)/cropland (20-50%); yellow: Mosaic cropland (50-70%)/vegetation (20-50%); green: closed (> 40%) broadleaved deciduous forest (> 5m). Dashed line: smoothed S10 long term average profile. Symbols mark the timing of largest increase, maximum and largest decrease.

6.2.5 Spatial heterogeneity

Fig. 6.16 shows the spatial heterogeneity of the timing of largest increase, maximum and largest decrease, based on S10s NDVI. Especially the timing of the maximum shows an interesting north-south gradient.

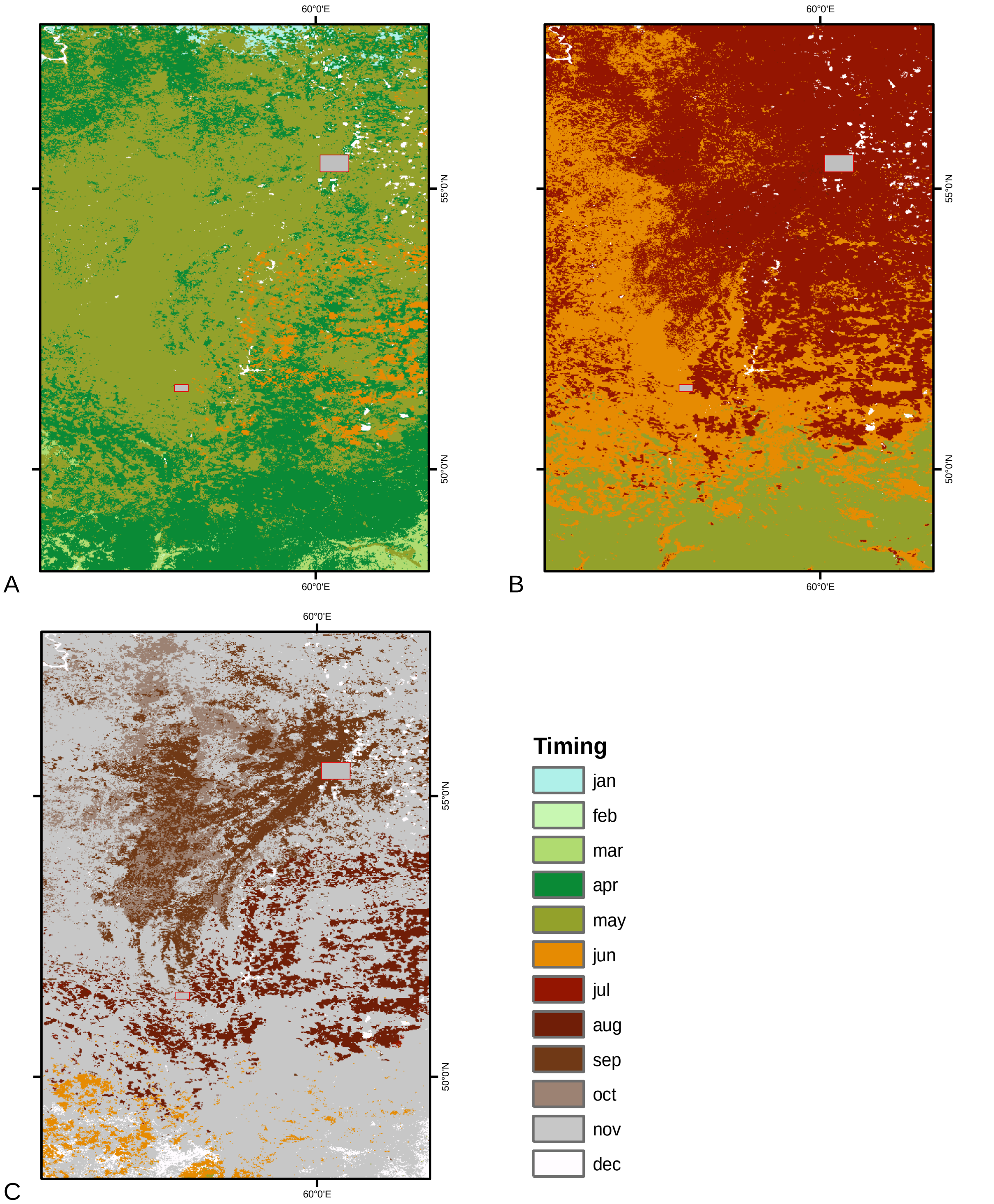

Fig. 6.16 Timing of A. largest increase, B. maximum, and C. largest decrease of the long term average S10s NDVI profile derived from SPOT-Vegetation

6.2.6 Trend analysis

In order to evaluate trends over time, a linear least squares trend analysis was applied on the entire monthly SDVI time series (Z_{NDVI} and Z_{fAPAR}, each with n=156), resulting in maps with Pearson correlation coefficients (*r*): $r[Z_{NDVI}]$ and $r[Z_{fAPAR}]$. Fig. 6.17 shows the $r^2[Z_{NDVI}]$ and the slope of the linear trend through Z_{NDVI} for the entire study area. It is clear that in the Mednogorsk area, slopes are not significant and close to zero. However, near Karabash, a general trend of increase in photosynthetic activity is observed.

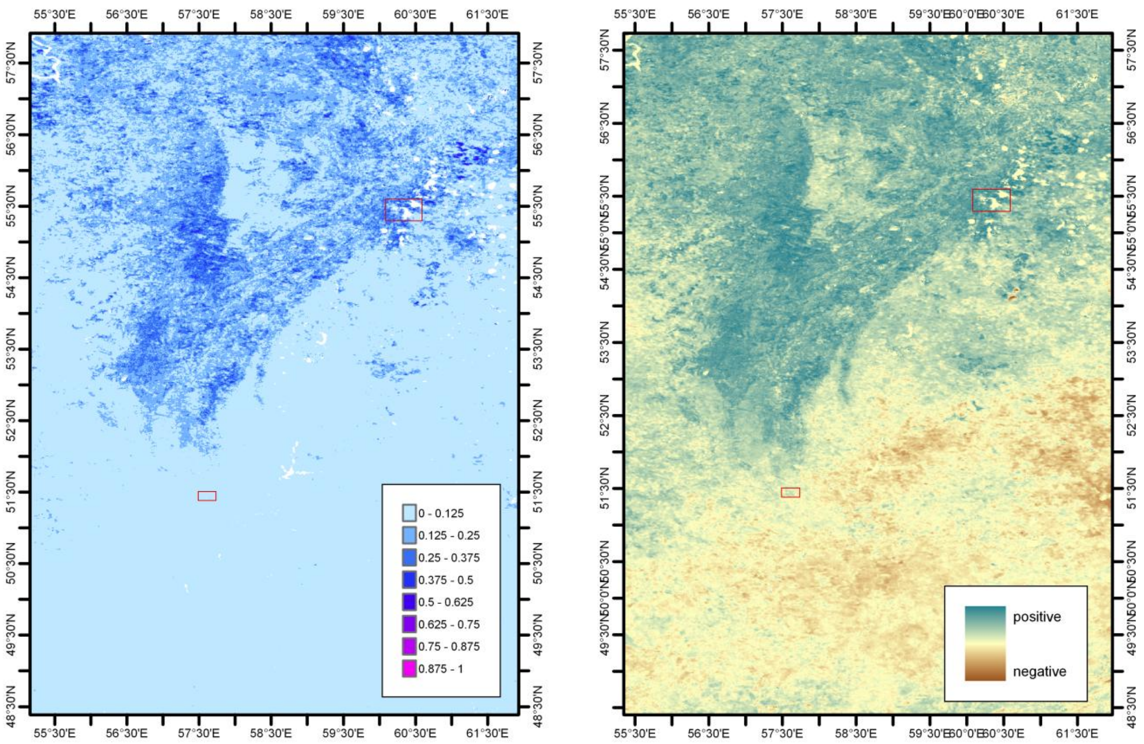

Fig. 6.17 R^2 (left) and slope (right) of linear trend through ZNDVI

Fig. 6.18 shows an overview of the procedure for three pixels with different land cover in close proximity of the Karabash smelter. Fig. 6.19 gives the trend analysis for Z_{NDVI} for three pixels close to Mednogorsk.

Karabash

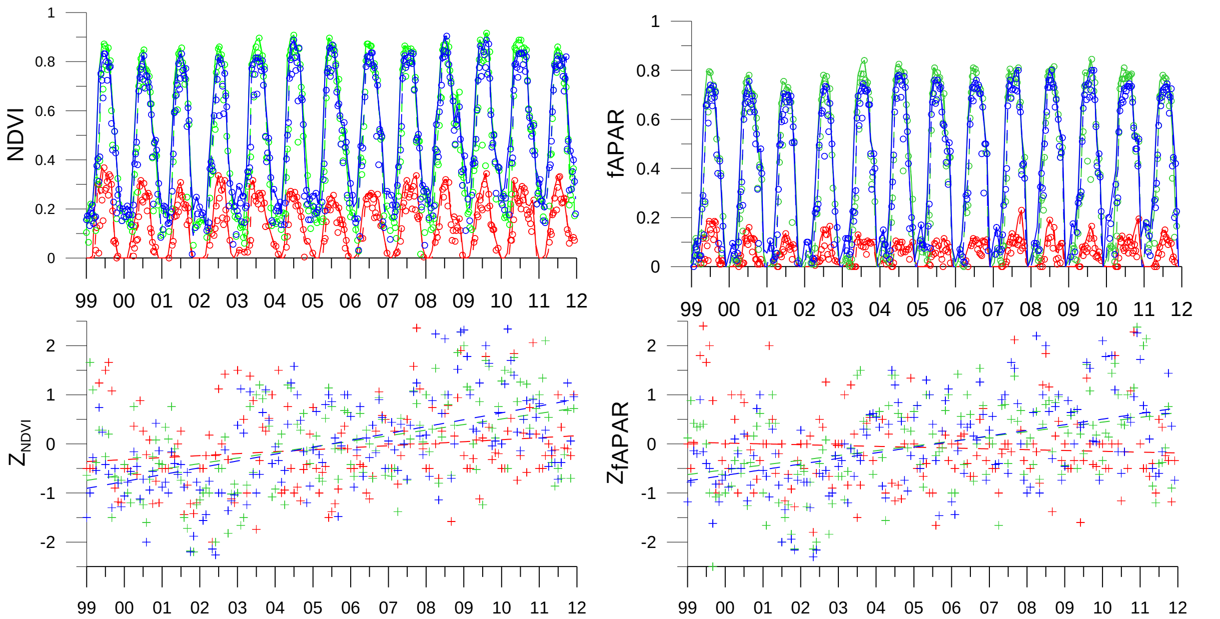

Fig. 6.18 Trend analysis based on Z profiles derived from S30 NDVI and fAPAR from SPOT-Vegetation for individual pixels in the Karabash area. Land cover type derived from the GlobCover dataset (Arino et al., 2007). Red: sparse (< 15%) vegetation; blue: open (15-40%) needleleaved deciduous or evergreen forest; green: closed (> 40%) broadleaved deciduous forest (> 5m). Crosses: 10-daily SDVI. Dashed line: linear trends.

Mednogorsk

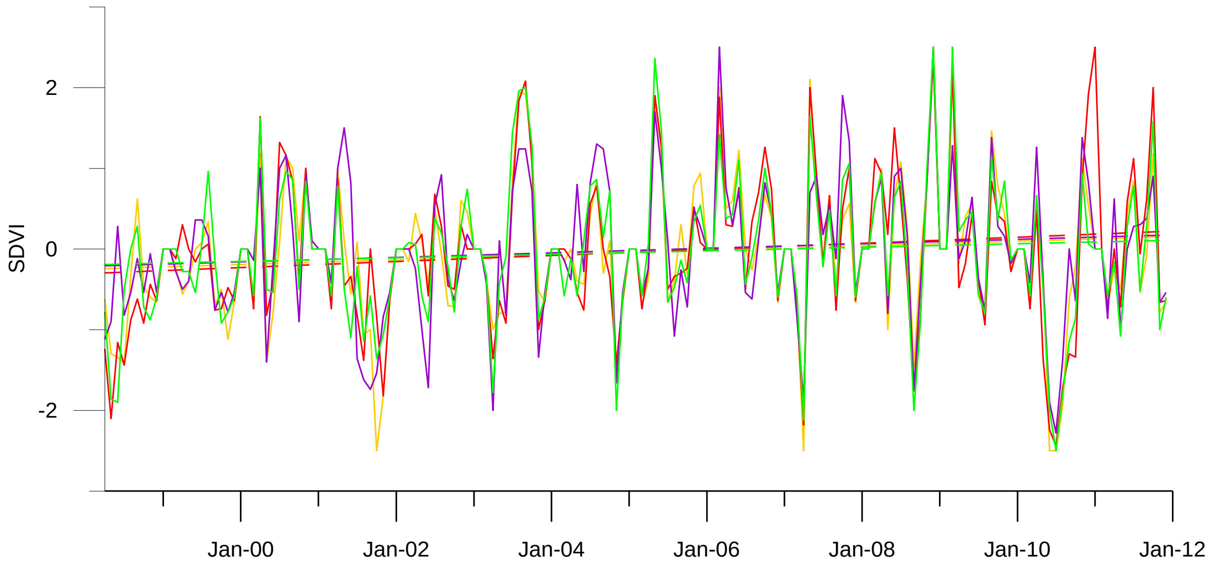

Fig. 6.19 Trend analysis based on ZNDVI profiles derived from S10s NDVI from SPOT-Vegetation for individual pixels in the Mednogorsk area. Land cover type derived from the GlobCover dataset (Arino et al., 2007). Red: sparse (< 15%) vegetation; purple: mosaic vegetation (50-70%)/cropland (20-50%); yellow: Mosaic cropland (50-70%)/vegetation (20-50%); green: closed (> 40%) broadleaved deciduous forest (> 5m). Solid line: 10-daily SDVI. Dashed line: linear trends.

6.2.7 Spatial heterogeneity and relation to vegetation stress

Karabash

Fig. 6.20 illustrates the relation between several SPOT-vegetation derived indices with the distance to the Karabash smelter. The values were extracted for all pixels classified as ‘sparse vegetation’, ‘open forest’ and ‘closed forest’, according to the GlobCover dataset (Arino et al., 2007), and a distinction is made between pixels in closer proximity of the smelter (< 10 km) and pixels located at further distances. $\mu[NDVI_{i..}]$ and $\mu[fAPAR_{i..}]$ show an increase with the distance to the smelter. This is partially related to the land cover, which is sparser in areas more close to Karabash. However, at larger distances, the distinction between ‘sparse vegetation’, ‘open’ and ‘closed forest’ is not clear. In contrast, the $CV[NDVI_{i..}]$ and $CV[fAPAR_{i..}]$ decrease with larger distances. Also the coefficient of variation is related to the land cover class: the sparser the vegetation, the higher the variation over time. However, at larger distances this difference is again less clear. Also $r[Z_{NDVI}]$ and $r[Z_{fAPAR}]$ show a clear relation with distance to the smelter (see also Fig. 6.21). In general, the Z_{NDVI} and Z_{fAPAR} series of pixels in the wider area (10 to 30 km) around Karabash show a positive trend over time, indicating an increase of photosynthetic activity over the last 12 years. Nevertheless, pixels in closer proximity (<10 km) to Karabash show a gradual decrease of the linear trend slope towards the smelter.

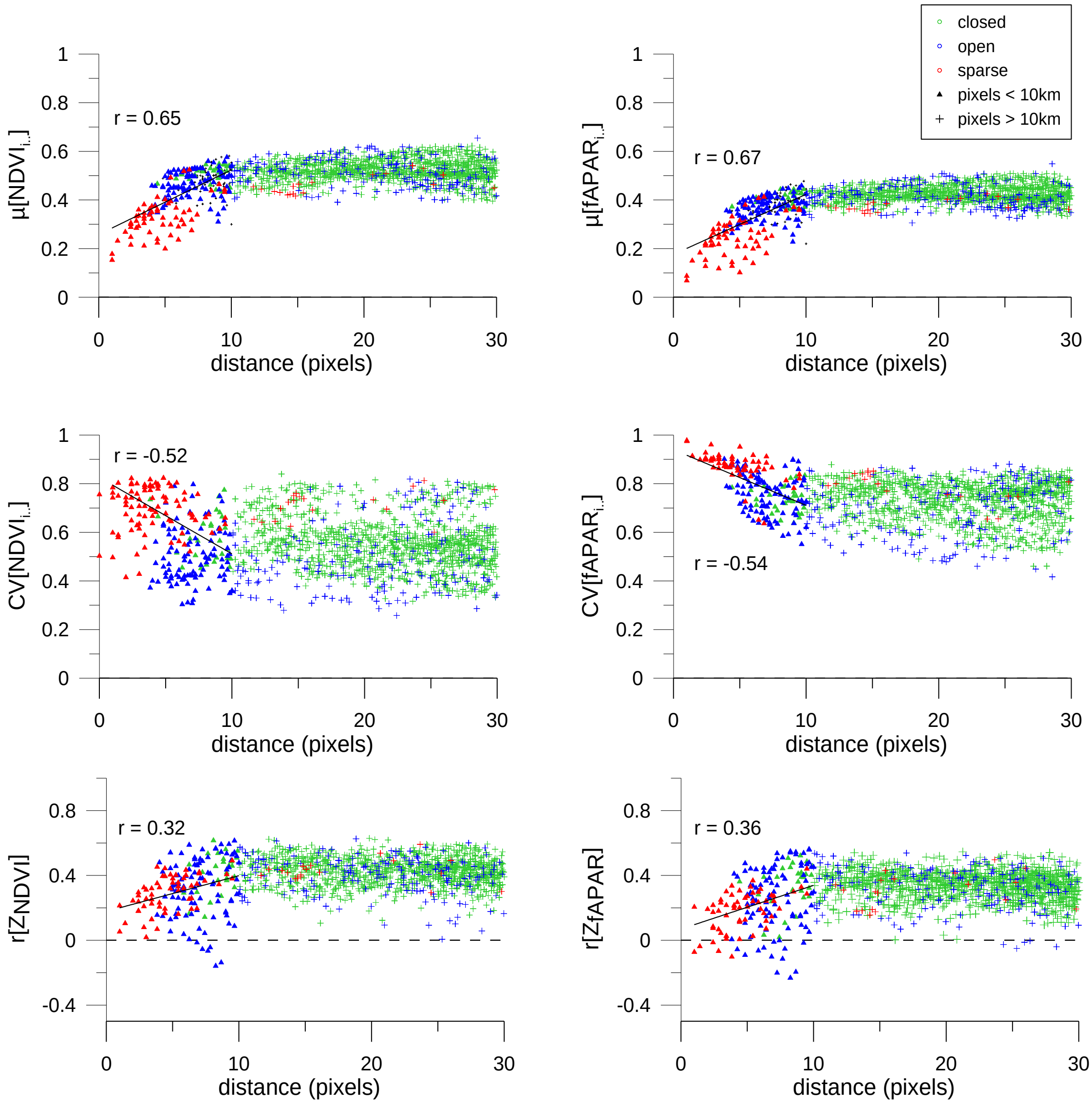

Fig. 6.20 Relation between SPOT-Vegetation derived indices and the distance to the Karabash smelter (in pixels). Pixels within a distance of 10 km (triangles) with correlation and Pearson correlation coefficients, and beyond 10 km (crosses). Land cover types derived from the GlobCover dataset (Arino et al., 2007), red: 'sparse vegetation', blue: 'open forest' and green: 'closed forest'.

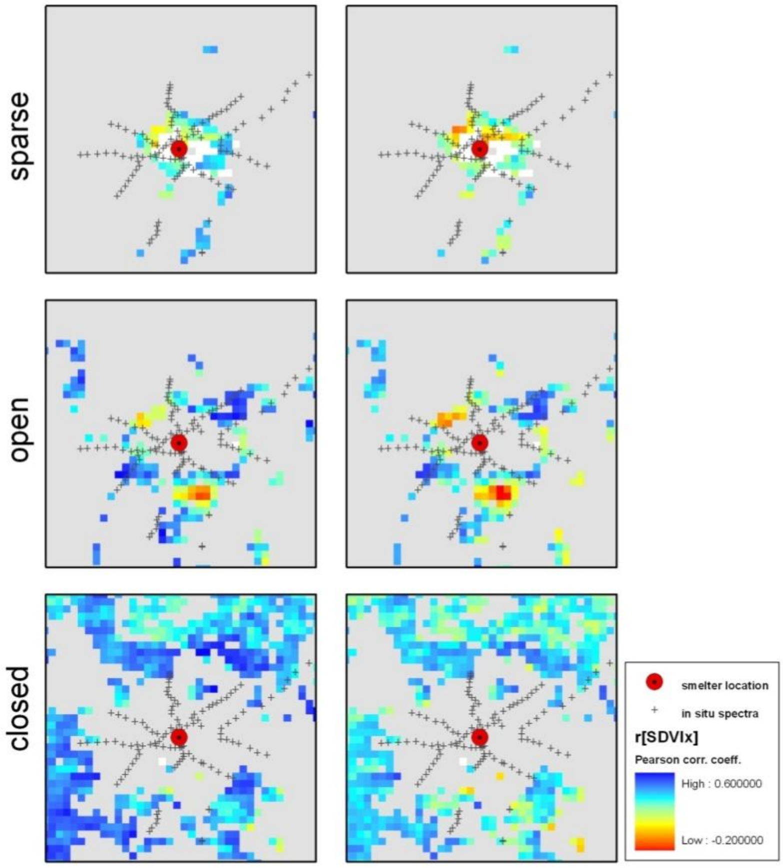

Fig. 6.21 Spatial distribution of r[ZNDVI] (left) and r[ZfAPAR] (right) around the Karabash smelter

The pixel-values of the 32 time series derived indices were extracted at the position of the 140 *in situ* vegetation spectra. Pearson's correlation coefficients (*r*) were calculated between all spectral vegetation indices, the distance to the smelter, the latitude and longitude, the altitude above sea level and the extracted NDVI and fAPAR time series indices, in order to determine associations between leaf reflectance derived indices and the results of time series analysis. This correlation analysis was performed on groups of indices, defined by the distance to the smelter (<10 km or >10 km).

Table 6.2 and Fig. 6.22 show the Pearson correlation coefficients of the correlation analysis between distance, all spectral indices derived from *in situ* birch samples and time series indices for all sampling points at a shorter or larger distance than 10 km, respectively. All spectral indices of *in situ* samples close to Karabash show a significant positive correlation with the distance to the smelter, indicating a decrease of vegetation stress with increasing distance, while this is not the case for any of the spectral indices for the sampling points at more than 10 km distance (Table 6.3). Almost none of the spectral indices show a significant correlation with the altitude, latitude or longitude, which indicates no relation between vegetation stress and height above sea level, or orientation towards the smelter.

For *in situ* samples close to Karabash, significant positive relations are found between the spectral indices and $\mu[NDVI_{i..}]$, $\mu[fAPAR_{i..}]$, $r[Z_{NDVI}]$ and $r[Z_{fAPAR}]$. Correlations are significantly negative for the both the overall coefficients of variation $CV[NDVI_{i..}]$ and $CV[fAPAR_{i..}]$, and the between-years coefficients of variation $CV[NDVI_{i.}]$ and $CV[fAPAR_{i.}]$. Fig. 6.22 illustrates the correlation between the spectral ratio index $RVI_{760\text{-}900}$ and the time series derived indices.

Table 6.2 Pearson correlation coefficients between distance, spectral indices and time series indices for in situ sampling points at less than 10km distance from the Karabash smelter.

Pearson[a]	Distance	$\mu[NDVI_{i..}]$	$CV[NDVI_{i..}]$	$CV[NDVI_{i.}]$	$r[Z_{NDVI}]$	$\mu[fAPAR_{i..}]$	$CV[fAPAR_{i..}]$	$CV[fAPAR_{i.}]$	$r[Z_{fAPAR}]$
Distance		**0.83**	**-0.72**	**-0.61**	**0.65**	**0.84**	**-0.71**	**0.28**	**0.65**
$RVI_{760\text{-}900}$	**0.53**	**0.57**	**-0.45**	**-0.52**	**0.29**	**0.58**	**-0.47**	-0.06	**0.26**
TVI	**0.50**	**0.42**	**-0.31**	**-0.37**	**0.26**	**0.42**	**-0.34**	-0.13	0.19
SAVI	**0.49**	**0.43**	**-0.30**	**-0.43**	**0.25**	**0.44**	**-0.33**	0.01	0.17
MSAVI	**0.49**	**0.43**	**-0.30**	**-0.42**	**0.24**	**0.43**	**-0.33**	0.02	0.17
OSAVI	**0.47**	**0.41**	**-0.29**	**-0.41**	**0.23**	**0.42**	**-0.32**	0.03	0.16
NGRDI	**0.42**	**0.30**	**-0.24**	**-0.27**	0.17	**0.30**	**-0.26**	-0.11	0.13
NDVI	**0.41**	**0.36**	**-0.26**	**-0.37**	0.19	**0.36**	**-0.28**	0.05	0.14
TCI	**0.34**	0.18	-0.17	-0.10	0.13	0.16	-0.18	**-0.23**	0.10
TGI	**0.33**	0.18	-0.17	-0.09	0.14	0.16	-0.19	**-0.26**	0.12
MCARI	**0.32**	0.15	-0.15	-0.08	0.12	0.14	-0.16	**-0.25**	0.10
TCARI	**0.32**	0.15	-0.15	-0.08	0.12	0.14	-0.16	**-0.25**	0.10

[a]Correlations in bold are significant with $p < 0.05$.

Table 6.3 Pearson correlation coefficients between distance, spectral indices and time series indices for in situ sampling points 10 to 33 km distance from the Karabash smelter.

Pearson[a]	Distance	$\mu[NDVI_{i..}]$	$CV[NDVI_{i..}]$	$CV[NDVI_{i.}]$	$r[Z_{NDVI}]$	$\mu[fAPAR_{i..}]$	$CV[fAPAR_{i..}]$	$CV[fAPAR_{i.}]$	$r[Z_{fAPAR}]$
Distance		**-0.37**	0.29	**0.39**	**-0.56**	**-0.40**	0.32	-0.21	**-0.68**
$RVI_{760\text{-}900}$	0.17	-0.15	0.13	0.48	-0.02	-0.13	0.07	0.09	-0.08
TVI	0.17	0.17	-0.16	0.29	0.03	0.19	-0.17	0.08	0.14
TGI	0.12	0.16	-0.16	0.20	0.08	0.15	-0.11	0.21	0.23
TCARI	0.09	0.16	-0.16	0.19	0.08	0.15	-0.11	0.22	0.23
MCARI	0.09	0.16	-0.16	0.19	0.08	0.15	-0.11	0.22	0.23
TCI	0.04	0.13	-0.13	0.14	0.05	0.12	-0.07	0.23	0.21
SAVI	0.01	0.01	0.00	0.01	-0.09	0.03	-0.06	-0.12	-0.08
MSAVI	-0.06	-0.06	0.06	-0.08	-0.11	-0.03	0.01	-0.13	-0.11
NGRDI	-0.09	0.03	-0.04	-0.09	-0.02	0.04	-0.02	0.13	0.13
OSAVI	-0.11	-0.08	0.08	-0.15	-0.13	-0.06	0.03	-0.13	-0.13
NDVI	-0.20	-0.15	0.15	-0.30	-0.15	-0.14	0.10	-0.13	-0.17

[a]Correlations in bold are significant with $p < 0.05$.

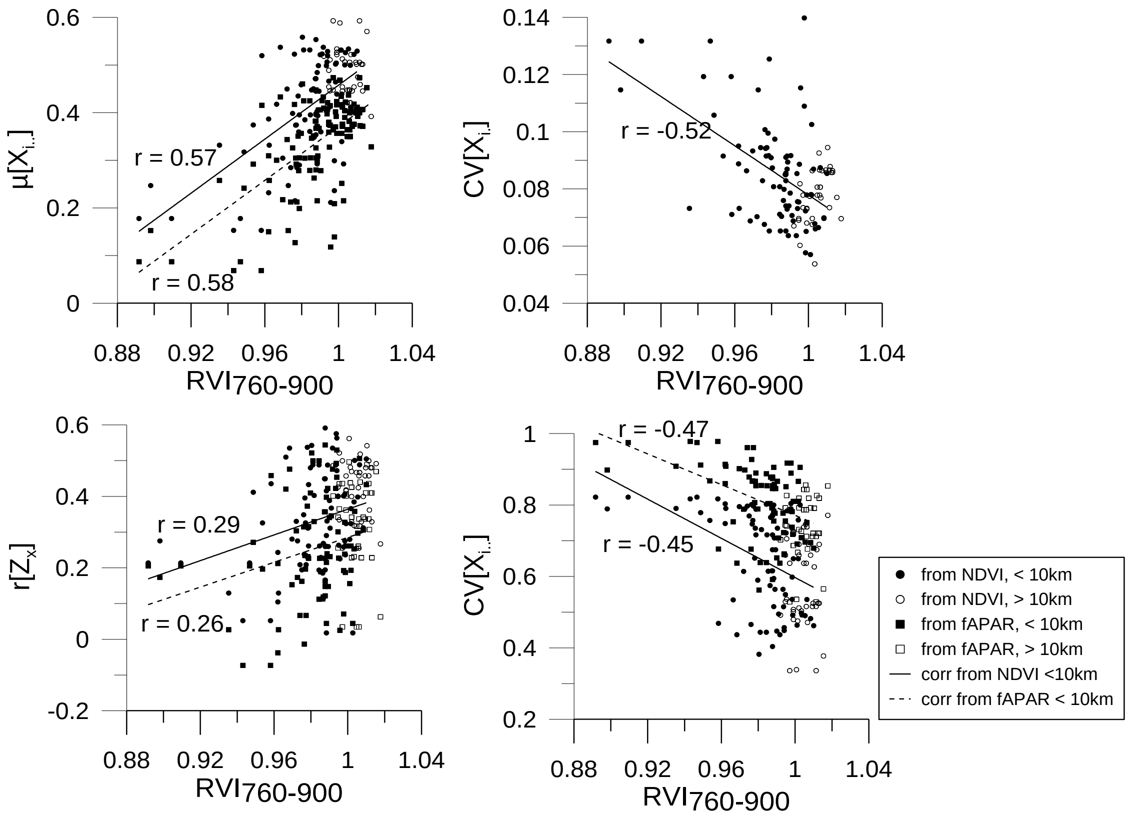

Fig. 6.22 Relation between $RVI_{760-900}$ and the time series indices derived from SPOT-Vegetation for both NDVI (squares) and fAPAR (circles). Sampling points within a distance of 10 km with correlation and Pearson correlation coefficients.

Mednogorsk

Fig. 6.23 and Fig. 6.24 illustrate the absence of any relation between the slope of the linear trend through the Z_{NDVI} series derived from SPOT-vegetation with the distance to Mednogorsk.

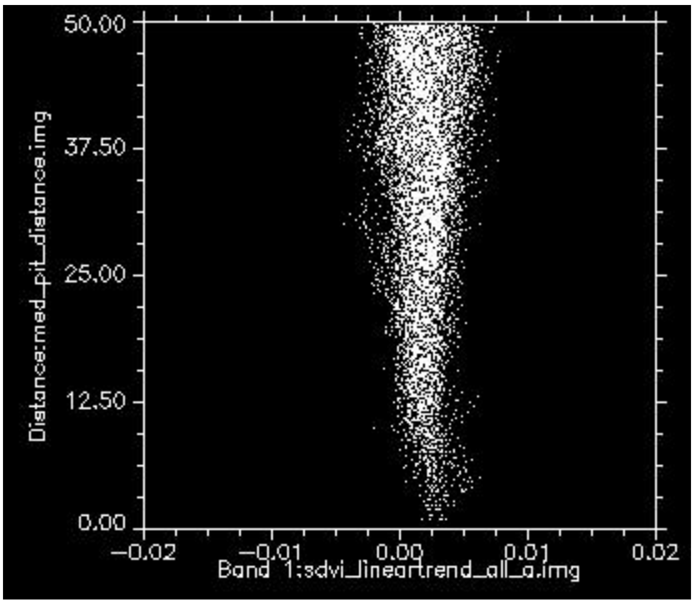

Fig. 6.23 Relation between the slope of the linear trend through ZNDVI derived from SPOT-Vegetation and the distance to Mednogorsk (in pixels).

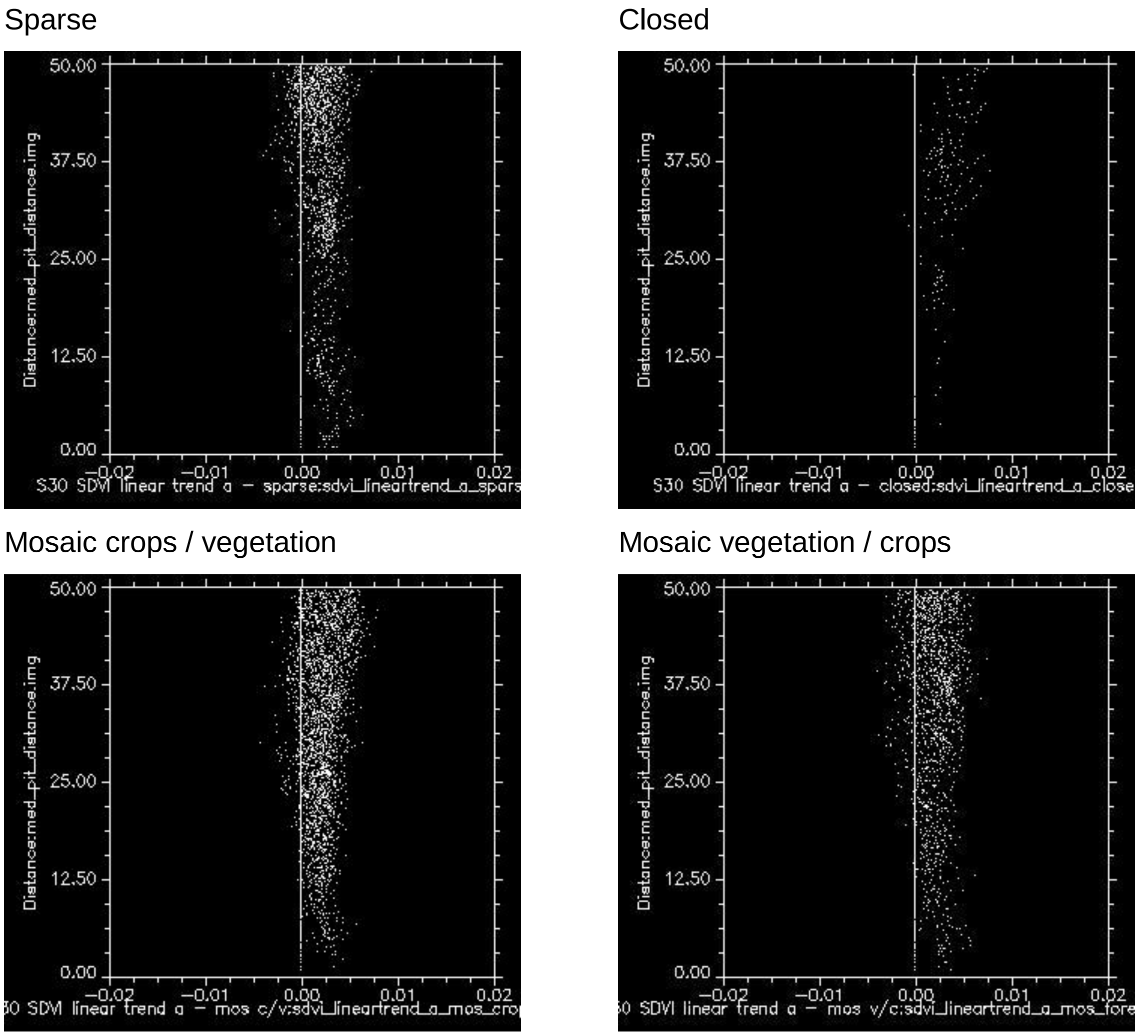

Fig. 6.24 Relation between the slope of the linear trend through ZNDVI derived from SPOT-Vegetation and the distance to Mednogorsk (in pixels) for different land cover types.

6.2.8 Changes in phenology

Karabash

Fig. 6.25 shows the results of the linear least squares trend analysis on $Z_{NDVI,m}$ and $Z_{fAPAR,m}$ over ‘sparse vegetation’, ‘open forest’ and ‘closed forest’ at distances < 10 km smaller and 10 to 30 km, respectively. In general, the *r[NDVI,m]* is higher in both the summer (June-August) and winter (December-January) months, compared to almost no change in spring (February-May). The three land cover classes show a similar pattern, with lower *r[NDVI,m]* values in February, April and May, and more significant trends from July-January. Nevertheless, the ‘sparse vegetation’ shows the largest differences between pixels <10 km and >10 km distance: although the sparse vegetation close to Karabash also shows a positive trend, especially in July-December, the trend is less pronounced. Also the ‘open forest’ class shows more significant trends over time in February-June.

The *r[fAPAR,m]* shows similar results, both in the similarities between land cover classes and the differences related to the distance to the smelter, and the general pattern, except for the winter period (December-February), where very low and even some negative *r[fAPAR,m]* appear, and more pronounced positive trends in early spring (March) and autumn (October).

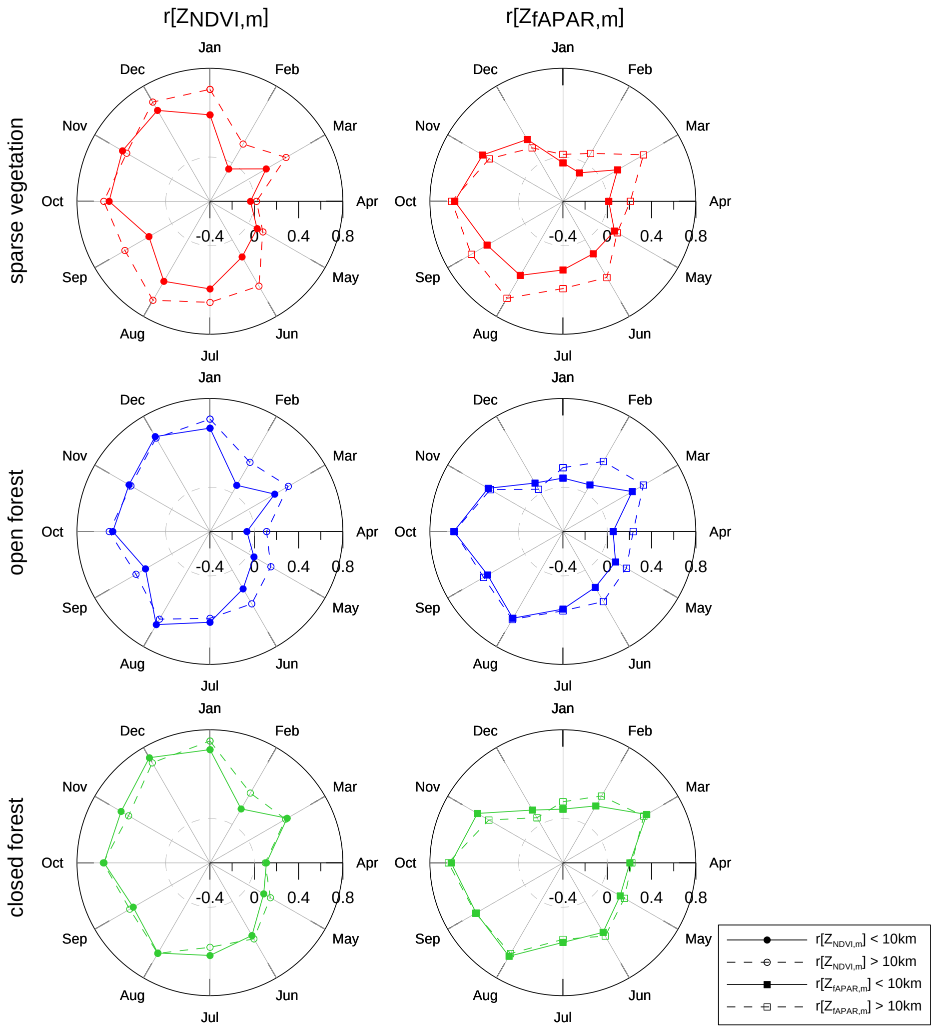

Fig. 6.25 *r[NDVI,m]* and *r[fAPAR,m]* for each month, for groups of pixels with different land cover types and located at distances < 10 km and 10-30 km from the Karabash smelter. Land cover types derived from the GlobCover dataset (Arino et al., 2007), red: sparse vegetation, blue: open forest and green: closed forest.

7 DISCUSSION – IMPACT ASSESSMENT AT THE DEMO SITES

Impacts on the environment in areas around both Karabash and Mednogorsk are dominantly related to smelter emissions. For this reason, the following discussion will focus on the assessment of impacts from these sources. Other impacts, largely from acid mine drainage emanating from waste dumps and abandoned mines, are generally relatively localized, or specific to channelized systems, and can be efficiently assessed using in situ measurements, as demonstrated in the EU FP5 MinUrals project.

The methods for assessing impacts from smelter emissions were relatively low cost compared with simultaneous instrumental monitoring over large areas. The methods employed, mainly lichen monitoring, the collection and analysis of environmental media such as tree bark, and remote sensing are all discrete which is important given the politically and socially sensitive nature of monitoring in the region where the smelter is the major employer.

7.1 Atmospheric dispersion of SO_2 and acid aerosols around Karabash

The Karabash smelter is known to be emitting high levels of SO_2 and metal-rich particulate (Williamson et al., 2004b). SO_2 levels in the atmosphere can be measured using ground based instrumental methods such as LIDAR, however these would have been of little practicable use and expensive where sampling needed to be carried out over long time periods (months), and simultaneously over large areas, up to 40 km from the smelter. The effects of SO_2 in the environment were therefore assessed from studying lichen frequency and birch bark and twig pH along the lichen transects.

Lichens are excellent biomonitors of the effects of a wide range of pollutants responding at the cellular, thallus and community levels (Nimis et al., 2002). Links between lichen abundance and human activities were made in 1797 at the Mynydd Parys Cu-Pb-Zn mines in Wales which dominated Cu production in the early industrial revolution (Purvis, 2010). However, it was not until forests and other vegetation began to die out in the vicinity of smelters in Central Europe and Britain in the late 1800s that SO_2 was identified as being a major factor (Bell and Treshow, 2002). In the 1960's and 70's studies carried out by Gilbert and others established links between atmospheric SO_2 concentrations and S contents of lichens (Gilbert, 1969, 1970, Hawksworth, 1973). Gilbert and other pioneers established that shrubby beard-like lichens were most sensitive to SO_2 and crustose lichens least sensitive. Recovery in lichen diversity has been recorded in many areas following pollutant reductions, including near major point sources of pollution.

From the lichen frequency data on birch trunks and twigs from the NE-SW and W-E transects in Fig. 5.5, a virtual lichen ‘desert’ exists within a few km of the smelter. This area contrasts markedly with the reference site 'UO' (39 km from the smelter) where 18 (9 crustose, 6 foliose and 3 fruticose lichens) were identified. Lichens on twigs, only present at site 3 (27 km SW of Karabash), are particularly sensitive indicators of atmospheric chemistry (Wolseley, 2002).

Bark pH values were found to be acidic throughout the study area ranging from 3.6-5.5, a value of pH 3-5 generally being considered typical for birch. Although trunk bark pH was generally higher than twig pH (Fig. 5.6), these data are not comparable in view of the very different nature of these natural records. Never-the-less, spatial relationships (Fig. 5.6) and the highly correlated trunk bark and twig pH values across NE-SW (8 sites) and W - E (7 sites) transects clearly reflect atmospheric deposition.

One of the most surprising results from the ground-based studies is the increase in bark and twig pH towards the smelter (in the SW, W and E transects), within a 15 to 25 km zone, varying by transect (Fig. 5.1). Given that the smelter is a point source of acid aerosols, we had expected the opposite trend. One possible explanation could be that, in addition to SO_2 and metal-rich particles, the smelter emits relatively alkaline particulates which are large and therefore deposit from the plume relatively close to the smelter. Such particles could include limestone or lime (CaO), or its hydrated equivalent (calcium hydroxide $CaOH_2$). Limestone and lime are often used as a flux in smelter operations, which is assumed to be the case for the Karabash smelter (although no data is available). In order to investigate this possibility the pH of smelter stack dusts was determined by IMIN. Blast furnace dust, from the Ausmelt process, had a pH of 4.70, roughly mid range in the composition of the bark and twigs, and cannot therefore account for the relatively high pH nearer the smelter. However, converter dust, although not containing lime or limestone (Williamson et al., 2004b), had a pH of 6.08, more than adequate to increase the pH of bark and twigs near the smelter. However, this is unlikely to be the explanation because from source apportionment studies of metals in lichens from the NE-SW transect (Williamson et al., 2008), particles from the converter were shown to be deposited at relatively greater distances compared with those from the blast furnace. This was due to their small particle size, being gas condensates rather than the physically larger splash droplets from the blast furnace.

A second hypothesis being tested is that the conversion of SO_2 to acid aerosols involves a lag time, due to kinetic factors, and therefore a 'shadow' of relatively less acid deposition exists closer to the smelter (see Fig. 7.3). The increase in pH at distances >15 to 25 km could be due to the majority of the SO_2 having been converted to acid aerosols, and/or to dilution with increasing distance from the point source. Evidence to support this is that bark pH (see NE compared with SW, W and E trends on Fig. 5.1) and leaf damage from acid aerosols is patchy, depending on climatic factors and topography. Where inversions occur, local residents have reported thick clouds of smoke from the smelter hanging over their gardens for many hours at a time which severely damages, or in some cases completely devastates, their vegetable crops.

Such effects can also be observed on a much wider scale, to a distance of at least 5 km from the smelter, where irregular patches of forest are damaged. This is demonstrated in Fig. 7.1, where we compare a GeoEye image from July 27, 2010 with WV-2 image from September 1st, 2011 and from September15th, 2011.

Fig. 7.1 Left: GeoEye image of July 27th 2010, showing green birch-tree forest. Center: WV-2 image from September 1st, 2011. Quality of this image is poor because of haze, but the browning-effect is very clear. Right: WV-2 image of September 15th, 2011 showing the same area where leaves are brown.

Most of the forest in this area consists of birch trees. In 2010, these trees looked relatively green, whereas in 2011, the trees have turned almost completely brown in a large area. Although it could be argued that this might be related to an early onset of autumn, this is not likely because during our visit in July 2011, the leaves in this area were already brown (see Fig. 7.2).

One likely mechanism to cause this leaf browning is that sulphate particles are deposited on leaves (Fig. 7.2a) and with some rain these sulphates react with water to form sulphuric acid which begins to destroy the chlorophyll in the leaves (Fig. 7.2b).

Fig. 7.2 a: leaves with sulphate particles on their surfaces; b: leaves with acid damage after formation of sulphuric acid from the reaction of rain with the sulphate particles.

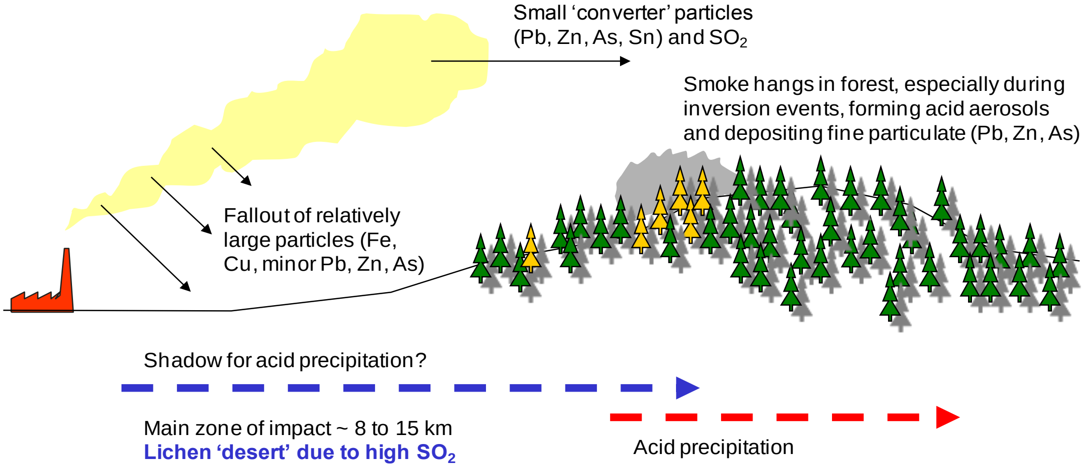

Fig. 7.3 Schematic diagram showing hypothesized processes leading to the yellowing of portions of the forest due to blanketing with smelter smoke which can occur in a single area for many hours per day. This blanketing allows the formation of acid aerosols and subsequent deposition on leaf surfaces. The diagram also shows proximal deposition of relatively large Fe, Cu-rich blast furnace (now Ausmelt process) particles and distal Pb- and Zn-rich converter particles. The innermost zone up to ca 5 km from the smelter is a virtual *Hypogymnia* lichen desert due to high pollution levels.

7.2 Fallout of metal-rich particulate around Karabash

Data for *Hypogymnia* frequency (Fig. 5.5), pH of tree bark and twigs (Fig. 5.6), metals in lichens, twig bark and soils (Fig. 5.7) all show curvo-linear (in many cases "power law") trends away from the smelter indicative of emissions from a point source (Purvis et al., 2004; Spiro et al., 2004). In the lichen transplants, over the 3 month exposure period in 2011, Pb (Fig. 5.8), showed more than a 12x increase in concentration near the smelter compared with those from the 'reference' site U0. From source apportionment studies for the metals in the lichen transplants from the 2001 field campaign (as part of the EU FP5 MinUrals project, Williamson et al., 2008), the smelter blast furnace was the dominant source at distances <10 to 15 km and the converter at >15 km.

Spatial relationships for bark and *Hypogymnia* (naturally occurring and transplants) confirm a smelter influence for the elements S, Zn, Pb, Cu, Sn, As, Cd and Sb across the entire monitoring area.

7.3 Temporal pattern of contamination from the Karabash smelter

An important aspect of being able to map the effects of environmental impact is to monitor these processes over longer periods. In the Karabash case, the pollution has been taking place for over a century, and will continue to take place as long as the smelter exists, unless significant improvements are implemented.

A major plan for improvement of the situation was initiated in 2006 by the modernisation of the smelter.

"Karabash now has a hi-tech and environmentally safe metallurgical plant which, apart from the Ausmelt furnace, also includes a modern waste treatment, sulphuric acid and effluent treatment plants. The Karabash plant is now one of the most modern plants of its type in Russia and the complex is among the most up-to-date and environmentally safe copper smelters globally. The Ausmelt-Karabash smelter has won two significant government awards: in 2005 the Ministry of Natural Resources of the Russian Federation awarded ZAO Karabashmed the honorary title of "Leader of Environment Protection Activity in Russia", and in 2006 the plant General Director and the Chief Engineer were awarded "the Ecological Shield of Russia" for the achievements in environment preservation. http://www.sulphuric-acid.com/sulphuric-acid-on-the-web/acid%20plants/ZAO%20Karabashmed%20-%20Karabash.htm

It is five years since these improvements were made and it should therefore be possible to see significant improvements to the environment. From ground-based studies it is difficult to make direct, quantitative, comparisons between the state of the environment in 2001 (MinUrals project, pre installation of the Ausmelt smelter) and 2011. However, from visits to various field sites in and around Karabash, the general feeling was that the area had not improved. During field studies in July 2011, the smelter was still emitting large plumes of dark smoke. Airborne particulate collected downwind of the smelter largely consisted of Pb, Zn and As (see Section 5). However, the most evocative ground evidence for the relative state of the environment is from the lichen sampling. Lichens found growing naturally on birch trees, generally at distances >15 km from the smelter, were sampled in the same way in 2001 as in 2011 and their contents of metals should therefore be directly comparable. From Fig. 7.15, the Pb contents of the lichens collected in 2011 are consistently (in all collection periods) higher than those for 2001. The repeated sampling is likely to negate the possibility that this trend is due to seasonal effects. For Cu, the datasets are more similar (Fig. 7.15). This is likely to be because the Ausmelt process largely replaced the blast furnace process in the smelter, which was known to be the main source of Cu-rich particulate rather than the converter which emits most Pb (Williamson et al., 2004b). Why the levels of Pb in the lichens are higher in 2011 than 2001 is not clear, possibly relating to an increase in smelter production or to a change in the nature of the feedstock (no information was available from the smelter company).

These results, relating to relative levels of Pb in the environment, are particularly worrying and potentially sensitive and therefore, before publication, will be revalidated. This is because, despite secondary standards (including the same lichen reference material BCR 482) having been analysed alongside the samples in both 2001 and 2011, always giving accuracies within 10%, the samples were prepared and analysed in different laboratories (2001 Natural History Museum, London, and 2011 in IMIN, Russia (and also UNEXE using slightly different methods)). To be entirely comparative the samples from 2001 and 2011 will be prepared in the same laboratory in 2013.

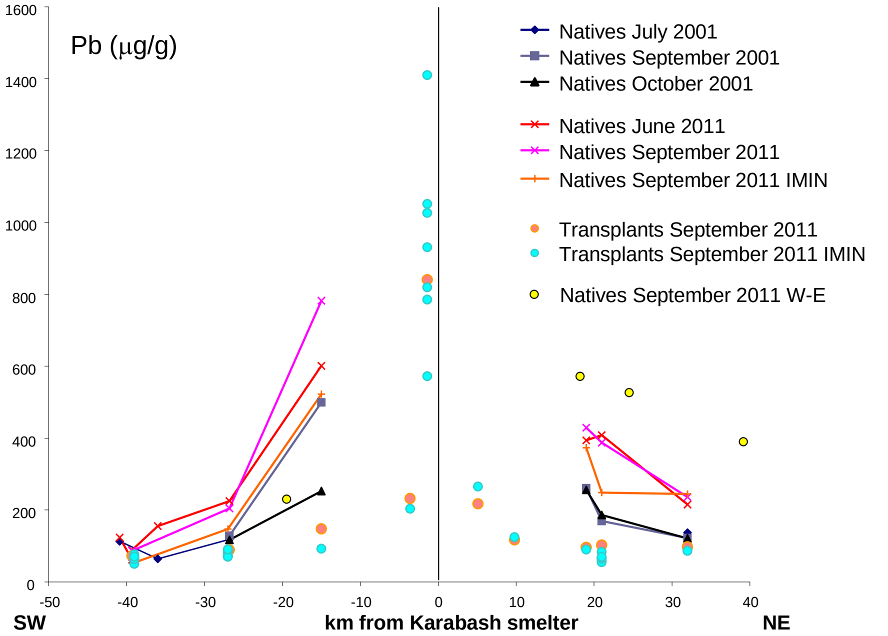

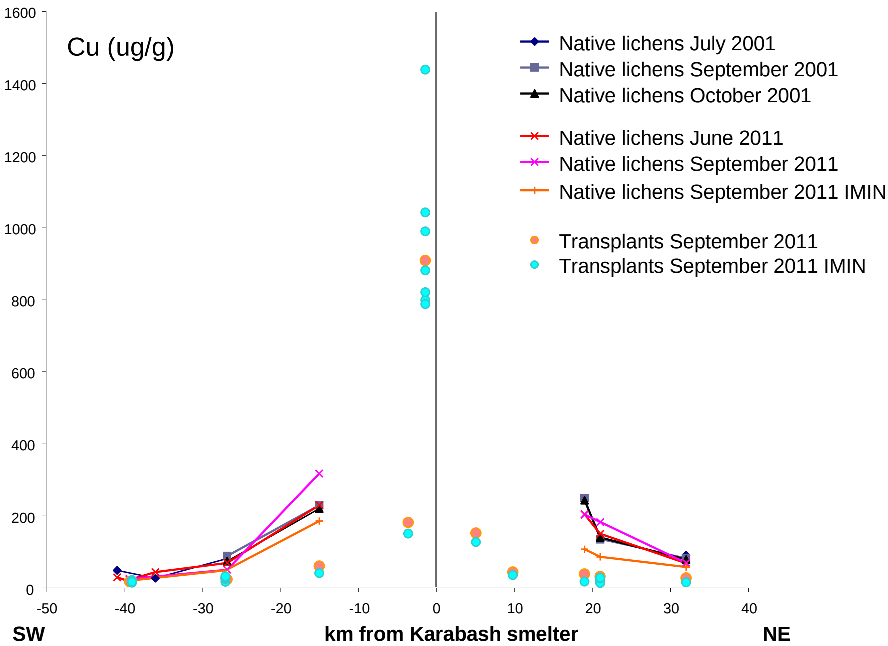

Fig. 7.4 Comparison of Pb and Cu concentrations in native lichens from around Karabash collected in 2001 (analysed at the Natural History Museum, London) and 2011 (analysed at UNEXE and IMIN).

7.4 Short-term changes from remote sensing studies

Earlier in this report we documented local changes in vegetation health that may be attributed to pulses of locally high levels of acid aerosols. We argued that these pulses can cause rapid destruction of leaf-chlorophyll, and the resulting vegetation changes seem to manifest themselves in irregular patterns of vegetation damage across the area, which can probably be related to wind-direction at the time of the emissions and topographic effects. On the basis of a visual comparison between the 2011 and 2010 imagery we demonstrated that this was clearly the case in the 2011 image, and it would be of interest to investigate the vegetation changes during the summer of 2011.

Comparison of the NDVI of the Landsat image of August 5th, 2011 image with the NDVI of the September 15th WV2-image is best done by subtracting one from the other. The result of this is shown in Fig. 7.5 where a number of areas stand out because the NDVI has dropped to a value > 0.2 within one month. Such a drop implies a significant deterioration of the amount of active biomass in the vegetation. For most of the southern area we observe a fairly uniform decrease of the NDVI between 0 and 0.1. This could be related to colouring of leaves as a result of the onset of autumn.

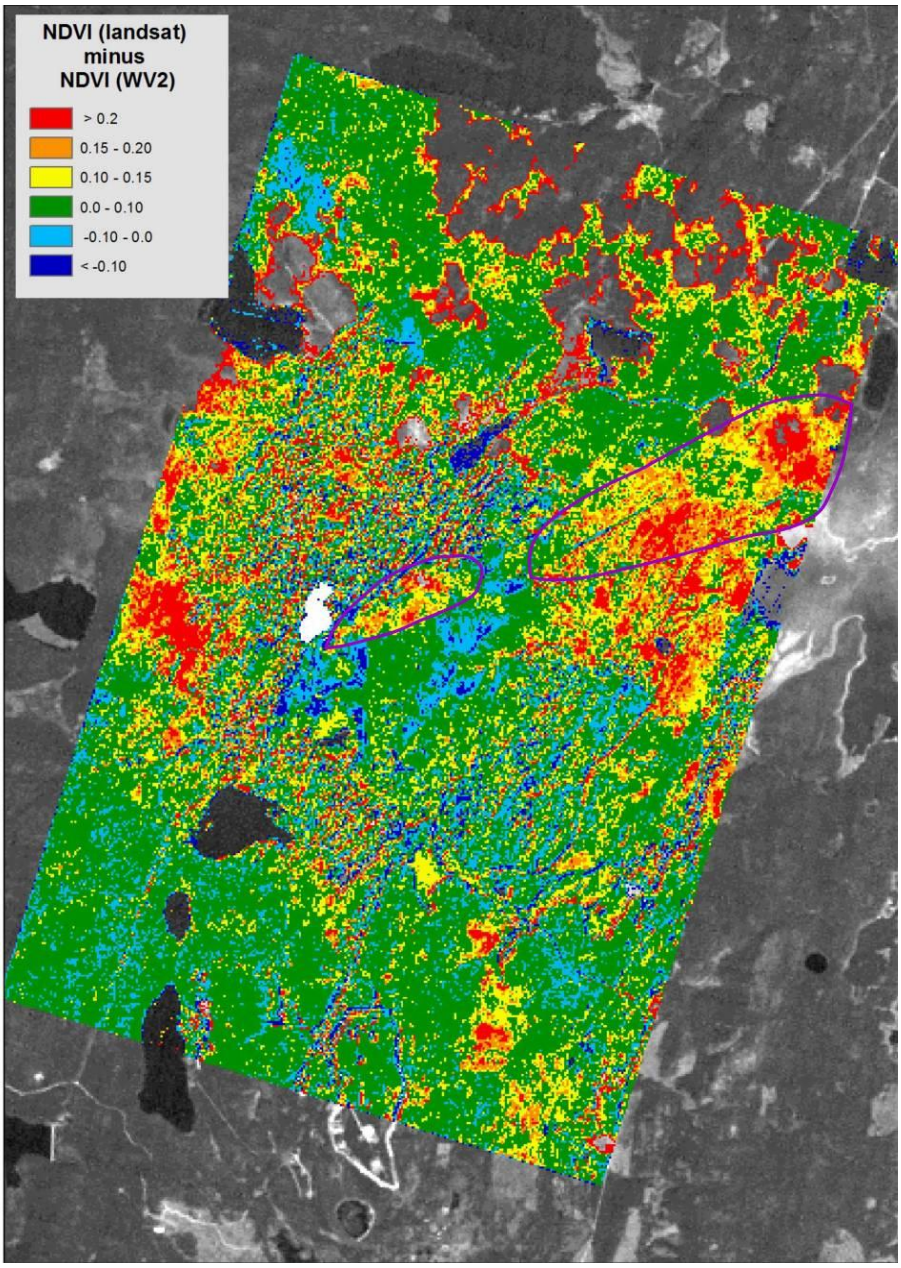

Fig. 7.5 Difference between NDVI images (August-September), obtained by subtracting the September WV2-NDVI from the August Landsat NDVI. The purple lines mark the outlines of the smoke plume from the smelter, present in the WV2-image.

7.5 Long-term changes from remote sensing

The fact that the NDVI can change so strongly in such a short period indicates that the timing of image acquisition is a very important parameter when investigating the changes over periods of years or decades. Clearly, it would be desirable to have good imagery at regular intervals during the period May to September. Unfortunately we do not have that luxury in this study. As indicated before, the availability of imagery for this area is very limited. For most years, there are only a few Landsat images available for the summer-season, and about 90% of these cannot be used because of heavy cloud cover. In addition, the post May 2003 Landsat 7 imagery cannot be used because of Scan-Line Corrector failure (http://landsat.usgs.gov/using_Landsat_7_data.php). Nevertheless, we were at least able to find a number of fairly good quality Landsat images (Fig. 7.5) that allowed us to investigate the changes prior to the closure of the smelter (May 20th, 1987; July 28th, 1989), a few years after the closure (September 12th, 1994), and after the re-opening of the smelter (June 19th, 2001 and August 10th, 2011).

In order to be able to map changes by comparing Landsat imagery it is essential that the images are well calibrated. This is a difficult task, as we have used two generations of Landsat imagery (L5 and L7), atmospheric conditions are far from ideal, and we noticed quality issues in some of the scenes that are probably related to degradation of the sensors. After much experimenting we found that the best solution for the calibration was to use the calibrated WV2 as the baseline for our Landsat calibration. Since the WV2 image was calibrated using a number of ground control spectra, which gave sufficiently accurate results (see Fig. 6.3), we concluded that the appropriate approach was to match the Landsat images with the WV2 image by retrieving gain- and offset coefficients from the scattergrams (see Fig. 6.8). There were two ways to do this: 1) to correlate each Landsat image with the WV2 image; 2) match the 2011 Landsat image to the 2011 WV2 image, the 2001 Landsat image to the corrected 2011 Landsat image, the 1994 Landsat image to the corrected 2001 Landsat image etcetera. We decided that the second approach was more suitable, as major changes probably will have occurred in the area over time, which would have made it hard to correlate the 2001 WV2 image with e.g. the 1987 Landsat image, which will potentially introduce many additional uncertainties.

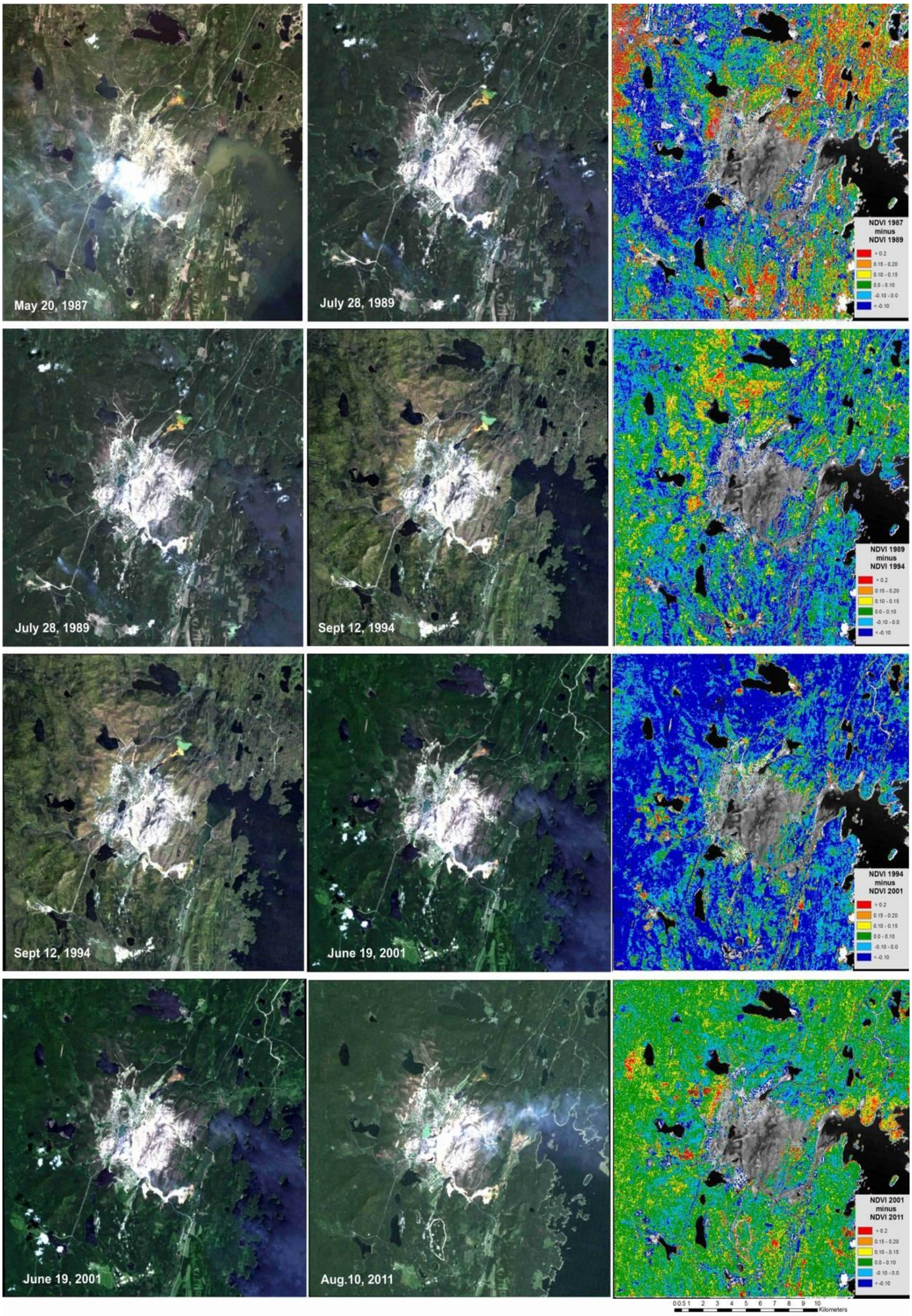

Fig. 7.6 Landsat image pairs used for computation of NDVI-change between two successive Landsat images. Colour scale in the difference image is the same as in Fig. 7.5.

This procedure produced very acceptable results, and we were able to compute NDVI-images from each Landsat image, and subsequently detect changes by computing the difference between two subsequent NDVI images (Fig. 7.7), in order to identify the changes in vegetation quality between two successive images. In the difference images, the red colours indicate that the difference is positive, which means that the NDVI in the later image is lower (and hence the vegetation less vital) than in the earlier image. Green and cyan colours indicate a more or less steady situation, and the dark blue colours indicate that the NDVI in the later image is higher (and hence the vegetation more vital) than in the earlier image.

From 1987 to1989 we observe a significant deterioration, which is a bit surprising, as we are comparing an image from the start of the growing season with an image in the middle of the growing season. The fact that the red areas correspond with prevailing wind directions increases the likelihood that this deterioration is indeed related to the smelter emissions. The dark blue areas indicate local improvement of vegetation health, but as the blue area corresponds with some haze in the 1987 image, we are not sure if these values are realistic, as smoke, clouds and haze tend to depress the NDVI.

From 1989 to 1994 we observe a further deterioration towards the NW and NE. Between 1994 and 2001 we find an overall and fairly uniform improvement of the vegetation conditions, except for a zone of a few km wide in the direct vicinity of the smelter area, which – judging by the green-magenta colours - appears unchanged. Some larger NDVI-changes are related to changes in land-use (e.g. new farmland). The overall improvement makes it very attractive to conclude that the closure of the smelter (between 1991 and 1997) has indeed given the vegetation the opportunity to recover somewhat. However, we have to be careful in drawing this conclusion to firmly, as in this image pair we are comparing an image from the end of the growing season (September) with an image in the middle of the growing season (June).

The last image pair (2001-2011) should reflect continuous operation of the smelter, and indeed shows an over-all deterioration of the vegetation. The affected region in the north-west of the smelter area, which we described in a previous section, is marked by particularly strong decrease in vegetation vitality. In the previous sections we described how our field data clearly revealed serious damage to the vegetation health, and it is therefore not surprising to see this confirmed by the comparison of these two images.

From the data presented above it is clear that the smelter is having an increasing impact on the vitality of the vegetation, which corresponds well with the result of the lichen monitoring. For that reason we have also made the comparison between the 1989-image and the 2011-image (Fig. 7.7). The results show that the vegetation status in 2011 is similar to slightly better compared to 1989 for most of the area (cyan-green colours). The significantly healthier areas (marked by dark blue in the image) can be attributed to changes in land use. The green-red-yellow zones however indicate a lower NDVI in 2011 compared to 1989, which implies that in these regions the vegetation is in a worse shape in 2011 than in 1989. The affected areas seem to display a vague plume-like pattern, and the observed directions (white arrows) seem to correspond with dominant wind-directions, and hence emphasize the airborne nature of the pollution.

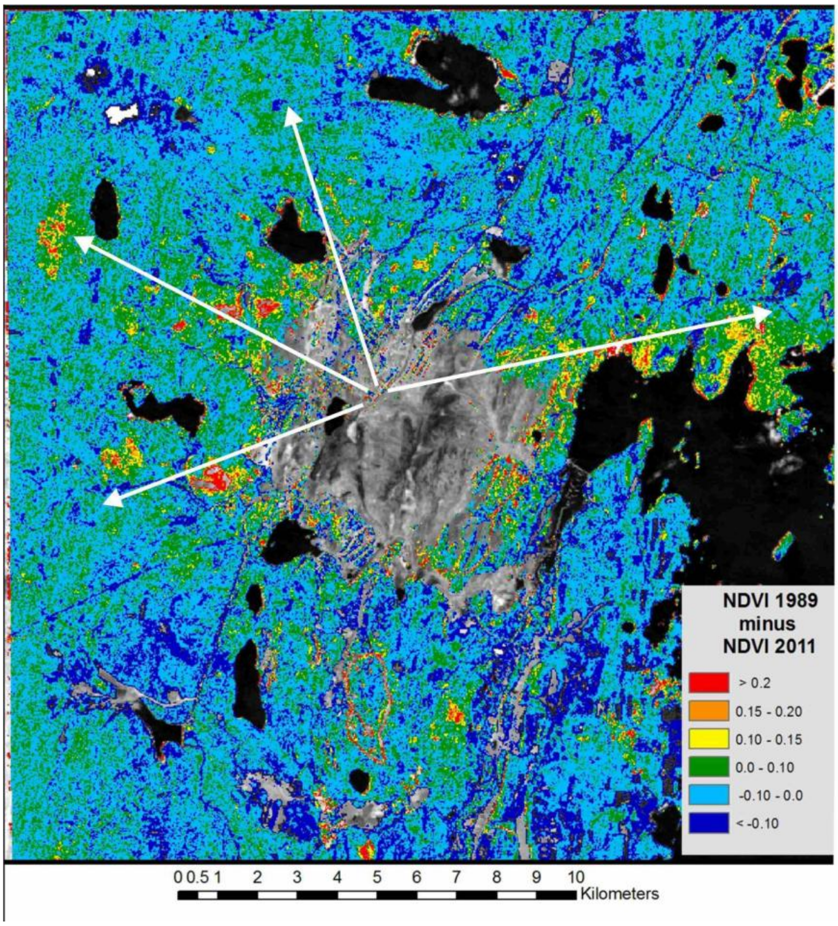

Fig. 7.7 Results of the comparison of the NDVI from the 1989-image and the 2011-image. The white arrows mark the directions in which the effects of pollution seem to be most noticeable.

The analysis of hypertemporal SPOT-Vegetation derived NDVI and fAPAR and the comparison with spectral indices derived from in situ samples showed that vegetation at distances >10 km from the smelter is healthier, showing higher chlorophyll content, better leaf structure, and higher vegetation densities. These indices are not correlated with distance from Karabash, and the effects of the smelting operation on the environment are less obvious (or cannot be identified). This is not to say that smelter emissions have no impact at distances >10 km. Studies of naturally growing and transplanted lichens have identified the fallout of metal-rich particulate for >30 km from the smelter (Williamson et al., 2008). However, the levels of metals deposited at this distance are low due to increasing dispersion away from the smelter.

For *in situ* samples close to Karabash, the spectral indices also correlate with the time series derived indices. A positive relationship between the spectral indices and $\mu[X_{i..}]$ indicates that less stressed vegetation shows higher vegetation densities. Healthier vegetation also shows less overall and between-years variation: spectral indices correlate negatively with $CV[X_{i..}]$ and $CV[X_{i.}]$. This indicates that less stressed vegetation shows more resilience towards other factors and is thus more stable over time. The positive relation between $r[Z_X]$ and spectral indices indicate that healthier vegetation, located at further distances from Karabash, shows a gradually more significant increase of photosynthetic activity over time, while this is not the case for the vegetation close to the smelter, where apparently vegetation stress impedes this trend over time.

At greater distances from Karabash, seasonal and in-between year variations in vegetation density, and trends over time, are not related to spectral vegetation stress indicators.

The general positive trend of vegetation indices over time at further distances from Karabash can possibly be attributed to the prolongation of the growing season. Other studies have linked the increase of photosynthetic activity over time to climate change. The analysis of changes in phenology shows that vegetation gradually reaches higher peaks in summer months. In particular, the late autumn months show a positive trend of photosynthetic activity. This indicates a prolongation of the vegetative season towards the late autumn, thereby also leading to lower dips in the winter months. This is especially clear from the $Z_{NDVI,m}$ series trends. Since the fAPAR time series was validated using data during the crop season, the uncertainty of fAPAR in winter months is higher, and no conclusions can be drawn from the lower $r[Z_{fAPAR,m}]$ values in these months.

In Karabash, both spectral indices, related to leaf pigments, internal leaf structure and thus plant health, derived from *in situ* birch spectra, and indices derived from NDVI and fAPAR time series, have shown that the most affected area ranges up to 10 km distance from the smelter. Correlation analysis between the spectral and time series indices have revealed that vegetation stress impedes a gradual increase of photosynthetic activity in close proximity to the smelter, which is observed at larger distances. Healthier vegetation at larger distances from the smelter shows higher vegetation densities, lower overall and between-year variation and a more positive trend over time. In these areas, our analysis showed gradually higher summer peaks and a prolongation of the growing season towards the autumn months. According to other authors, this increase can be related to climate change (Tucker et al., 2001). The analysis targeted different land cover classes, in order to focus on a range of vegetation densities. Although there is a gradual increase of vegetation density with increasing distance from the smelter, and the land cover classes show a concentric pattern around Karabash, the analysis showed similar results, independent of the land cover class. The differences between vegetation status and vegetation stress is more defined by the distance to the Karabash smelter, and thus vegetation stress, than the vegetation density or land cover class.

7.6 Environmental impacts at Mednogorsk

7.6.1 Heavy metal pollution

In order to determine to what extent the spectral properties of the soil are related to the observed pollution with heavy metals, we generated scatter plots comparing the two spectral ratios with the chemical data for the same samples (Fig. 7.8 and Fig. 7.9). Fig. 7.8 shows that the spectral ratio 650/465 correlates strongly with Sb and Cd. For the other elements the correlation is weaker, but we believe that there is a trend (red arrows), especially if we exclude the samples with extremely high metal contents from our comparison. Also the samples with high band ratio values should probably be ignored, as these represent samples from the open pit and the settling ponds, and as such have no direct relation with the pollution by the smelter.

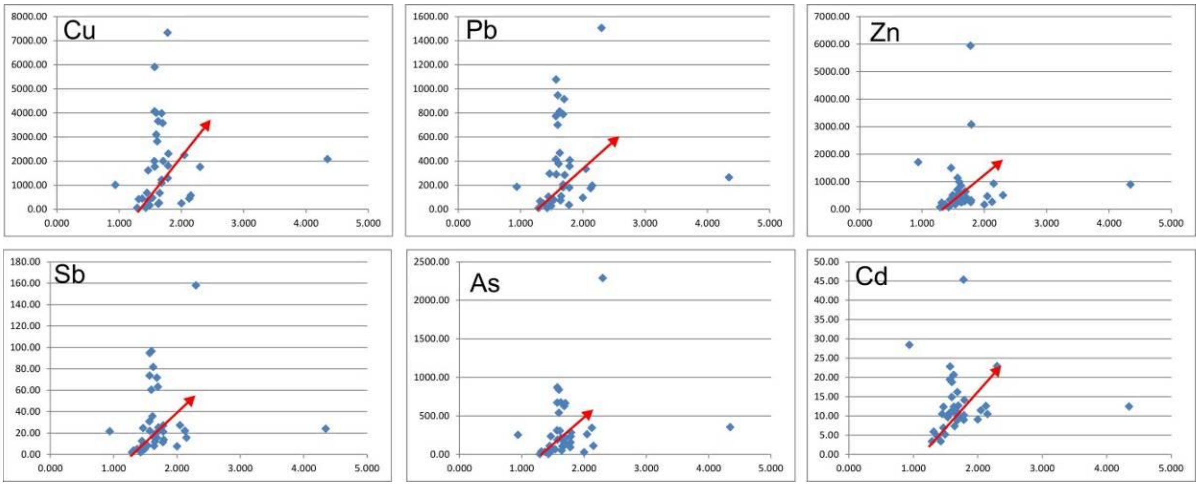

Fig. 7.8 Scatter plots for the spectral ratio 650/465nm with elements that were found to be significantly enhanced in the vicinity of the smelter. Red arrows indicate the interpreted trends.

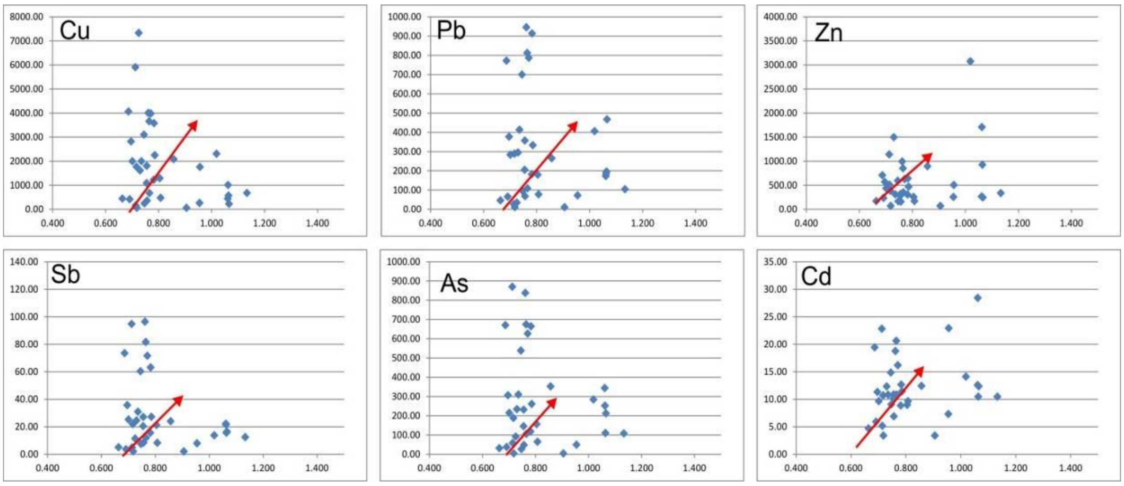

Fig. 7.9 Scatter plots for the spectral ratio 759/937nm with elements that were found to be significantly enhanced in the vicinity of the smelter. Red arrows indicate the interpreted trends.

The scatter plots in Fig. 7.10 show significantly more scatter, but if we disregard the high ratio values, which correspond with the mine-dumps, and the extreme values for the chemical elements, we believe that there is still a fairly significant correlation, in particular for Cd, As and Sb.

7.6.2 Vegetation stress

From our field observations we have concluded that there appears to be a direct relationship between the density of vegetation and the distance to the smelter. This conclusion is very well supported by an image of the Normalized Difference Vegetation Index (NDVI) calculated from a Landsat image acquired on July 03, 2009 (Fig. 7.10), showing a strong halo of low vegetation around the smelter.

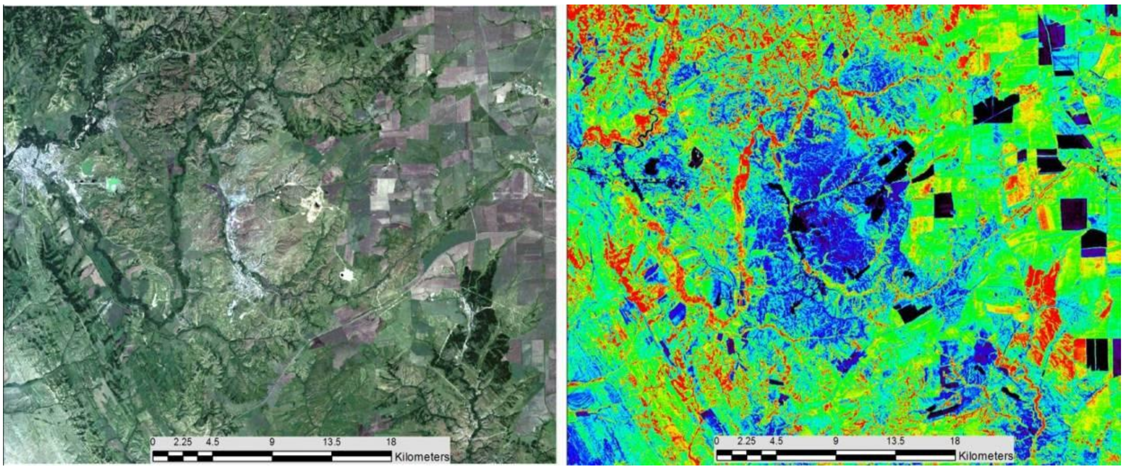

Fig. 7.10 a (left): Landsat image acquired on July 03, 2009; b(right): NDVI from the 1988 Landsat image.

As explained in a previous section, the NDVI allows us to make an estimation of the amount of chlorophyll in a pixel. However, since in this case most pixels will be a mixture of soil/rock and vegetation, the NDVI-signature we have obtained here will mostly tell us something about the vegetation density, and not so much about the status of individual plants. In order to determine if we could correlate changes in the vegetation density with changes in the health of the vegetation, we have measured birch leaf spectra on a section through the halo that stands out so clearly in the NDVI-image.

Unfortunately, as can be seen on the photographs in Figs. 5.30 and 5.31, the amount of birch trees in this area is very limited, and most of them are small and shrub-like, which is not optimal for sampling. Also, we have to keep in mind that the spectrometer that was used during that field trip was damaged, and the spectra may not be very reliable.

Because of the problems with the spectrometer we decided that we could only use the position of the red edge, and that the other parameters, which rely on absolute reflectance values (and hence accurate spectra), could not be used with any confidence.

The red-edge position of the birch-leaves (Fig. 7.11) shows a pattern that we cannot explain, as from our data it appears that the leaves with higher red-edge positions, and hence less stressed, are located in the impacted area around the smelter, directly in the prevailing directions of the smoke plume and that the areas at the margin and outside of the impacted halo have much lower red-edge positions, which suggests that these trees are more under stress.

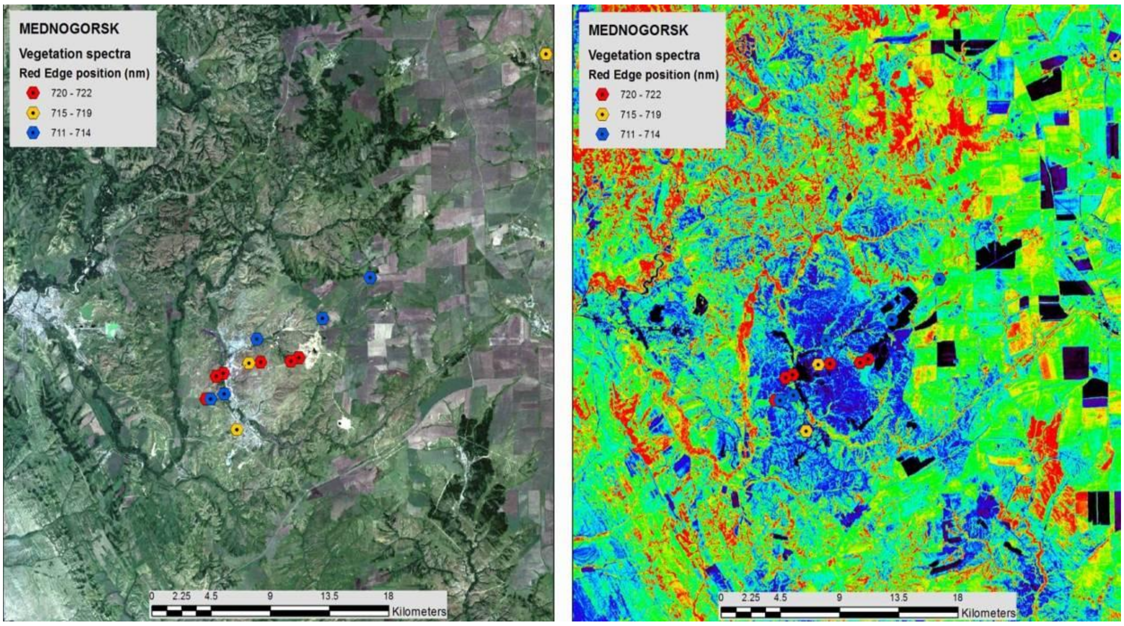

Fig. 7.11 a(left): Red edge position (in nanometers) for birch leaves plotted on the Landsat image. B(right) Red edge position for birch leaves plotted on the NDVI-image.

In early summer 2011 a new worldview acquisition was requested, and the image was captured on Sept.1, 2011 and subsequently processed and analyzed for variations in soils and vegetation. Since we did not have suitable ground control data for the atmospheric correction of the WV2-image, we had to find a workable substitute for the atmospheric correction. After some experimenting we decided to use the Internal Average Relative Reflection (IARR) method, followed by a subtraction of the darkest pixel spectrum. The latter spectrum was obtained from the pit-lake.

We have demonstrated that we are able to identify a large halo with anomalous vegetation around the smelter on the basis of a Landsat NDVI. However, as explained before, the NDVI-signature we have obtained here will most likely tell us something about the vegetation density, and not so much about the health status of individual plants.

For the Karabash region we established a number of very useful parameters, derived from leaf spectra, very clearly demonstrating the changing health status of birch trees as a function of proximity to the smelter. However, these parameters could be established with a fair degree of reliability because we had many measurements, and they were made with a reliable spectrometer. In addition, they could successfully be reproduced in WorldView2-imagery because the imagery was very well calibrated, which is extremely important when looking at such subtle spectral variations.

Such quality data are unfortunately not available for the Mednogorsk area, and for that reason we decided to limit this study to testing the parameters that were found to be meaningful in the Karabash area, using the WorldView2-imagery that was radiometrically corrected by means of the IARR-correction.

The Worldview image was acquired in September, after our field campaign in July, see Figs. 5.30 and 5.31. At the time of the field work the area was already very dry. Green vegetation was mostly restricted to the creek beds, which was relatively dense and looked green and healthy (Fig. 7.12).

In the Mednogorsk area, the WV7/WV8 ratio, which gave the best results for Karabash, was not informative (Fig. 7.13). Other indices that we calculated seem to be much more effective, as they show patterns that correlate well with the Pb content of soils, and also with the area where the surface shows a dark stain (Fig. 7.14).

Fig. 7.12 Vegetation in the creek bed just west of the smelter. Distance to the smelter is about 1.5 km.

Particularly encouraging are the results for the band ratio WV8/WV6. This image (Fig. 7.14) shows a very clear zone adjacent to the smelter where the ratio values are much lower than in other vegetated parts of the image. Since this ratio is a good indicator of the relation between the red edge and the NIR, it allows us to map the chlorophyll content of the leaves. On the basis of this figure we can conclude that the pollution from the smelter has a direct impact on the chlorophyll content of the leaves.

In Mednogorsk, no evidence from the effect of mining on vegetation health could be found from time series analysis of SPOT-Vegetation derived indicators.

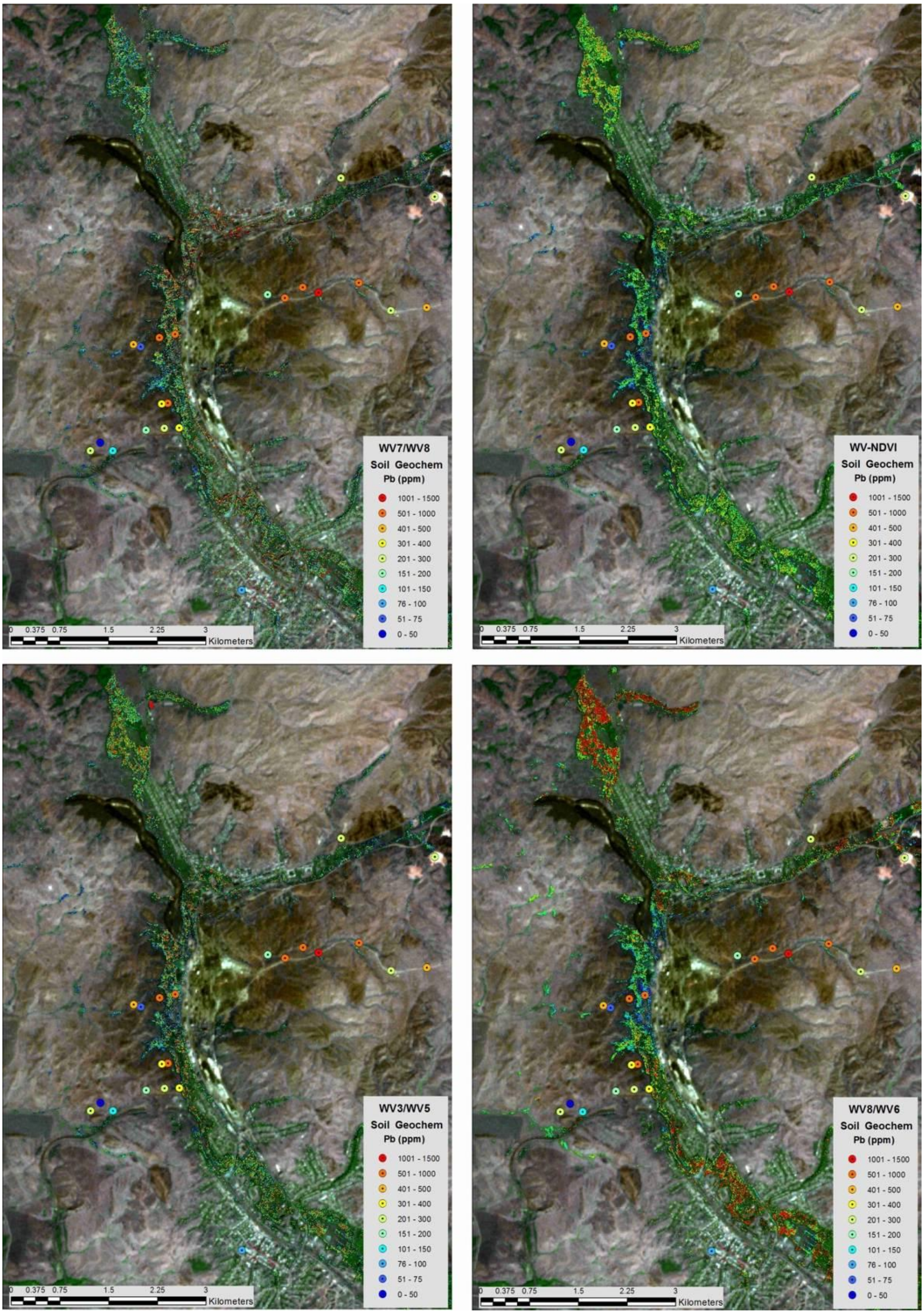

Fig. 7.13 a(top-left) ratio of WV2 bands 7/8 for vegetation. B(top right) WV2-NDVI for vegetation showing slightly lower values in vicinity of the smelter. C(bottom-left) ratio of WV2 bands 3/5 which corresponds to green over red, and is a good indicator for the greenness of the vegetation. D(bottom-right) ratio of WV2 bands 8/6, which is a good indicator for the amount of chlorophyll in the leaves, and hence for the vitality of the vegetation.

7.6.3 Contamination of soils

The observed correlation between band ratios from the soil spectra and the soil geochemistry is very encouraging. It implies that spectral remote sensing could be a useful alternative to estimate the spatial extent of the pollution in an efficient manner. Provided that we use the appropriate type of satellite imagery, we should be able to use remotely sensed data in order to map the trends we identified on the basis of the field spectra.

The band ratios (650/465nm and 759/937nm) used for correlation of the soil spectra with soil chemistry correspond roughly with WV5/WV2 and WV6/WV8 (Fig. 7.14). In order to be able to directly compare the field spectra with WV2-ratios we have resampled the field spectra to the successive WV2-band positions using the Envi spectral Library resampling module, and plotted the samples on the respective ratio images.

The first image shows that the WV5/WV2 band ratio yields the expected results for the open-pit areas and the settlement ponds, but not for the area that surrounds the smelter. Although we do not have a full explanation for this, we suspect that this has to do with the contrast between the material we sampled and the real composition of the surface. The material we sampled was typically fine-grained clayish brown-red soil and this material probably contained enough goethite to detect with the spectrometer.

In reality however, most of the surface is dominated by hematitic gravel and rock covered with a very dark kind of varnish (see Fig. 5.31), and we suspect that the dominance of this dark material effectively masked out the subtle goethite-signatures. This dark material is very visible in a colour composite of WV2 bands 8-6-5 (Fig. 7.15), and can be mapped efficiently using principal component analysis of bands 5-8.

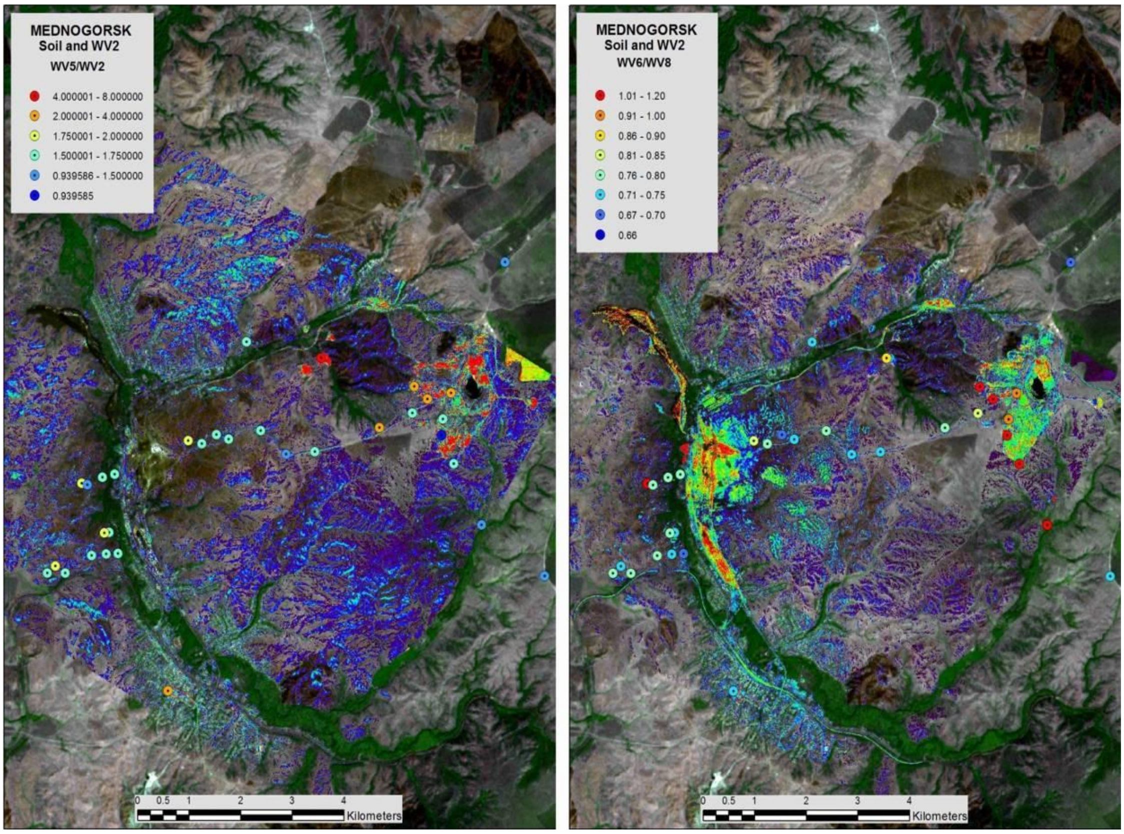

Fig. 7.14 a(left) Band ratio image for WV5/WV2 with corresponding band ratio values of resampled soil spectra; b(right) Band ratio image for WV6/WV8 with corresponding band ratio values of resampled soil spectra. The back ground image is an Aster synthetic true-colour image.

Much better results were obtained for the WV6/WV8-ratio (Fig 7.15 b) which we consider to represent not just goethite, but also other minerals that contain ferric Iron, such as hematite.

This image shows a much better correlation with the band ratios that we derived from the field spectra.

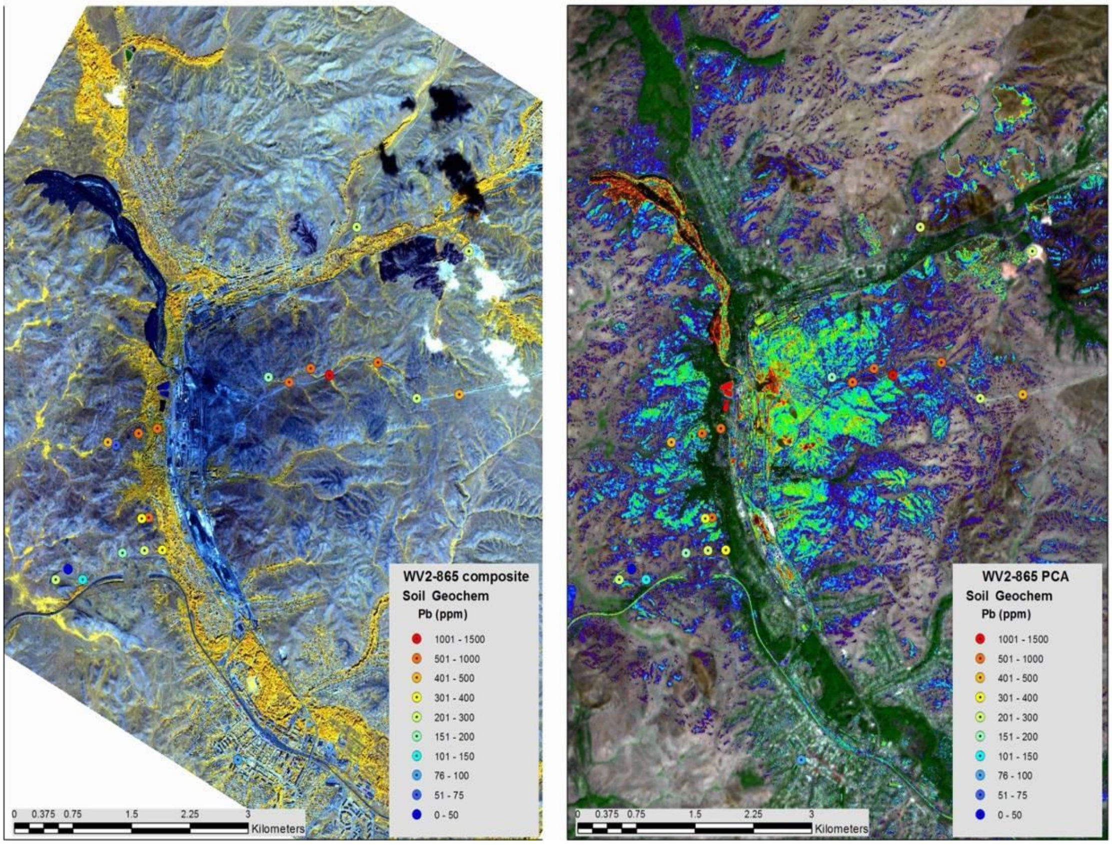

Fig. 7.15 a(left) colour composite of WordlView bands 865. b(right) colour coded first principal component of WV-bands 5678. Lead analysis overlain for comparison with soil contamination

7.7 Socio-economic aspects

Socio-economic aspects of the study were dealt with in the report for ImpactMin WP3. The original intention, in the WP7.0.4 Implementation Plan, was to integrate the outcomes of the ground-based and remote sensing environmental studies with the socio-economic data to determine the relationship between actual and perceived mining-related impacts. Unfortunately, there was a general reluctance amongst the population of both Karabash and Mednogorsk to discuss their views relating to the environmental impacts of the smelters. This is thought to stem from the fact that the smelters are the main employers in each area, and that environmental concerns may lead to their closure and therefore the loss of a significant number of jobs. The closure of the Karabash smelter in 1991 led to significant economic hardship; the smelter was reopened in 1997 to alleviate this. The number of surveys collected in Karabash and Mednogorsk was therefore limited, enough to give a very general impression of the views of certain members of the community, but was far from representative. The sampling was inadequate to determine if there was any spatial relationship between proximity to sources of pollution and the views of the townspeople.

7.8 Publications resulting from the ImpactMin study in Karabash and Mednogorsk

Goossens M.A. 2012. Environmental Impact Monitoring using vegetation and soils in the Karabash Smelter area, Mednogorsk, Central Urals. GRSG Annual General Meeting, London Dec 11-13, 2012

Goossens M.A., Tote C., Williamson B., Udachin V. and Gyuris P., 2012. Environmental Monitoring of Mining areas. EAGE, Paris, Sept 2-5, 2012.

Goossens M.A. and Gyuris P., 2011. IMPACTMIN: Monitoring Mining-related Environmental Impact. GRSG Annual General Meeting, Frascati, Dec 7-9, 2011.

Purvis O.W., Williamson B.J., Spiro B., Udachin V., Mikhailova I.N. and Dolgopolova A., in press. Lichen monitoring as a potential tool in environmental forensics: case study of the Cu smelter and former mining town of Karabash, Russia. Geological Society of London.

Spiro B., Udachin V., Williamson B.J., Purvis O.W., Tessalina S.G. and Weiss D.J., 2012. Lacustrine sediments and lichen transplants: two contrasting and complimentary environmental archives of natural and anthropogenic lead in the South Urals, Russia. Aquatic Sciences, 1-14.

Tote C., Delalieux S., Goossens M., Williamson B. J. and Swinnen E., submitted. Monitoring environmental health using SPOT-Vegetation derived indices in Karabash, Russia. International Journal of Remote Sensing.

Tote, C., Goossens, M., Williamson, B., Purvis, W., Bellis, D., Udachin, V., Swinnen, E. and Reusen, I. (2012) Vegetation stress due to mining impact in Karabash using TSA of SPOT-VGT. *1st EARSeL Workshop on Temporal Analysis of Satellite Images.* Mykonos, Greece, 23rd – 25th May, 2012.

Williamson B. J., 2012. Is the Karabash smelter cleaning up its act? Evidence from lichen and satellite monitoring. The Quarries and Mines Directory.

8 CONCLUSIONS

For Karabash, and to a somewhat lesser extent for Mednogorsk, it has been demonstrated that with respect to different environmental media/indices (soils, vegetation diversity, lichens, tree-bark, birch leaf stress), clear trends exist with distance from the smelter. We were able to reproduce these trends very effectively in the various types of satellite imagery, obviously at different spatial and spectral resolutions. Using multi-temporal imagery (Spot-vegetation, Landsat, Worldview2) we could map both short-term changes and long-term changes in vegetation health. The data show that there can be very severe short-term vegetation damage as a result of emissions of sulphuric acid and acid-generating metal sulphate particles, also shown from pH data for twig and trunk bark in the area.

From a long-term point of view it was of particular interest to investigate whether the installation of a new Ausmelt smelter in 2006 resulted in corresponding environmental improvements. Using a time series of Landsat images from 1998 to 2011 we could identify different phases of environmental deterioration and improvement. Importantly, we could demonstrate that the environmental situation in 2011 is similar and locally even worse compared to the situation in 1998, which implies that the improvements made to the smelter may not have been as effective as was planned. Comparison of lichen transplant data from the MinUrals project (2001) with that from ImpactMin (2011) supports this observation

The main conclusions from the project for the Karabash demo-site are:

a) The main zone of impact extends around 8 to 15 km from the Karabash smelter, depending on wind direction;

b) Soil Pb concentrations are ca. 15 times greater than background levels (~20 ppm) at a distance of 5 km, and 150 times background levels within 2 km of the smelter. Similar enrichment factors were observed for Cd, Mo, Cu, Zn and As;

c) From preliminary geochemical data, Pb concentrations in native lichens (our proxy for Pb deposited in the environment) were higher in 2011 than in 2001, despite the installation of the Ausmelt system. Particles from the smelter could be identified in lichens for up to 30 km from Karabash. Lichens have once again proven to be particularly sensitive and effective for monitoring the nature and spatial distribution of heavy metal fallout from point sources;

d) SO_2 and airborne particulate from different processes in the smelter are decoupled during atmospheric transport, with large Cu-Fe-rich (30 to >100 μm) particulate from the blast furnace deposited in lichens closest to the smelter (<12 km), finer (<2 μm) particulate from the converter carried up to and probably beyond 30 km, and SO_2 (and related secondary particulate) impacting the forest either locally, in discrete areas (as identified from airborne imagery) due to temperature inversions and topographic effects, or carried along with the converter particulate to greater distances;

e) There is an excellent correlation in the zonal pattern of impact around the smelter between the data from the IR spectral analysis of birch leaves, the results from time series analysis of hypertemporal satellite imagery and the geochemical data for lichens, trunk and twig bark and soils.

The main conclusions from the Mednogorsk site are:

a) From the Landsat NDVI, there is a large halo of anomalous vegetation around the smelter. However, as explained before, the NDVI-signature we have obtained here will most likely tell us something about the vegetation density, and not so much about the health status of individual plants.

b) An observed correlation between band ratios from the in situ soil spectra and the soil geochemistry implies that spectral remote sensing could be a useful alternative to ground-based studies to estimate the spatial extent of the pollution. Provided that we use the appropriate type of satellite imagery, we should be able to use remotely sensed data in order to map the trends we identified on the basis of the field spectra.

Concluding remarks: The case studies at Karabash and Mednogorsk have shown that the implementation of existing, adapted and new methodologies, whereby in-situ field and remote sensing data are combined, may provide a highly sensitive suite of tools for impact monitoring of mining-related activities at different spatial and temporal scales. Although the environmental impacts of mining-related activities around Karabash are severe, the nature of these impacts is common to many other mining centres worldwide, which is what makes our study so relevant. Besides this, we have generated interesting and publishable scientific results for the Karabash and Mednogorsk case study sites to demonstrate how a combination of smart and innovative ground investigations and remote sensing can contribute significantly to the understanding of the nature, spatial and temporal extent of environmental impacts from mining-related activities.

9 REFERENCES

Adams, M., Philpot, W. and Norvell, W., 1999. Yellowness index: An application of spectral second derivatives to estimate chlorosis of leaves in stressed vegetation. International Journal of Remote Sensing, 20 (18): 3663-3675.

Adamsen, F., Pinter, P., Barnes, E., LaMorte, R., Wall, G., Leavitt, S., and Kimball B., 1999. Measuring wheat senescence with a digital camera. Crop Science, 39:719–724.

Arino, O., Gross, D., Ranera, F., Bourg, L., Leroy, M., Bicheron, P., Latham, J., Di Gregorio, A., Brockman C., Witt, R., Defourny, P., Van Cutsem, C., Herold, M., Sambale, J., Achard, F., Durieux, L., Plummer, S. and Weber, J.-L., 2007. GlobCover: ESA service for global land cover from MERIS. In: International Geoscience and Remote Sensing Symposium.

Asner, G., Hicke, J., and Lobell, D., 2003. Per-pixel analysis of forest structure: Vegetation indices, spectral mixture analysis and canopy reflectance modeling. In Remote sensing of forest environments: concepts and case studies, edited by M. Wulder, and S. Franklin: Kluwer Academic Publishers).

Ayala-Silva, T., and Beyl, C., 2005. Changes in spectral reflectance of wheat leaves in response to specific macronutrient deficiency. Advances in Space Research 35 (2): 305-317.

AZoM News, 2007. Non-Ferrous Alloys and Metals. Russian Copper Company Commissions Ausmelt Copper Smelter. 07/03/2007.

Baret, F., and Guyot, G., 1991. Potentials and limits of vegetation indices for LAI and APAR assessment. Remote Sensing of Environment 35: 161-173.

Bargagli, R., 1998. Trace Elements in Terrestrial Plants: An Ecophysiological Approach to Biomonitoring and Biorecovery; Springer: Berlin.

Bell, J. N. B. and Treshow, M., 2002. Historical perspectives. In: Air Pollution and Plant Life (eds. J. N. B. Bell and M. Treshow), pp. 5–21. John Wiley and Sons, Chichester, UK.

Blackburn, G. 1998. Spectral indices for estimating photosynthetic concentrations: a test using senescent tree leaves. International Journal of Remote Sensing 19: 657-675.

Blackburn, G. A., and Steele, C. M., 1999. Towards the remote sensing of matorral vegetation physiology: Relationships between spectral reflectance, pigment, and biophysical characteristics of semiarid bushland canopies. Remote Sensing of Environment, 70: 278–292.

Broge, N. H., and Leblanc, E., 2000. Comparing prediction power and stability of broadband and hyperspectral vegetation indices for estimation of green leaf area index and canopy chlorophyll density. Remote Sensing of Environment 76: 156-172.

Brooks, S. J., Udachin, V. and Williamson, B.J., 2005. Impact of copper smelting on lakes in the southern Ural Mountains, Russia, inferred from chironomids. Journal of Paleolimnology, 33:229-241.

Curran, P., Dungan, J. and Gholz H., 1990. Exploring the relationship between reflectance red edge and chlorophyll content in slash pine. Tree Physiology 7: 33-48.

Daughtry, C., Walthall, C., Kim, M., Brown de Colstoun, E., and McMurtrey J., 2000. Estimating corn leaf chlorophyll concentration from leaf and canopy reflectance. Remote Sensing of Environment, 74 (2): 229-239.

Dawson, T. P. and Curran, P. J., 1998. A new technique for interpolating the reflectance red edge position. International Journal of Remote Sensing, 19: 2133–2139.

Diaz, J., Bernal, A., Pomar, F. and Merino, F., 2001. Induction of shikimate dehydrogenase and peroxidase in pepper (*Capsicum annuum* L.) seedling in response to copper stress and its relation to lignification. Plant Science, 161: 179–188.

Dixon, R.A., Achnine, L., Kota, P., Liu, Ch.-J., Reddy, M.S.S. and Wang, L., 2002. The phenylpropanoid pathway and plant defence — a genomics perspective. Molecular Plant Pathology, 3: 371–390.

Eitel, J.U.H, Keefe, R.F., Long, DS.S., Davisand, A.S. and Vierling, L.A., 2010. Active Ground Optical Remote Sensing for Improved Monitoring of Seedling Stress in Nurseries. Sensors 2010, *10*, 2843-2850; doi:10.3390/s100402843.

Elvidge, C. and Chen Z., 1995. Comparison of broad-band and narrow-band red and near-infrared vegetation indices. Remote Sensing of Environment, 54: 38-48.

Ferriera-Marques, C., 2003. World Environment News. Russia's industrial wasteland chokes on fumes. 23/04/2003

Gallagher, F.J., Pechmann, I., Bogden, J.D., Grabosky, J. and Weis, P., 2008. Soil metal concentrations and productivity of *Betula populifolia* (gray birch) as measured by field spectrometry and incremental annual growth in an abandoned urban Brownfield in New Jersey. Environmental Pollution, 156: 699–706.

Gamon, J.A. and Surfus, J., 1999. Assessing leaf pigment content and activity with a reflectometer. New Phytologist, 143 (1): 105–117.

Gilbert, O. L., 1969. The effect of SO_2 on lichens and bryophytes around Newcastle upon Tyne. Air Pollution, Proceedings of the first European Congress on the Influence of Air Pollution on Plants and Animals, April 22–27, 1968. Centre for Agricultural Publishings and Documentation, Wageningen, the Netherlands, pp. 223–233.

Gilbert, O. L., 1970. A biological scale for the estimation of sulphur dioxide pollution. New Phytologist 69: 629–634.

Glenn, E.P., Huete, A.R., Nagler, P.L. and Nelson, S.G., 2008. Relationship Between Remotely-sensed Vegetation Indices, Canopy Attributes and Plant Physiological Processes: What Vegetation Indices Can and Cannot Tell Us About the Landscape. Sensors, 8: 2136-2160.

Haboudane, D., Miller, J., Tremblay, N., Zarco-Tejada, P. J. and Dextraze, L., 2002. Integrated narrow-band vegetation indices for prediction of crop chlorophyll content for application to precision agriculture. Remote Sensing of Environment 81 (2-3): 416-426.

Haboudane, D., Tremblay, N., Miller, J. and Vigneault, P., 2008. Remote estimation of crop chlorophyll content using spectral indices derived from hyperspectral data. IEEE Transactions of Geoscience and Remote Sensing 46 (2): 423-437.

Hagner, O., and Rigina, O., 1998. Detection of forest decline in Monchegorsk area. Remote Sensing of Environment 63: 11-23.

Harris, J.R., Rencz A.N., Ballantiyne B. and Sheridon, C., 1998. Mapping altered rocks using Landsat TM and Lithogeochemical data: Sulphurets-Brucejack Lake District, British Columbia, Canada. Photogrammetric engineering and Remote sensing, Vol 64, No 4, April 1998, pp. 309-322.

Hawksworth, D. L., 1973. Mapping Studies. In: Air Pollution and Lichens (eds. B. W. Ferry, M. S. Baddeley and D. L. Hawksworth), pp. 38–76. Athlone Press, London.

Holben, B. 1986. Characteristics of maximum-value composite images from temporal AVHRR data. International Journal of Remote Sensing 7 (11): 1417-1434.

Horler, D. N. H., Dockray, M. and Barber J., 1983. The red edge of plant leaf reflectance. International Journal of Remote Sensing, Vol. 4, No. 2: 273-288.

Huete, A. 1988. A soil-adjusted vegetation index (SAVI). Remote Sensing of Environment, 25 (3): 295-309.

Hunt, E., Daughtry, C., Eitel, J., and Long, D., 2011. Remote sensing leaf chlorophyll content using a visible band index. Agronomy Journal, 103 (4): 1090-1099.

Khokhar, M., Frankenberg, C., Hollwedel, J., Beirle, S., Kühl, S., Grzegorski, M., Wilms-Grabe, W., Platt, U. and Wagner, T., 2004. Satellite remote sensing of atmospheric SO2: volcanic eruptions and anthropogenic emissions. Proceedings of the ENVISAT & ERS Symposium, 6-10 September 2004, Salzburg, Austria, ESA publication SP-572.

Janas, K.M., Cvikrova, M., Pałagiewicz, A., Szafrańska, K. and Posmyk, M.M., 2002. Constitutive elevated accumulation of phenylpropanoids in soybean roots at low temperature. Plant Science, 163: 369–373.

Jbir, N., Chaib, W., Amma, S., Jemmali, A. and Ayadi, A., 2001. Root growth and lignification of two wheat species differing in their sensitivy to NaCl, in response to salt stress. CR Academy Sciences Paris, 324: 863–868.

Jouili, H. and Ferjani, E.E., 2003. Changes in antioxidative and lignifying enzyme activities in sunflower roots (*Helianthus annus* L.) stressed with copper excess. CR Biologies, 326: 639–644.

Justice, C., J. Townshend, B. Holben, and C. Tucker. 1985. Analysis of the phenology of global vegetation using meteorological satellite data. International Journal of Remote Sensing (8): 1271-1318.

Kanke, Y., Raun, W., Solie, J., Stone, M. and Taylor, R., 2012. Red Edge as a potential index for detecting differences in plant nitrogen status in winter wheat. Journal of Plant Nutrition, 35: 1526-1541.

Khokhar, M., Frankenberg, C., Hollwedel, J., Beirle, S., Kühl, S., Grzegorski, M., Wilms-Grabe, W., Platt, U. and Wagner, T., 2004. Satellite remote sensing of atmospheric SO2: volcanic eruptions and anthropogenic emissions, Proceedings of the ENVISAT & ERS Symposium, 6-10 September 2004, Salzburg, Austria, ESA publication SP-572.

Klisch, A., Royer, A., Lazar, C., Baruth, B. and Genovese, G., 2006. Extraction of phenological parameters from temporally smoothed vegetation indices. ISPRS Archives XXXVI-8/W48 Workshop proceedings: Remote sensing support to crop yield forecast and area estimates. pp. 91-95.

Kovacik, J. and Klejdus, B., 2008. Dynamics of phenolic acids and lignin accumulation in metal-treated *Matricardia chamomilla* roots. Plant Cell Reports, 27: 605–615.

Kriegler, F.J., Malila, W.A., Nalepka, R.F. and Richardson, W., 1969. Preprocessing transformations and their effects on multi-spectral recognition. In *Proceedings of the Sixth International Symposium on Remote Sensing of Environment*, University of Michigan, Ann Arbor, MI, USA, 1969; pp. 97-131.

La Franiere, S., 1999. Town Sacrifices Health for Jobs. Moscow Times online. www.themoscowtimes.com/news/article/town-sacrifices-health-for-jobs/274474.html (16/2/2011) .

Latifovic, R., Fytas, K. and Paraszczak, J., 2005. Assessing land cover change resulting from large surface mining development. International Journal of Applied Earth Observation and Geoinformation, 7(1): 29-48.

Li, B., Liew O. and Asundi, A., 2006. Pre-visual detection of iron and phospohorus deficiency by transformed reflectance spectra. Journal of Photochemistry and Photobiology 85 (2): 131-139.

Lin, Ch.-Ch., Chen, L.-M. and Liu, Z.-H., 2005. Rapid effect of copper on lignin biosynthesis in soybean roots. Plant Science, 168: 855–861.

Lottermoser, B., 2007. Mine Wastes - Characterization, Treatment, Environmental Impacts. Springer Berlin.

Loughlin, W.P., 1991. Principal component analysis for alteration mapping. Photogrammetric Engineering and Remote Sensing, 57 (9): 1163-1169.

Mandre, M., 2002. Relationships between lignin and nutrients in *Picea abies* L. under alkaline air pollution. Water Air and Soil Pollution, 133: 361–377.

Martin, J.-M. and M. Whitfield, 1983. The significance of the river input of chemical elements to the ocean. p. 265–296. In Trace Metals in Sea Water, ed. by C. S. Wong, E. Boyle, K. W. Bruland, J. D. Burton and E. D. Goldberg, Plenum Press, New York and London.

Mikhailova, I., 2002. Transplanted Lichens for Bioaccumulation Studies. *In:* Nimis, P. L., Scheidgger, C. and Wolseley, P. A. (eds.) *Monitoring with lichens-Monitoring lichens.* Dordrecht, The Netherlands: Kluwer Academic. 301-309.

Mikhailova, I. and Vorobeichik, E. L., 1995. Epiphytic lichenosynusia under conditions of chemical pollution: dose-effect dependencies. Russian Journal of Ecology**,** 26: 425-431.

Mikkola, K. 1996. A remote sensing analysis of vegetation damage around metal smelters in the Kola Peninsula, Russia. International Journal of Remote Sensing, 17 (18): 3675-3690.

Moran, M. S., Maas, S. J., Vanderbilt, V. C., Barnes, M., Miller, S. N., and Clarke, T. R., 2004. Application of image-based remote sensing to irrigated agriculture. In S. L. Ustin (Ed.), Remote sensing for natural resource management and environmental monitoring, Manual of remote sensing (pp. 617–676). Hoboken: John Wiley & sons.

Mutanga, O. and Skidmore, A. K., 2007. Red edge shift and biochemical content in grass canopies. Isprs Journal of Photogrammetry and Remote Sensing, 62: 34–42.

Nestersnko, V., 2006. Urban associations of elements- environmental pollutants in Karabash city (Chelyabinsk oblast) as a reflection of ore-chemical descriptions of mineral raw material. Proceedings of the Chelyabinsk Scientific Center, 3: 58-62.

Nimis, P. L., Scheidegger, C. and Wolseley, P. A. (eds.), 2002. Monitoring with Lichens - Monitoring Lichens, Dordrecht: Kluwer Academic Publishers.

Peñuelas, J. and Filella, I., 1998. Visible and near-infrared reflectance techniques for diagnosing plant physiological status. Trends in Plant Science 3: 151–156.

Peters, A., Walter-Shea, E., A Vina, L. Ji., Hayes M. and Svoboda M., 2002. Drought monitoring with NDVI-based standardized vegetation index. Photogrammetric Engineering and Remote Sensing, 68: 71-75.

Polluted Places, 2005. Karabash, Russia. Nomination/Initial Report. Blacksmith Institute, http://www.pollutedplaces.org/region/e_europe/russia/karabash.shtml

Prakash, A. and Gupta, R., 1998. Land-use mapping and change detection in a coal mining area - a case study in the Jharia coalfield, India. International Journal of Remote Sensing, 19(3): 391-410.

Pu, R. L., Gong, P., Biging, G. S., and Larrieu, M. R., 2003. Extraction of red edge optical parameters from Hyperion data for estimation of forest leaf area index. IEEE Transactions on Geoscience and Remote Sensing, 41: 916–921.

Purvis, O. W., 2010. Chapter 3. Lichens and Industrial Pollution. In: Batty, L. C. and Hallberg, K. (eds.) Ecology of Industrial Pollution. Cambridge: Cambridge University Press.

Purvis, O. W., Chimonides, P. J., Jones, G. C., Mikhailova, I. N., Spiro, B., Weiss, D. and Williamson, B. J., 2004. Lichen biomonitoring near Karabash Smelter Town, Ural Mountains, Russia, one of the most polluted areas in the world. Proceedings of the Royal Society of London B 271: 221-226.

Purvis, O.W., Longden, J., Shaw, G., Chimonides, P.D.J., Jeffries, T.E., Jones, G.C., Mikhailova, I.N. and Williamson, B.J., 2006. Biogeochemical signatures in the lichen *Hypogymnia physodes* in the mid Urals. Journal of Environmental Radioactivity, 90: 151-162.

Qi, J., Chehbouni, A., Huete, A., Kerr, Y. and Sorooshian, S., 1994. A modified soil adjusted vegetation index. Remote Sensing of Environment 48: 119-126.

Rees, W. and Williams, M., 1997. Monitoring changes in land cover induced by atmospheric pollution in the Kola Peninsula, Russia, using Landsat-MSS data. International Journal of Remote Sensing 18 (8): 1703-1723.

Rigina, O., 2002. Environmental impact assessment of the mining and concentration activities in the Kola Peninsula, Russia, by multidate remote sensing. Environmental Monitoring and Assessment, 75(1): 13.

Rondeaux, G., Steven, M. and Baret, F., 1996. Optimization of soil-adjusted vegetation indices. Remote Sensing of Environment 55: 95-107.

Sellers, P. 1985. Canopy reflectance, photosynthesis and transpiration. International Journal of Remote Sensing 6 (8): 1335-1372.Serranoa, L., Penuelasa, J. and Ustinb, S.L., 2002. Remote sensing of nitrogen and lignin in Mediterranean vegetation from AVIRIS data: Decomposing biochemical from structural signals. Remote Sensing of Environment 81: 355–364.

Slayback, D., J. Pinzon, S. Los, and C. Tucker. 2003. Northern hemisphere photosynthetic trends 1982-99. Global Change Biology 9 (1): 1-15.Spiro, B., Weiss, D.J., Purvis, O.W., Mikhailova, I., Williamson, B. J., Coles, B.J. and Udachin, V., 2004. Lead isotopes in lichen transplants around a Cu smelter in Russia determined by MC-ICP-MS reveal transient records of multiple sources. Environmental Science and Technology, 38: 6522-6528.

Tarpley, L., Reddy, K. R., and Sassenrath-Cole, G. F., 2000. Reflectance indices with precision and accuracy in predicting cotton leaf nitrogen concentration. Crop Science, 40: 1814–1819.

Tucker, C., Slayback, D., Pinzon, J., Los, S., Myneni, R. and Taylor, M., 2001. Higher northern latitude normalized difference vegetation index and growing season trends from 1982 to 1999. International Journal of Biometeorology, 45(4), pp. 184-190.Tucker, C., 1979. Red and photographic infrared linear combinations for monitoring vegetation. Remote Sensing of Environment, 8: 127-150.

Udachin, V., Kitagawa, R., Williamson, B. and Sugakhara, T., 2002. Ores and metallurgical slags from the Karabash deposit (the South Urals) and Ashio Japan: composition and potential influence on the environment. In: The Metallogeny of Ancient and Modern Oceans – 2002 (Eds. V. Zaykov, E. Belogub) Miass: Inst. Mineral., Urals Branch of RAS, p. 267-275 (in Russian).

Udachin, V., Williamson, B. J., Purvis, O. W., Spiro, B., Dubbin, W., Brooks, S., Coste, B., Herrington, R. J., Mikhailova, I., 2003. Assessment of environmental impacts of active smelter operations and abandoned mines in Karabash, Ural Mountains of Russia. Sustainable Development, 11: 1-10.

Udachin, V., Yershov, V. and Lansiart, M., 1998. Environmental conditions in the area of exploited massive sulfide deposits of the South Ural. Final Report for TACIS contract FINRUS.

Udelhoven, T., 2011. TimeStats: A software tool for the retrieval of temporal patterns from global satellite archives. IEEE Journal of Selected Topics in Applied Earth Observations and Remote Sensing, 4(2): 310-317.

Verhulst, N. and Govaerts, B., 2010. The normalized difference vegetation index (NDVI) GreenSeeker handheld sensor: Toward the integrated evaluation of crop management. Part A: Concepts and case studies. Mexico, D.F.; CIMMYT.

Voskresensky, G., 2002. The most polluted city on the planet to breathe easier. In Eurasian Metals.

Weiss, M., Baret, F., Eerens, H. and Swinnen, E., 2010. FAPAR over Europe for the past 29 years: a temporally consistent product derived from AVHRR and VEGETATION sensor. Proceedings of the 3rd International symposium on Recent Advances in Quantitative Remote Sensing.

Williamson, B.J., Mikhailova, I., Purvis, O.W. and Udachin, V., 2004a. SEM-EDX analysis in the source apportionment of particulate matter on *Hypogymnia physodes* lichen transplants around the Cu smelter and former mining town of Karabash, South Urals, Russia. The Science of the Total Environment, 332: 139-154.

Williamson, B.J., Purvis, O.W., Mikhailova, I.N. Spiro, B. and Udachin, V., 2008. The lichen transplant methodology in the source apportionment of metal deposition around a copper smelter in the former mining town of Karabash, Russia. Environmental Monitoring and Assessment, 141: 227-236.

Williamson, B.J., Udachin, V., Purvis, O.W., Spiro, B., Cressey, G. and Jones, G.C., 2004b. Characterisation of airborne particulates in the Cu smelter and former mining town of Karabash, South Ural Mountains of Russia. Environmental Monitoring and Assessment, 98: 235-259.

Winkel-Shirley, B., 2002. Biosynthesis of flavonoids and effects of stress. Current Opinion in Plant Biology, 5: 218–223.

Wolseley, P. A., 2002. Using lichens on twigs to assess changes in ambient atmospheric conditions. *In:* Nimis, P. L., Scheidegger, C. and Wolseley, P. A. (eds.) *Monitoring with lichens-Monitoring lichens.* Dordrecht, The Netherlands: Kluwer Academic. pp 291-294.

World Bank Group, 1998. Base Metal and Iron Ore Mining. In: World Bank Group, International Finance Corporation (Eds.), Pollution Prevention and Abatement Handbook: Toward Cleaner Production.

Yang, Y.-J., Cheng, L.-M. and Liu, Z.-H., 2007. Rapid effect of cadmium on lignin biosynthesis in soybean roots. Plant Science, 172: 632–637.

Yokogawa, 2010. Ausmelt Global Environmental Technologies. http://www.yokogawa.com/iab/suc/metals/iab-suc-ausmelt-en.htm (accessed 21/11/10).

Zarco-Tejada, P. J., Miller, J. R., Morales, A., Berjon, A., and Agóera, J., 2004. Hyperspectral indices and model simulation for chlorophyll estimation in open canopy tree crops. Remote Sensing of Environment, 90: 463-476.